Durham E-Theses

The dynamics and ISM properties of high-redshift dusty star-forming galaxies

BIRKIN, JACK,EDWARD

How to cite:

BIRKIN, JACK,EDWARD (2022) *The dynamics and ISM properties of high-redshift dusty star-forming galaxies*, Durham theses, Durham University. Available at Durham E-Theses Online: http://etheses.dur.ac.uk/14586/

Use policy

The dynamics and ISM properties of high-redshift dusty star-forming galaxies

Jack Birkin

A thesis presented for the degree of
Doctor of Philosophy

Centre for Extragalactic Astronomy
Department of Physics
Durham University
United Kingdom

August 2022

The dynamics and ISM properties of high-redshift dusty star-forming galaxies

Jack Birkin

Abstract: In this thesis we present a range of observations of submillimetre galaxies (SMGs), a subclass of dust-obscured star-forming galaxies (DSFGs) at redshifts of $z \sim 1$–5. SMGs are among the most actively star forming sources ever observed, believed to contribute significantly to the star-formation rate density (SFRD) at its peak, so-called "cosmic noon", at $z \sim 2$. Given their extreme nature, SMGs provide a strong test of galaxy formation and evolution models. Advancements in instrumentation, in particular with the Submillimetre Common-User Bolometer Area 2 (SCUBA-2) and the Atacama Large (sub-)Millimeter Array (ALMA), have driven significant progress in SMGs studies over the last decade. We have now identified samples of hundreds of SMGs in survey fields with a plethora of photometric coverage, such as the Cosmic Evolution Survey (COSMOS), the UKIDSS Ultra Deep Survey (UDS) and the Extended Chandra Deep Field Survey (ECDFS). Indeed, the main motivation of this thesis is to exploit these samples of SMGs, with a particular focus on the molecular and ionised gas properties, using state-of-the-art instrumentation such as ALMA and the Northern Extended Millimeter Array (NOEMA) for the former, and the K-band Multi-Object Spectrograph (KMOS) mounted on the Very Large Telescope for the latter.

Firstly, in Chapter 2 we present ^{12}CO observations of 47 SMGs, providing one of the largest and highest quality samples of its kind. With this study we demonstrate the capability of ALMA and NOEMA to undertake blind redshift scans in the $3\,\mathrm{mm}$ waveband, and in doing so add significantly to the number of SMGs with spectroscopic redshifts, which prior to the work presented in this thesis was small. We also exploit the multi-wavelength coverage of the samples, together with the robust new spectroscopic redshifts, to model their spectral energy distributions (SEDs) with the MAGPHYS code and subsequently estimate key physical properties such as stellar masses and star-formation rates.

Perhaps more importantly, this survey has allowed us to characterise the molecular gas content in the SMG population, along with its excitation properties, results from which we present in Chapter 3. We also show that the gas depletion timescale in SMGs remains con-

stant, and given that SMGs are significant contributors to the star-formation rate density (SFRD) at $z \sim 2$, the global evolution of star-formation in SMGs appears to coincide with the evolution of the molecular gas content, as opposed to any variation in star-formation efficiency. We provide a new test of the SMG population as descendants of massive local early-type galaxies, using the derived CO linewidths and baryonic masses.

In Chapter 4 we present our Large Programme with KMOS which, when completed, will have observed ~ 400 SMGs in the COSMOS, UDS and ECDFS fields. Expanding on the work of Chapters 2 and 3 this is designed to further add to the catalog of SMGs with spectroscopic redshifts by detecting the Hα and/or [OIII] emission, which probes ionised gas and can also be used to estimate star-formation rates. We detail the target selection and observing strategy of this survey, before presenting early results for 43 emission line-detected sources, including the Hα-derived star-formation rates, the mass-metallicity relation and BPT diagram. We also compare the Hα, rest-frame optical/near-infrared and dust sizes where available, finding median radii of $R_e = 3.6 \pm 0.3\,\mathrm{kpc}$, $R_{\mathrm{H}\alpha} = 4.2 \pm 0.4\,\mathrm{kpc}$ and $R_{\mathrm{dust}} = 1.2 \pm 0.3\,\mathrm{kpc}$. Additionally, the sample are consistent with a median Sérsic index of $n = 1$, i.e. with an exponential disc-like light profile.

The integral field spectrograph (IFS) capabilities of KMOS allow us to spatially resolve the Hα/[OIII] emission when it is sufficiently bright and extended, and this provides valuable diagnostics of the galaxy kinematics. Therefore, in Chapter 5 we present resolved Hα/[OIII] velocity and velocity dispersion maps for 36 SMGs, from which we derive rotation curves and dispersion profiles. We compare the derived kinematics of our SMGs with less active galaxies at lower redshifts, and divide the sample into 28 *ordered* sources with clear velocity gradients, and rotation curves which can be modelled as Freeman disks, and eight *disordered* sources with much more messy velocity maps, from which little reliable kinematic information can be obtained. We measure a median rotational velocity of $v_{\mathrm{rot}} = 190 \pm 20\,\mathrm{km\,s^{-1}}$ and a median intrinsic velocity dispersion of $\sigma_0 = 87 \pm 5\,\mathrm{km\,s^{-1}}$ from the *ordered* subset, both of which are significantly higher than the less actively star-forming galaxies to which we compare. The median ratio of rotational velocity to intrinsic velocity dispersion in the *ordered* sample is $v_{\mathrm{rot}}/\sigma_0 = 2.2 \pm 0.5$, indicating that our sources are somewhat rotationally supported, and we therefore suggest that our SMG sample likely represents "scaled-up" versions of more "normal" star-forming galaxies, rather than merger-dominated systems.

Contents

List of Figures

List of Tables

Declaration

The work in this thesis is based on research carried out in the Centre for Extragalactic Astronomy, Department of Physics, Durham University, United Kingdom while the author was a research student working under the supervision of Prof. Ian Smail and Prof. Mark Swinbank, between October 2018 and July 2022. No part of this thesis has been submitted elsewhere for any other degree or qualification and it is the sole work of the author unless referenced to the contrary in the text.

The majority of the content presented in Chapter 2 and Chapter 3 has been published in:

- *"An ALMA/NOEMA survey of the molecular gas properties of high-redshift star-forming galaxies"* Birkin, Weiss, Wardlow et al. MNRAS, 501, 3926 (2021)

The author of the thesis was primarily responsible for all aspects of this publication. In addition to the work presented in this thesis, the author also contributed to the following publications during their PhD:

- *"An ALMA survey of the SCUBA-2 Cosmology Legacy Survey UKIDSS/UDS field: halo masses for submillimetre galaxies"* Stach, Smail, Amvrosiadis et al. MNRAS, 504, 172 (2021)

- *"An ALMA survey of the S2CLS UDS field: optically invisible submillimetre galaxies"* Smail, Dudzevičiūtė, Stach et al. MNRAS, 502, 3426 (2021)

- *"FIR-luminous [C II] Emitters in the ALMA-SCUBA-2 COSMOS Survey (AS2COSMOS): The Nature of Submillimeter Galaxies in a 10 Comoving Megaparsec-scale Structure at $z \sim 4.6$"* Mitsuhashi, Matsuda, Smail et al. ApJ, 907, 122 (2021)

- *"An ALMA survey of the brightest sub-millimetre sources in the SCUBA-2-COSMOS field"* Simpson, Smail, Dudzevičiūtė et al. MNRAS, 495, 3409 (2020)

- *"An ALMA survey of the SCUBA-2 CLS UDS field: physical properties of 707 sub-millimetre galaxies"* Dudzevičiūtė, Smail, Swinbank et al. MNRAS, 494, 3828 (2020)

- *"SCUBA-2 Ultra Deep Imaging EAO Survey (Studies). III. Multiwavelength Properties, Luminosity Functions, and Preliminary Source Catalog of 450 µm Selected Galaxies"* Lim, Wang, Smail et al. ApJ, 889, 80 (2020)

Acknowledgements

I am lucky to be surrounded by many people who have been incredibly supportive of me throughout the last four years, and it is the least I can do to thank these people here.

Firstly, I am very grateful to my two supervisors, Ian Smail and Mark Swinbank, for offering me the position in the first place, and for constant advice and guidance without which the work presented would, I am sure, be of a much lower quality. At times I found the many emails and seemingly infinite scribbled comments to be frustrating, but you have both pushed me to work hard and set high standards, and I believe that this thesis reflects that. Thanks as well for sending me to Hawaii for two weeks.

I would also like to thank Alastair Edge and John Lucey for their support throughout both my undergraduate and postgraduate studies, along with Julie Wardlow and Axel Weiss for generously providing a large portion of the data used in Chapters 2 and 3, and for writing references when I was applying for postdocs. Thanks also to all co-authors who have provided feedback on papers and proposals. Big thanks to Shufei Rowe and Lindsay Borrero for general support, and for all their help with arranging travel for observing trips and conferences.

I have been very fortunate to have worked with several friendly and intelligent postdocs in the SMG group at Durham. In particular I want to thank Annagrazia Puglisi for her invaluable help with postdoc applications, for providing loads of comments and moral support during the writing of this thesis, and for always being willing and available to talk through problems with my research. Also big thanks to Stuart Stach for being a great friend and mentor in

the early phase of my PhD, along with Bitten Gullberg, Lizzie Cooke and Soh Ikarashi, all of whom have made it a pleasure to be part of the SMG group.

I have made many great friends among my peers in the department, and these friendships have got me through some difficult times over the last four years. Thank you to Vicky for being my best friend here in Durham. We've been through a lot, and I am so thankful to have you on my team. Thanks to Henry for being a great mate over the last eight years, a lot has changed in that time, but you've been the one constant presence in Durham, and for that I am really lucky. I am very grateful to Ugnė for her support and friendship, and for making our observing trip to Hawaii one of the highlights of my PhD, and to Aidan for all the music chat, along with last-minute proof reading of this piece of work which helped to mitigate much of the stress in the final days of writing. Enormous thanks as well to Giorgio, Amy, Matteo, Anna, Miguel and Alice for being great office mates, and to Cameron, Ed, Jake, Ellen, Joaquin, Carol, Emmy, Scott, Max, Duncan, Martina, Victor, Arnau, Louise, Tom R., Tom C., Chris D., Ra'ad, Calvin and Steve for being good friends over the years. You have all made me smile and laugh on many, many occasions, for which I am extremely grateful.

Away from Durham, I want to say a big thank you to Jack Heslop, Matt Roberts and Oli Shepherd, as well as my old school mates James Sutton, Nick West and Jordan Crawford, who have provided great laughs and support.

Although they won't be able to comprehend this, I want to thank my dogs, Gitte and Luna, who only entered my life within the last couple of years but never fail to make me smile when I visit home. Lastly, and most significantly, I thank my parents, Jane and Jon, for always believing in me when I often didn't believe in myself. I am very sorry for all the time spent whining to you over the phone, particularly during the last couple of weeks of writing this thesis, when I was really miserable and probably quite unpleasant to listen to. I really appreciate you putting up with me in these moments. I owe everything to you both, and I hope that I have made you proud.

Dedicated to

Mum and Dad

Introduction

1.1 The diverse properties of galaxies

1.1.1 The local Universe

In the local Universe, galaxies display a variety of colours, morphologies and sizes. Edwin Hubble was one of the first to attempt to summarise these by creating the Hubble tuning fork (Hubble, 1936, Fig. 1.1), which separates galaxies into three broad categories. On the left of Fig. 1.1, elliptical galaxies (E), or "early types", are numbered according to their observed ellipticity, $e = 1 - b/a$, where b/a is the ratio of the minor-to-major axis sizes. Therefore E0 galaxies appear to be circular, and E9 galaxies appear to be highly elliptical. Elliptical galaxies are most commonly found in dense galaxy clusters, and they are red in colour due to their very old stellar populations and lack of ongoing star formation. Early-type galaxies are gravitationally supported by the random motions of the stars, and are thus referred to as "dispersion-dominated".

Conversely, on the right of Fig. 1.1, spiral galaxies are divided into "normal" spirals (S) and "barred" spirals (SB) and classified according to how tightly wound the spiral arms are. These galaxies host ongoing star formation, and therefore massive and short lived O and B stars make them appear blue in colour. Spiral galaxies appear more like discs, with a central bulge containing older stars. These discs are "rotation-dominated", in contrast with elliptical galaxies, as they rotate at much faster velocities than the random motions of their
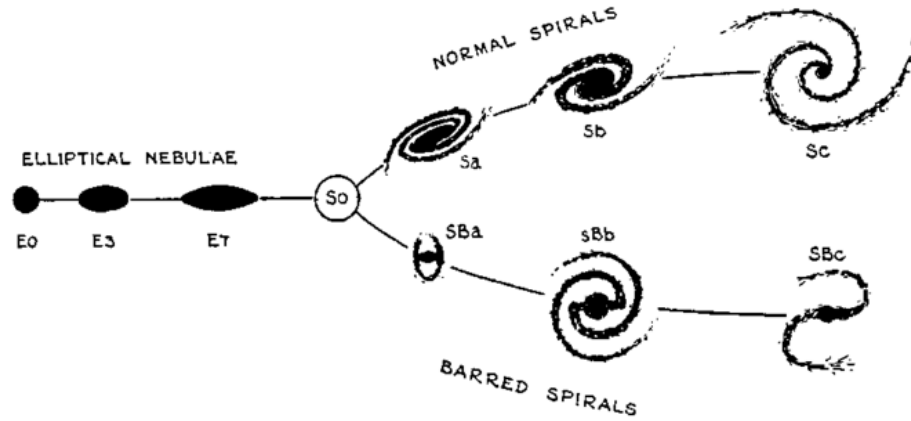
Figure 1.1: Edwin Hubble's classification scheme for the morphology of galaxies (Hubble, 1936), displaying the diversity of structures observed. The majority of galaxies can be placed into one of the categories in the Hubble tuning fork, although some fall into the category of "irregulars", particularly high-redshift galaxies which are typically more turbulent than their local counterparts.

stars. Additionally, spiral galaxies show a strong positive correlation between their rotational velocities and their stellar masses, or luminosities, the so-called "Tully-Fisher" relation (Tully & Fisher, 1977). This relation is often used as a distance indicator for galaxies, but can also be used to study the buildup of mass through cosmic time. The third category of galaxy, lenticular galaxies (S0), are somewhere in the middle, with a disc-like component and a central bulge, but no spiral arms.

While often misinterpreted as an evolutionary sequence, there is no indication that galaxies follow the path implied by the terms "early" and "late" type. In any case, elliptical galaxies are more common in the low-redshift Universe, i.e. at late times, and it is believed that they may form from the merging of late-type galaxies over time, which destroys disc structure. Understanding how different types of galaxy relate to one another has been an area of significant ongoing research for the last three decades, in particular since the *Hubble Space Telescope* (*HST*) provided images of the high-redshift Universe in unprecedented detail.

1.1.2   The high-redshift Universe

One of the most basic observations from *HST* is that galaxies at high redshifts appear much less ordered structurally, and we rarely observe the impressive grand-design spirals that are common locally. Given that observing galaxies that are billions of light-years away means looking back billions of years into the past, the highly unordered galaxies we see at high redshifts are in fact the predecessors of the nearby systems described above. How do galaxies

go from being chaotic to ordered and passive over the intervening billions of years?

As a result of the disorderly nature of high-redshift galaxies and the obvious difficulties in observing more distant sources, Hubble's classification scheme becomes more troublesome to apply. Galaxies are instead divided into smaller classes based on their selection criteria, with examples such as Lyman Break Galaxies (LBGs; e.g. Shapley et al., 2003; Bouwens et al., 2011), Extremely Red Objects (EROs; Daddi et al., 2000), Submillimetre Galaxies (SMGs; e.g. Smail et al., 1997; Blain et al., 2002) and Ultra-Luminous Infrared Galaxies (ULIRGs; e.g. Sanders & Mirabel, 1996), with galaxies often fitting into multiple classes. This makes galaxy evolution an extremely complex field to navigate. However, thanks largely to advances in instrumentation, symbolised by the recent launch of the *James Webb Space Telescope* (*JWST*; Gardner et al., 2006), progress is being made in resolving galaxies on smaller spatial scales, and with greater sensitivity. This is enabling more precise measurements of, among other things, kinematics, molecular gas reservoirs and morphologies, and with advances in computational modelling we can test theoretical models of these parameters to great precision. The motivation behind this thesis specifically is to exploit state-of-the-art observational instrumentation in an attempt to study high-redshift galaxies, and to better understand in particular the population of highly star-forming dust-obscured galaxies, which we will introduce in the following section.

1.2 The formation and evolution of galaxies

Under the currently accepted paradigm of cosmology, the Lambda-CDM model, the Universe began as a random density field of dark matter and baryons. Under the influence of gravity, regions of dark matter overdensity grow and eventually collapse to form dark matter halos. This creates a potential well into which the gas, comprised of baryonic matter, can fall, decoupling from the dark matter and subsequently cooling to form stars and galaxies (see e.g. Wechsler & Tinker, 2018, for a review).

The evolution of galaxies is then governed by the balance between the formation of stars, which consumes molecular gas, and accretion from the intergalactic medium (IGM) which replenishes molecular gas (Scoville et al., 2017). The observation that ∼5-10% of the matter in the Universe is in stars and cold gas (e.g. Bell et al., 2003) suggests that star formation is remarkably inefficient, and that other processes must be active. For example, feedback from active galactic nuclei (AGN; see Hickox & Alexander, 2018, for a review), massive stars and

supernovae can heat gas, preventing it from cooling to form stars, or eject it from the galaxy entirely. Heavier elements that are formed in stars enrich the interstellar medium (ISM), allowing molecular gas to cool more easily. Additionally, galaxies may interact and merge, compressing large amounts of gas and resulting in violent episodes of star formation (e.g. Mihos & Hernquist, 1996), also potentially destroying pre-existing disc structures.

Thus the study of galaxy evolution is the study of these processes, and how they are affected by the basic properties of the galaxy. In this section, we provide context around the evolution of high-redshift galaxies, in particular the population of dust-obscured star-forming galaxies (DSFGs) which will be the main focus of this thesis.

1.2.1   The star-formation rate density history

The evolution of the star-formation rate per unit volume, or the *star-formation rate density* (SFRD; Madau & Dickinson, 2014), as a function of redshift provides a useful observational tool to understand how star formation proceeds globally across cosmic time. This has been constrained over the last three decades by combining different tracers of the star-formation rate, such as the far-ultraviolet and infrared continuum (e.g. Lilly et al., 1996; Bouwens et al., 2012; Gruppioni et al., 2013; Bourne et al., 2017; Liu et al., 2018), along with nebular emission lines such as Hα and Lyα which directly probe the emission from O and B stars (e.g. Geach et al., 2008; Dale et al., 2010), radio emission which traces accelerated electrons in supernovae (e.g. van der Vlugt et al., 2022) and even X-ray emission which is produced by young stellar populations (see Kennicutt & Evans, 2012, for a review of SFR tracers).

The SFRD is observed to increase from the evolution of the first galaxies at $z > 10$ (e.g. Bromm & Yoshida, 2011) up until $z \sim 2$, before declining towards the present day, with the peak at $z \sim 1$–3 commonly referred to as "cosmic noon". This represents the epoch over which the majority of the stellar mass observed in the local Universe was assembled (e.g. Dickinson et al., 2003b; Pérez-González et al., 2008; Menéndez-Delmestre et al., 2013). Therefore studying galaxies at this epoch is crucial to developing a complete picture of how galaxies evolved from high redshifts to the present day, and indeed, it is this epoch which motivates the work presented in this thesis.

1.2.2   Obscured star formation

Until the 1990s measurements of the SFRD were entirely made using UV/optical data, however it soon emerged that this approach lead to an incomplete picture after the *Infrared As-*
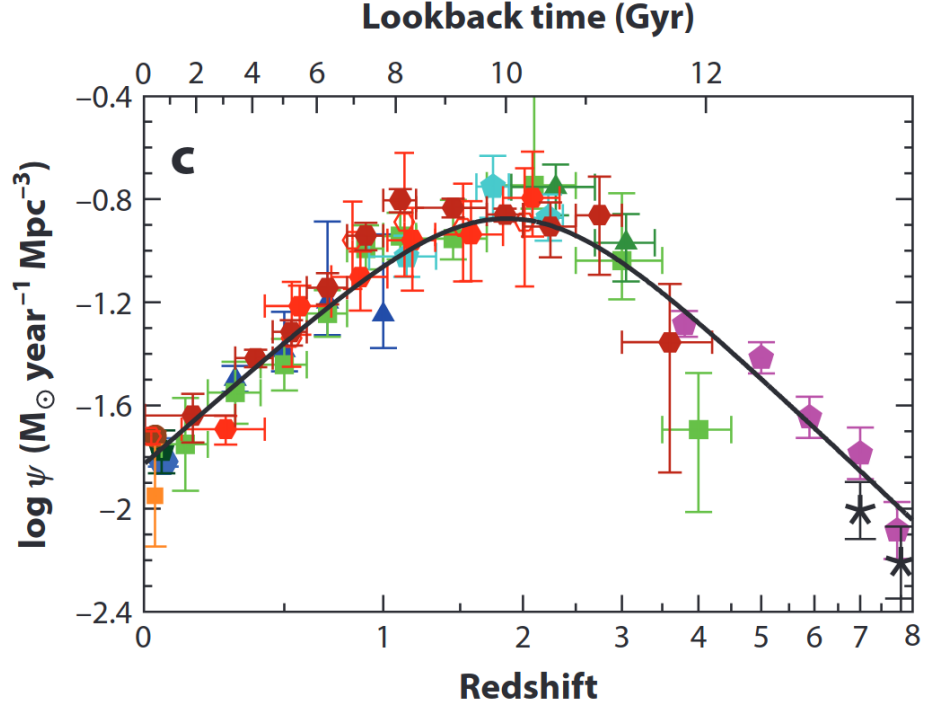
Figure 1.2: Rest-frame far ultraviolet + infrared measurements of the star-formation rate density (SFRD) history of the Universe, from Madau & Dickinson (2014). The SFRD is observed to increase until $z \sim 2$ ("cosmic noon"), at which time most of the stellar mass seen in the local Universe is assembled, before decreasing until $z = 0$.

tronomy Satellite (IRAS; Neugebauer et al., 1984) and *Cosmic Background Explorer* (COBE; Puget et al., 1996) satellites opened an entirely new window on astronomy with the discovery of the far-infrared (FIR)/submillimetre background emission. This is primarily composed of reprocessed rest-frame UV/optical light from young O and B type stars in high-redshift galaxies, which is absorbed by dust grains in the interstellar medium (ISM) and re-emitted in the FIR when the dust cools. By comparing the FIR background emission with the UV and optical background it was inferred that approximately half of all the star formation that has ever occurred was obscured by dust (e.g. Puget et al., 1996). This can be seen in Fig. 1.3 from Dole et al. (2006), which shows that the Universe emits roughly comparable energy density in both the optical and infrared. In fact, there appears to have been a transition from the majority of star formation occurring in unobscured, to dust-obscured environments, at $z \sim 5$ (Bouwens et al., 2020). Therefore, observations in the far-infrared are key to studying star formation at high redshifts, and therefore in understanding galaxy formation and evolution.

In the 1980s *IRAS* discovered a heavily dust-obscured galaxy population in the local Universe – the Luminous Infrared Galaxies (LIRGs) – comprised of galaxies with infrared luminosities
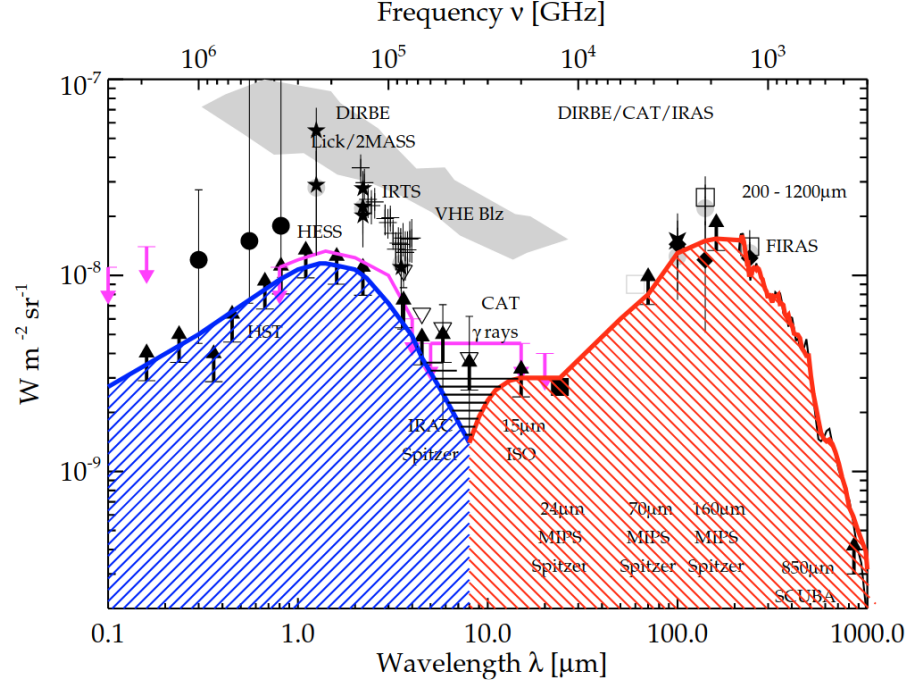
Figure 1.3: Measurements of the Cosmic Optical Background (blue) and the Cosmic Infrared Background (red), from Dole et al. (2006). This highlights the fact that the energy density is comparable in the optical and infrared, making it vital to study both if we are to fully understand the star-formation history of the Universe.

$L_{IR} > 10^{11} L_{\odot}$[1], the most well-studied of which make up the IRAS Revised Bright Galaxy Sample (RBGS; Sanders et al., 2003), along with more populations that were later discovered by *ISOPHOT* (Lemke et al., 1996). The extremely high infrared luminosities in these sources arise from the dust, which re-emits the optical/UV light from young stars at far-infrared wavelengths when it cools. Most local galaxies observed by *IRAS* and *ISOPHOT* were LIRGs, but a subset of 12 sources had $L_{IR} > 10^{12}$ and were termed Ultra Luminous Infrared Galaxies (ULIRGs). Among the ULIRGs, those with SFRs of $> 50\,M_{\odot}\,yr^{-1}$ were determined to be major mergers from morphological analysis at multiple wavelengths (e.g. Soifer et al., 1984; Veilleux et al., 2002, and for a review see Sanders & Mirabel 1996). In a cosmological context, local ULIRGs contribute to a small fraction of the global SFRD, but at $z \gtrsim 1$ their contribution is much more significant (Magnelli et al., 2013; Dudzevičiūtė et al., 2020).

1.2.3 Submillimetre galaxies

At high redshifts, an analogous population to local ULIRGs are submillimetre galaxies (SMGs; Smail et al., 1997; Blain et al., 2002), a prominent class of dust-obscured star-forming

---

[1]In this thesis we define L_{IR} to be measured across the wavelength range $\lambda = 8$–$1000\,\mu m$.
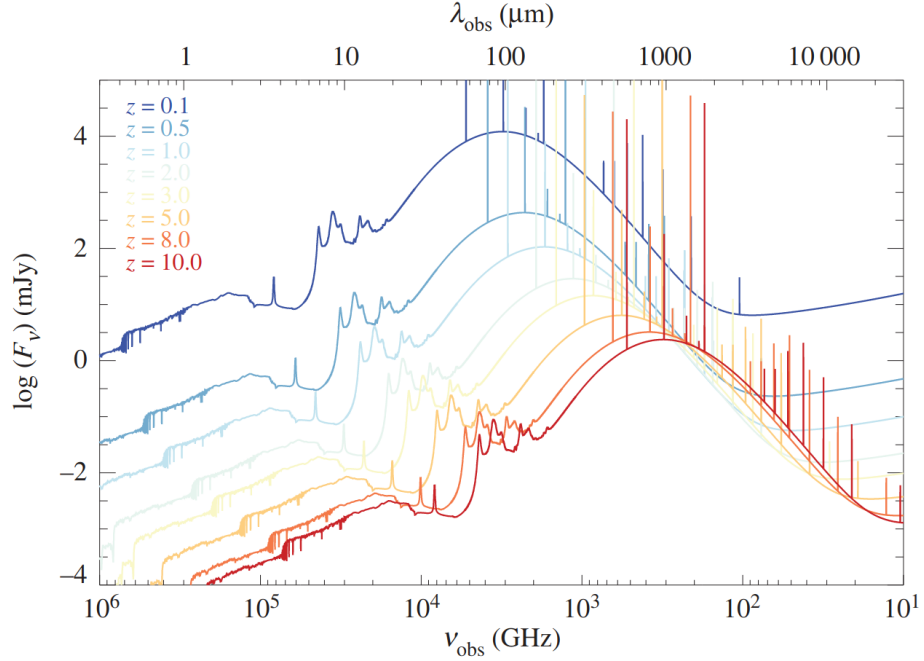
Figure 1.4: Median spectral energy distribution (SED) of SMGs from the ALESS sample (da Cunha et al., 2015), evolved to redshifts $z = 0.1$–10.

galaxies (DSFGs) with $870 \, \mu$m flux densities ($S_{870} \gtrsim 1 \, $mJy), which were first observed using the Sub-millimeter Common User Bolometric Array (SCUBA) on the James Clerk Maxwell Telescope (JCMT; e.g. Coppin et al., 2006). The selection at $850 \, \mu$m^2 (which corresponds to a gap in the atmospheric water vapour absorption) means that observations benefit from a negative K-correction. This is due to the fact that the dust emission resembles a modified blackbody with a peak at $\lambda_{\mathrm{rest}} \sim 100 \, \mu$m, and so the $\lambda_{\mathrm{rest}} \sim 850 \, \mu$m emission corresponds to the tail of the Rayleigh-Jeans (RJ) slope, and as the source moves to higher redshifts the rest-frame $850 \, \mu$m point moves closer towards the peak, thus becoming brighter at this observed wavelength (see Fig. 1.4). In fact, this correction is so strong that it approximately cancels out cosmological dimming over the range $z \sim 1$–8, meaning that SMGs have roughly constant brightness (see Casey et al., 2014, for a review).

SCUBA has since been upgraded to SCUBA–2 (e.g. Holland et al., 2013; Mairs et al., 2021), and along with the Large APEX BOlometer CAmera (LABOCA; Siringo et al., 2009) and the Astronomical Thermal Emission Camera (AzTEC; Wilson et al., 2008) is one of the instruments used in wide-field single-dish surveys to detect SMGs (e.g. Geach et al., 2013, 2017; Barger et al., 2022). These instruments have angular resolutions of around half an

---

[2]For clarity, SCUBA(–2) operates in the atmospheric transmission window at $\lambda_{\mathrm{obs}} \sim 850 \, \mu$m, whereas ALMA follow-up is carried out at the slightly longer $\lambda_{\mathrm{obs}} \sim 870 \, \mu$m.

arcminute, and therefore the beam can contain tens of galaxies. Without higher-resolution imaging it is difficult to verify the multi-wavelength counterparts to these sources, and initially studies relied on cross-matching to radio or $24\,\mu$m catalogues (e.g. Ivison et al., 2007).

As a result the study of dust-obscured sources is challenging, but significant progress has been made in the last decade largely thanks to the construction of the Atacama Large (sub)-Millimetre Array (ALMA, e.g. Wootten & Thompson, 2009). ALMA is an interferometer located on the Chajnantor plateau, in the Atacama Desert, Chile, at an altitude of over $5000\,$m. The array is comprised of 66 antennae, the main array of 50 $12\,$m antennae, an array of twelve $7\,$m antennae (Atacama Compact Array; ACA), and a further four $12\,$m antennae (Total Power Array; TPA). The main array offers angular resolutions from a few arcseconds to milliarcseconds, which means it can probe scales down to a few hundred parsecs for unlensed sources at $z \sim 2$. Therefore for SMGs detected in single-dish surveys by e.g. SCUBA-2 or LABOCA, ALMA can be used for follow-up in order to determine the precise position of the $850\,\mu$m emission (e.g. Stach et al., 2019).

Additionally, ALMA has frequency coverage over the range 90–950 GHz (which in a couple of years time is expected to expand to 35–950 GHz), meaning that for high-redshift SMGs it can cover the thermal dust emission, the peak of the SED and the Rayleigh-Jeans tail, along with many molecular and atomic emission lines (which we will discuss further in §1.3.3). Finally, ALMA is far more sensitive its predecessors, a factor of 10–20$\times$ higher for spectral line detections and 10–100$\times$ higher for continuum (see Hodge & da Cunha, 2020, for a review of ALMA and how it has contributed to SMG research in the last decade).

One of the biggest contributions of ALMA to the literature on SMGs is in the identification of large samples. While the initial SCUBA-2 maps have resolutions of roughly half an arcminute, which can encompass tens of sources, ALMA follow-up allows us to pinpoint the position of the emission to within fractions of an arcsecond. Three of the largest such samples are the ALMA LABOCA survey of the Extended *Chandra* Deep Field South (ALESS; Hodge et al., 2013), the ALMA SCUBA-2 UKIDSS Ultra Deep Survey (AS2UDS; Stach et al., 2018, 2019) and the ALMA SCUBA-2 Cosmic Evolution Survey (AS2COSMOS; Simpson et al., 2020), which cumulatively contain over 1000 ALMA-identified sources.

1.3 Observational tools

Studying the dust-obscured population at high redshift is highly important in bridging the gap between the high- and low-redshift populations of galaxies. We will now move on to a

discussion of which galaxy properties can be measured, in the context of high-redshift dust-obscured galaxies, and how they can inform us of the ongoing processes that shape their evolution.

1.3.1 Photometric and spectroscopic redshifts

One of the most fundamental properties of a galaxy is its redshift. Obtaining robust redshifts for many SMGs is a necessity if we are to study the bulk properties of the population, in many areas such as SED fitting (e.g. Danielson et al., 2017), clustering analyses (e.g. Stach et al., 2021) and kinematic studies (e.g. Alaghband-Zadeh et al., 2012).

Generally both photometric and spectroscopic redshifts can be used to study galaxies at high-redshift. Photometric redshifts are cheaper to measure in terms of telescope time, but less precise (see Casey et al., 2014, for a review), and given the dust-obscured nature of SMGs they are often more accurate for low-redshift sources (e.g. Dudzevičiūtė et al., 2020) which creates a bias in any subsequent analyses. The rise of deep extragalactic fields such as the Cosmic Evolution Survey (COSMOS; Scoville et al., 2007), the UKIDSS Ultra Deep Survey (UDS; Lawrence et al., 2007) and the Great Observatories Origins Deep Survey (GOODS; Dickinson et al., 2003a), however, is improving the reliability of photometric redshifts. For example, in deriving photometric redshifts for the AS2UDS sample Dudzevičiūtė et al. (2020) found a median offset of $(z_{\mathrm{spec}}$-$z_{\mathrm{phot}})/(1+z_{\mathrm{spec}}) = -0.005 \pm 0.003$ for 44 SMGs with pre-existing spectroscopic redshifts, although these were mostly sources at $z < 3$.

Spectroscopic redshifts are the gold standard, as they can be measured to extremely high precisions. However they are not easy to obtain in bulk, particularly for heavily dust-obscured sources are high redshifts. Rest-frame optical spectroscopic surveys with multi-object spectrographs (MOS) such as the Fibre-Multi-Object Spectrograph (FMOS; Kimura et al., 2003), the Multi-Object Infrared Camera and Spectrograph (MOIRCS; Ichikawa et al., 2006) and the Visible Multi-Object Spectrograph (VIMOS Le Fevre et al., 2000) allow for blind redshift surveys of large numbers of galaxies simultaneously (e.g. Stott et al., 2016; Tiley et al., 2021), but for heavily dust-obscured sources these are more likely to detect the optically bright and therefore low-redshift end of the population (e.g. Chapman et al., 2005; Danielson et al., 2017; Dudzevičiūtė et al., 2020).

Alternatively, targeting the CO transitions at millimetre wavelengths (see §1.3.3) is an efficient method of obtaining unbiased redshifts for SMGs, as the large bandwidths of ALMA and NOEMA allow for blind scans of large volumes (e.g. Bothwell et al., 2013; Weiß et al.,

2013; Spilker et al., 2014). Spectroscopic redshifts have the additional caveat that it is necessary to identify which emission line is being observed (e.g. Bakx & Dannerbauer, 2022) which is usually trivial if multiple lines are detected at high S/N but with only one emission line, or when the observed lines are low S/N, one may need to rely on the photometric redshift to inform the line identification. This can introduce biases in the derived results, as low-redshift SMGs are more likely to have better-constrained photometric redshifts.

For sources at higher redshifts, which are typically optically fainter (e.g. Dudzevičiūtė et al., 2020), spectroscopic redshifts remain far more reliable. They are also necessary for deriving line luminosities, gas masses, kinematics and for studying SMGs in the context of other galaxy populations. Indeed, one of the fundamental goals of this thesis is to significantly boost the proportion of SMGs with robust spectroscopic redshifts (see Chapters 2, 3 and 4).

1.3.2   Spectral energy distribution

Observing galaxies at different wavelengths addresses different questions, probing different components and processes. For example, observations at rest-frame optical wavelengths generally probe the stellar emission, whereas studying the far-infrared emission traces the dust emission which emits approximately as a modified blackbody. Constructing a complete picture of the galaxy demands observations at all wavelengths. This allows one to model the spectral energy distribution (SED) of the galaxy – the flux density received as a function of wavelength.

The fundamental idea behind SED modelling is to combine an initial mass function (IMF) with population synthesis models and star-formation histories (SFHs) in order to reconstruct the observed emission from a galaxy (e.g. Conroy, 2013). SED fitting codes such as MAGPHYS (da Cunha et al., 2015; Battisti et al., 2019) use energy balance techniques to consistently model both the UV and IR emission, making it highly useful for studying SMGs where reprocessed IR emission dominates the bolometric luminosity (e.g. da Cunha et al., 2015; Dudzevičiūtė et al., 2020).

As discussed in §1.2.3 and §1.3.1 the study of SMGs has benefited from the wealth of multi-wavelength coverage from the ultraviolet (UV) to the radio in survey fields such as COSMOS, UDS and GOODS, along with precise identifications with ALMA allowing us to match counterparts at these different wavelengths. In these fields, maps at different wavelengths can be compared to identify and classify sources, and the emission can be modelled using an
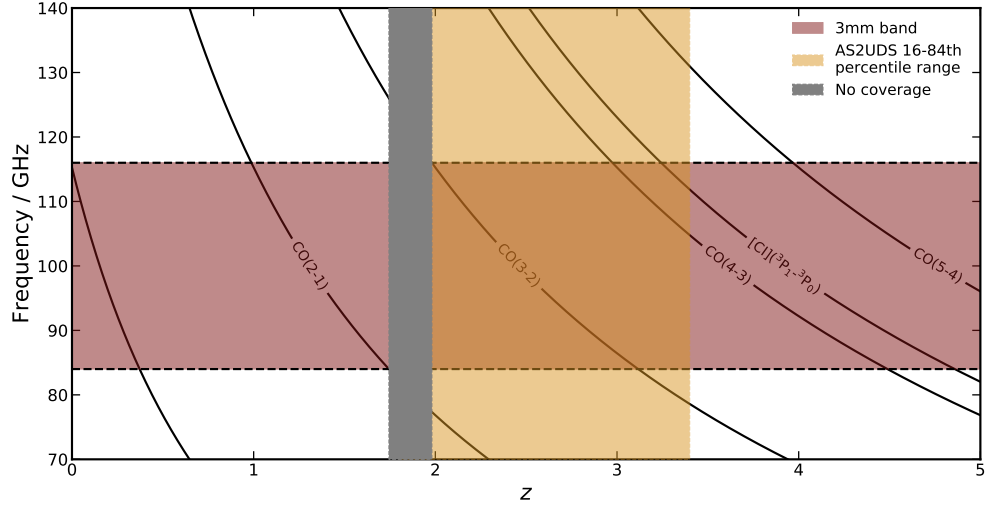
Figure 1.5: The 3 mm waveband, as covered by e.g. ALMA and NOEMA, showing the frequencies of CO emission lines (and the $[CI](^3P_1$-$^3P_0)$ fine structure line) for $z = 0$–7. The 16th-84th percentile range of photometric redshifts for AS2UDS SMGs is shown in yellow, with the 5th-95th percentile range shown as yellow dashed vertical lines. This demonstrates the power of blind 3 mm scans with ALMA and NOEMA – only the redshift range $z \sim 1.75$–2.0 is free of CO emission meaning SMGs can be targeted without prior knowledge of their redshifts. This removes the bias towards low-redshift SMGs from which optical/NIR surveys suffer.

SED fitting code to estimate fundamental properties such as the stellar mass, dust mass and star-formation rate (e.g. da Cunha et al., 2015; Dudzevičiūtė et al., 2020; Barger et al., 2022).

One of the most important properties that can be derived from SED fitting is the stellar mass, however, this is also arguably the most difficult property to measure accurately (e.g. Hainline et al., 2011; Michałowski et al., 2012), as the IMF and SFH are not well known, and the dust component needs to be accurately modelled in order to infer the "unattenuated" rest-frame optical/UV spectrum. Additionally, the presence of AGN can complicate the SED fitting as codes such as MAGPHYS itself does not include an AGN component and can therefore lead to overestimates of the stellar mass. A non-negligible fraction of SMGs are expected to be AGN hosts (e.g. Coppin et al., 2010a; Stach et al., 2019), and therefore this bias must be taken into account when deriving and using stellar masses.

1.3.3 Molecular gas reservoirs

As discussed in §1.2, the evolution of galaxies is largely governed by the consumption of molecular gas, the fuel for star formation, and therefore the molecular gas content of galaxies is one of the most important properties to measure, particularly for such highly star-forming

sources as SMGs. To understand how SMGs reach such high SFRs and subsequently evolve it is necessary to understand how much molecular gas they currently contain in relation to their stellar mass content, and how quickly they are consuming it. On its own M_{gas} is an informative quantity, but it can also be used to estimate further properties if one has knowledge of SED-derived properties such as stellar masses, SFRs and dust masses (see the previous section). Three such examples of these are the gas depletion timescale $t_{\mathrm{dep}} = M_{\mathrm{gas}}/\mathrm{SFR}$, the gas-to-stellar mass ratio $\mu_{\mathrm{gas}} = M_{\mathrm{gas}}/M_*$ and the gas-to-dust ratio $\delta_{\mathrm{gdr}} = M_{\mathrm{gas}}/M_{\mathrm{dust}}$. t_{dep} is related to how efficient the galaxy is at converting its molecular gas into stars, and μ_{gas} describes how gas rich it is (e.g Geach et al., 2011). These two quantities have been suggested to be fundamental in scaling relations which result from the star-forming main sequence (see Tacconi et al., 2020, for a review).

Carbon monoxide as a molecular gas tracer

The primary constituent of the molecular gas is molecular Hydrogen (H_2), and ideally observations would probe the emission lines of this molecule as it provides the most reliable tracer of the molecular gas. However, the lowest-energy roto-vibrational transitions of H_2 have extremely high excitation requirements which are not found in cold molecular clouds, and therefore another tracer must be used. As the second most abundant molecule in the ISM after H_2, and with low excitation requirements for its ground-state roto-vibrational transitions, the most commonly used tracer is carbon monoxide (CO) (Carilli & Walter, 2013, for a review). The ideal transition to target is CO(1–0) (e.g. Sharon et al., 2013; Riechers et al., 2020; Jin et al., 2021; Frias Castillo et al., 2022) as it has the lowest excitation energy and therefore traces the bulk of the cold gas (the higher J_{up} transitions trace warmer, more compact components), however this line is typically very faint and therefore requires long integration times to be detected.

The most accessible transitions are the $J_{\mathrm{up}} \sim 2$–5 lines as they are the brightest in terms of line intensity and can be observed fairly easily at millimetre wavelengths (e.g. Greve et al., 2005; Coppin et al., 2010b; Tacconi et al., 2010; Bothwell et al., 2013; Wardlow et al., 2018; Valentino et al., 2020a; Chen et al., 2022). They also cover a wide range of redshifts (see Fig. 1.5. Measurements of the CO line luminosity L'_{CO} can be used to estimate molecular gas masses according to

$$M_{\mathrm{gas}} = 1.36\alpha_{\mathrm{CO}}L'_{\mathrm{CO(1-0)}}, \tag{1.3.1}$$

where

$$L'_{\mathrm{CO}} = 3.25 \times 10^7 I_{\mathrm{CO}} \frac{D_L^2}{(1+z)^3 \nu_{\mathrm{obs}}} \,\mathrm{K\,kms^{-1}\,pc^{-2}},\tag{1.3.2}$$

α_{CO} is the CO-H$_2$ conversion factor in $M_\odot\,(\mathrm{K\,km\,s^{-1}\,pc^2})^{-1}$, I_{CO} is the velocity-integrated line intensity in $\mathrm{Jy\,km\,s^{-1}}$, D_L is the luminosity distance in Mpc and ν_{obs} is the observed frequency of the CO emission line. The factor of 1.36 in Eq. 3.3.2 accounts for the presence of Helium in the ISM (Solomon et al., 1997; Bolatto et al., 2013). An additional inconvenience for $J_{\mathrm{up}} > 1$ CO lines is the necessity to adopt an assumed set of line ratios to infer the CO(1–0) luminosity, which is needed to derive more robust gas masses. This is discussed further in §1.3.4.

One of the most significant CO studies of SMGs was carried out by Bothwell et al. (2013), who surveyed low- to mid-J CO emission in 40 SMGs with the Plateau de Bure Interferometer (PdBI; Guilloteau et al., 1992), which remains one of the largest samples of its kind nearly ten years later, and while this sample has provided many useful results, such as in measuring CO line ratios and molecular gas fractions, it is based on selection of sources with known spectroscopic redshifts and radio identifications, and therefore biased towards lower-redshift galaxies and sources with stronger AGN components. With the capabilities of ALMA and the large samples of ALMA-identified SMGs, in addition to PdBI's successor the NOrthern Extended Millimeter Array (NOEMA) we are ready to make vast improvements on the characterisation of the cold ISM properties of SMGs, and a significant portion of this thesis is dedicated to doing so (see Chapters 2 and 3).

In addition to CO, the emission lines of atomic and ionised carbon have been proposed as alternate tracers of the molecular gas. Unlike the low-J CO emission lines, the two [CI] lines are optically thin, and appear at frequencies that make them easier to detect with ALMA than the low-J CO lines. It has been suggested that atomic carbon is well mixed within molecular clouds (Papadopoulos & Greve, 2004), and the [CI] lines can be combined with CO to infer properties of the ISM such as temperature and density. However, the [CI]-H$_2$ conversion factor is even less well known than the CO-H$_2$ conversion factor, an issue which must be addressed to enable [CI]-based gas mass estimates.

The [CII] line has also been suggested to be a suitable tracer of the molecular gas. This line is very bright, and therefore easy to detect, but [CII] can trace both star-forming and molecular regions and it can be difficult to disentangle the two. Additionally, studies have shown that the strength of the [CII] line depends on the radiation field strength and metallicity (e.g. Rybak et al., 2019).

The CO-H$_2$ conversion factor

The CO-H$_2$ conversion factor is a considerable source of uncertainty in gas mass estimates for high-redshift galaxies (see Bolatto et al., 2013, for a review). It is well-measured for the Milky Way from giant molecular clouds with results in the range $\alpha_{CO} \sim 1\text{–}9\,M_\odot\,(\mathrm{K\,km\,s^{-1}\,pc^2})^{-1}$ – the variation being related to metallicity (Solomon et al., 1987; Leroy et al., 2011; Casey et al., 2014), which is expected to extend to galactic scales (Bolatto et al., 2013), although some authors have found only a weak dependence (Sandstrom et al., 2013). It is not yet clear whether these measurements hold at earlier times. At high redshifts, the two most common values to be adopted are $\alpha_{CO} = 1$ and $\alpha_{CO} = 4$, with the split being between "starburst" galaxies and "normal" (main sequence) star-forming galaxies, respectively. In one of the most notable attempts to constrain α_{CO} Daddi et al. (2010) estimated $\alpha_{CO} \sim 3.6$ from the CO(2–1) emission line in three galaxies. For ULIRGs and high-redshift SMGs, which are expected to have more turbulent interstellar media, $\alpha_{CO} \sim 0.8\text{–}1$ are commonly adopted following Downes & Solomon (1998) who placed the constraints using local ULIRGs.

It is extremely difficult to measure α_{CO} at high redshift however, and it is not well understood how its value is related to the many complex physical processes that occur in galaxies. Attempts to constrain it at such redshifts are therefore mostly empirical and often involve estimating dynamical masses, adopting an assumed dark matter fraction and combining them with stellar masses (Downes & Solomon, 1998; Daddi et al., 2010; Bothwell et al., 2013; Calistro Rivera et al., 2018; Frias Castillo et al., 2022). Indeed, as we have already discussed, stellar masses are highly difficult to measure, and dark matter fractions are equally uncertain for high-redshift star-forming galaxies (e.g. Lang et al., 2019; Tiley et al., 2019). We attempt to provide constraints on the CO-H$_2$ conversion factor for SMGs in Chapters 3 and 5.

1.3.4 CO line excitation

Observations of the molecular and atomic emission lines can provide useful constraints on the gas excitation properties in the ISM. For the molecular CO gas the relative line fluxes of the different roto-vibrational transitions, also known as the CO spectral line energy distribution (SLED), can be modelled to estimate, for example, the kinetic temperature T_{kin} and H$_2$ density of the ISM. This is also necessary to derive line ratios for estimating CO(1–0) luminosities from observations of $J_{\mathrm{up}} > 1$ transitions.

The simplest method for constructing a CO SLED is to observe a single source in multiple CO transitions, as was done by Danielson et al. (2011, 2013) for the lensed submillimetre galaxy

SMM J2135$-$0102 (the "Cosmic Eyelash"). The authors detected 11 separate transitions, including eight ^{12}CO transitions, finding that SMM J2135$-$0102 displays increasing CO line flux up to $J_{\text{up}} = 6$, and declines beyond. Papadopoulos et al. (2014) carried out a similar study for the merger/starburst systems NGC 6240 and Arp 193, constructing CO SLEDs covering $J_{\text{up}} = 4$–13 transitions and finding the two to contain small and large reservoirs of dense ($n \geq 10^4 \, \text{cm}^{-3}$) gas respectively. Finally, Yang et al. (2017) and Cañameras et al. (2018) observed $J_{\text{up}} \sim 3$–11 CO emission for 27 lensed SMGs with the IRAM 30m telescope, finding the majority of sources to peak in line flux at $J_{\text{up}} \sim 4$–7. For context, the SLED of the Milky Way, which has a star-formation rate of $\sim 1 \, \text{M}_\odot \, \text{yr}^{-1}$ (e.g. Licquia & Newman, 2015), peaks at $J_{\text{up}} \sim 2$–3, suggesting that SMGs and starburst galaxies contain hotter and denser gas than less actively star-forming systems.

Alternatively, one can construct a statistical SLED, as in Bothwell et al. (2013), which involves observing many sources in individual transitions and combining them at each J_{up}. A complication of this is that one must normalise the observations in some way. For example, Bothwell et al. (2013) normalised all sources to the same CO luminosity using the scaling between L'_{CO} and L_{IR} (the integrated Schmidt-Kennicutt relation). Spilker et al. (2014) combined ALMA observations of 22 lensed SMGs discovered by the South Pole Telescope (SPT), rescaling all sources to a common redshift of $z = 3$ and also normalising by their 1.4 mm flux at this redshift. Their resultant CO SLED shows high-critical density emission lines such as HCN, HNC, HCO$^+$ and CN, indicating a warm and dense interstellar medium (the stack from Spilker et al. 2014 is shown in Fig. 1.6). Despite the potential difficulties in normalising all observations before stacking, this method of constructing a SLED has the advantage that it is easier to obtain observations of individual transitions for multiple sources, rather than targeting a single source with multiple instruments. We apply this method of building a CO SLED ourselves in Chapter 3.

1.3.5 Rest-frame optical emission line diagnostics

In addition to the millimetre emission lines, the rest-frame optical spectra of star-forming galaxies provide many diagnostics of its properties. Young OB stars emit UV radiation which ionises the surrounding gas, producing H$\alpha\lambda6563$, the dominant rest-frame optical emission line in SFGs. Therefore, the rate of Hα photons observed from a galaxy can be used as a direct indicator of the star-formation rate, SFR$_{\text{H}\alpha}$ (Kewley et al., 2002). Indeed, the Hα emission line is a popular indicator of the SFR for local and high-redshift galaxies due to its

Figure 1.6: Composite rest-frame 0.4–1.2 mm spectrum of 22 $z = 2$–5.7 SPT DSFGs, from Spilker et al. (2014). The spectrum clearly shows the CO ladder as well as other emission lines such as high-critical density emission lines such as HCN, HCO$^+$ and H$_2$O, which imply warm and dense interstellar media in the DSFGs.

strength which makes it easy to detect and model (Kennicutt & Evans, 2012). Additionally, this feature is well-studied in the literature and numerous calibrations have been provided (Kennicutt & Evans, 2012). This ionised emission line, however, is subject to dust attentuation and therefore often underestimates the SFR in dust-obscured galaxies in the absence of an A_V correction (Dopita et al., 2002; Hogan et al., 2021). This can be corrected for with measurements of the Balmer decrement Hα/Hβ (e.g. Kewley et al., 2002), although the Hβ line is typically weak in SMGs.

Along with the Hα line, the other key rest-frame optical features are the forbidden doublets of ionised Nitrogen [NII]$\lambda\lambda$6548,6583, ionised Sulphur [SII]$\lambda\lambda$6716,6731 and ionised Oxygen [OIII]$\lambda\lambda$4959,5007, along with the Hβ line. The relative fluxes of these lines can indicate the processes that produce the most ionising radiation, and therefore to classify galaxies as AGN-dominated or star-formation dominated, a diagnostic encompassed by the Baldwin, Terlevich and Philips (BPT; Baldwin et al., 1981) diagram which has been well studied for local and high-redshift galaxies (e.g. Kewley et al., 2001; Tremonti et al., 2004; Kewley et al., 2013; Steidel et al., 2014; Shapley et al., 2015).

For star-forming galaxies the [NII]/Hα ratio can also trace the metallicity, typically expressed as the quantity $12 + \log(O/H)$ where O and H are the oxygen and hydrogen abundance, re-

spectively. This is because oxygen is often the most abundant heavy element in the ISM, and the definition usually involves the assumption that the abundance of the other chemical elements scales while maintaining solar ratios (see Maiolino & Mannucci, 2019, for a review). Scaling relations have been derived between the metallicity and other properties of galaxies, and Mannucci et al. (2010) combined this to produce a three-dimensional relation between mass, metallicity and star-formation rate, named the Fundamental Metallicity Relation (FMR), showing that it does not evolve up to $z \sim 2.5$. The FMR has the general property that galaxies display increasing metallicity with stellar mass until $M_* \sim 10^{10.5-11}$ (apparently comparable stellar masses to the majority of SMGs) where the metallicity plateaus (Mannucci et al., 2010), and at fixed stellar mass lower redshift sources have higher metallicities. These ideas will be explored in Chapter 4.

1.4 The current state of SMG research

In the last two decades observations of SMGs have led to the following conclusions: they reside predominantly at $z \sim 2$–3 (e.g. Chapman et al., 2005; da Cunha et al., 2015; Wardlow et al., 2018), with a handful of detections out to $z \sim 5$ (e.g. Coppin et al., 2010b), and have enormous infrared luminosities of $L_{\mathrm{IR}} \gtrsim 10^{12}$–$10^{13}\,\mathrm{L_\odot}$ (Dudzevičiūtė et al., 2020). These IR luminosities are a result of huge dust reservoirs ($\mathrm{M_{dust}} \sim 10^8\,\mathrm{M_\odot}$) which heat up and re-emit the vast majority of the optical/UV light from young O and B stars in the infrared. The implied star-formation rates are $\mathrm{SFR} \sim 100$–$1000\,\mathrm{M_\odot\,yr^{-1}}$ (e.g. Magnelli et al., 2012a; Swinbank et al., 2014; Miettinen et al., 2017; Dudzevičiūtė et al., 2020), and it has therefore been suggested that SMGs contribute significantly to the SFRD at cosmic noon (Barger et al., 2000; Swinbank et al., 2014; Dudzevičiūtė et al., 2020).

1.4.1 Triggering of star formation in SMGs

As SMGs are such an extreme population, one of the tests that they pose to models of galaxy evolution is finding a suitable mechanism to generate such intense levels of star formation. For SMGs, we may look to their local analogues, the ULIRGs, which are theorised to participate in evolutionary sequence for high-L_{IR} systems, first proposed by Sanders et al. (1988). The sequence is as follows: an isolated disc undergoes secular growth before experiencing a major merger from a similar-mass companion accreted by the halo. This leads to a starburst (the ULIRG phase we observe), causing rapid growth of the central black hole (Hopkins

et al., 2012a,b) which expels the remaining dust and leaves an unobscured Quasi-Stellar Object (QSO), a particuly radio luminous type of AGN. The QSO eventually fades, and star formation is quenched leaving a "red and dead" early-type galaxy. Observational studies have provided support to this model (e.g. Coppin et al., 2010a). In SMGs, high-resolution studies have shown that the star formation occurs in compact dust structures with diameters of ~ 2–$3\,\mathrm{kpc}$ (Tacconi et al., 2006; Simpson et al., 2015; Ikarashi et al., 2015; Gullberg et al., 2019; Hodge et al., 2019), in support of the merger triggering theory (McAlpine et al., 2019).

One of the most significant results in the field of galaxy evolution in recent years is the positive correlation between the stellar mass of star-forming galaxies and their star-formation rates, termed the galaxy "main sequence", i.e. analogous to the main sequence for stellar evolution (e.g. Brinchmann et al., 2004; Elbaz et al., 2007; Noeske et al., 2007; Whitaker et al., 2012; Speagle et al., 2014; Renzini & Peng, 2015; Schreiber et al., 2015). Some authors have fit large numbers of galaxies to determine the scaling relation between the two quantities (Whitaker et al., 2012; Speagle et al., 2014; Schreiber et al., 2015), showing that the zero-point evolves to higher SFRs with redshift (e.g. Popesso et al., 2019; Leslie et al., 2020). The majority of star-forming galaxies are observed to lie on, or near, the main sequence, and this tight correlation is used to suggest that galaxy star-formation rates are mostly controlled by steady gas accretion, with "starburst" galaxies representing outliers which are triggered by stochastic processes such as major mergers. Alternatively, they may have higher star-formation efficiencies (SFEs), and therefore convert more of their molecular gas into stars (e.g Hodge & da Cunha, 2020). However, current measurements of stellar masses and star-formation rates indicate that some high-redshift $850\,\mu$m-selected SMGs may be classified as main-sequence galaxies despite having SFRs of over $100\,\mathrm{M_\odot\,yr^{-1}}$ (e.g. da Cunha et al., 2015; Koprowski et al., 2016; Elbaz et al., 2018; Dudzevičiūtė et al., 2020). This may imply that smooth gas accretion can generate the rapid star formation in SMGs at $z \gtrsim 3$, and indeed, theoretical models have been developed to test this (e.g. Kereš et al., 2005; Dekel & Birnboim, 2006; Davé et al., 2010).

The question we have posed is: are the high SFRs in SMGs triggered by major mergers? Or are they simply "scaled-up" versions of less-active galaxies that are simply being fuelled by accreting greater amounts of gas from the ISM? In reality, the answer is likely to be a combination of the two – the selection of SMGs at $870\,\mu$m results in samples of galaxies that span over an order of magnitude in star-formation rate, infrared luminosity and stellar mass (e.g. da Cunha et al., 2015; Dudzevičiūtė et al., 2020), and it is therefore unreasonable to simply expect the entire population to behave in the same way. For example, it may be

possible that the brightest and most massive SMGs are merger driven, while the lower-mass sources are scaled-up versions of less-active SFGs.

1.4.2 SMG kinematics

As we discussed in §1.1.1, one of the major distinctions between early- and late-type galaxies is their kinematics – early-types are "dispersion-dominated" and late-types are "rotation-dominated". How is this defined, and measured?

The kinematics of a galaxy can be traced by spatially resolving a bright emission line, such as Hα, and modelling it to determine the variation of the redshift across the source. Combining this with the systemic redshift, one can also calculate how the velocity, in the rest-frame of the galaxy, varies as a function of radius. Two basic measurements used to parameterise the kinematics are the rotational velocity $v_{\rm rot}$ and the intrinsic velocity dispersion σ_0. The ratio of these two quantities $v_{\rm rot}/\sigma_0$ can be used to describe the level of rotational support in a galaxy (Weiner et al., 2006; Newman et al., 2013; Wisnioski et al., 2015), for example, a system with $v_{\rm rot}/\sigma_0 > 1.5$ may be classified as rotationally supported (Stott et al., 2016; Tiley et al., 2021), whereas one with $v_{\rm rot}/\sigma_0 < 1.5$ may be classified as dispersion dominated. Whether or not a galaxy is rotation dominated can provide useful insight into the triggering of star formation (Shapiro et al., 2008) – for example a system may be highly turbulent because it is experiencing a major merger event (e.g. Swinbank et al., 2006; Alaghband-Zadeh et al., 2012).

In the local Universe surveys such as the Calar Alto Legacy Integral Field Area (CALIFA; Sánchez et al., 2012), the Sydney–Australian–Astronomical Observatory Multi-Object Integral-field Spectrograph (SAMI; Croom et al., 2012) and Mapping Nearby Galaxies at Apache Point Observatory (MANGA; Bundy et al., 2015) have provided a comprehensive view of thousands of $z \sim 0$ galaxies. These surveys have verified scaling relations such as the Schmidt-Kennicutt law, the resolved star-forming main sequence and the mass-metallicity relation down to $\sim$ kpc scales in local galaxies (see Sánchez, 2020, for a review). At high redshifts however, kinematic studies are much more difficult – firstly due to the fact that more distant galaxies are fainter and require higher resolutions to observe on small scales, but also due to significant sky contamination in the near-infrared where the Hα emission line is found for $\gtrsim 1$. At the $z \sim 2$ epoch, disc morphologies are beginning to dominate the star-forming galaxy population (Mortlock et al., 2013; Tiley et al., 2021), and therefore overcoming these issues is crucial. IFU instruments such as the Spectrograph for INtegral Field Observations
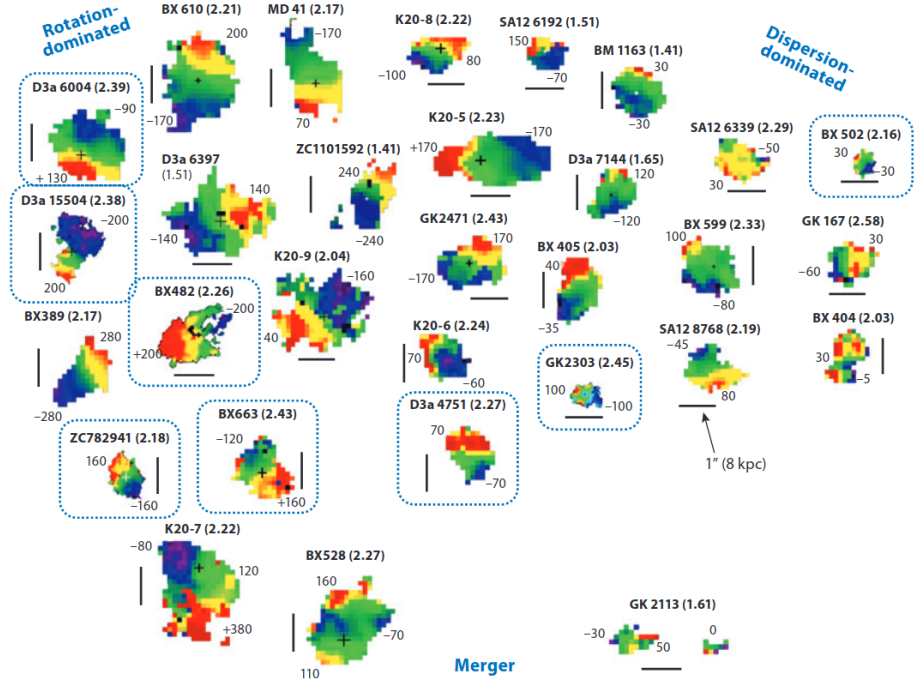
Figure 1.7: Hα velocity maps from approximately half of the SINS survey (from Förster Schreiber et al., 2009). This is one of the earliest examples of resolved kinematic studies of high-redshift star-forming galaxies.

in the Near Infrared (SINFONI; Bonnet et al., 2004), the OH-suppressing Infrared Field Spectrograph (OSIRIS; Larkin et al., 2006) on the Keck Telescope and the K-band Multi Object Spectrograph (KMOS; Sharples et al., 2013) can be used to observe Hα and/or [OIII] at these redshifts.

The first survey to spatially resolve galaxies at the cosmic noon epoch was the Spectroscopic Imaging survey in the Near-Infrared with SINFONI (SINS; Förster Schreiber et al., 2006), which included 62 SFGs with $M_* \gtrsim 10^{10}\,\mathrm{M_\odot}$ in the redshift range $z \sim 1.3$–2.6. The SINS sources are divided into three approximately equally sized subsets – rotation-dominated sources, mergers (Shapiro et al., 2009) and dispersion-dominated sources (see Fig. 1.7). One of the findings from SINS was that high-redshift star-forming galaxies have more turbulent ISM than their local counterparts, with velocity dispersions of $\sigma \sim 30$–$90\,\mathrm{km\,s^{-1}}$. Another early kinematic study was carried about by Law et al. (2009) with OSIRIS on 12 UV-selected SFGs in the redshift range $z \sim 2.0$–2.5 and marginally lower masses and SFRs than the SINS sample. The Law et al. (2009) sample contained $\sim 50\,\%$ dispersion-dominated sources, and like the SINS sample, showed high velocity dispersions $\sigma \sim 60$-$100\,\mathrm{km\,s^{-1}}$.

There have been many other surveys of $z \gtrsim 1$ star-forming galaxies with KMOS, including the KMOS Redshift One Spectroscopic Survey (KROSS; Stott et al., 2016), the KMOS^{3D} survey (Wisnioski et al., 2015, 2019), the KMOS Deep Survey (KDS; Turner et al., 2017) and the

KMOS Galaxy Evolution Survey (KGES; Tiley et al., 2021). For example, the ongoing KGES survey, which covers 288 K-band-selected galaxies with $z \sim 1.2$–1.8 and $M_* \sim 10^9$–$10^{11.5}\,\mathrm{M_\odot}$, has already revealed that the prevalence of discs does not change significantly from $z \sim 1.5$ to $z \sim 0.04$ at fixed stellar mass.

At the current time however, kinematic studies of dust-obscured systems are much more limited in scope. Alaghband-Zadeh et al. (2012) observed nine SMGs at $z \sim 2.0$–2.7 with SINFONI and the Gemini-North/Near-Infrared Integral Field Spectrograph (NIFS), finding an enormous average velocity dispersion of $\sigma = 220 \pm 80\,\mathrm{km\,s^{-1}}$, with multiple kinematically distinct components in six of the nine sources. These show average velocity offsets of $200 \pm 100\,\mathrm{km\,s^{-1}}$, implying that the six sources are merging systems. Therefore, while difficult for dust-enshrouded galaxies, studying the kinematics is a powerful tool for understanding the triggering mechanisms of their star formation. Chen et al. (2017) carried out a rare study of spatially resolved dust, cold gas and Hα in ALESS067.1, an SMG at $z = 2.12$, using dynamical modelling to suggest that the source is a merger.

1.4.3 SMGs as progenitors of early-type galaxies

As previously discussed, the galaxies that we observe at high redshifts are progenitors of galaxies in the nearby Universe. Therefore, given what we know about the highly star-forming dust-obscured population at high redshift, and given the hypothesised evolutionary sequence for ULIRGs, a natural question to ask is: what are the descendants of 850-μm-selected systems in the local Universe? And what processes drive the evolution between these two phases?

It is hypothesised that the SMG population are the progenitors of massive local galaxies (e.g. Blain et al., 2002; Coppin et al., 2008; Simpson et al., 2014), via a compact quiescent phase at $z \sim 2$, which requires a rapid "quenching" of star formation. Proposed mechanisms for quenching include AGN feedback (e.g. Croton et al., 2006; Bell et al., 2012), shock heating of infalling gas (e.g. Kereš et al., 2005; Dekel & Birnboim, 2006) and bulge formation which stabilises the disc (e.g. Martig et al., 2009). The advancements in studying SMGs, and the higher quantity and quality of physical parameters that have been derived, have allowed several tests of this theory. For example, Hodge et al. (2016) argued that the expected sizes, gas surface densities and stellar masses of the $z \sim 0$ descendants of SMGs are consistent with the most massive and compact local early types. Stach et al. (2021) predicted that the $z \sim 0$ descendants of SMGs will reside in dark matter halos of masses $\log_{10}(M_{\mathrm{halo}}/M_\odot) \sim 13.2$,

consistent with present-day massive spheroidal galaxies. Coppin et al. (2010b) used CO(2–1) observations of a $z = 4.76$ SMG to estimate its gas mass and depletion timescale, and argued that it could plausibly have reached the "red and dead" stage by $z \sim 3$.

In contrast, Miettinen et al. (2017) found that their sources at $z < 3$ would not be able to evolve into lower-mass compact quiescent galaxies. The galaxies used in this work are more massive than the majority of SMGs, however, which highlights the fact that the $870\,\mu$m selection produces samples with a wide range of properties, as discussed in §1.4.1. Therefore a one-size-fits-all approach is unlikely to match observations. Indeed, there has been suggested to be a dichotomy in the local early-type galaxy population: *elliptical* galaxies which generally have a merger origin and *spheroidal* galaxies which are typically more disc-like, having lost their gas supplies through e.g. supernova feedback (Kormendy et al., 2009). It is therefore important to study samples of SMGs that are representative of the whole population in order to fully understand any potential variations with, for example, mass or SFR.

1.5 Thesis aims and outline

Having outlined the motivations behind studying galaxy evolution and in particular the dust-obscured star-forming population at high redshifts, along with the tools that can be used to do so, we now provide an outline of the work presented in this thesis. Our aims are as follows:

- Boost the number of SMGs with secure spectroscopic redshifts using blind emission line scans, and use these to provide improved constraints on physical parameters derived from spectral energy distribution, such as stellar mass and star-formation rate

- Derive robust gas masses, gas fractions and gas depletion timescales for the SMG population, study how they evolve with properties as redshift, star-formation rate and stellar mass, and compare them with samples of more typical galaxies

- Determine whether SMGs are primarily rotationally supported or turbulent merging systems, and also whether SMGs appear to be "scaled up" versions of normal galaxies or entirely distinct systems

- Test the proposed link between SMGs and massive local early-type galaxies

- Study the ISM conditions in SMGs by constructing a CO spectral line energy distribution and placing SMGs on the BPT diagram

- Attempt to place constraints on the CO-H_2 conversion factor for SMGs, which would lead to improved gas mass estimates

- Estimate the prevalence in AGN in the SMG population, and test whether this varies with other properties such as redshift and SFR

We will exploit the observational tools described in §1.3 to meet these aims. We now summarise the content of the chapters in this thesis below. Chapters 2 and 3 present published work, while Chapters 4 and 5 are from an ongoing study.

- Chapter 2 presents techniques used in the reduction and analysis of 3 mm NOEMA and ALMA data, along with the selection details of our CO survey of 61 SMGs. This includes careful line identification and fitting along with an SED fitting analysis to determine the physical properties of the CO-detected targets.

- Chapter 3 presents analysis of the molecular gas properties of 47 SMGs in the COSMOS, UDS and ECDFS fields, as traced by the carbon monoxide CO, atomic carbon [C I] and 3 mm continuum, along with the physical properties derived from SED fitting using the spectroscopic redshifts. This is one of the largest samples of its kind and is less susceptible to biases from which earlier samples suffer, such as AGN contamination. Along with significantly increasing the sample of 870 μm-selected SMGs with secure spectroscopic redshifts, we also derive gas mass estimates for the sample along with molecular gas fractions, depletion timescales and gas-to-dust ratios. In addition, we supplement our sample with literature measurements to derive a statistical CO spectral line energy distribution (SLED) and study the molecular gas excitation properties of the population.

- Chapter 4 presents the KMOS Large Programme "KMOS+ALMA Observations of Submillimetre Sources" (KAOSS; Programme ID: 1103.A-0182). This is an ongoing survey of over 400 SMGs in the COSMOS, UDS and GOODS-S fields. We present the sample selection and observing strategy of KAOSS, along with the integrated Hα and [O III] properties of 44 sources with Hα and/or [O III] line detections. Physical properties of the sample are estimated from SED fitting, and we assess the level of AGN activity in the sample before studying it in the context of the Fundamental Metallicity Relation and the BPT diagram. We also present optical, Hα and dust size and shape measurements, which are used in Chapter 5.

- Chapter 5 presents a study of 37 sources from KAOSS with bright and extended enough Hα and/or [OIII] line detections to allow us to spatially resolve the emission. We derive resolved velocity and velocity dispersion maps and rotation curves, studying the ratio of v/σ to determine the degree to which our sources are rotationally supported, and using the velocities to measure the offset of the stellar and baryonic Tully-Fisher relation (TFR) for SMGs at $z \sim 2$. By comparing KAOSS sources with galaxies in the EAGLE simulations we estimate their halo masses, which provides diagnostic information on how they are supplied with cold gas.

- Chapter 6 presents the main results and conclusions of this thesis, along with a brief discussion of future work which can build on the work done here in order to further improve our understanding of the high-redshift dust-obscured SFG population, and galaxy formation/evolution in general.

3 mm observations of high-redshift dust-obscured star-forming galaxies

Preamble

In this chapter we introduce our 3 mm survey of SMGs in the COSMOS, UDS and ECDFS fields with ALMA and NOEMA. The survey is motivated by the need to obtain precise spectroscopic redshifts for SMGs, as well as more accurate estimates of their molecular gas masses, the latter of which can be traced by carbon monoxide (CO) gas. The low- to mid-J rotational lines of CO ($J_{\mathrm{up}} \sim 2$–5) are relatively easy to observe at $\lambda \sim 3$ mm, and are not strongly affected by dust attenuation, making them a highly useful tracer of the molecular gas in SMGs. Here we detail our target selection and data reduction, along with line analysis techniques and MAGPHYS SED fitting, the latter of which we use to study the AGN fraction in our sample and place our sources in relation to the star-forming main sequence. We proceed to present the molecular gas properties of the CO-detected SMGs in Chapter 3.

2.1 Introduction

The multi-wavelength properties of submillimetre galaxies (SMGs) have been studied by fitting the dust spectral energy distribution (SEDs) using codes such as MAGPHYS (e.g. da

Cunha et al., 2015; Dudzevičiūtė et al., 2020; Barger et al., 2022), with the large sample size of AS2UDS in particular allowing us to derive statistical measurements of photometric redshifts, star-formation rates, infrared luminosities and many other properties. The majority of SMGs are still without secure spectroscopic redshifts (but see e.g. Chapman et al., 2005; Danielson et al., 2017; Wardlow et al., 2018), without which it is challenging to place them into the broader picture of galaxy evolution. In addition, many of the derived photometric redshifts are highly uncertain due to the obscured nature of the population.

An efficient technique for obtaining precise spectroscopic redshifts is to target the rotational transitions of the carbon monoxide (CO) gas, which appear at wavelengths of $\lambda \sim 1\,\text{mm}$ and can therefore be observed with (sub-)millimetre interferometers such as the Atacama Large (sub)-Millimetre Array (ALMA; e.g. Wardlow et al., 2018) and the NOrthern Extended Millimeter Array (NOEMA; Daddi et al., 2008; Chapman et al., 2015), along with also single-dish telescopes such as LABOCA (Weiß et al., 2008). SMGs are much brighter in this wavelength range than in the optical/near-infrared (NIR), and with technological advancements allowing wider frequency coverage, the success rate at detecting emission and determining redshifts is higher than rest-frame optical surveys (Weiß et al., 2009; Swinbank et al., 2010), with the derived redshifts less biased towards low-redshift, optically-bright sources. NOEMA has recently become a powerful tool for blind CO surveys, owing to a new wideband receiver and the *PolyFix* correlator, along with the addition of new antennae, giving the instrument 16 GHz of bandwidth at 3 mm. ALMA is the most powerful telescope of its kind, and can also achieve large bandwidths with multiple frequency tunings. As an example of the success rate of such blind scans, Weiß et al. (2013) conducted a blind 3 mm ALMA survey of 26 strongly dusty star-forming galaxies selected at 1.4 mm, using the South Pole Telescope (SPT), successfully detecting at least one CO, [C I] or H_2O feature in 23 of their targets (also see e.g. Vieira et al., 2013).

In addition to providing unbiased redshifts, the CO emission is a standard tracer of the molecular hydrogen H_2 which otherwise cannot be observed due to its lack of a permanent dipole moment, preventing any transitions from being appreciably excited in the cold interstellar medium (ISM) of SMGs (e.g. Solomon et al., 1992; Omont, 2007; Carilli & Walter, 2013). H_2 is the dominant component of the molecular gas in galaxies and the main fuel for star formation, so it is vital to be able to characterise the H_2 mass, and consequently the CO mass, in order to understand the nature of star formation in these extreme starbursts. The key properties that can be measured from CO emission are the line luminosity and line profiles (e.g. Bothwell et al., 2013). The former provides a measure of the amount of CO gas,

from which one can estimate the H_2 or total gas mass (Solomon & Vanden Bout, 2005), and the latter provides a measure of the total mass and dynamics.

Observations of CO have provided useful constraints on the molecular gas in SMGs. The first studies of this kind were performed by Frayer et al. (1998, 1999), showing that SMGs have broad and often double-peaked CO lines, gas masses of order $10^{10}\,M_\odot$, and short gas depletion timescales of $t_{\rm dep} \sim 50\,{\rm Myr}$. High-resolution CO observations showed that the SMG population displays a mix of sources with complex gas motions, indicative of major mergers, and sources with compact gas discs, although the former model seems to be favoured (Tacconi et al., 2008; Engel et al., 2010). Other major studies include Greve et al. (2005), who found broad lines indicating dynamical masses of order $10^{11}\,M_\odot$, Daddi et al. (2010), who found gas fractions of ~ 50–65 percent in $z \sim 1.5$ BzK galaxies, and Ivison et al. (2011), who resolved four SMGs with the Extended Very Large Array, finding typical sizes of $\sim 16\,{\rm kpc}$. Chen et al. (2017) provided a spatially resolved study of an ALESS SMG (ALESS67.1), finding its morphology to be indicative of a merger. Bothwell et al. (2013) surveyed CO emission in 40 SMGs with the Plateau de Bure Interferometer with 26 firm detections and six candidate detections, and used this to derive molecular gas masses, along with a median CO spectral line energy distribution (SLED) for SMGs. Although their work provided useful constraints on the molecular emission, the sample was biased towards sources with known spectroscopic redshifts and radio identifications, and hence towards the optically-bright, lower-redshift and potentially AGN-dominated end of the population.

To build on the above we have undertaken a survey of 61 SMGs with precise ALMA $870\,\mu$m continuum detections from the ALMA SCUBA-2 Cosmic Evolution Survey (AS2COSMOS; Simpson et al., 2020), ALMA SCUBA-2 UKIDSS Ultra Deep Survey (AS2UDS; Stach et al., 2018, 2019) and the ALMA LABOCA survey of the Extended *Chandra* Deep Field South (ALESS; Hodge et al., 2013) samples with ALMA and NOEMA at $\lambda \sim 3\,{\rm mm}$, aiming to provide secure spectroscopic redshifts and estimate their molecular gas masses. We have compiled targets from a number of programmes to include sources with a wide range of K-band magnitude and S_{870}, which will allow us to study parameter correlations within the population. Our sample is one of the largest of its kind, and with it we take advantage of the unmatched sensitivity of ALMA/NOEMA and the wealth of multi-wavelength data available in the COSMOS, UDS and ECDFS fields. We will address the redshift distribution, gas excitation, dynamics and gas masses of SMGs, the evolution of their gas fractions and gas depletion timescales, along with their relation to the star-forming main sequence. As a study of similar size and intent, we will compare throughout to Bothwell et al. (2013).

	Spec-z	*Scan*	Total
	Number of targets		
AS2COSMOS	0	5	5
AS2UDS	4	13	17
ALESS	26	13	39
Total sources	30	31	61
Median S_{870} [mJy]	4.2 (2.6–6.0)	8.8 (4.4–13.9)	5.9 (2.8–10.5)
Median K [mag]	21.2 (20.3–22.7)	22.9 (22.1–23.7)	22.3 (20.7–23.5)
Median V [mag]	24.3 (22.9–25.4)	26.0 (24.8–27.2)	25.1 (23.8–26.8)
$N_{\mathrm{detected,cont.}}$	13	26	39
$N_{\mathrm{detected,CO}}$	19	26 (+5 serendip.)	50

Table 2.1: Summary of our source selection and the 870-μm fluxes of our subsamples. When reporting the median $S_{870}/K/V$ we also give the 16–84 th percentile ranges in parentheses.

The outline of this chapter is as follows: in §2.2 we outline the sample selection for this survey, and in §2.3 we describe the observations carried out and data reduction. We then go on to discuss our data analysis methods in §2.5, before discussing initial conclusions from the survey in §2.6. The main science results of the survey are presented and discussed in Chapter 3. Throughout this chapter we adopt a flat Λ-CDM cosmology defined by $(\Omega_{\mathrm{m}}, \Omega_{\Lambda}, H_0) = (0.27, 0.73, 71\,\mathrm{km\,s^{-1}\,Mpc^{-1}})$.

2.2 Sample selection

Our 61 targets are selected from ALMA-identified 870-μm-selected SMGs in the ALMA-SCUBA-2 Cosmic Evolution Survey (AS2COSMOS; Simpson et al., 2020), the ALMA-SCUBA-2 Ultra Deep Survey (AS2UDS; Stach et al., 2019) and the ALMA-LABOCA ECDFS Sub-millimetre Survey (ALESS; Hodge et al., 2013). These targets are divided into two samples based on the observing mode used in their 3-mm follow-up:

1. ***Scan* sample**: 31 sources which lack existing spectroscopic redshifts, which were targeted with scans in the 3-mm band. These sources comprise two subsets, firstly SMGs with the brightest 870-μm fluxes in the AS2COSMOS and AS2UDS surveys, and a second subset of sources from ALESS which span a wider range in submillimetre flux, but are chosen to be faint in the optical/near-infrared (to complement the *spec-z* sample discussed below). The selection for this sample is then as follows:

   - 18 sources representing the brightest submillimetre sources in their respective sur-
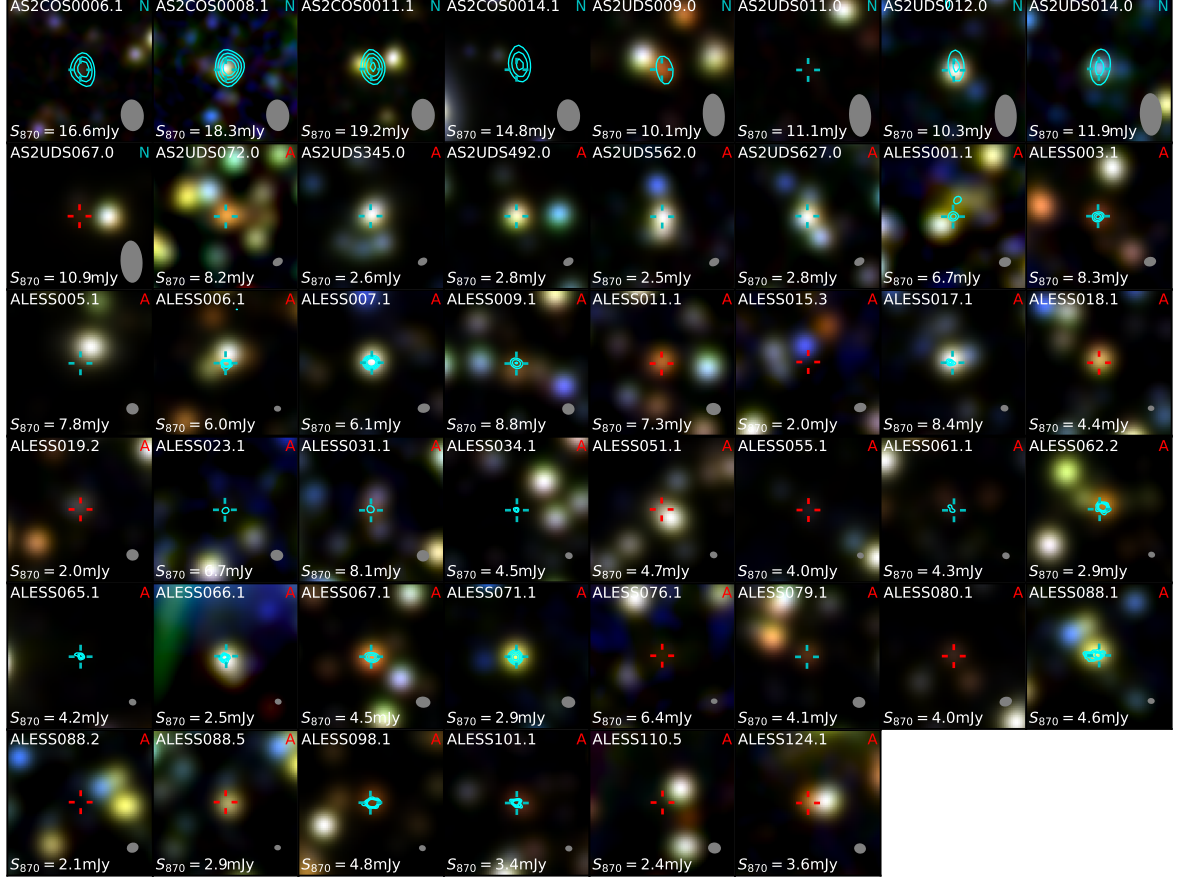
Figure 2.1: $25'' \times 25''$ ($\sim 200\,\mathrm{kpc}$ at the median redshift of our sample) colour thumbnails composed of K-band, IRAC $3.6\,\mu$m and IRAC $4.5\,\mu$m images of the targets in our sample for which this imaging is available. We see that SMGs are in general redder than field galaxies, but this is not the case for all sources. The crosshair (cyan for CO-detected and red for CO non-detected) indicates the position of the 870-μm emission detected by ALMA, with a typical beam size of ~ 0.3–$0.5''$, the 870-μm flux density of which is reported in each frame. The cyan contours represent CO emission at the 5-, 7-, 9- and 11-σ levels. We indicate whether the CO observations of the target come from ALMA (A) or NOEMA (N) and show the synthesised beam in the top- and bottom-right corners, respectively. The ALMA 3-mm beam sizes range between $0.8'' \times 0.6''$ and $2.2'' \times 1.8''$, whereas for NOEMA they are typically $\sim 6'' \times 4''$.

vey fields, resulting in five AS2COSMOS sources with $S_{870} = 15$–$20\,\mathrm{mJy}$ and thirteen AS2UDS sources with $S_{870} = 8$–$14\,\mathrm{mJy}$.

- 13 sources from ALESS which are selected to be optically/near-infrared faint (typically $R \gtrsim 25$ or $K \gtrsim 22$) with $S_{870} = 2$–$9\,\mathrm{mJy}$.

The brightness of the majority of these sources at $870\,\mu\mathrm{m}$ indicates significant cold dust masses and so suggests that they will also be bright CO emitters, but they also have poorly constrained redshifts. Therefore we have scanned the full 3-mm band using multiple tunings to effectively guarantee that we detect their CO emission[1]. The relative brightness of the sources in part reflects the survey volume of the corresponding fields.

2. ***Spec-z* sample**: 30 sources with existing rest-frame optical/UV spectroscopic redshifts. Four of these sources are taken from AS2UDS (Dudzevičiūtė et al., 2020), and the remaining 26 are taken from ALESS (Danielson et al., 2017). These sources are typically brighter in the optical and near-infrared, and fainter in the submillimetre than the *scan* sample (see Table 2.1).

Fig. 2.1 shows K/IRAC $3.6\,\mu\mathrm{m}$/IRAC $4.5\,\mu\mathrm{m}$ colour images (where imaging is available) for our targets, showing that SMGs are typically redder than nearby field galaxies. In Fig. 2.2(a) we show the distribution of S_{870} and K-band magnitude for our targets compared with their parent SMG samples[2]. In Fig. 2.2(b) we show histograms of S_{870} and K for the different subsamples, compared to the parent samples from which they were selected. By combining samples with different selection criteria we are able to efficiently cover a large fraction of the parameter space covered by the general SMG population. The *scan* sources selected on 870-$\mu\mathrm{m}$ flux by definition cover the submillimetre-bright end of the parameter space, while the *spec-z* and K-faint *scan* sources cover the submillimetre-faint end. In terms of K-band magnitude, the *scan* sources are mostly K-faint both for the sources selected on that basis, and for the submillimetre-bright sources which are also typically faint in K. Finally, the *spec-z* sources are generally K-bright as they are selected to have optical/near-infrared spectroscopic redshifts, which are only robustly measurable in such sources.

We note that due to our strategy of trying to cover a large region of the SMG parameter space, our sample is not flux-limited (other than at the highest 870-$\mu\mathrm{m}$ fluxes) and so we

---

[1]There is a small gap in CO coverage of the 3-mm band in the range $z \sim 1.75$–2.0.

[2]Some sources fall outside the K-band coverage of their respective survey field, and in these cases we estimate K from their 3.6-$\mu\mathrm{m}$ magnitudes, where IRAC photometry is available, using the $K - 3.6\,\mu\mathrm{m}$ colours of AS2UDS SMGs at similar redshifts.
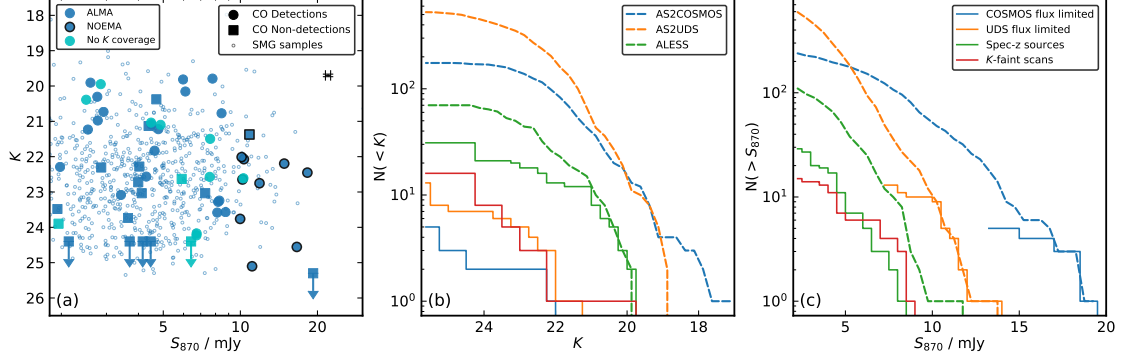
Figure 2.2: **(a)** K-band magnitude versus 870-μm flux density for sources targeted in this work (filled), with the parent samples of SMGs from AS2COSMOS, AS2UDS and ALESS represented by the small points. For our targets, symbol shapes differentiate CO detections from non-detections. ALMA or NOEMA observations are differentiated by the symbol outline. Our sample covers the range of K magnitudes (median $K = 22.3$; 16–84th percentile range 20.7–23.5) spanned by the SMG population, while we typically select sources that are bright at 870 μm (median $S_{870} = 5.9$ mJy; 16–84th percentile range 2.8–10.5 mJy). 3-σ upper limits for K non-detections are plotted, and we show a representative error bar for the whole population in the top-right corner. Four sources are undetected in the K-band and 14 have no K-band photometry. In the latter cases we estimate K from the typical $K - 3.6\,\mu$m colour at the appropriate redshift, where IRAC 3.6 μm coverage is available (cyan points). Seven of our targets have no K or IRAC 3.6 μm coverage, and therefore do not appear in this panel. **(b)**: Cumulative histogram of K-band magnitude for our targets compared with their parent samples. Non-detected sources are shown at the relevant 3-σ flux limit of their respective survey, as for simplicity are the seven sources that are not covered in K or IRAC 3.6 μm. We see that the K- and S_{870}-selected sources mostly sample the K-faint end of the parent sample, whereas the ALESS *spec-z* sources are complete above $K \sim 21$. **(c)**: Cumulative histogram of S_{870} for our targets compared with their parent samples. The S_{870}-selected *scan*-mode sources are mostly complete above ~ 15 mJy and ~ 10 mJy in AS2COSMOS and AS2UDS, respectively, whereas the K-selected and *spec-z* sources cover the fainter end of this parameter space.

must also be aware of potential biases arising from this. In particular, we caution that it is not trivial to reconstruct statistically-complete samples of fainter submillimetre sources from this survey owing to the mix of selection criteria, with similar limitations applying to other studies such as the A3COSMOS archival compilation work by Liu et al. (2019a,b).

The sample is summarised in Table 2.1, and details of the individual source properties are given in Tables 2.2 and 2.3. We reiterate here that the aim of this study is to provide an analysis of the molecular gas in submillimetre galaxies, building on the work highlighted earlier with a large sample of high quality data. We will, for the majority of this analysis, consider the entire sample as one, noting that the wide range in 870-μm flux, redshift and optical/near-infrared brightness of our targets make the sample well suited for studying correlations in the properties of the population.

2.3   Observations and data reduction

Observations were obtained from six projects, four with ALMA and two with NOEMA/*PolyFix*, between 2017 and 2020. Fifteen targets from the *scan* sample, five from AS2COSMOS and ten from AS2UDS, were observed with NOEMA/*PolyFix* in projects S18CG and W18EL. Targets were observed with two spectral setups, each using a pair of 8-GHz sidebands, to achieve a total contiguous bandwidth of 32 GHz covering ~ 82–114 GHz. Each target was observed for an integration time of 1.5 hours per setup using the combined CD array configuration which is suitable for low-resolution detection experiments. Reduction of the data was carried out using the GILDAS software. The raw data were calibrated using standard pipelines, with bad visibilities flagged and removed in the process. For bandpass and flux calibration we observed J1018+055, 0906+015 and J0948+003 for AS2COSMOS sources and 0238−084, 0215+015 and J0217−083 for AS2UDS sources. Calibrated uv tables were imaged using natural weighting with the MAPPING routine in GILDAS, and the resultant dirty cubes were outputted to FITS format for analysis with our own PYTHON routines. Typical synthesised beam sizes for the NOEMA data are $6'' \times 4''$ at 3 mm, with the observations achieving a typical 1-σ depth of 0.6 mJy in 100 km s^{-1} channels.

The remaining 46 targets were observed with ALMA in projects 2016.1.00564.S, 2017.1.01163.S, 2017.1.01512.S and 2019.1.00337.S. Sixteen of the targets in the *scan* sample (three from AS2UDS, thirteen from ALESS) were observed using five tunings to achieve 32 GHz of bandwidth covering ~ 82–114 GHz, with integration times of ~ 15 minutes per tuning. All thirty

Source ID	Subsample	R.A. (J2000)	Dec (J2000)	S_{870} [mJy]	$z_{\rm phot}$	$z_{\rm spec}$	$M_{\rm dust}$ [$10^8 {\rm M}_\odot$]	M_* [$10^{10} {\rm M}_\odot$]	SFR [${\rm M}_\odot {\rm yr}^{-1}$]
AS2COS0006.1	Scan	09:59:57.29	+02:27:30.59	16.6 ± 0.4	$3.52^{+-0.00}_{-0.00}$	...	$11.4^{+2}_{-0.3}$	$4.4^{+8}_{-0.2}$	414^{+110}_{-5}
AS2COS0008.1	Scan	10:02:49.19	+02:32:55.47	18.3 ± 0.4	$3.35^{+0.05}_{-0.00}$	...	21^{+3}_{-3}	51^{+12}_{-7}	1400^{+100}_{-140}
AS2COS0011.1	Scan	10:01:41.76	+02:27:12.90	19.2 ± 0.4	$4.29^{+0.66}_{-0.00}$	...	14^{+2}_{-2}	60^{+40}_{-20}	1100^{+400}_{-700}
AS2COS0014.1	Scan	10:01:41.04	+02:04:04.87	14.8 ± 0.4	$3.25^{+0.02}_{-0.00}$	...	$14.7^{+1}_{-0.8}$	18^{+3}_{-3}	1090^{+50}_{-110}
AS2COS0031.1	Scan	09:59:23.01	+02:51:37.51	18.1 ± 0.5	$3.31^{+0.00}_{-0.00}$	...	10^{+3}_{-1}	$4.57^{+8}_{-0.10}$	449^{+5}_{-5}
AS2UDS009.0	Scan	02:16:43.71	−05:17:53.75	10.1 ± 0.6	$2.63^{+0.32}_{-0.32}$	...	12^{+2}_{-1}	$23^{+0.5}_{-9}$	703^{+170}_{-8}
AS2UDS010.0	Scan	02:15:55.96	−04:55:08.58	10.3 ± 0.8	$3.94^{+0.19}_{-0.32}$	...	15^{+3}_{-3}	35^{+18}_{-14}	570^{+90}_{-120}
AS2UDS011.0	Scan	02:16:30.82	−05:24:03.31	11.1 ± 0.7	$3.73^{+1.07}_{-0.90}$	...	10^{+2}_{-1}	32^{+16}_{-13}	960^{+170}_{-190}
AS2UDS012.0	Scan	02:18:03.56	−04:55:27.25	10.3 ± 0.7	$2.43^{+0.20}_{-0.20}$	...	13^{+3}_{-2}	$20.9^{+8}_{-0.5}$	400^{+100}_{-5}
AS2UDS014.0	Scan	02:17:44.26	−05:20:08.59	11.9 ± 0.6	$3.68^{+0.22}_{-0.12}$	...	11^{+2}_{-2}	14^{+2}_{-2}	690^{+160}_{-40}
AS2UDS019.0	Scan	02:15:55.11	−05:24:56.57	13.6 ± 0.4	$3.03^{+1.34}_{-0.77}$	...	28^{+17}_{-15}	50^{+70}_{-30}	700^{+1300}_{-500}
AS2UDS026.0	Scan	02:19:02.09	−05:28:56.89	10.0 ± 0.7	$3.83^{+1.02}_{-0.43}$	...	10^{+2}_{-2}	28^{+12}_{-9}	350^{+80}_{-100}
AS2UDS029.0	Scan	02:19:27.16	−04:45:06.15	10.2 ± 0.7	$1.95^{+0.31}_{-0.33}$	...	32^{+2}_{-4}	$1.05^{+0.02}_{-0.05}$	110^{+3}_{-6}
AS2UDS067.0	Scan	02:18:16.49	−04:55:08.84	10.9 ± 0.8	$1.46^{+0.02}_{-0.02}$	...	36^{+1}_{-4}	$6.2^{+0.4}_{-0.4}$	449^{+10}_{-5}
AS2UDS072.0	Scan	02:18:36.91	−05:17:53.61	8.2 ± 0.8	$2.88^{+0.12}_{-0.12}$	...	20^{+2}_{-2}	$2^{+0.04}_{-5}$	130^{+3}_{-90}
AS2UDS112.0	Scan	02:15:40.93	−05:13:21.23	7.9 ± 0.6	$1.80^{+0.80}_{-0.47}$	...	28^{+4}_{-4}	40^{+60}_{-30}	130^{+100}_{-80}
AS2UDS126.0	Scan	02:15:46.70	−05:18:49.21	11.2 ± 0.4	$2.58^{+0.62}_{-0.62}$	...	20^{+3}_{-3}	70^{+90}_{-40}	700^{+300}_{-300}
AS2UDS231.0	Scan	02:18:52.86	−04:38:24.20	7.6 ± 0.7	$2.95^{+0.12}_{-0.08}$	...	21^{+6}_{-5}	40^{+18}_{-14}	410^{+110}_{-110}
AS2UDS345.0	Spec-z	02:18:03.67	−04:59:30.55	2.6 ± 0.6	$1.65^{+0.03}_{-0.06}$	1.264	7^{+1}_{-2}	$30^{+0.7}_{-2}$	183^{+6}_{-14}
AS2UDS492.0	Spec-z	02:18:09.56	−05:02:00.33	2.8 ± 0.7	$1.80^{+0.06}_{-0.06}$	1.268	6^{+2}_{-2}	2^{+2}_{-5}	96^{+80}_{-1}
AS2UDS562.0	Spec-z	02:18:50.34	−04:46:34.80	2.5 ± 0.3	$2.42^{+0.06}_{-0.05}$	2.465	7^{+2}_{-2}	15^{+2}_{-3}	180^{+18}_{-20}
AS2UDS627.0	Spec-z	02:17:41.56	−04:54:11.71	2.8 ± 0.3	$1.23^{+0.20}_{-0.02}$	...	$7^{+0.5}_{-4}$	$7.1^{+0.5}_{-0.9}$	200^{+14}_{-18}
ALESS001.1	Scan	03:33:14.46	−27:56:14.52	6.7 ± 0.5	$4.78^{+2.65}_{-1.81}$	4.954	10^{+3}_{-2}	9^{+3}_{-3}	680^{+200}_{-190}
ALESS003.1	Scan	03:33:21.50	−27:55:20.29	8.3 ± 0.4	$3.88^{+0.90}_{-0.76}$	4.237	12^{+2}_{-1}	19^{+8}_{-8}	710^{+130}_{-110}
ALESS005.1	Scan	03:31:28.91	−27:59:09.02	7.8 ± 0.7	$3.67^{+0.05}_{-0.20}$	...	9^{+1}_{-1}	$23.4^{+30}_{-0.5}$	900^{+20}_{-300}
ALESS006.1	Spec-z	03:32:56.96	−28:01:00.68	6.0 ± 0.4	$2.88^{+0.15}_{-0.10}$	2.334	20^{+6}_{-6}	10^{+30}_{-7}	210^{+40}_{-80}
ALESS007.1	Spec-z	03:33:15.42	−27:45:24.30	6.1 ± 0.3	$1.98^{+0.60}_{-0.50}$	2.692	$9^{+0.9}_{-2}$	74^{+8}_{-3}	578^{+90}_{-7}
ALESS009.1	Scan	03:32:11.34	−27:52:11.93	8.8 ± 0.5	$4.88^{+1.24}_{-1.66}$	...	12^{+2}_{-1}	72^{+40}_{-14}	550^{+300}_{-160}
ALESS011.1	Spec-z	03:32:13.85	−27:56:00.25	7.3 ± 0.4	$3.03^{+0.25}_{-0.45}$	2.683	13^{+4}_{-4}	17^{+20}_{-13}	500^{+200}_{-300}
ALESS015.3	Spec-z	03:33:33.59	−27:59:35.43	2.0 ± 0.5	$3.42^{+4.11}_{-2.34}$	3.425	3^{+8}_{-3}	3^{+1}_{-2}	130^{+500}_{-120}
ALESS017.1	Spec-z	03:32:07.30	−27:51:20.75	8.4 ± 0.5	$2.12^{+0.35}_{-0.60}$	1.540	24^{+2}_{-2}	18^{+8}_{-5}	140^{+100}_{-90}

Table 2.2: CO survey target details. Targets are separated into blind spectral scans (S) and those that have been targeted based on pre-existing spectroscopic redshifts (T). Photometric redshifts, along with dust and stellar masses, are derived from SED fitting with MAGPHYS (da Cunha et al., 2015; Dudzevičiūtė et al., 2020). Spectroscopic redshifts are taken from Danielson et al. (2017).

Source ID	Subsample	R.A. (J2000)	Dec (J2000)	S_{870} [mJy]	$z_{\rm phot}$	$z_{\rm spec}$	$M_{\rm dust}$ [$10^8 M_\odot$]	M_* [$10^{10} M_\odot$]	SFR [$M_\odot {\rm yr}^{-1}$]
ALESS018.1	*Spec-z*	03:32:04.88	−27:46:47.74	4.4 ± 0.5	$2.03^{+0.30}_{-0.20}$	2.252	8^{+2}_{-3}	$35^{+0.8}_{-13}$	552^{+300}_{-13}
ALESS019.2	*Scan*	03:32:07.89	−27:58:24.06	2.0 ± 0.5	$2.17^{+0.36}_{-0.75}$	...	18^{+30}_{-11}	5^{+2}_{-2}	500^{+700}_{-400}
ALESS022.1	*Scan*	03:31:46.92	−27:32:39.30	4.5 ± 0.5	$2.42^{+0.46}_{-0.75}$	...	$6.6^{+1.0}_{-0.8}$	47^{+11}_{-7}	300^{+100}_{-90}
ALESS023.1	*Scan*	03:32:12.01	−28:05:06.46	6.7 ± 0.4	$4.07^{+1.55}_{-0.95}$	...	10^{+2}_{-1}	28^{+18}_{-12}	560^{+160}_{-120}
ALESS029.1	*Spec-z*	03:33:36.90	−27:58:09.33	5.9 ± 0.4	$3.62^{+0.95}_{-0.54}$	1.439	18^{+8}_{-5}	45^{+13}_{-16}	9^{+40}_{-8}
ALESS031.1	*Scan*	03:31:49.79	−27:57:40.76	8.1 ± 0.4	$4.22^{+1.46}_{-1.19}$	...	11^{+2}_{-1}	33^{+9}_{-9}	650^{+180}_{-140}
ALESS034.1	*Spec-z*	03:32:17.96	−27:52:33.28	4.5 ± 0.6	$1.87^{+0.29}_{-0.32}$	2.511	5^{+2}_{-1}	$4.6^{+0.8}_{-0.9}$	330^{+130}_{-110}
ALESS035.1	*Scan*	03:31:10.51	−27:37:15.42	4.4 ± 0.3	$3.58^{+0.95}_{-0.86}$	...	$6.6^{+0.8}_{-0.8}$	43^{+20}_{-18}	440^{+140}_{-130}
ALESS041.1	*Spec-z*	03:31:10.07	−27:52:36.66	4.9 ± 0.6	$2.17^{+0.61}_{-0.65}$	2.546	8^{+1}_{-1}	70^{+30}_{-20}	280^{+120}_{-120}
ALESS051.1	*Spec-z*	03:31:45.06	−27:44:27.32	4.7 ± 0.4	$1.33^{+0.19}_{-0.10}$	1.364	15^{+4}_{-5}	13^{+3}_{-2}	100^{+40}_{-30}
ALESS055.1	*Spec-z*	03:33:02.22	−27:40:35.45	4.0 ± 0.4	$2.28^{+0.25}_{-0.20}$	1.356	8^{+4}_{-2}	$0.4^{+0.0}_{-0.0}$	$83.6^{+40}_{-1.0}$
ALESS061.1	*Spec-z*	03:32:45.87	−28:00:23.36	4.3 ± 0.5	$6.12^{+1.44}_{-1.44}$	4.419	7^{+2}_{-2}	$2.14^{+1}_{-0.05}$	264^{+120}_{-6}
ALESS062.2	*Spec-z*	03:32:36.58	−27:34:53.83	2.9 ± 0.7	$1.35^{+0.08}_{-0.11}$	1.361	7^{+1}_{-1}	$5^{+0.2}_{-5}$	475^{+11}_{-5}
ALESS065.1	*Spec-z*	03:32:52.27	−27:35:26.27	4.2 ± 0.4	$5.68^{+1.79}_{-2.76}$	4.444	7^{+3}_{-2}	$3.0^{+2}_{-0.8}$	300^{+80}_{-90}
ALESS066.1	*Spec-z*	03:33:31.93	−27:54:09.52	2.5 ± 0.5	$1.98^{+0.49}_{-1.00}$	2.554	$1.8^{+0.3}_{-0.2}$	26^{+30}_{-17}	450^{+120}_{-120}
ALESS067.1	*Spec-z*	03:32:43.20	−27:55:14.34	4.5 ± 0.4	$2.08^{+0.30}_{-0.35}$	2.123	$9^{+1.0}_{-3}$	$17.8^{+8}_{-0.4}$	156^{+2}_{-5}
ALESS068.1	*Scan*	03:32:33.33	−27:39:13.57	3.7 ± 0.6	$3.78^{+1.90}_{-1.06}$	...	$5.5^{+1}_{-1.0}$	9^{+8}_{-4}	340^{+100}_{-80}
ALESS071.1	*Spec-z*	03:33:05.65	−27:33:28.19	2.9 ± 0.6	$1.77^{+0.21}_{-0.39}$	3.697	$4^{+0.5}_{-2}$	204^{+8}_{-14}	2640^{+400}_{-90}
ALESS076.1	*Spec-z*	03:33:32.34	−27:59:55.63	6.4 ± 0.6	$3.97^{+1.71}_{-0.94}$	3.389	13^{+15}_{-6}	5^{+2}_{-2}	400^{+500}_{-200}
ALESS079.1	*Scan*	03:32:21.14	−27:56:26.99	4.1 ± 0.4	$3.53^{+1.09}_{-0.86}$	...	$3.4^{+0.5}_{-0.4}$	46^{+16}_{-4}	450^{+140}_{-130}
ALESS080.1	*Spec-z*	03:31:42.80	−27:48:36.88	4.0 ± 0.9	$2.58^{+1.14}_{-0.41}$	4.665	4^{+3}_{-2}	$7.94^{+0.19}_{-0.18}$	1600^{+200}_{-1300}
ALESS082.1	*Spec-z*	03:32:54.00	−27:38:14.89	1.9 ± 0.5	$3.47^{+2.65}_{-1.95}$	...	2^{+6}_{-1}	10^{+5}_{-6}	200^{+600}_{-200}
ALESS088.1	*Spec-z*	03:31:54.76	−27:53:41.49	4.6 ± 0.6	$1.58^{+0.15}_{-0.06}$	1.268	14^{+2}_{-2}	1^{+8}_{-5}	70^{+100}_{-90}
ALESS088.2	*Spec-z*	03:31:55.39	−27:53:40.30	2.1 ± 0.5	$4.28^{+3.10}_{-1.80}$	2.519	4^{+9}_{-2}	4^{+2}_{-3}	150^{+300}_{-110}
ALESS088.5	*Spec-z*	03:31:55.81	−27:53:47.21	2.9 ± 0.7	$2.47^{+0.61}_{-0.64}$	2.294	4^{+3}_{-2}	$2.3^{+0.9}_{-0.5}$	410^{+90}_{-50}
ALESS098.1	*Spec-z*	03:31:29.92	−27:57:22.74	4.8 ± 0.6	$3.33^{+0.01}_{-0.01}$	1.373	$12.5^{+3}_{-0.7}$	30^{+4}_{-3}	270^{+20}_{-20}
ALESS101.1	*Spec-z*	03:31:51.60	−27:45:52.98	3.4 ± 0.8	$3.49^{+3.52}_{-2.00}$	2.800	11^{+5}_{-3}	16^{+8}_{-6}	150^{+50}_{-50}
ALESS110.5	*Scan*	03:31:22.96	−27:54:14.42	2.4 ± 0.6	$3.62^{+3.70}_{-2.74}$	...	4^{+10}_{-4}	4^{+2}_{-3}	150^{+500}_{-150}
ALESS112.1	*Spec-z*	03:32:48.86	−27:31:13.30	7.6 ± 0.5	$2.72^{+1.14}_{-0.25}$	2.315	18^{+4}_{-3}	16^{+5}_{-4}	270^{+40}_{-50}
ALESS124.1	*Scan*	03:32:04.04	−27:36:06.37	3.6 ± 0.6	$2.42^{+0.80}_{-0.94}$	...	8^{+8}_{-4}	13^{+6}_{-9}	140^{+300}_{-110}

Table 2.3: Table 2.2 continued.

targets in the *spec-z* sample were observed using single tunings centred on the frequency of the CO line expected in the 3-mm band (ALMA band 3). Integration times ranged from ~ 25–40 minutes. All of these programmes were executed using the 12-m array in compact configurations. Reduction of the data was carried out using the COMMON ASTRONOMY SOFTWARE APPLICATIONS (CASA; McMullin et al., 2007) software, employing standard pipelines to produce naturally-weighted dirty cubes, which we then outputted to FITS format for analysis with our own PYTHON routines. For bandpass and flux calibration we observed J0423$-$0120, J0238+1636 and J0217$-$0820 for AS2UDS sources and J0522$-$3627, J0342$-$3007, J0317$-$2803 and J0334$-$4008 for ALESS sources. Synthesised beam sizes for the ALMA data range between $0.8'' \times 0.6''$ and $2.2'' \times 1.8''$, with the observations achieving a typical 1-σ depth of $0.3\,\mathrm{mJy}$ in $100\,\mathrm{km\,s^{-1}}$ channels.

2.4 Line detection

From our reduced data cubes we extract spectra in an aperture centred on the position of the 870-μm emission. As our observations include (marginally) resolved and unresolved sources we adopt two separate recipes for determining line and continuum fluxes. For sources in the *scan* sample, which are typically unresolved in the lower angular resolution observations, we use an aperture of diameter 1.5 times the FWHM of the synthesised beam (with the value chosen to maximise the signal-to-noise, S/N, of the measurements), and then convert these to an equivalent total flux. For sources in the *spec-z* sample, which were observed with ALMA at typically higher resolution, we use an aperture of diameter three times the FWHM of the synthesised beam to ensure all the flux is captured while maintaining a high S/N. We also collapse the cubes to create a 3-mm continuum image and check for any offset between the 870-μm and 3-mm continuum emission that could result in the aperture not encapsulating all of the line flux. If an offset is discovered we measure the position of the 3-mm source and extract spectra from this position instead. This is required for six sources, with a median shift of $0.35''$.

To search for CO emission from the $870\,\mu$m-detected SMG we first estimate the noise in the cubes by extracting spectra in equivalent apertures from 100 random positions within the primary beam (masking the 3-mm source) and calculating their RMS noise. We then generate a histogram of channel S/N in the original and inverted spectra in order to determine a S/N cut and corresponding false positive rate. This is done using spectra that are continuum-subtracted with a running median (choosing an averaging window large enough so as not to be
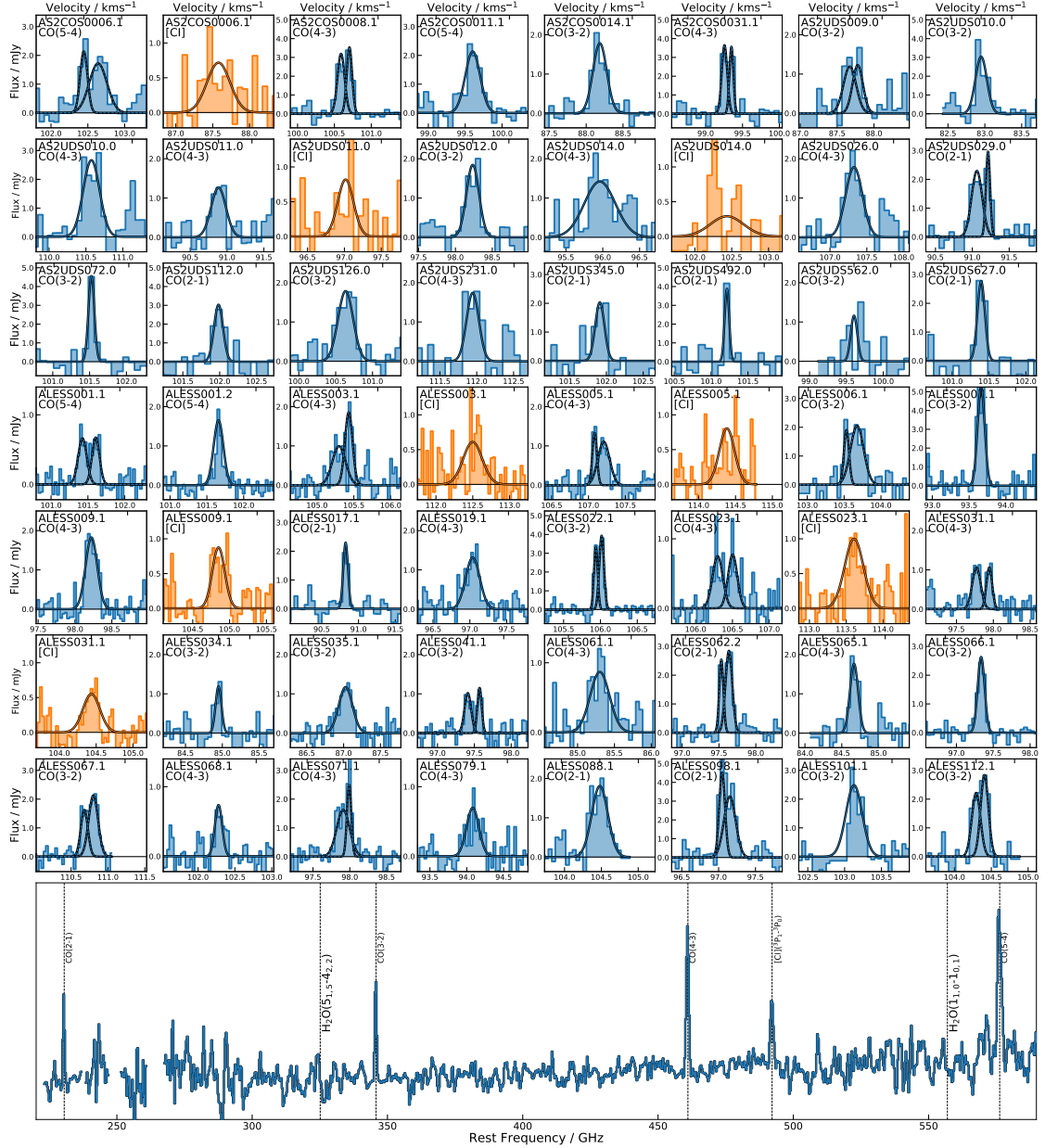
Figure 2.3: Emission-line detections in the continuum-subtracted 3-mm spectra of our sample of SMGs, with the fit to each line overlaid. In total, we show 56 emission lines, 46 CO lines from our 61 targets with $J_{up} = 2$–5 (blue, the spectrum of AS2UDS010.0 shows two CO lines: 4–3 and 3–2), two CO lines in nearby ALMA-detected SMGs (ALESS001.2 and ALESS019.1) and eight $[C\,I](^3P_1 - ^3P_0)$ lines (orange). In addition, three serendipitously detected CO emitters are not shown here. The CO emission in our sources is typically detected at high S/N, with a median $S/N = 8.2 \pm 0.6$. We fit and plot single- and double-Gaussian profiles to each line, finding that 38 ± 9 per cent display double-Gaussian profiles, indicative of disc dynamics or multiple components in these sources. The bottom panel shows a median composite of all CO-detected spectra in the rest frame, clearly showing the CO ladder and $[C\,I]$ lines. We also indicate where two of the rotational transitions of H_2O would appear, however we see no trace of these emission lines (see §3.2). All spectra are binned to a velocity resolution of $\sim 150\,km\,s^{-1}$, and tick marks on the top axis in each panel represent $1500\,km\,s^{-1}$, $0\,km\,s^{-1}$ and $-1500\,km\,s^{-1}$ from left to right, respectively.

influenced by any line emission) and rebinned to channel widths of 300, 600 and $900\,\mathrm{km\,s^{-1}}$. We adopt S/N cuts of 4, 3.75 and 3.5 for these channel widths based on the requirement that there are no false positives in our sample. For sources in the *spec-z* sample we search for >3.5-σ features within $100\,\mathrm{km\,s^{-1}}$ of the frequency of the spectroscopic redshift. Following Wardlow et al. (2018) we also perform a blind search of the 3-mm cubes for serendipitous CO/continuum emitters. This is done by spatially rebinning to ensure Nyquist sampling of the synthesised beam, and spectrally rebinning to channel widths of 150, 300 or $600\,\mathrm{km\,s^{-1}}$, then searching the cubes for >5-σ channels within the primary beam area.

From our line search we find 50 sources displaying CO emission. 45 of these come from our 61 targets (one source, AS2UDS010.0, shows two CO lines, Fig. 2.3), 26 from the *scan* sample and 19 from the *spec-z* sample, with a further two ALMA-detected SMGs (ALESS001.2 and ALESS019.1) not targeted in this survey, but close to a target source, displaying CO emission. Finally, three serendipitous CO emitters are also uncovered, however, as we lack 870-μm continuum counterparts to these sources we do not include them in the majority of our analysis, leaving a total sample size of 47 detected with a median $\mathrm{S/N} = 8.2 \pm 0.6$.

2.5   Analysis

2.5.1   Line identification

For the *scan* sample, where redshifts are not known a priori, galaxies at $z > 3$ are expected to display either two CO lines or one CO line and the [C I] $(^3\mathrm{P}_1 - {}^3\mathrm{P}_0)$ line in our frequency coverage, in which case identifying the detected transition is trivial. In contrast, galaxies at $z \lesssim 3$ are only expected to display one line meaning that there is potentially ambiguity in identifying the transition. In the latter case we use the redshift probability distribution functions (PDFs) from SED fitting with the photometric redshift extension of the MAGPHYS code (Battisti et al., 2019) to determine the most-likely redshift, given the observed frequency of the line. MAGPHYS uses an energy balance technique to model the SED of the sources from the UV/optical to the submillimetre/radio wavebands, to derive constraints on the redshifts and properties. Star-formation histories are modelled as continuous delayed exponentials with the peak of star formation occurring at a randomly drawn time, with random bursts superimposed to model starbursts (Lee et al., 2010). In fitting the photometry MAGPHYS creates a library of SED templates for each star-formation history, determining which is the best fit to the data by using a χ^2 test.

MAGPHYS is chosen as it is optimised for high-redshift ($z > 1$) galaxies, and given the importance of both stellar and dust emission in SMGs, the ability to couple these components in the fitting is highly advantageous, giving more robust constraints on parameters such as stellar mass and SFR. We refer the reader to da Cunha et al. (2008, 2015) for a more comprehensive discussion of MAGPHYS and the energy balance technique, and Battisti et al. (2019) for details on the photometric redshift extension of MAGPHYS. For further details of the photometry used we refer the reader to Simpson et al. (2020) for sources in AS2COSMOS, Dudzevičiūtė et al. (2020) for AS2UDS and da Cunha et al. (2015) for ALESS.

Of the 28 sources without spectroscopic redshifts in which we detect CO emission (26 from the *scan* sample and two other ALMA-identified SMGs), one displays two CO emission lines (AS2UDS010.0) and eight display an additional $[\mathrm{C\,I}](^{3}\mathrm{P}_1 - ^{3}\mathrm{P}_0)$ emission line, therefore nine of the 28 redshifts are unambiguous and correspond to $J_{\mathrm{up}} = 4$ or 5. From the 19 *spec-z* sources which have detected CO emission, 18 are detected at the expected redshift and are therefore identified unambiguously, with the remaining source (ALESS088.1) displaying emission which is offset from the expected frequency by $\sim 3\,\mathrm{GHz}$ ($\sim 8500\,\mathrm{km\,s}^{-1}$). Therefore a total of 27 out of 47 sources (57 per cent) in our sample have unambiguous redshifts.

This leaves 20 sources which lack existing spectroscopic redshifts and whose spectra exhibit a single CO line. We use the MAGPHYS redshift PDFs to identify these 20 transitions. Firstly, we test the accuracy of using the MAGPHYS PDFs to predict the correct line identification. For this test we use the 16 SMGs with unambiguous redshifts and $K < 23$, where this limit is chosen to ensure this training set is matched in K-band brightness with the ambiguous line source sample. We then identify the probabilities for the two most-likely CO transitions based on the corresponding redshifts in the PDFs of these 16 SMGs, including a prior to weight the selection to the lower-J_{up} line in the event that the two lines are close in likelihood. Based on this test we recover the correct transition for 14 out of 16 (88 per cent) of these sources. Applying the same methodology to the 20 single-CO-line sources we estimate that these comprise: three $J_{\mathrm{up}} = 5$, six $J_{\mathrm{up}} = 4$, eight $J_{\mathrm{up}} = 3$ and three $J_{\mathrm{up}} = 2$ emitters. We confirm that for those lines identified as higher-J_{up} CO that this identification does not conflict with the absence of a second CO or $[\mathrm{C\,I}]$ line which is predicted to be observable in our spectra. We note that the success rate from the test of PDF-based line selection would suggest that in our sample of 47 sources, with 20 ambiguous line identifications, we expect ~ 2–3 redshifts to be incorrect. We assess the impact of this on our results in the following by randomly removing 2–3 of the sources in the ambiguous sample from our analysis and we confirm that this does not change any of the claimed results outside their quoted 16–84th percentile

confidence ranges.

2.5.2 SED fitting

After identifying the detected transitions we fit SEDs to our sources with the high-redshift version of MAGPHYS, but now including our 3-mm continuum measurement (or limit) and fixing the redshift as that corresponding to our adopted CO transition, in order to derive key physical parameters of our sources. Of the 47 sources we fit, 23 (49 per cent) have *Spitzer*/MIPS 24-μm detections and 41 (87 per cent) have at least one *Herschel*/SPIRE detection, in addition to the 870-μm detection and 3-mm detection or limit.

We show the observed flux measurements or limits and the corresponding best-fit MAGPHYS SEDs for the 47 sources in Fig. 2.4. In the vast majority of cases, MAGPHYS provides a good fit to the observed photometry. However, we note that for ALESS071.1, although the redshift is secure as it agrees with the optical/UV spectroscopic value, and the photometry appears to be reasonably fit by the SED model, it has an unusually high best-fit stellar mass of $M_* \sim 2 \times 10^{12}\,\mathrm{M_\odot}$ at the CO redshift ($z_{\mathrm{CO}} = 3.707$, $J_{\mathrm{up}} = 4$). Hence, we attempted to fit the source at redshifts corresponding to the $J_{\mathrm{up}} = 2$, 3 or 5 transitions, but these did not provide better fits to the SED. As the MIPS 24-μm photometry does not suggest the presence of an AGN, we view it as likely that this source is lensed, or contaminated by a projected foreground source (see Fig. 2.1). As a consequence, we have checked the sensitivity of our results to the inclusion of this source in figures throughout this chapter and Chapter 3 where it appears as a noticeable outlier, and confirm that it does not bias our conclusions.

We caution that the version of MAGPHYS we use does not account for potential contributions to the continuum emission from an AGN. However, there is little evidence that AGN emission significantly contaminates the optical or infrared emission of the majority of SMGs (Stach et al., 2019), including those with the most massive cool dust and gas reservoirs, which we expect to detect here. Nevertheless, to assess the potential level of AGN contamination in our sample, we apply the IRAC colour-colour AGN classification criteria from Donley et al. (2012), see also Stach et al. (2019). We can apply this test to the 35 out of 47 sources in our sample with photometry in all four IRAC bands, in addition to five sources that have detections in one of the 4.5-μm or 8.0-μm bands and one of the 3.6-μm or 5.8-μm bands (Fig. 2.5(a)). Unfortunately, this classification can only be reliably applied to sources at $z \lesssim 2.5$–3.0, as at higher redshifts the characteristic 1.6-μm stellar bump shifts into the reddest IRAC 8.0-μm channel, making the colours of highly-reddened star-forming and power-
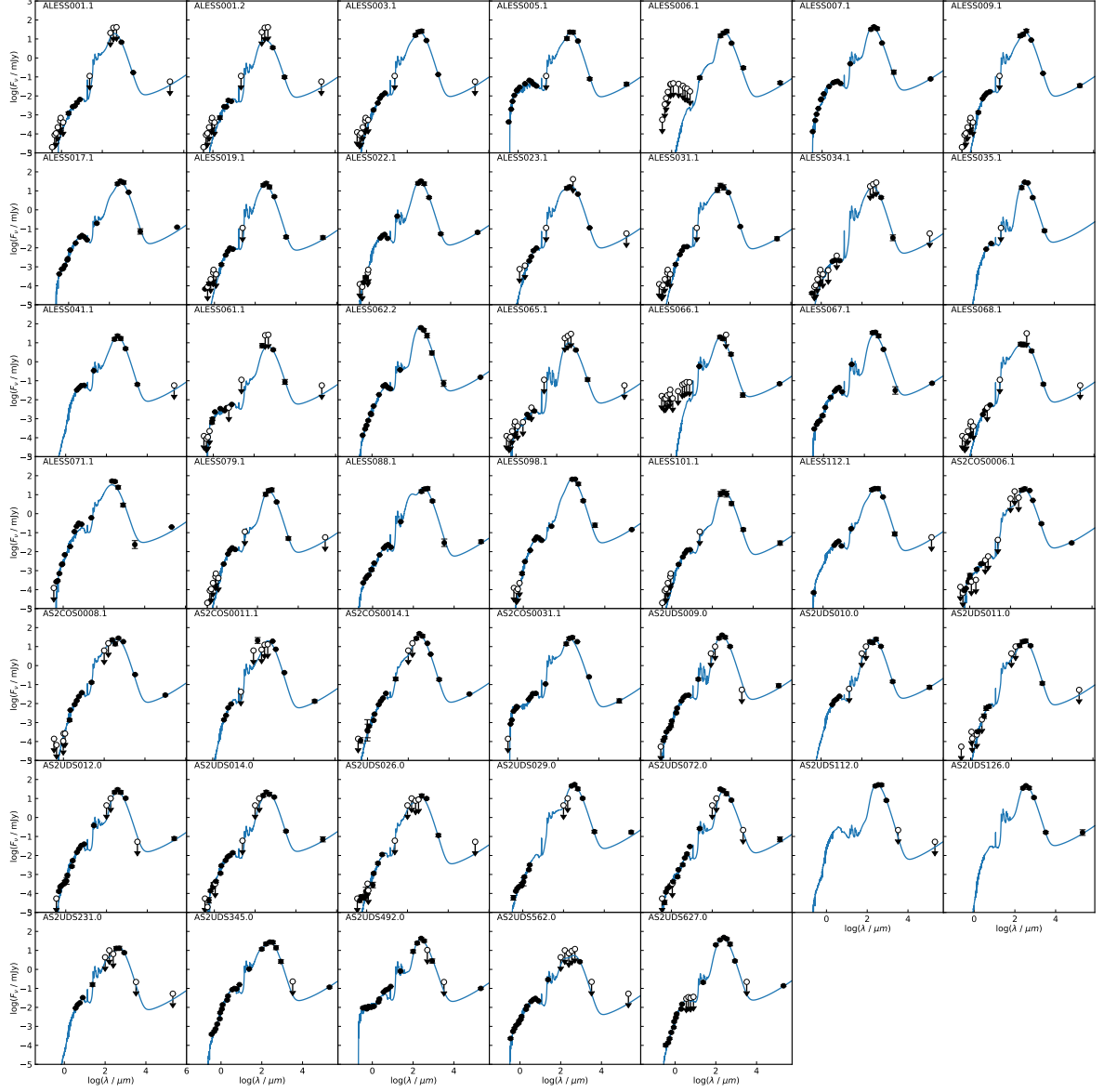
Figure 2.4: MAGPHYS SED fits for our 47 CO-detected sources. While we use the high-z version of MAGPHYS, which does not include an AGN component, we find that at best five sources below $z \sim 3$ exhibit AGN-like IRAC colours, and we also determine that there is likely to be no significant bias from these sources in our results. These sources are ALESS101.1, AS2COS0014.1, AS2UDS012.0, AS2UDS072.0 and AS2UDS0492.0.

law AGN sources indistinguishable. Hence, we assess the IRAC colours of the 20 sources at $z < 3$ in our sample (this includes all the sources plotted with limits in one or more of their IRAC bands), finding that five (25 per cent) fall within the AGN classification region, see Fig. 2.5(a). Naively, we would expect a similarly low level of contamination by AGN in the $z > 3$ population, where we are unable to use the IRAC classification method.

To assess the level of possible contributions from the AGN to the derived stellar masses for the five AGN candidate SMGs, we repeat their SED fitting, first removing all four IRAC data points and secondly removing just the $5.8\,\mu$m and $8.0\,\mu$m points, which are expected to show the largest contribution from an AGN compared to the stellar populations. We find in the former case that the stellar masses decrease by 0.18 ± 0.13 dex (larger than the median 1-σ uncertainty of 0.08 dex for the typical stellar mass), and in the latter case that they decrease by 0.01 ± 0.09 dex. We conclude that the effect of AGN contamination in these five sources is modest, but not negligible. We therefore flag these five $z < 3$ SMGs which are classified as hosting AGN by the Donley et al. (2012) criteria in Figs. 2.5, 3.5, 3.6 and 3.7, where stellar masses are used, and in Tables 2.2–3.4. Nonetheless, we expect this small bias in a fraction of our sample to have little effect on our conclusions.

The median properties of the whole sample found from SED fitting at the spectroscopic redshift and including the 3-mm continuum measurement are $L_{\rm IR} = (4.6 \pm 0.8) \times 10^{12}\,{\rm L_\odot}{}^3$, $M_* = (2.1 \pm 0.4) \times 10^{11}\,{\rm M_\odot}$, $M_{\rm dust} = (1.05 \pm 0.08) \times 10^9\,{\rm M_\odot}$, and SFR $= 400 \pm 50\,{\rm M_\odot}\,{\rm yr}^{-1}$. The best-fit parameters for the sources are listed in Table 3.3 and Table 3.4. We also note that for our CO sample, running MAGPHYS with the spectroscopic redshift fixed does not result in any significant change of the parameters when compared to those previously found from running the photometric redshift extension of the code (da Cunha et al., 2015; Danielson et al., 2017; Dudzevičiūtė et al., 2020), although it does reduce their uncertainties. Nevertheless, we caution that the stellar masses derived from the SED fitting are likely to be subject to systematic uncertainties of a factor of ~ 2–3, due to uncertainties in the constraints on the star-formation histories (Hainline et al., 2011; Dudzevičiūtė et al., 2020).

In terms of our median stellar masses, the uncertainties associated with these measurements are discussed in detail in Dudzevičiūtė et al. (2020) for modelling of the sources in the UDS field. The median stellar mass derived in that analysis of a large complete sample is $(1.26 \pm 0.04) \times 10^{11}\,{\rm M_\odot}$. The median mass for the sample analysed here is higher than that, $(2.1 \pm 0.4) \times 10^{11}\,{\rm M_\odot}$, but this is primarily because our sample are typically brighter

---

[3]$L_{\rm IR}$ is measured across the range $\lambda = 8$–1000 μm.

at $870\,\mu$m (and have correspondingly larger dust masses) than the sources in the AS2UDS study. This difference means that our sources are expected to also have higher stellar masses (see e.g. Dudzevičiūtė et al., 2020).

We next show in Fig. 2.5(b) and Fig. 2.5(c) the position of our CO-detected SMGs in relation to the star-forming main sequence, adopting the prescription of Speagle et al. (2014) (given the uncertainties in defining the main sequence, we also show the prescription of Whitaker et al. (2012), for comparison). We see that just four of the galaxies at $z = 1$–3 have star-formation rates more than a factor of four above the main sequence (commonly used to define a starburst), and at $z = 3$–5 all galaxies lie within a factor of four of the main sequence, owing to its proposed evolution with redshift. This plot shows that in terms of star-formation rate, our sample consists of main sequence galaxies out to $z \sim 4.5$, albeit with high stellar masses ($M_* > 10^{11}\,\mathrm{M_\odot}$) and high star-formation rates for the majority of the sample. While the main sequence is well studied at low redshift, our sample presents an opportunity to extend the work of lower-redshift studies such as PHIBSS (Tacconi et al., 2018) and ASPECS (Walter et al., 2016) to $z > 3$ and higher gas masses. We note that in Fig. 2.5 it is clear that in the higher-redshift bin, there is marginal difference between the two main sequence prescriptions we plot, while at low redshift the Whitaker et al. (2012) track predicts higher SFRs, which would indicate that fewer of our sample are starbursts than indicated by the Speagle et al. (2014) prescription. We note this discrepancy here, but to allow an easier comparison with the literature we use the Speagle et al. (2014) main sequence prescription in what follows, and in Chapter 3.

2.5.3 Line fitting

We simultaneously fit single-/double-Gaussian profiles plus a continuum level to the lines recovered from our spectra, employing a Markov Chain Monte Carlo (MCMC) technique implemented in the EMCEE package of PYTHON (Foreman-Mackey et al., 2013). For sources in the *scan* sample, the spectral slope becomes significant over the 32-GHz bandwidth, therefore we fit a power-law continuum, rather than just a constant continuum as is done for the *spec-z* sources (which have narrower frequency coverage). Uncertainties on the fits are calculated by refitting bootstrapped spectra and measuring the dispersion in the resultant parameter distributions. To determine whether the single- or double-Gaussian profile is the more suitable fit we compute the Akaike Information Criterion (AIC; Akaike, 1974), which penalises models that benefit from a larger number of parameters to obtain a good fit, and take the model
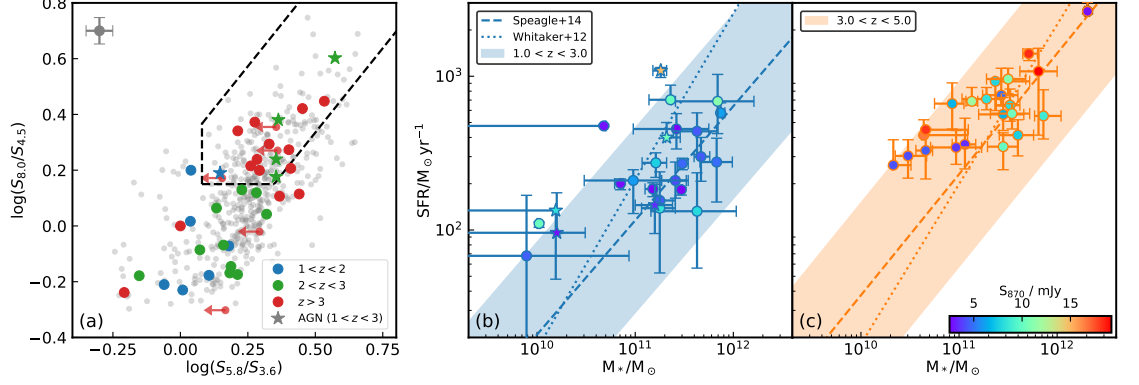
Figure 2.5: **(a)** IRAC colour-colour AGN selection criteria defined by Donley et al. (2012), with our CO-detected sources indicated and colour-coded by redshift (where IRAC photometry is available). We demarcate by dashed lines the boundaries of the region in which AGN in sources at $z \lesssim 2.5$–3.0 are expected to lie and we show the distribution of the full AS2UDS sample in grey. In the redshift range $z = 1$–3, where the AGN classification can be employed, we find that the majority of our sample (~ 75 per cent) lie outside of the AGN classification region, and we highlight those falling into the AGN region by plotting them as stars. The distribution of colours for SMGs at $z > 3$ shows more overlap with the AGN classification region, but these classifications are not reliable as dusty star-forming galaxies and AGN have similar colours at these redshifts. In the top-left corner we show a representative error bar for AS2UDS sources. **(b)/(c)** The relation of our CO-detected sources to the star-forming main sequence at $z = 1$–3 and $z = 3$–5. We show the main sequence as predicted by two different prescriptions (see text), and highlight a spread of a factor of four in SFR (0.6 dex), above which a galaxy is considered to be a starburst. 42 of our 47 CO-detected sources lie within the expected spread of the main sequence. SMGs have been typically difficult to characterise with respect to this plane, but we show that with our precise CO redshifts we have been able to derive stellar masses and SFRs robust enough to securely place our sources on or near the main sequence, particularly at high redshift. We plot as stars those SMGs classified as AGN by the Donley et al. (2012) criteria (see **(a)**), which may have stellar masses biased high by our MAGPHYS SED fitting, as this does not include an AGN component in the fit.

with the lowest AIC to be the most appropriate. The continuum-subtracted spectra and line fits are shown in Fig. 2.3, and the corresponding fit parameters are tabulated in Chapter 3, where we present the CO line properties, in Tables 3.3 and 3.3.

We now measure the properties of our CO lines. While many of our sources are well described by Gaussian profiles, we use the intensity-weighted moments of the spectrum to obtain a profile-independent measurement (Bothwell et al., 2013). To ensure consistency in all measurements, we employ the same method of deriving moments regardless of whether the line profile is deemed to be single- or double-peaked. The zeroth moment gives the intensity of the line:

$$M_0 = I_{CO} = \int I_v dv, \tag{2.5.1}$$

where I_v is the flux in a channel with velocity v. The first moment gives the centroid of the line:

$$M_1 = \bar{v} = \frac{\int v I_v dv}{\int I_v dv} \tag{2.5.2}$$

which we use to calculate the redshift. The second moment is the velocity dispersion, from which we can estimate the equivalent full-width at half-maximum (FWHM) as:

$$\text{FWHM} = 2\sqrt{2\ln 2} M_2 = 2\sqrt{2\ln 2} \sqrt{\frac{\int (v - \bar{v})^2 I_v dv}{\int I_v dv}}. \tag{2.5.3}$$

To calculate moments we integrate the spectra in a velocity window twice the FWHM of the Gaussian fit. We confirm this range based on simulations where we insert Gaussians with known amplitudes and linewidths at random frequencies in our spectra and attempt to recover the input value using Eq. 2.5.3. Uncertainties on the second moment are estimated by resampling the spectrum with the noise spectrum, then calculating the dispersion in the recovered line widths.

We note that the CO line emission in ALESS101.1 falls onto a band gap meaning that a number of channels are missing from the line. In this case summing channels across the line results in underestimates of the linewidth and line flux, and we therefore use the properties of the Gaussian fit when deriving these quantities.

Finally, we derive the CO line luminosity of the observed transition

$$L'_{CO,J} = 3.25 \times 10^7 I_{CO,J} \nu_{obs}^{-2} D_L^2 (1+z)^{-3}, \tag{2.5.4}$$

where $L'_{CO,J}$ is in units of $\text{K km s}^{-1} \text{pc}^2$, $I_{CO,J}$ is the velocity-integrated intensity of the line in Jy km s^{-1}, ν_{obs} is the observed frequency of the line in GHz, D_L is the luminosity distance

of the source in Mpc, calculated using our chosen cosmology, and z is the redshift (Solomon & Vanden Bout, 2005). The [C I](^{3}P$_1$–^{3}P$_0$) line luminosity $L'_{\text{[CI]}}$ is calculated in the same way. Due to these being typically fainter lines, the frequency of the [C I](^{3}P$_1$–^{3}P$_0$) line is fixed to the CO redshift when fitting Gaussians, and the [C I] linewidth is fixed to be the value derived from the CO line fit. We still derive the linewidth using the moments of the spectrum as with the CO (see §2.5.3). These spectra, along with the Gaussian fits, are also shown in Fig. 2.3, and the de-redshifted spectra are displayed together in Fig. 2.6.

We overlay the CO contours of these sources onto K/IRAC 3.6 μm/IRAC 4.5 μm colour images (where imaging is available), shown in Fig. 2.1. Due to the array configurations of our millimetre observations we do not resolve the CO in most cases (the synthesised beam is shown in each panel). However, a number of the ALESS *spec-z* targets were observed at higher resolution with ALMA and display some structure (see e.g. ALESS098.1). High-resolution millimetre imaging for some of our CO sources has been presented in Chen et al. (2017), Calistro Rivera et al. (2018) and Wardlow et al. (2018), showing spatially-resolved velocity gradients in the CO emission consistent with rotation.

Finally, we create a median rest-frame stack of all 47 spectra with CO detections to search for other weak emission lines, which is also shown in Fig. 2.3. Other than CO emission with $J_{\text{up}} = 2$–5 and the [CI](^{3}P$_1$–^{3}P$_0$) line, we check for H$_2$O($1_{1,0}$–$1_{0,1}$) and H$_2$O($5_{1,5}$–$4_{2,2}$) emission. We see no trace of these emission lines, and we place 3-σ limits of $L_{\text{H}_2\text{O}}/L_{\text{IR}} < 4 \times 10^{-3}$. In addition, we centroided the 47 emission lines and stack them together to search for any wings in the emission which could provide evidence of outflows. The median stack is well fit by a single Gaussian component, with no broad component necessary to explain the observed emission. We therefore conclude that our observations provide no evidence for large-scale outflows of molecular gas in our sample.

2.6 Conclusions

In this chapter we have presented our survey of the molecular gas in 61 submillimetre galaxies (SMGs), as traced by the carbon monoxide (CO). We observed the targets at $\lambda \sim 3$ mm ($\nu \sim 100$ GHz) with ALMA and NOEMA and detected $J_{\text{up}} = 2$–5 emission in 47 SMGs, with serendipitous detections of a further three sources. 27 of the emission lines are unambiguously identified yielding secure spectroscopic redshifts, and we use existing photometric redshifts to inform our identifications of the remaining 20 lines. By testing the photometric redshifts
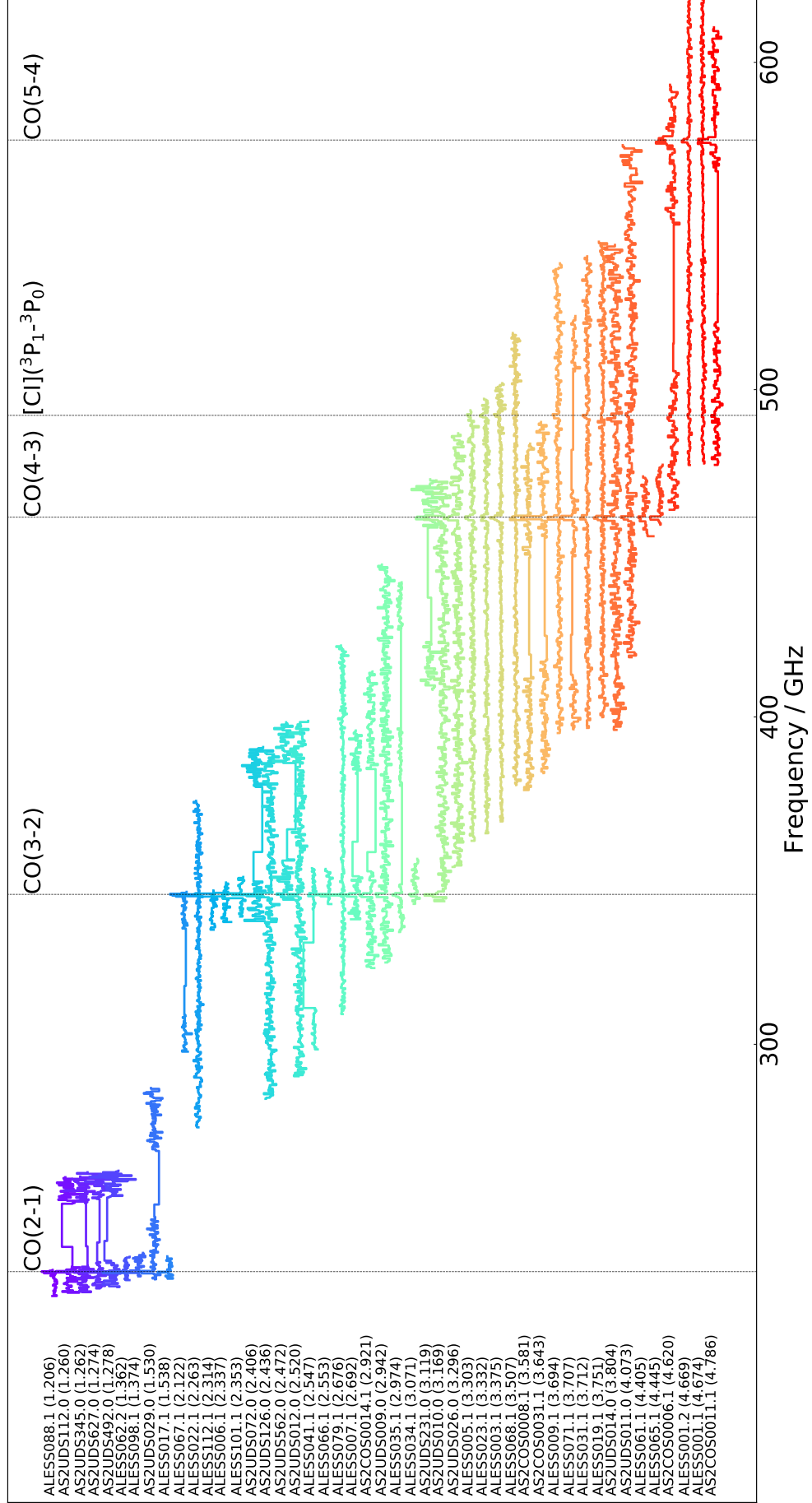
Figure 2.6: All 47 ALMA/NOEMA 3 mm spectra with CO detections, de-redshifted and plotted in the rest-frame. Sources are ordered from top to bottom in order of increasing redshift, and also coloured from blue to red. We indicate by vertical lines the frequencies of the $J_{\mathrm{up}} \sim 2\text{--}5$ CO lines and the [CI]($^{3}P_{1}\text{--}^{3}P_{0}$) line.

against the robust spectroscopic redshifts, we suggest that only 2–3 of the ambiguous line identifications are likely to be incorrect ($\sim 5\%$). This demonstrates the power of ALMA and NOEMA to carry out efficient blind redshift scans of SMGs.

We then improve the existing MAGPHYS SED fitting for the CO-detected sources, which was previously carried out with the redshift as a free parameter. By fixing the redshift at the CO value and including the 3 mm continuum measurements, we obtain more precise constraints on the SEDs, and therefore, the star-formation rates, stellar masses and dust masses of our sample (reducing the fractional uncertainties by a factor of ~ 2 in far-infrared luminosities and ~ 3 in dust masses). The 47 SMGs have median properties of $L_{\mathrm{IR}} = (4.6 \pm 0.8) \times 10^{12}\,\mathrm{L}_{\odot}$, $M_* = (2.1 \pm 0.4) \times 10^{11}\,\mathrm{M}_{\odot}$, $M_{\mathrm{dust}} = (1.05 \pm 0.08) \times 10^9\,\mathrm{M}_{\odot}$, and $\mathrm{SFR} = 400 \pm 50\,\mathrm{M}_{\odot}\,\mathrm{yr}^{-1}$, confirming that the sample is composed of massive and highly star-forming systems, with large reservoirs of dust.

Using the derived stellar masses and SFRs we find that 42 of our 47 CO-detected sources lie within the expected spread of the main sequence at their redshifts, an interesting result given that $870\,\mu$m-selected SMGs are commonly thought of as "starburst" galaxies, but this result reflects the evolution of the main-sequence offset to high SFRs at $z > 3$. Finally, we investigate the AGN fraction of the sample through the IRAC colour-colour AGN classification criteria from Donley et al. (2012), finding 25 per cent of the SMGs at $z \lesssim 2.5$–3.0 to display AGN-like IRAC colours. This is consistent with the values of 17^{+16}_{-6} per cent and 8–28 per cent found by Wang et al. (2013) and Stach et al. (2019) for the ALESS and AS2UDS samples, respectively. We attempt to understand the effects of AGN contamination on the stellar mass estimates, finding them to be modest but non negligible.

In Chapter 3 we present a full analysis of the CO data, including molecular gas masses, gas fractions and gas depletion timescales, a statistical CO spectral line energy distribution (SLED), a comparison of three different molecular gas mass tracers and a dynamical test of SMGs as the progenitors of massive local early-type galaxies.

The molecular gas properties of high-redshift dust-obscured star-forming galaxies

Preamble

In Chapter 3 we introduced our $3\,\mathrm{mm}$ survey of SMGs in the COSMOS, UDS and ECDFS fields with ALMA and NOEMA, which yielded carbon monoxide (CO) redshifts for 47 SMGs, and in this chapter we present the complete analysis of the emission line data. First, we present the redshift distribution of the sample, before studying the CO gas excitation through a statistical CO spectral line energy distribution (SLED) which we use to derive line ratios for future studies. We then estimate molecular gas masses from the CO emission, the $3\,\mathrm{mm}$ continuum emission, and atomic carbon [CI] emission where available, comparing the three tracers as a consistency check. Combining the CO luminosities with the physical properties derived in Chapter 2 we derive molecular fractions, gas depletion timescales and gas-to-dust ratios, before finally carrying out a dynamical test of SMGs as the progenitors of massive local early-type galaxies in the Coma cluster.

3.1 Introduction

It is believed that approximately half of all star formation activity that has ever occurred is obscured by dust (Puget et al., 1996; Dole et al., 2006), with this optical/UV light being absorbed and then re-emitted in the far-infrared (Blain et al., 2002). The most highly-obscured sources in the local Universe are Ultra-Luminous Infrared Galaxies (ULIRGs), galaxies with infrared luminosities greater than $10^{12}\,\mathrm{L_\odot}$, which were discovered by the *InfraRed Astronomy Satellite* (*IRAS*; Neugebauer et al., 1984). It was subsequently found that local ULIRGs typically have high star-formation rates of SFR $\gtrsim 50\,\mathrm{M_\odot\,yr^{-1}}$, driven by the strong compression and cooling of gas triggered by a major merger (see Sanders & Mirabel, 1996, for a review). In a cosmological context, while ULIRGs only contribute a small fraction of the global star-formation rate density (SFRD) at $z \sim 0$, they make a much larger contribution at $z \gtrsim 1$ (Magnelli et al., 2013; Dudzevičiūtė et al., 2020). Understanding the processes which drive the strong evolution of this population of dusty, strongly star-forming galaxies at $z \gtrsim 1$ is therefore an important element in understanding galaxy formation at high redshift and high mass (Hodge & da Cunha, 2020).

Among the high-redshift counterparts of ULIRGs are submillimetre galaxies (SMGs; Smail et al., 1997; Hughes et al., 1998) – a population of dust-obscured star-forming galaxies (DSFGs) selected by their long-wavelength dust continuum emission, corresponding to flux densities of $\gtrsim 1\,\mathrm{mJy}$ at observed-frame $870\,\mu\mathrm{m}$, i.e. on the Rayleigh-Jeans tail of the dust spectral energy distribution (SED), where observations benefit from a negative K-correction. Surveys of SMGs are thus dust mass-limited across $z \sim 1$–6, with a peak in space density at $z \sim 2$–3 (Chapman et al., 2005; Weiß et al., 2013; Brisbin et al., 2017; Cowie et al., 2018; Dudzevičiūtė et al., 2020), i.e. around so-called "cosmic noon", at which time they are believed to account for a significant fraction of the global SFRD (Barger et al., 2000; Swinbank et al., 2014; Dudzevičiūtė et al., 2020). Following rapid progress in the last decade, we are now in a position to undertake statistical studies of the SMG population, with homogeneous samples of $\gtrsim 1000$ sources having been catalogued from single-dish bolometer surveys and identified with ALMA (Hodge et al., 2013; Hatsukade et al., 2016; Miettinen et al., 2017; Cowie et al., 2017; Franco et al., 2018; Stach et al., 2019), the PdBI/NOEMA (Smolčić et al., 2012) and SMA (Iono et al., 2006; Barger et al., 2012; Hill et al., 2018).

Two key observables needed to further our understanding of high-redshift dust-obscured galaxies are their gas and dynamical masses: the former being the fuel for star formation, the main component of which is the molecular hydrogen (H_2). Carbon monoxide (CO) emission

is a commonly used tracer of H_2, which has too high excitation energies to be strongly excited in the cold interstellar medium (ISM) of SMGs (Solomon et al., 1992; Omont, 2007; Carilli & Walter, 2013). Moreover, observations of CO emission lines can provide insights into both galaxy gas masses, from the line luminosities, and also dynamical masses, from the line width – where the CO emission has the added benefit of being relatively immune to the influences of dust obscuration and biases due to outflows or AGN activity, which plague many of the emission lines used to trace dynamics in the rest-frame optical/UV (Swinbank et al., 2006).

With precise redshifts, gas masses and dynamical masses from CO detections for representative samples of SMGs, we would be in a position to place this population in the wider context of galaxy evolution. In recent years studies of this field have also begun to focus on the properties of more "typical" high-redshift galaxies. These include the so-called "main sequence" population, which is defined in terms of the apparent correlation between stellar mass and star-formation rate (Noeske et al., 2007; Whitaker et al., 2012). For submillimetre galaxies, which are usually considered to be "starburst" galaxies given their high star-formation rates, it is particularly challenging to measure stellar masses due to their heavy dust obscuration, and therefore it is not entirely clear where they lie in the SFR–M_* plane (e.g. Hainline et al., 2011). There is evidence, however, that due to the claimed evolution of the main sequence, an increasing fraction of SMGs may in fact lie close to or on it at higher redshifts (da Cunha et al., 2015; Koprowski et al., 2016; Elbaz et al., 2018; Dudzevičiūtė et al., 2020). The implications of this for our understanding of the processes in SMGs, especially at higher redshifts, including the relative roles of triggering mechanisms in SMGs, are unclear and will remain so until more sources in this regime are studied. For example, the existence of the main sequence has been interpreted to indicate that star formation in these galaxies is maintained by steady gas accretion, however, more work is needed to understand whether this applies to SMGs lying within the sequence, especially as the main sequence itself is subject to selection effects (Hodge & da Cunha, 2020).

We have therefore undertaken a survey of 61 submillimetre galaxies with precise ALMA 870-μm continuum identifications from the AS2COSMOS, AS2UDS and ALESS surveys, using observations from ALMA and NOEMA in the 3-mm band, which we presented in Chapter 2. Our aim is to derive precise spectroscopic redshifts and characterise their molecular gas content. To ensure our survey covers both a broad range of submillimetre flux and optical/near-infrared brightness, representative of that seen in the population, we combined two selection methods: including both a survey of typically submillimetre-bright SMGs lacking spectroscopic redshifts, which make ideal targets for blind CO scans; and a study of

generally submillimetre-fainter SMGs with pre-existing restframe optical/UV spectroscopic redshifts. Together these provide a sample with the wide range in 870-μm flux (S_{870}) and optical/near-infrared brightness needed to study the properties of a representative cross-section of the population. Our sample is one of the largest of its kind, and with it we take advantage of the sensitivities of ALMA and NOEMA and the wealth of multi-wavelength data available in our target fields to address a range of questions about SMGs. These include investigating the redshift distribution, gas excitation, dynamics and gas masses of SMGs, the evolution of their gas fractions and gas depletion timescales, along with their relation to the star-forming main sequence.

The outline of this chapter is as follows: in §3.2 we review the findings from Chapter 2 and summarise the line properties, before moving on to present and discuss the results and their implications in §3.3. In §3.4 we conclude our findings. Throughout this chapter we use the AB magnitude system, a Chabrier IMF, a CO–H_2 conversion factor of $\alpha_{CO} = 1\,M_\odot$ $(K\,km\,s^{-1}\,pc^2)^{-1}$ for all galaxies, and adopt a flat Λ-CDM cosmology defined by $(\Omega_m,\ \Omega_\Lambda,\ H_0) = (0.27,\ 0.73,\ 71\,km\,s^{-1}\,Mpc^{-1})$.

3.2   CO detections

First, we briefly review the findings from Chapter 2 and summarise the median line properties. CO emission lines are detected in 50 sources: 45 of the 61 targets (74 per cent), two ALMA-identified SMGs that are close to one of the targets, and three serendipitously detected CO line emitters which are not ALMA-identified SMGs. We also detect eight $[C\,\textsc{i}](^3P_1-^3P_0)$ emission lines. The CO lines have a median FWHM linewidth of $540 \pm 40\,km\,s^{-1}$, comparable with that of Bothwell et al. (2013), who found a value of $500 \pm 60\,km\,s^{-1}$. Our sources also have comparable infrared luminosities to Bothwell et al. (2013): our sample has a median $L_{IR} = (4.6 \pm 0.8) \times 10^{12}\,L_\odot$, consistent with the median $L_{IR} = (5.4 \pm 0.7) \times 10^{12}\,L_\odot$ found by Bothwell et al. (2013).

We find that 38 ± 9 per cent of our CO-detected sources display double-peaked CO emission line profiles according to the AIC test described in §2.5.3, marginally higher than the 20–28 per cent reported by Bothwell et al. (2013), potentially due to our typically higher S/N line detections. The median separation between peaks is $380 \pm 50\,km\,s^{-1}$, which we interpret as evidence that the gas reservoirs in these sources are typically fast rotating discs, as (spatially unresolved) sources so close in velocity would likely have already coalesced, if they represent

distinct gas components within a merger. To assess whether this high fraction of double-peaked lines in the SMGs is consistent with a disc geometry for the gas reservoirs in the whole population, we create a simulation using a simple disc model with a rotation curve described by an arctangent model (Courteau, 1997) and an exponential intensity profile. Assuming that our viewing angles of the sources are randomly distributed, we draw random inclination angles with a probability proportional to the sine of the angle (see Law et al., 2009), finding that the predicted fraction of AIC-classified double-peaked sources in the simulation is consistent with that seen in our sample. This suggests that the gas reservoirs in our sample of SMGs may represent rotating discs, although we stress that the presence of a rotating gas disc does not rule out a merger origin for the system as the gas can settle back into such a disc-like configuration after a merger (e.g. Lotz et al., 2008; Bournaud et al., 2011). Moreover, we caution that either some of these discs are highly asymmetric (as indicated by double-peaked lines with very large flux or line width ratios between the two peaks) or that these systems may represent pre-coalescence mergers, where the gas reservoirs in the two components are still distinct. Nevertheless, in the following we consider all double-peaked sources in the same way.

By performing a blind scan of the cubes we uncovered three serendipitously detected line emitters in the fields of three ALMA-detected SMGs targeted in our survey. These line emitters fall outside the 870-μm continuum imaging in these fields, so we are unable to constrain their submillimetre fluxes, and none have 3-mm continuum detections above 3.5-σ, but all three have IRAC counterparts. To infer line identifications, and therefore redshifts for these three sources, we compare their IRAC colours/magnitudes with those of the AS2UDS sample and adopt the CO transition corresponding to the median redshift of the ten closest AS2UDS SMG matches. The CO line properties of these sources are tabulated in Table 3.3 and Table 3.4.

In their sensitive CO study of the environment of SMGs, Wardlow et al. (2018) found that 21 ± 12 per cent of SMGs have CO-detected companion galaxies at similar velocities and within 150 kpc in projection, suggesting gravitational interactions within these systems may act to increase their star-formation rates. It is important to note that the number of such sources detected is dependent on the depth of the data, and as the bulk of our data is not as deep as that of Wardlow et al. (2018), we cannot compare the statistics of the two studies directly. However, there is no evidence that the three serendipitously detected sources we found are physically associated with the targeted ALMA SMGs in these fields, as the lines are offset by $\gg 1000 \, \mathrm{km \, s^{-1}}$ relative to the primary targets.
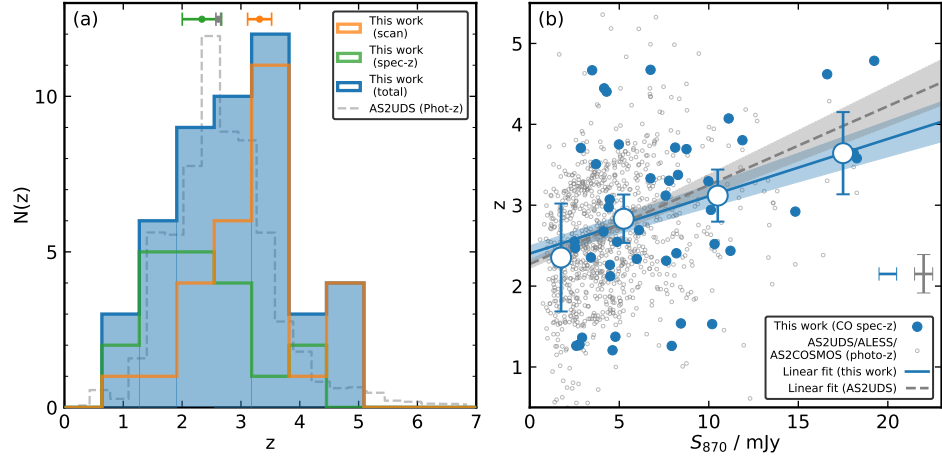
Figure 3.1: **(a)** The redshift distribution of our CO sample. We show both the total distribution and the distributions of the *scan* and *spec-z* subsamples, and compare these with the photometric redshifts of the AS2UDS sample (scaled for clarity). The medians of each sample are shown by markers at the top of the panel. The submillimetre-bright *scan* sources generally lie at higher redshifts (median $z = 3.32 \pm 0.17$) than the typically fainter *spec-z* sample ($z = 2.3 \pm 0.3$), and the AS2UDS population ($z = 2.61 \pm 0.08$). **(b)** Redshift versus 870-μm flux density for our CO sample and the SMGs with photometric redshifts from the AS2COSMOS, AS2UDS and ALESS surveys (da Cunha et al., 2015; Dudzevičiūtė et al., 2020, Ikarashi et al. 2020 in prep.). Our CO sources, binned by S_{870}, are fit with a linear model of increasing redshift with S_{870}, yielding a modest positive correlation with a best fit slope of $0.07 \pm 0.01 \, \mathrm{mJy}^{-1}$. This is consistent with the $0.06 \pm 0.01 \, \mathrm{mJy}^{-1}$ gradient measured by Simpson et al. (2020) for AS2COSMOS and $0.09 \pm 0.02 \, \mathrm{mJy}^{-1}$ measured by Stach et al. (2019) for AS2UDS, supporting the downsizing trend reported by others (see §3.3.1). Representative error bars for our sample and AS2UDS are shown in the bottom-right corner of the panel.

We next investigate the cause of the non-detection of emission lines in sources we observed. 16 of the 61 galaxies (26 per cent) we targeted are not detected in CO, five from the *scan* sample and 11 from the *spec-z* sample. Among the *scan* sample, the CO-detected SMGs have a median $S_{870} = 8.5 \pm 0.9$ mJy, whereas the non-detections have a median $S_{870} \sim 4$ mJy. Sources with lower 870-μm flux densities are expected to have lower dust masses, and they are therefore also more likely to have lower gas masses, making them CO faint and so less likely to be detected. One potential explanation of the non-detected sources in the *scan* sample is the existence of a narrow redshift range $z \sim 1.75$–2.0 within which sources would not exhibit a CO emission line in the 3-mm band. Given that ~ 4 per cent of AS2UDS SMGs lie in this range, based on their photometric redshifts, this could account for at most one non-detection in the *scan* sample, and more likely none. Another possibility is that these CO-undetected sources lie at $z > 5$ and would therefore display $J_{\mathrm{up}} > 6$ emission in the 3-mm band, which may be faint compared to the lower-J_{up} transitions (we investigate the CO excitation in the sample in §3.3.2). We view this as unlikely if these sources have CO excitation properties comparable to the detected population, as their higher-J_{up} emission should still be detectable. Instead, we note that in the *scan* sample, we detect CO in ~ 92 per cent of our targets that are brighter than $S_{870} = 5$ mJy (22/24 detections), with the non-detections predominantly in the faintest sources. Therefore we believe that the non-detections in the *scan* sample are most likely to be SMGs at $z \sim 3$ with faint CO emission, rather than sources that lie in the redshift gap ($z \sim 1.75$–2.0) or beyond $z \sim 5$. Indeed, the non-detected sources in our sample have a median photometric redshift of $z = 2.8 \pm 0.3$.

Turning now to the 11 non-detections in the *spec-z* sample, these can be due to either incorrect optical/UV spectroscopic redshifts or the faintness of the CO lines. Danielson et al. (2017) provide a quality factor Q to describe how secure the derived redshift is, with $Q = 1$ redshifts derived from multiple spectral features, $Q = 2$ redshifts derived from one or two bright emission lines and $Q = 3$ redshifts tentatively derived from one emission line and guided by the photometric redshift. Of the 26 sources taken from Danielson et al. (2017), we detect CO in 11 of the 13 (85 per cent) sources with $Q = 1$ redshifts, four of the nine (44 per cent) with $Q = 2$ redshifts, and none of the four with $Q = 3$ redshifts. Therefore we are more successful at detecting CO in the sources with secure spectroscopic redshifts, as expected. There are also two cases where sources in the *scan* sample have CO redshifts that rule out the spectroscopic optical/UV redshift from Danielson et al. (2017), namely ALESS001.1 and ALESS003.1 which both have $Q = 3$ redshifts. Additionally, in the *spec-z* sample, as in the scans, the non-detections are marginally fainter at 870 μm (median 4.0 ± 0.8 mJy) than the

detections (median $4.3 \pm 0.5\,\mathrm{mJy}$), although this difference is not formally significant. We conclude that the majority of the incompleteness in the *spec-z* sample arises from incorrect spectroscopic redshifts, combined with the typically fainter submillimetre fluxes of these sources (and hence the likely lower CO brightnesses).

3.3   Results and discussion

3.3.1   Redshift Distribution

Estimates of the redshift distribution of (unlensed) SMGs based on spectroscopic redshifts have been typically restricted to sources with brighter optical/near-infrared counterparts and/or to those with detectable counterparts in the radio or mid-infrared (Chapman et al., 2005; Danielson et al., 2017). Measurements of photometric redshifts from SED fitting to ALMA-identified samples have been more complete (da Cunha et al., 2015; Dudzevičiūtė et al., 2020), but these are also uncertain, particularly in the case where sources are faint and/or the photometric coverage is poor. For example, some optically faint sources have insufficient photometry to establish whether they are highly obscured at low redshifts or simply lie at high redshifts (Simpson et al., 2014; Smail et al., 2020). In contrast, our sample is large enough to provide a statistically robust redshift distribution, our CO spectroscopic redshifts are precise and our selection is not biased by the need for radio or MIPS counterparts for identifications.

In Fig. 3.1(a) we show the redshift distribution of our CO sources. The median CO redshift of our whole sample is $z = 2.9 \pm 0.2$ (interquartile range 2.3–3.7), and the median redshifts of the *scan* and *spec-z* samples are $z = 3.32 \pm 0.17$ and $z = 2.3 \pm 0.3$, respectively. Therefore the *spec-z* sources preferentially lie at lower redshifts, which is expected as sources typically must be brighter in the optical or near-infrared (and hence typically lower redshift) in order that a restframe optical/UV spectroscopic redshift can be successfully measured. Our results for the *scan* sources suggest that the optically faint SMG population lie at higher redshifts than the median, although we find no sources in the extended tail of the photometric redshift distribution at $z > 5$. Among the ~ 1000 SMGs in AS2UDS and AS2COSMOS only ~ 1 per cent have photometric redshifts of $z > 5$ (Dudzevičiūtė et al., 2020; Simpson et al., 2020), and hence this result is not surprising. This reflects the apparently exponential decline in the number of massive gas-rich sources at high redshift, and deeper surveys may be needed to find such sources, although at least one $z > 5$ AzTEC SMG has been detected in the COSMOS

field (Smolčić et al., 2015).

The median redshift of our *scan* sample is relatively high, approaching that reported for the 1.4 mm-selected SPT sources observed by Spilker et al. (2014) ($z = 3.5$), although this is likely a selection effect given that the *scan* sources were selected to be faint in the infrared or bright in the submillimetre. Comparing with the photometric redshifts of these sources, we find a median $|z_{\mathrm{phot}} - z_{\mathrm{CO}}|/z_{\mathrm{CO}}$ of 0.11 ± 0.05, and the median redshift of our sample as a whole is consistent with that of the AS2UDS sample, which has a median photometric redshift of $z = 2.79 \pm 0.07$ for a complete flux-limited sample above $S_{870} \geq 3.6\,\mathrm{mJy}$ (Dudzevičiūtė et al., 2020).

In Fig. 3.1(b) we show the variation of redshift as a function of S_{870}, including our CO redshifts and photometric redshifts from AS2COSMOS, AS2UDS and ALESS as a comparison. We estimate the gradient of the trend of redshift with S_{870} for the CO sample as $0.07 \pm 0.01\,\mathrm{mJy}^{-1}$, which agrees with the estimates of $0.06 \pm 0.01\,\mathrm{mJy}^{-1}$ and $0.09 \pm 0.02\,\mathrm{mJy}^{-1}$ previously derived using photometric redshifts for the AS2COSMOS and AS2UDS samples by Simpson et al. (2020) and Stach et al. (2019), respectively. While our sample size is smaller than employed in those two studies, our spectroscopic redshifts should be more precise than their photometric redshifts. These results add support for the positive correlation between S_{870} and redshift that has been previously proposed in the literature (e.g Archibald et al., 2001; Dannerbauer et al., 2002; Ivison et al., 2007; Younger et al., 2007; Smolčić et al., 2012; Stach et al., 2019). This trend could be accounted for by more massive galaxies forming earlier, so-called "downsizing" (Cowie et al., 1996). Due to our selection criteria, our sample contains the galaxies with the highest dust masses (and by implication gas masses) at $z \sim 1$–5, which also includes many of the most massive galaxies in terms of stellar mass (Dudzevičiūtė et al., 2020). The trend we see therefore suggests an increasing upper bound on the gas and dust mass in the most massive star-forming galaxies out to $z \sim 5$, as we show later this is likely driven by an increasing gas fraction in these galaxies with redshift (see §3.3.5).

3.3.2 Gas Excitation

The detection of CO line emission in our 3-mm observations allows us to probe the properties of the star-forming gas in submillimetre galaxies, which, given their high dust masses and star-formation rates should be dense and highly excited (e.g. Spilker et al., 2014). CO traces molecular clouds, with its rotational transitions being excited by collisions with H_2 (Solomon & Vanden Bout, 2005). An understanding of the CO excitation in SMGs is important as it

Line ratio	N_{sources}	This work	SMM J2135$-$0102	Bothwell et al. (2013)
r_{11}	11	1.0	1.0	1.0
r_{21}	25	0.9 (fixed)	...	0.84 ± 0.13
r_{31}	39	0.63 ± 0.12	0.68 ± 0.03	0.52 ± 0.09
r_{41}	28	0.34 ± 0.04	0.50 ± 0.04	0.41 ± 0.07
r_{51}	7	0.36 ± 0.07	0.35 ± 0.02	0.32 ± 0.05
r_{61}	4	0.27 ± 0.07	0.28 ± 0.02	0.21 ± 0.04
r_{71}	5	0.26 ± 0.05	0.119 ± 0.008	0.18 ± 0.04

Table 3.1: Median CO line/brightness temperature ratios for the emission lines of 119 SMGs, comprising 47 lines from this study and a further 72 lines in similarly-selected sources from the literature (see §3.3.2), where $r_{J1} = L'_{\text{CO}(J-J-1)}/L'_{\text{CO}(1-0)}$. The number of sources used in our median calculation for each transition is also displayed. As CO(1–0) data is sparse for these populations, we normalise to the CO(2–1) transition and assume $r_{21} = 0.9$. Uncertainties are estimated from bootstrap resampling.

provides a measure of ISM properties such as temperature and density, but it is also vital in deriving gas masses, as it is frequently necessary to estimate the CO(1–0) luminosity by extrapolating from the mid- to high-J_{up} transitions based on such CO spectral line energy distributions.

The simplest approach to constructing a CO SLED is to observe a single source at a wide range of frequencies to detect multiple CO transitions. For example Danielson et al. (2011, 2013) observed the lensed SMG SMM J2135$-$0102 (the "Cosmic Eyelash"), detecting 11 separate transitions including ^{12}CO from $J_{\text{up}} = 1$ to $J_{\text{up}} = 9$ from which they constructed a CO SLED. SMM J2135$-$0102 displays increasing CO line flux up to $J_{\text{up}} = 6$, beyond which it declines (see Fig. 3.2). Papadopoulos et al. (2014) carried out a similar study, observing the merger/starburst systems NGC 6240 and Arp 193 with *Herschel*/SPIRE to construct CO SLEDs covering $J_{\text{up}} = 4$–13 transitions, finding Arp 193 and NGC 6240 to contain respectively small and large reservoirs of dense ($n \geq 10^4\,\text{cm}^{-3}$) gas. Yang et al. (2017) and Cañameras et al. (2018) used the IRAM 30 m telescope to study $J_{\text{up}} \sim 3$–11 CO emission for 27 lensed SMGs and found the majority of sources to peak in line flux at $J_{\text{up}} \sim 4$–7.

Where there is a large sample of sources observed in only a few, or even just individual CO lines, it is possible to build a statistical SLED (Bothwell et al., 2013; Spilker et al., 2014; Boogaard et al., 2020). This method is subject to more uncertainties and biases, particularly in how to normalise the sources used, as well as variations within the population and the fact that sources at different redshifts contribute to the different J_{up} (a particular issue where observations have been obtained in only a single millimetre band, as done here). This is therefore not a preferred method of constructing a SLED, but can still provide useful
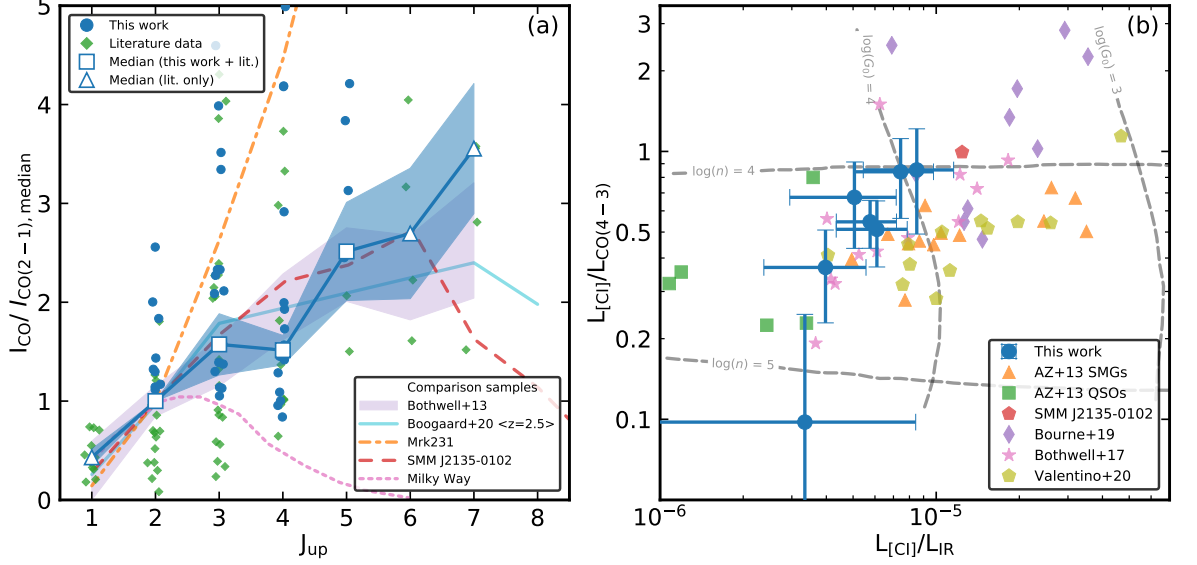
Figure 3.2: **(a)** A statistically derived CO SLED constructed from our CO observations of AS2COSMOS, AS2UDS and ALESS SMGs, along with a compilation of literature observations of SMGs. Our composite SLED displays an increase in excitation up to $J_{up} \sim 6$, beyond which coverage is limited. All I_{CO} are normalised to the median $I_{CO(2-1)}$ of their respective SLED. We also overlay the SLEDs of the lensed SMG SMM J2135−0102 (the "Cosmic Eyelash"; Danielson et al., 2011), the local ULIRG Markarian 231 (which hosts a Seyfert 1 AGN; van der Werf et al., 2010) and the Milky Way (Fixsen et al., 1999). Our SMG SLED is consistent with that of SMM J2135−0102, albeit with slightly lower excitation at $J_{up} = 4$, and agrees within the respective uncertainties with the statistical SLEDs of Bothwell et al. (2013), while potentially showing slightly higher excitation compared to the SLED of less active galaxies at $z \sim 2.5$ from Boogaard et al. (2020). Markarian 231 displays stronger high-J_{up} emission, the absence of which in the SMGs suggests that they are typically not dominated by an AGN component. The Milky Way SLED peaks at $J_{up} \sim 2$–3 and declines rapidly beyond, indicating a much cooler and less excited ISM than in the SMGs. We identify those transitions in the composite SLED which rely solely on the literature samples, and uncertainties on the median are estimated from bootstrap resampling. We note that by considering only our SMG sample we derive a SLED that is consistent with the median shown in the plot for $J_{up} = 2$–5.**(b)** $L_{[CI]}/L_{CO(4-3)}$ versus $L_{[CI]}/L_{IR}$. This plot is an indicator of both gas density (n) and radiation field strength (G_0), and we indicate tracks of constant n (in units of cm^{-3}) and G_0 (in units of the Habing field, $1.6 \times 10^{-3}\,\mathrm{erg\,s^{-1}\,cm^{-2}}$) estimated from the photon dissociation region models of Kaufman et al. (1999). We also include measurements for SMGs and Quasi-stellar Objects (QSOs) from Alaghband-Zadeh et al. (2013), $z \sim 1$ star-forming galaxies from Bourne et al. (2019) and Valentino et al. (2020b), and lensed $z \sim 4$ SMGs from Bothwell et al. (2017), as well as SMM J2135−0102 (Danielson et al., 2011). Our seven sources are broadly consistent with having a single n and G_0, with a density of $\log_{10}(n) \sim 4.5$ and a radiation field of $\log_{10}(G_0) \sim 4$. We note that considering a wider variety of sources, including $z \sim 1$ star-forming galaxies and QSOs, reveals a mild positive correlation between n and G_0 suggesting a link between ISM density and activity.

information nonetheless. Bothwell et al. (2013) built such a statistical SLED from their survey of 40 SMGs, supplemented by sources from the literature, and Spilker et al. (2014) similarly used their 1.4 mm-selected lensed DSFGs to construct a composite statistical SLED.

We construct an updated statistical SLED for SMGs, using our 47 CO-detected sources in addition to a further 72 lines in similar star-forming sources from the literature to create a superset of 119 CO lines. Sources are taken from Bothwell et al. (2013) and the following: Bothwell et al. (2010), Carilli et al. (2010), Carilli et al. (2011), Daddi et al. (2009), Engel et al. (2010), Ivison et al. (2011), Riechers et al. (2010), Riechers et al. (2011a), Riechers et al. (2011b), Schinnerer et al. (2008), Tacconi et al. (2006), Walter et al. (2012), and Zhao et al. (2020). The data used from our survey and these literature sources can be found in the online supplementary material for Birkin et al. (2021).

We follow a similar prescription to that used in Bothwell et al. (2013), exploiting the fact that CO luminosity is expected to broadly scale with far-infrared luminosity: $L'_{CO} \propto L_{IR}^a$ (with $a \sim 1$) and using these trends to normalise all L'_{CO} to the same L_{IR}:

$$L'_{CO,corr} = L'_{CO} \times \left(\frac{\langle L_{IR} \rangle}{L_{IR}} \right)^a, \tag{3.3.1}$$

where $L'_{CO,corr}$ is the CO line luminosity a source would have at $L_{IR} = \langle L_{IR} \rangle$, and in this case we choose $\langle L_{IR} \rangle$ to be the sample median. a is the slope of the relevant $L_{CO,J}$–L_{IR} relation. We then convert L'_{CO} to I_{CO} using Eq. 2.5.4, adopting the median redshift of the superset. Bothwell et al. (2013) adopt $a = 1$ for all J_{up}, although a is expected to vary with J_{up} as higher-J_{up} transitions more closely trace the warm star-forming gas, while low-J_{up} transitions trace cooler gas (Greve et al., 2014; Rosenberg et al., 2015; Daddi et al., 2015). We follow Bothwell et al. (2013) in adopting $a = 1$, however, we note that adopting $a = 0.6$–0.8 changes the results only within the 1-σ error bars.

We estimate $L'_{CO,corr}$ using $\langle L_{IR} \rangle = 6.0 \times 10^{12} \, L_\odot$ (the median L_{IR} of the superset) and use Eq. 2.5.4, adopting $z = 2.52$ (the median redshift of the superset), to convert them to I_{CO}, which we plot in Fig. 3.2(a). The median SLED is calculated from the median intensity at each J_{up}, with bootstrapped uncertainties. We also normalise all measurements to the median $I_{CO(2-1)}$ of our sample to allow a clearer comparison with other SLEDs, where the CO(2–1) transition is chosen as we have better coverage in our sample than for the CO(1–0) transition (see Table 3.1). The SLED shows an increase in excitation up to $J_{up} = 6$, however we note that few sources with $J_{up} > 5$ are included here, and therefore the uncertainties are much greater in this regime. We also see a considerable scatter in the scaled line luminosities

of the SMGs at each transition, suggesting a large variation in either excitation, optical depth or gas depletion timescale. We suggest that it may be the latter factor, gas depletion, which is causing the scatter as it is expected to vary rapidly in a strongly star-forming population such as SMGs, resulting in them showing a wide range in CO line luminosity at a fixed far-infrared luminosity.

In Fig. 3.2(a) we also show the SLEDs of the Milky Way (Fixsen et al., 1999), the local ULIRG Markarian 231 (van der Werf et al., 2010), the aforementioned SMM J2135−0102 (Danielson et al., 2011), as well as the median SLEDs derived by Bothwell et al. (2013) for their luminous SMG sample in addition to literature sources, and by Boogaard et al. (2020) for a CO-selected sample of star-forming galaxies at $z \sim 2.5$. Compared to the local galaxy templates shown, our SMG SLED agrees with Markarian 231 at $J_{\mathrm{up}} \sim 2$–3, but at higher-J_{up} the latter displays much more highly-excited gas. van der Werf et al. (2010) showed that in the $J_{\mathrm{up}} \leq 8$ regime this can be explained by heating from star formation, however above $J_{\mathrm{up}} = 8$ the observed line ratios require X-ray heating from the galaxy's supermassive black hole. It is therefore unlikely that the moderate-J_{up} CO emission from most SMGs is dominated by an AGN component (consistent with the small fraction of AGN-dominated SMGs in our sample, §2.5.2). By contrast, the Milky Way SLED peaks at $J_{\mathrm{up}} \sim 2$–3, displaying declining emission at higher J_{up}, very different from that seen for the much more actively star-forming SMGs.

We see relatively good agreement in Fig. 3.2(a) between our SLED and those for SMGs from Bothwell et al. (2013) and Danielson et al. (2011), although we find a lower line flux at $J_{\mathrm{up}} = 4$ when compared to the median SLED of Bothwell et al. (2013) and the SLED of SMM J2135−0102. We note here that changing the L'_{CO}–L_{IR} scaling from $a = 1$ to $a = 0.8$ results in better agreement between the two statistical SLEDs, however we use the $a = 1$ result here, as found for local ULIRGs for $J_{\mathrm{up}} = 2$–5 (see Greve et al., 2014), and to remain consistent with Bothwell et al. (2013), although we comment that the L_{IR} estimates used by the latter in their scaling are very uncertain. Given the relatively close agreement we see to the SLED of SMM J2135−0102, as measured by Danielson et al. (2011), we adopt this when deriving $L_{\mathrm{CO(1-0)}}$ for our sources. We also compare our SLED to that derived for a CO-selected sample of star-forming galaxies at similar redshifts, $z \sim 2.5$, by Boogaard et al. (2020). The SMGs exhibit higher ratios of moderate- and high-J_{up} CO emission, relative to CO(2–1), compared to these typically less actively star-forming galaxies.

In addition to these empirically derived SLEDs, attempts have also been made to predict CO SLEDs for galaxies from numerical simulations. For example Lagos et al. (2012) modelled the

CO emission from SMGs by coupling the SHARK semi-analytic models of galaxy formation with a photo-dissociation region (PDR) code. The SLED of a typical source in their model was found to peak at $J_{\rm up} = 4$, and quickly decline at higher $J_{\rm up}$, although the presence of an AGN led to enhanced emission beyond $J_{\rm up} \sim 6$. This behaviour differs from that seen for our composite SLED, reflecting the general difficulties in reproducing the observed properties of submillimetre galaxies in theoretical models.

[CI] properties

As an alternate probe of the ISM, we discuss the [C I] properties of our sample. [C I] emission has been proposed as an effective tracer of the molecular gas in galaxies (Papadopoulos & Greve, 2004), and while it is not as well-studied at high redshift as CO, in recent years there have been several studies published on this topic (e.g. Valentino et al., 2018, 2020b). Fig. 3.2(b) shows the ratio between the [C I]($^3{\rm P}_1-^3{\rm P}_0$) and CO(4–3) luminosity as a function of the ratio between the [C I]($^3{\rm P}_1-^3{\rm P}_0$) and infrared luminosity. To interpret the distribution we overlay tracks as a function of gas density (n; in units of cm^{-3}) and average far-ultraviolet radiation field strength (G_0; in units of the Habing field, $1.6 \times 10^{-3}\,{\rm erg\,s^{-1}\,cm^{-2}}$) predicted by the PDR model of Kaufman et al. (1999). As our [C I] sample is small however, we limit ourselves to a qualitative discussion only. The [C I] measurements for our sample are presented in Table 3.2.

Our seven [C I] -detected sources show very similar line ratios, and may even be consistent with a single value of $L_{\rm [CI]}/L_{\rm IR}$ and $L_{\rm [CI]}/L_{\rm CO(4-3)}$, corresponding to a typical ISM density of $\log_{10}(n) \sim 4.5$ and a radiation field of $\log_{10}(G_0) \sim 4$. The uncertainties are large however, and we are limited in that our sample contains only sources at $z \gtrsim 3.2$, where [C I]($^3{\rm P}_1-^3{\rm P}_0$) is redshifted into the 3-mm band. Compared to samples from the literature, including $z \sim 1$ star-forming galaxies from Bourne et al. (2019) and Valentino et al. (2020b), and other SMGs (and QSOs) from Alaghband-Zadeh et al. (2013) and Bothwell et al. (2017), we see that our SMGs lie in a similar region to the published SMGs, but have typically lower ratios of $L_{\rm [CI]}/L_{\rm IR}$ compared to the less active $z \sim 1$ star-forming galaxies, but not as low as the QSOs from Alaghband-Zadeh et al. (2013). This PDR model suggests that all the galaxy samples have similar ISM densities, but with the SMGs exhibiting higher radiation fields as a result of their more intense activity (although not as high as those seen in QSOs). We note that taking all the samples together, there is a possible positive correlation between G_0 and n, suggesting that sources with a typically denser ISM exhibit a stronger radiation field.
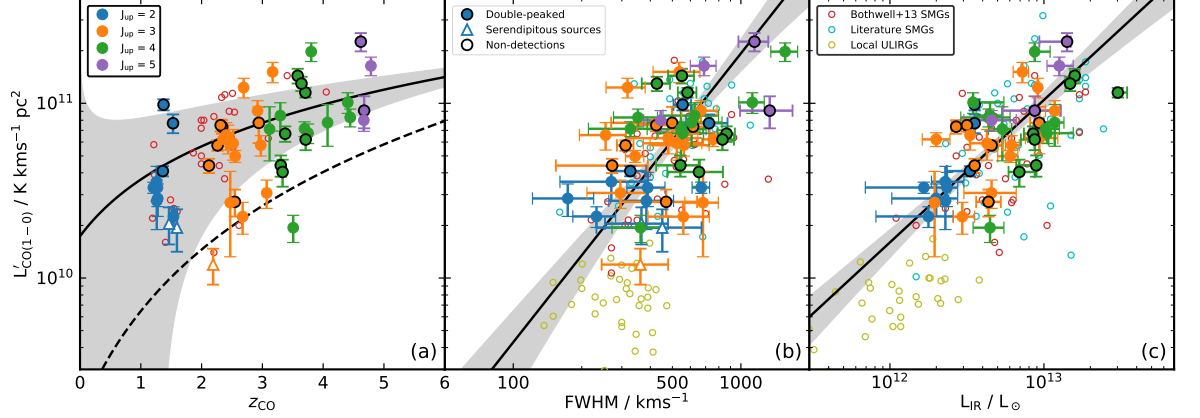
Figure 3.3: **(a)** L'_{CO} versus CO redshift for our SMG sample, showing a clear trend of increasing CO luminosity with redshift which we fit with the model $L'_{CO} \propto (1 + z)^b$, finding $b = 1.1 \pm 0.2$. This plot indicates that the gas mass in our dust-mass-selected SMGs exhibits a steady rise with redshift, although this is partly driven by the increase in the sensitivity limit at higher redshifts (roughly indicated by the dashed line as our data have a range of sensitivities). **(b)** L'_{CO} versus FWHM for our sample along with SMGs from the literature compilation described in §3.3.2 and local ULIRGS from Downes & Solomon (1998). For our sources we indicate the transition in which the source was detected, however all sources have been corrected to $L'_{CO(1-0)}$ as described in §3.3.2. Most SMGs lie at the high-luminosity end of this trend, with the brightest and broadest lines indicating that they are the most massive galaxies in terms of both gas content and dynamical mass. We generally find that higher-J_{up} sources have larger linewidths which might suggest that on-average the higher-redshift sources we detect are more massive. Also included are the three serendipitous sources described in §3.2, which lie at the lower end of the trend, suggesting that they may be scaled down versions of SMGs. Our data are fit with the model $\log_{10} L'_{CO} = a \log_{10} (\mathrm{FWHM}/\mathrm{FWHM}_{med}) + b$, with $a = 1.7 \pm 0.3$, consistent with a rotating disc model. We also find that the median linewidth of the double-peaked sources is consistent with that of the single-peaked sources, within their 1-σ uncertainties. ULIRGs display lower line luminosities for a given linewidth, likely because their dynamical masses have an increasing contribution from their stellar component, rather than being dominated by the gas. **(c)** L'_{CO} versus L_{IR} for the same sample as in the middle panel. Again the SMGs lie at the extreme end of the trend, indicating large gas reservoirs and high star-formation rates. We fit our data with the model $\log_{10} L'_{CO} = a \log_{10} (L_{IR}/L_{IR,med}) + b$, finding $a = 0.82 \pm 0.11$. Our data show a scatter of 0.22 dex around this relation, which is likely driven by the scatter in our CO SLED (see Fig. 3.2(a)). We also indicate 3-σ upper limits on our CO non-detections.

ID	J_{up}	z_{CO}	$I_{[\mathrm{CI}]}$ [Jy kms^{-1}]	$L'_{[\mathrm{CI}]}$ [10^{10} K kms^{-1} pc^{-2}]
ALESS003.1	4	3.375	0.52 ± 0.13	1.4 ± 0.4
ALESS005.1	4	3.303	0.47 ± 0.15	1.2 ± 0.4
ALESS009.1	4	3.694	0.51 ± 0.09	1.6 ± 0.3
ALESS023.1	4	3.332	0.52 ± 0.15	1.4 ± 0.4
ALESS031.1	4	3.712	0.30 ± 0.11	0.9 ± 0.3
AS2COS0006.1	5	4.620	1.1 ± 0.3	4.7 ± 1.1
AS2UDS011.0	4	4.073	0.7 ± 0.2	2.7 ± 0.9
AS2UDS014.0	4	3.804	0.2 ± 0.4	7.9 ± 1.2

Table 3.2: Properties of the [CI] detections in our sample. When fitting the [CI] emission lines we have fixed the linewidth to be equivalent to the CO linewidth, i.e. FWHM$_{[\mathrm{CI}]}$ = FWHM$_{\mathrm{CO}}$.

3.3.3   CO(1–0) luminosities

Having established the excitation properties of the SMGs in our sample we can use these to estimate their CO(1–0) luminosities, before moving on to study their gas masses. This will allow us to investigate how our sources fit within the L'_{CO}–FWHM and L'_{CO}–L_{IR} relations. In what follows we use $L_{\mathrm{CO}(1-0)} = L_{\mathrm{CO,J}}/r_{j1}$, adopting the r_{j1} measured by Danielson et al. (2011) for SMM J2135−0102, to estimate CO(1–0) luminosities. We derive a median CO(1–0) luminosity of $(6.7 \pm 0.5) \times 10^{10}$ K km s^{-1} pc^2 for our sample.

In Fig. 3.3(a) we show the variation of $L'_{\mathrm{CO}(1-0)}$ with redshift for our sample, from which we see a positive correlation between the two, suggesting an increasing gas mass at higher redshifts. However, we note that this is potentially influenced by the effects of incompleteness for the less luminous sources at the highest redshifts, which we indicate on the figure for a representative sensitivity of one of the observations from our study. Non-detected CO sources are shown as limits in Fig. 3.3(a), where *spec-z* sources are plotted at their optical spectroscopic redshift and *scan* sources are plotted at their photometric redshift from MAGPHYS SED fitting. We fit the trend in our data with a simple parameterisation: $L'_{\mathrm{CO}} \propto (1 + z)^b$, estimating $b = 1.1 \pm 0.2$. This highlights an increasing gas mass for our SMG sample, which is approximately dust-mass-selected and may indicate an evolution in the gas mass fraction or gas-to-dust ratio. We return to this point in §3.3.5.

L'_{CO}–FWHM relation

The L'_{CO}–FWHM relation is useful as it provides a measure of the correlation between the gas mass and the galaxy dynamics (Harris et al., 2012). Our sample has a median $L'_{\mathrm{CO}(1-0)}$

of $(6.7 \pm 0.5) \times 10^{10}\,\mathrm{K\,km\,s^{-1}\,pc^2}$ and a median FWHM of $540 \pm 40\,\mathrm{km\,s^{-1}}$, indicating more gas-rich sources than the $(4.5 \pm 1.0) \times 10^{10}\,\mathrm{K\,km\,s^{-1}\,pc^2}$ and $500 \pm 60\,\mathrm{km\,s^{-1}}$ found from the Bothwell et al. (2013) sample. Fig. 3.3(b) shows the derived CO line luminosity as a function of line FWHM, where all line luminosities are converted to CO(1–0). For comparison we include SMGs from Bothwell et al. (2013), SMGs from the literature compilation described in §3.3.2 and local ULIRGs from Downes & Solomon (1998).

The variation of $L_{\mathrm{CO(1-0)}}$ with FWHM of the CO lines in Fig. 3.3(b) shows a 5-σ positive correlation, potentially indicative of increasing gas mass with dynamical mass. To interpret this we fit our data with a model of the form $\log_{10}(L'_{\mathrm{CO}}) = a \log_{10}(\mathrm{FWHM/FWHM_{med}}) + b$, using an orthogonal distance regression (ODR) technique which takes into account the uncertainties on both L'_{CO} and the FWHM. This method is implemented using the SCIPY package of PYTHON.

From this fitting we estimate $a = 1.7 \pm 0.3$ and $b = 10.93 \pm 0.05$, with a scatter of $0.34\,\mathrm{dex}$. If the line widths in our population reflect disc dynamics (see §3.2), we would expect the galaxy mass (and therefore the CO line luminosity) to increase with the square of the rotational velocity (and therefore the CO linewidth). The fitted trend indeed suggests that the dynamics of the CO in our sample are consistent with rotating discs (this idea is explored further in Chapter 5). A model of this kind was also shown to be a good fit to the sample of Bothwell et al. (2013), who suggested that this implies a constant ratio between the gas and stellar dynamical contributions in CO regions.[1]

We also indicate on this plot those sources which show double-peaked CO line profiles (as described in §3.2), finding these to have a median FWHM of $550 \pm 60\,\mathrm{km\,s^{-1}}$, consistent with the median of $520 \pm 60\,\mathrm{km\,s^{-1}}$ determined for the single-peaked sources, and a median $L'_{\mathrm{CO(1-0)}}$ of $(7.4 \pm 0.8) \times 10^{10}\,\mathrm{K\,km\,s^{-1}\,pc^2}$, which is marginally brighter than the $(6.3 \pm 0.8) \times 10^{10}\,\mathrm{K\,km\,s^{-1}\,pc^2}$ determined for the single-peaked sources.

$L'_{\mathrm{CO}} - L_{\mathrm{IR}}$ relation

The CO(1–0) line luminosity acts as a tracer of the reservoir of gas available in SMGs to form stars, and the infrared luminosity traces the star formation currently occurring. Therefore

---

[1] Unlike the SMGs, the local ULIRGs in this plot show no correlation between FWHM and L'_{CO}. Bothwell et al. (2013) suggested that this is a result of a wide range in gas fractions, a greater contribution to the dynamics from the stellar components, or thin nuclear gas discs/rings meaning that inclination differences cause significant scatter.

the $L'_{\rm CO}$–$L_{\rm IR}$ relation indicates what fraction of the total molecular gas is being converted into new stars: the star-formation efficiency. This is analogous to the Kennicutt-Schmidt relation (Kennicutt, 1998b) for galaxy-integrated properties. Fig. 3.3(c) shows the relationship between $L'_{\rm CO(1-0)}$ and $L_{\rm IR}$ for our SMG sample along with SMGs from Bothwell et al. (2013), SMGs from the literature compilation described in §3.3.2 and local ULIRGs from Solomon et al. (1997). We fit a parameterised model of the form $\log_{10}(L'_{\rm CO}) = a\log_{10}(L_{\rm IR}/L_{\rm IR,med}) + b$ to our data points using an ODR technique as described in the previous section, finding $a = 0.82 \pm 0.11$ and $b = 10.81 \pm 0.03$. The positive correlation between $L'_{\rm CO(1-0)}$ and $L_{\rm IR}$ is tight, with 0.22 dex of scatter, and most SMGs lie at the upper end of this trend indicating massive gas reservoirs and high star-formation rates.

We now compare our sub-linear slope for the $L_{\rm CO(1-0)}$–$L_{\rm IR}$ relation (estimated from observations of moderate-$J_{\rm up}$ CO) with similar studies in the literature. For example, Greve et al. (2005) found a slope of 0.62 ± 0.08 by fitting local (U)LIRGs and SMGs, although they assumed thermalised emission to convert their moderate-$J_{\rm up}$ CO line luminosities, which would tend to bias their result low at higher $L_{\rm CO(1-0)}$ and $L_{\rm IR}$ (yielding a flatter trend), while Genzel et al. (2010) found 0.87 ± 0.09, again from moderate-$J_{\rm up}$ (note that they fitted the inverse relation, and we have converted the slope for easier comparison with ours). On the other hand, Ivison et al. (2011) found a super-linear slope, $a = 1.5 \pm 0.3$ for SMGs with reliable CO(1–0) or CO(2–1) measurements, potentially indicating an additional reservoir of cool gas in the most massive and luminous systems. We note that our conclusions are unchanged if we adopt line ratios from our own statistical SLED instead of that of SMM J1235−0102. We caveat that direct comparisons between these values may not be reliable given the use of different fitting methods, for example Genzel et al. (2010) fitting the inverse relation to us, and giving equal weight to all data points. A more robust comparison would involve fitting all of the above samples using a consistent method, which we do not attempt to do here.

In theory, the slope of the $L'_{\rm CO}$–$L_{\rm IR}$ relation should vary with $J_{\rm up}$ as the low-$J_{\rm up}$ transitions trace the cooler gas, whereas the mid- to high-$J_{\rm up}$ transitions trace the warmer gas which is more closely linked to the star-forming regions. For the $J_{\rm up} = 2$–5 transitions, we find slopes of 2.7 ± 0.4, 0.8 ± 0.3, 1.0 ± 0.3 and 1.1 ± 0.4, respectively. For the $J_{\rm up} = 3$–5 transitions, this is consistent with Greve et al. (2014) who performed a similar analysis on local ULIRGs. The anomalous gradient of the $J_{\rm up} = 2$ relation may be a result of our small sample, which comprises just nine $J_{\rm up} = 2$ detections, or may be a reflection of the same behaviour reported by Ivison et al. (2011).

It has been similarly suggested that the CO(5–4) emission could be a good tracer of the star-forming gas, in which case it should correlate linearly with the infrared luminosity, with Daddi et al. (2015) finding a slope of 0.96 ± 0.04 for the $L_{\mathrm{CO(5-4)}}$–L_{IR} relation (see also e.g. Cassata et al., 2020; Valentino et al., 2020a). As reported above we find that the four sources detected in CO(5–4) display a gradient consistent with a linear relation between L'_{CO} and L_{IR}, found by Daddi et al. (2015). To increase our modest sample size, we also convert all our CO(4–3) detections to estimate the corresponding CO(5–4), ensuring that the correction factor is small and less uncertain. In this case we find a gradient of $\Delta L'_{\mathrm{CO}}/\Delta L_{\mathrm{IR}} = 1.2 \pm 0.3$ from 21 sources, also consistent with linearity.

3.3.4 Gas Mass Tracers

As a measure of the amount of fuel available for star formation, an accurate and precise knowledge of the molecular gas content is crucial in understanding the properties and subsequent evolution of galaxies. From our observations we are able to compare three different indirect tracers of the total (H_2 and He) gas mass: the inferred CO(1–0) luminosity, the $[\mathrm{C\,I}](^3\mathrm{P}_1-^3\mathrm{P}_0)$ luminosity and the cold dust mass. We can also compare three different methods of estimating the cold dust masses: from the rest-frame 870-μm (observed 3-mm) emission, the extrapolated observed-frame 870-μm emission and from SED modelling, all of which are similar but may have subtle differences. When estimating gas masses from these tracers all three require calibration factors which are subject to considerable uncertainty, therefore we focus only on the observed quantities and how well they correlate when providing a comparison. However, we will briefly discuss predicted values for gas masses using standard conversion factors.

CO–H_2 conversion

Having established the excitation properties of our sample in §3.3.2, and therefore the CO line ratios r_{J1}, we can calculate total gas masses from the CO luminosity using:

$$M_{\mathrm{gas}} = 1.36 \, \alpha_{\mathrm{CO}} \, \frac{L'_{\mathrm{CO,J}}}{r_{\mathrm{J1}}}, \tag{3.3.2}$$

where r_{J1} represents the line ratio of the J_{up} transition to the CO(1–0) transition (which we adopt from SMM J2135$-$0102, noting that this is consistent with our statistical SLED derived in §3.3.2), α_{CO} is the so-called CO–H_2 conversion factor given in units of $M_\odot$ $(\mathrm{K\,km\,s^{-1}\,pc^2})^{-1}$, $L'_{\mathrm{CO,J}}$ is the CO line luminosity of the relevant J_{up} transition in units

of $K\,km\,s^{-1}\,pc^2$, and the factor of 1.36 accounts for the abundance of Helium (e.g. Solomon et al., 1997). We note here that in what follows, all literature comparison data are rescaled to ensure that they include this factor of 1.36 in estimates of M_{gas}.

As discussed in §1.3.3, it is very difficult to measure α_{CO} and verify the appropriate value to adopt at high redshifts. Attempts to constrain α_{CO} are mostly empirical, often involving estimating dynamical masses and combining these with stellar masses and an assumed dark matter fraction (Downes & Solomon, 1998; Daddi et al., 2010; Bothwell et al., 2013; Calistro Rivera et al., 2018). α_{CO} is then estimated from the comparison of the dynamical mass determined from a scale size and the circular velocity, estimated from the CO linewidth, with the total mass derived from the sum of the gas, stellar and dark matter components:

$$M_{dyn} = \frac{M_* + M_{gas}}{1 - f_{DM}} = C\frac{\sigma^2 R}{G}, \tag{3.3.3}$$

where C is dependent on the mass distribution and inclination angle of the galaxy (e.g. Erb et al., 2006, and see §4.2.7). This can be used to derive M_{gas} and therefore α_{CO}. In our case this is difficult as we do not have the resolved CO(1–0) sizes or individual inclination angles for our sources necessary to determine R and the inclination angle corrections. However, our sample is larger than those used by many authors who have also attempted this. We therefore investigate the feasibility of placing constraints on α_{CO} with our sample here.

Returning to Eq. 3.3.3, we adopt $f_{DM} \sim 0.35$ following Smith et al. (2019) which was found for $z \sim 0.12$ ellipticals, expected to be the descendants of SMGs (see §3.3.6). We also adopt $C = 2.25$ following Binney & Tremaine (2008), a value we find to be consistent with our simulated rotation curves from §3.2. Other authors have found or adopted different values for C, such as Erb et al. (2006) who adopted $C = 3.4$ and Kohandel et al. (2019) who found $C = 1.78$ in simulations of spiral disc galaxies. Both of the above are consistent with our simulations. Most of our sources are completely unresolved and therefore we lack inclination corrections. We choose to make the assumption that our samples is comprised of randomly oriented discs which is consistent with the simulations described in §3.2. This would result in a median $i = 57°$ and a median $\sin(i) = 0.79$ (Law et al., 2009), and we adopt this value for all sources. Finally, we use an aperture of size $R = 14\,kpc$, which should capture the full extent of the CO(1–0) emission, and therefore the cold gas reservoirs (Ivison et al., 2011).

This yields a median value for the CO-H_2 conversion factor of $\alpha_{CO} = 1.0 \pm 0.7$ which is closer to the typical ULIRG value of ~ 1 (e.g. Solomon et al., 1997) than the "main-sequence" value of ~ 4 (e.g. Daddi et al., 2010). It is also consistent with the value of $\alpha_{CO} \sim 2$ estimated by

(Danielson et al., 2011, 2013) for the lensed submillimetre galaxy SMM J2135-0102.

Equally, if we instead adopt the "main-sequence" value of $\alpha_{\rm CO} \sim 3.6$ (Daddi et al., 2010), then this is also consistent with the line width constraints on the dynamics, when assuming a lower dark matter fraction of $f_{\rm DM} \sim 0.25$ and $C = 3.4$ (Erb et al., 2006), for the same R. We conclude that to derive a robust estimate of the CO–H_2 conversion factor in high-redshift galaxies will require high-resolution maps and velocity fields for a large number of sources (see, e.g. Calistro Rivera et al., 2018). We build on this in Chapter 5

In what follows we simply adopt $\alpha_{\rm CO} = 1$ for all galaxies, making our results easier to rescale for readers, resulting in a median gas mass of our SMG sample of $M_{\rm gas,med} = (9.1 \pm 0.7) \times 10^{10}\,{\rm M_\odot}$. We stress that our adoption of this simplified approach, rather than assuming different $\alpha_{\rm CO}$ for different populations (either based on initial selection, sSFR, $L_{\rm IR}$, etc.) means that our gas estimates for some comparison samples differ from those presented in the original studies.

Gas-to-dust conversion

The total gas mass can also be estimated from the cold dust mass using:

$$M_{\rm gas} = \delta_{\rm gdr}\, M_{\rm dust}, \tag{3.3.4}$$

where the gas-to-dust ratio $\delta_{\rm gdr}$ is simply the ratio of gas mass to dust mass (Leroy et al., 2011; Magdis et al., 2012). Unfortunately the gas-to-dust ratio may vary considerably with metallicity (Santini et al., 2014) and redshift (Saintonge et al., 2013) for metal-rich sources, although it is often assumed to be a constant $\delta_{\rm gdr} \sim 100$ (Swinbank et al., 2014; Scoville et al., 2016). Some authors have invoked scaling relations in order to estimate the gas-phase Oxygen abundance, and subsequently attempted to infer the gas-to-dust ratio, from the estimated stellar mass (Genzel et al., 2015; Tacconi et al., 2018). This method is, of course, not without very considerable uncertainties, both systematic and random, but as it relies on different assumptions to that of the CO-to-H_2 method it represents an independent estimate (although frequently based on the same underlying calibration sources). We note that Leroy et al. (2011) developed a technique to estimate $\alpha_{\rm CO}$ for resolved sources, assuming the gas-to-dust ratio holds constant over regions where molecular and ionised Hydrogen are in equal abundance, however, for high-redshift galaxies we are mostly concerned with galaxy-integrated properties, and this approach is not feasible.

The cold dust mass itself can also be estimated in several ways. Firstly, dust mass estimates are available from the MAGPHYS SED fitting to our sample (see §2.5.2), which utilises multi-
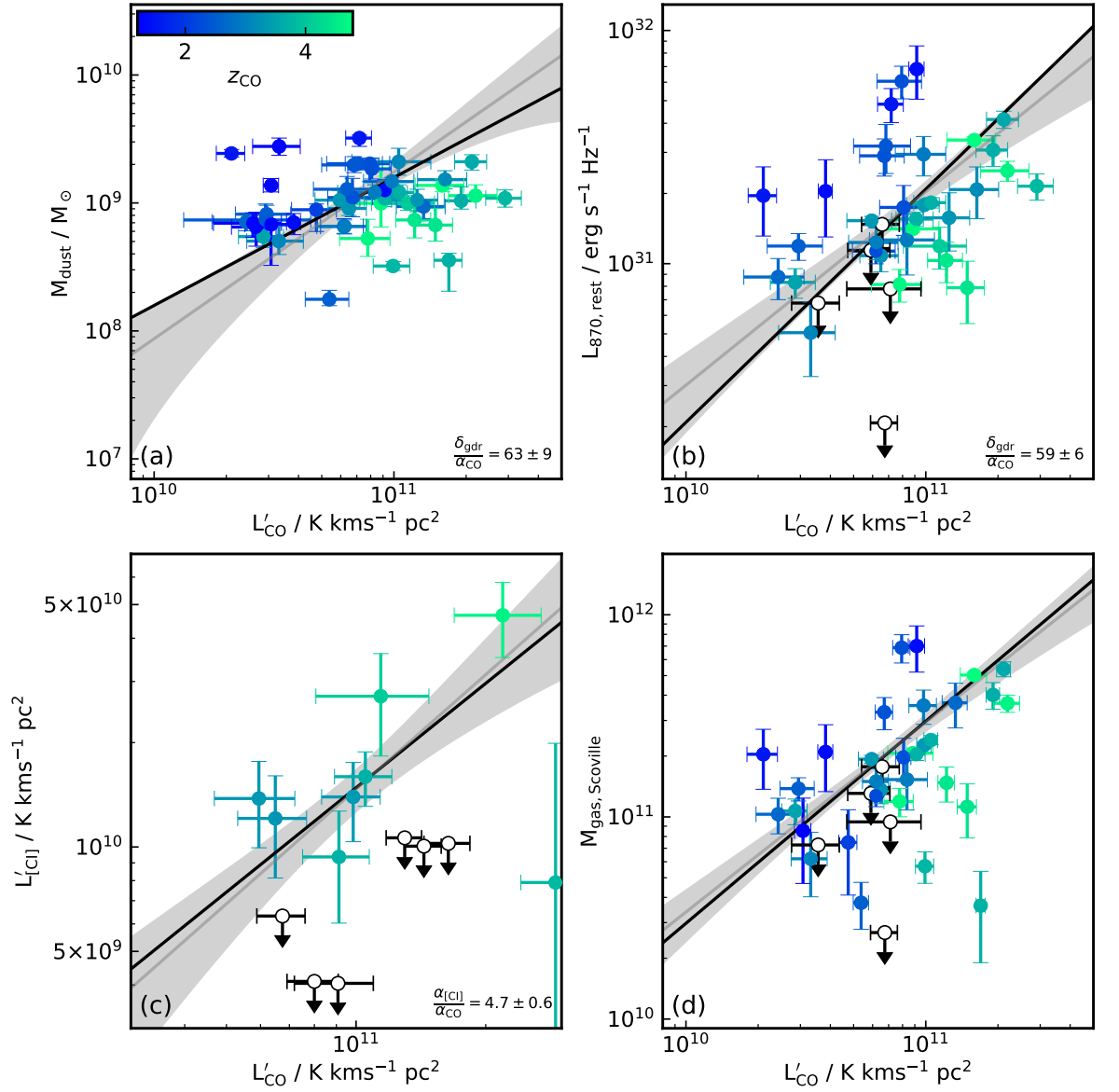
Figure 3.4: A comparison of different tracers of the gas mass in SMGs, where in all cases we perform a free fit (grey with shaded uncertainty) and a linear fit (black) in log space. We report the ratio of the corresponding pairs of calibration factors for each total gas mass tracer in the relevant panels. **(a)** and **(b)** Dust mass from MAGPHYS or the rest-frame 870-μm luminosity versus inferred CO(1–0) line luminosity. The CO(1–0) appears to correlate reasonably well with the rest-frame 870-μm luminosity, but poorly with the MAGPHYS dust mass estimates. **(c)** [C I](^{3}P$_1$–^{3}P$_0$) line luminosity versus inferred CO(1–0) line luminosity. The CO(1–0) and [C I] show a weak correlation, but are roughly consistent with a linear relation with considerable scatter, although we are limited by our modest [C I] sample size. **(d)** Gas mass estimated using the Scoville et al. (2016) calibration versus CO(1–0) line luminosity. The data show a large amount of scatter, but they are consistent with a linear trend. In **(a)**, **(b)** and **(d)** the higher-redshift sources appear to lie mostly below the fit, possibly indicative of an increasing gas-to-dust ratio, and/or a decreasing $\alpha_{\rm CO}$, with redshift. This is explored further in Fig. 3.6.

band photometry from e.g. ALMA and *Herschel* (da Cunha et al., 2015; Dudzevičiūtė et al., 2020, Ikarashi et al. 2020 in prep.). Our dust masses from MAGPHYS are presented in Table 3.3 and Table 3.4. However, the inclusion of shorter wavelength far-infrared photometry in this fitting may result in a bias towards warm dust, which could yield underestimates of the cold dust mass (Scoville et al., 2016). Secondly, the cold dust mass can be traced by the rest-frame 870-μm emission (Dunne et al., 2000). Given that the median redshift of our sample is $z \sim 3$, the 3-mm continuum photometry from our ALMA/NOEMA observations probes rest-frame $\sim 750\,\mu$m, close to $870\,\mu$m when compared to the rest-frame $\sim 220\,\mu$m traced by the observed 870-μm observations. Indeed, near the median redshift of the sample, the 3-mm photometry measurements closely match rest-frame $870\,\mu$m, providing estimates of the source luminosities with little uncertainty from the adopted spectral slope of the dust emission, β.

$$M_{\mathrm{gas}} = \delta_{\mathrm{gdr}} \times M_{\mathrm{dust}} = \delta_{\mathrm{gdr}} \times \frac{L_{870,\mathrm{rest}}}{\kappa_d(\nu) B(\nu, T_{\mathrm{d}})} \tag{3.3.5}$$

where κ_d here is the dust mass opacity coefficient (taken to be $0.077\,\mathrm{m^2\,kg^{-1}}$) and B is the Planck function, where we adopt $T_{\mathrm{d}} = 25\,\mathrm{K}$ (Dunne et al., 2000; Scoville et al., 2016). We note however that this becomes less reliable for sources at the lower- and higher-redshift ends of the sample where the observed $3\,\mathrm{mm}$ is further from rest-frame $870\,\mu$m.

Finally, we can use the fact that the dust on the Rayleigh-Jeans tail is optically thin to estimate the gas mass by extrapolating from the observed-frame 870-μm luminosities, using the calibration proposed in Scoville et al. (2016):

$$M_{\mathrm{gas}} = 1.78 S_{\nu_{\mathrm{obs}}} (1+z)^{-4.8} \times \left(\frac{\nu_{850\mu m}}{\nu_{\mathrm{obs}}} \right)^{3.8} D_L^2$$
$$\times \left(\frac{6.7 \times 10^{19}}{\alpha_{850}} \right) \frac{\Gamma_0}{\Gamma_{\mathrm{RJ}}} 10^{10} \mathrm{M}_\odot, \tag{3.3.6}$$

where $\nu_{\mathrm{obs}} = 100\,\mathrm{GHz}$, D_L is given in Gpc, Γ_{RJ} corrects for the departure of the Planck function from Rayleigh-Jeans (Scoville et al., 2016) and Γ_0 is its value adopting $z = 0$, $T_{\mathrm{d}} = 25\,\mathrm{K}$ and $\lambda_{\mathrm{obs}} = 850\,\mu$m, the latter of which is used to calibrate the conversion factor $\alpha_{850_{\mu\mathrm{m}}}$. We note that this calibration at high redshifts relies on gas mass estimates derived from CO(1–0) observations of a small sample of galaxies (mostly SMGs) and so this method is dependent upon those calibrations.

We compare all three dust-based tracers against CO(1–0) in §3.3.4. However, we note here that the median ratio of the $L_{870,\mathrm{rest}}$-based dust mass estimates to the MAGPHYS dust masses is 1.21 ± 0.09 for the adopted dust mass opacity coefficient and dust temperature, and for the Scoville et al. (2016) calibration the corresponding ratio is 1.94 ± 0.09 if we adopt $\delta_{\mathrm{gdr}} = 100$

and $\alpha_{850_{\mu m}} = 6.7 \times 10^{19}$. The value of $\alpha_{850_{\mu m}}$ we have used here is adopted by Scoville et al. (2016) based on observations of local ULIRGs and SMGs, although they come to this calibration using a near-galactic α_{CO}. We note again, however, that this systematic offset may be explained by MAGPHYS fitting being biased towards warm dust due to the inclusion of shorter wavelength far-infrared photometry (which probes the peak of the far-infrared SED rather than the Rayleigh-Jeans tail, and is therefore heavily dependent on the spectral slope β assumed in the fitting) and therefore underestimating the dust mass.

[CI]–H$_2$ conversion

Our third tracer of the total gas mass comes from the fine structure line of atomic Carbon (Weiß et al., 2003; Papadopoulos & Greve, 2004):

$$M_{gas} = 1.36\alpha_{[CI]}\, L'_{[CI]}, \qquad (3.3.7)$$

where $\alpha_{[CI]}$ is the [CI]–H$_2$ conversion factor in units of M$_\odot$ (K km s^{-1} pc^2)$^{-1}$. $L'_{[CI]}$ is the [CI] line luminosity in units of K km s^{-1} pc^2, and again we include a factor of 1.36 to account for the abundance of Helium.

The [C I] method benefits from the lines being optically thin which removes some of the transition ratio uncertainties that apply to estimates based on CO, and it is also expected to show smaller abundance variations as it is thought to be affected less by cosmic ray destruction (Papadopoulos et al., 2018). Due to their emitted frequencies [C I] is also much easier to observe at high redshift than the low-J_{up} CO transitions. It has been shown that the [C I] is distributed throughout molecular clouds, rather than only near their outer edges, and correlates well with the ^{13}CO (Keene et al., 1985). As with the CO–H$_2$ conversion however, the [CI]–H$_2$ conversion is not well understood at a theoretical level (Gaches et al., 2019).

Comparison of total gas tracers

We compare the total gas mass tracers from the above methods in Fig. 3.4, where we plot the observed quantities $L'_{CO(1-0)}$, $L'_{[CI]}$, M_{dust}, $L_{870,rest}$ and $L_{850,Scoville}$ against one another. In theory, if the three methods of deriving total gas masses are consistent then each pair of methods should be well-described by a linear fit with the normalisation reflecting the ratio of the two corresponding conversion factors, α_{CO}, δ_{gdr} or $\alpha_{[CI]}$. For example the normalisation of a linear fit to the plot of M_{dust} versus $L'_{CO(1-0)}$ yields the ratio δ_{gdr}/α_{CO}. To test these correlations we fit a model $\log_{10}(y) = a \log_{10}(x) + b$, both allowing a to vary freely and fixing

$a = 1$ (meaning the two gas mass tracers scale linearly). Non-detections are plotted as 2.5-σ limits and included in the fits as $1.5\,\sigma \pm 1\,\sigma$, and we confirm that including these limits does not significantly affect the results of the fits.

In Fig. 3.4(a) we see that the CO luminosity and the MAGPHYS dust mass correlate reasonably well with one another, with the free fit having a gradient of 1.2 ± 0.3, consistent with a linear relationship. From the fixed linear fit we derive an average ratio of $\delta_{\mathrm{gdr}}/\alpha_{\mathrm{CO}} = 63 \pm 9$. However, the data display a significant scatter, 0.36 dex, which combines uncertainties contributed by the dust SED fitting, as well as variations in the CO SLED and in α_{CO} or the gas-to-dust ratio. Alternatively, using the rest-frame 870-μm luminosity as a dust mass tracer, we find a gradient of 0.76 ± 0.14, i.e. only consistent with unity within 2-σ, but now with a lower scatter of 0.32 dex and a median $\delta_{\mathrm{gdr}}/\alpha_{\mathrm{CO}} = 59 \pm 6$.

We see that the [C I] and CO luminosity in Fig. 3.4 also roughly correlate, although we are limited by both the small number of [C I] detections in our sample and their low S/N. The free fit has a gradient of 0.8 ± 0.2 and is therefore consistent with unity. The scatter is 0.37 dex, and the linear fit implies that $\alpha_{\mathrm{[CI]}}/\alpha_{\mathrm{CO}} = 4.7 \pm 0.6$.

Finally, in Fig. 3.4(d) we compare the CO(1–0) luminosity with the gas mass estimated following Scoville et al. (2016). The free fit to the data gives a best-fit gradient of 0.94 ± 0.15, consistent with the linear fit as shown by the grey uncertainty region, and the data display 0.32 dex of scatter about the fit, similar to Fig. 3.4(b). In panels (a), (b) and (d) of this figure we see that high-redshift points lie preferentially below the fit which may indicate an increasing gas-to-dust ratio (or a decreasing α_{CO}) with redshift.

To summarise, Fig. 3.4 shows that the CO(1–0) luminosity and cold dust mass, whether determined by SED fitting, restframe 870-μm luminosity or extrapolated observed-frame 870-μm luminosity, are complimentary tracers of the gas mass. Before we can derive reliable gas mass estimates from these tracers, we must calibrate one or more methods. We can, however, compare literature measurements of α_{CO} and δ_{gdr} with our estimated ratios, to assess why combinations of gas and dust calibration factors are consistent with our observations. For example, based on our estimate of the ratio of $\delta_{\mathrm{gdr}}/\alpha_{\mathrm{CO}}$ of 63 ± 9 using the MAGPHYS dust masses, then the commonly-used value of $\delta_{\mathrm{gdr}} = 100$ yields $\alpha_{\mathrm{CO}} \sim 1.6$ in SMGs, broadly consistent with the classical "starburst" value. In contrast, if the appropriate CO–H$_2$ conversion factor for our sample is closer to $\alpha_{\mathrm{CO}} \sim 3.6$, as estimated by Daddi et al. (2015) for "normal" star-forming galaxies, then the corresponding gas-to-dust ratio would be $\delta_{\mathrm{gdr}} \sim 230$, higher than commonly adopted value for SMGs.
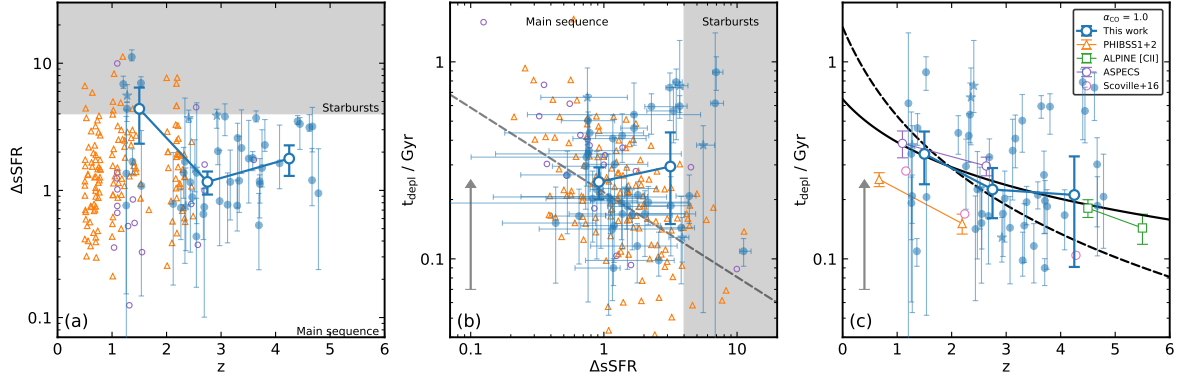
Figure 3.5: **(a)** Offset from the "main sequence", $\Delta\text{sSFR} = \text{sSFR}/\text{sSFR}_{\text{MS}}$, versus redshift for our sample, using the Speagle et al. (2014) prescription for sSFR_{MS}. We indicate the region where $\Delta\text{sSFR} > 4$, i.e. the loose definition of a "starburst" galaxy. The majority of the SMGs lie below this region, with the binned averages (shown by the connected large open symbols in each panel) suggesting that at $z = 2$–5 the majority of our sample comprise apparently "main sequence" systems. **(b)** The variation of gas depletion timescale ($t_{\text{dep}} = M_{\text{gas}}/\text{SFR}$) with ΔsSFR. We see no significant correlation between these two properties, although we caution that the two estimates are coupled as both use SFR. The dashed line shows the $t_{\text{dep}} \propto \Delta\text{sSFR}^{-0.43}$ behaviour predicted by Tacconi et al. (2018) for CO-detected star-forming galaxies, which diverges from the trend for the SMG binned averages. **(c)** Gas depletion timescale, t_{dep}, versus redshift for our SMG sample. We also plot the PHIBSS CO-detected galaxies, a compilation of star-forming galaxies from Scoville et al. (2016), and [Cɪɪ]-detected galaxies from the ALPINE survey (Dessauges-Zavadsky et al., 2020). Our SMGs have a median $t_{\text{dep}} = 210 \pm 40$ Myr and the binned averages show a moderate decline across $z \sim 1$–5. The dashed line shows the prediction of Davé et al. (2012) – $t_{\text{dep}} \propto (1 + z)^{-1.5}$, and the solid line shows our own fit of the form $t_{\text{dep}} \propto (1 + z)^a$ to our binned data, from which we estimate $a = -1.1 \pm 0.3$ at fixed stellar mass and ΔsSFR. In **(b)** and **(c)** we show a vector indicating by how much points would move if we were to adopt $\alpha_{\text{CO}} = 3.6$ instead of $\alpha_{\text{CO}} = 1$.

3.3.5 The star-forming main sequence

As previously highlighted, due to their luminosities and hence relative ease of detection, SMGs are a useful laboratory for investigating the formation and evolution of massive galaxies (as well as for calibrating methods to derive total gas masses discussed above). However, in order to fully understand the evolution of galaxies we must also target sources that are representative of the bulk population of less active galaxies across a wide redshift range – "normal" or so-called "main sequence" galaxies. One approach to categorising galaxies is to classify them according to the difference between their specific star-formation rate $\mathrm{sSFR} = \mathrm{SFR}/M_*$ and the specific star-formation rate expected for a galaxy on the "main sequence", $\mathrm{sSFR_{MS}}$, at the same stellar mass and redshift, according to some prescription. Specifically, this quantity is defined as $\Delta\mathrm{sSFR} = \mathrm{sSFR}/\mathrm{sSFR_{MS}}$, with $\Delta\mathrm{sSFR} > 4$ being the arbitrary definition of a "starburst" galaxy. We caution, however, that recent work (e.g. Puglisi et al., 2019) suggests that there is considerable variation in the properties of galaxies *within* the "main sequence". Specifically, Puglisi et al. (2019) found that $> 29\,\%$ of their sample of *Herschel*-selected main-sequence galaxies displayed compact star-formation sizes. The authors suggest that such compact sources on the main sequence may in fact be early post-starburst galaxies which are observed after the merger-driven boost in SFR has ended, calling into question the dichotomy between steadily growing disks and starbursts. Therefore, the concept of $\Delta\mathrm{sSFR}$, and the main sequence more generally, may be of limited value.

As early CO surveys were limited by sensitivity, the detected sources were typically the most submillimetre-luminous systems and therefore more often starbursts, but in recent years there has been an increased effort to target more "normal" galaxies, aided by the improving sensitivity of ALMA and NOEMA, and to systematically study the evolution of their characteristic properties, such as the gas depletion timescale and gas fraction (Genzel et al., 2015; Walter et al., 2016; Tacconi et al., 2018).

With large ALMA surveys of SMGs (e.g., Miettinen et al., 2017; Dudzevičiūtė et al., 2020) we are now able to establish the stellar content and star-formation rates of large and unbiased samples of reliably-identified SMGs. These studies indicate that although SMGs at $z = 1.5$–3 have typically higher specific star-formation rates than "normal" galaxies, they overlap substantially with the so-called main sequence, while at $z \gtrsim 3$ where SMGs have specific star-formation rates similar to the (increasingly more active) bulk population of galaxies. As we determined in Chapter 2, our sample contains almost exclusively SMGs within the scatter of the main sequence definition at $z \sim 3$–5, at somewhat higher redshifts than the samples used

in previous studies of the gas content of the main sequence.

In Fig. 3.5 we show the distribution of ΔsSFR for our sample (using the prescription of Speagle et al., 2014, see Fig. 2.5). We also plot data from the PHIBSS1 and PHIBSS2 surveys, specifically 148 CO-detected main sequence star-forming galaxies observed with PdBI/NOEMA in two samples at $z \sim 0.5$–2.5 (Genzel et al., 2015; Tacconi et al., 2018), and in addition the sources detected in the ALMA Spectroscopic Survey in the HUDF (ASPECS), a CO blind scan in which 22 galaxies are CO- or [CI]-detected at $z = 1.0$–3.6 (Walter et al., 2016). Finally, we show the data for the [CII]-detected galaxies from the ALPINE survey (Le Fèvre et al., 2019). We highlight again here that all gas masses are scaled to a CO–H_2 conversion factor of $\alpha_{CO} = 1\,M_\odot\,(K\,km\,s^{-1}\,pc^2)^{-1}$ and multiplied by a factor of 1.36 to account for Helium to ensure consistency between the samples, and that means that values may be plotted differently here when compared to their original studies. We show a vector to indicate how the data points would move if the Daddi et al. (2010) value of $\alpha_{CO} = 3.6$ was adopted instead.

Fig. 3.5(a) shows the evolution of ΔsSFR with redshift for our sources. We indicate the arbitrary threshold for starburst galaxies, and see that only four of our 47 (9 per cent) CO-detected ALMA-identified SMGs lie in this regime, with all four in the range $z \sim 1$–1.5. Binning the sample by redshift, we see that the SMGs fall within the broad scatter of the main sequence in the range $z \sim 2$–4, with a handful of galaxies at $z > 4$ on the boundary between main sequence and starbursts. The PHIBSS samples (Tacconi et al., 2018) are complementary to our own in that they are comprised of sources with similar ΔsSFR at typically lower redshifts than we probe.

Gas depletion timescale

The gas depletion timescale is given by

$$t_{dep} = \frac{M_{gas}}{SFR}, \tag{3.3.8}$$

i.e. the inverse of the star-formation efficiency, assuming no replenishment of the gas in the system and no outflows. It has been suggested that t_{dep} is mainly dependent on redshift and offset from the main sequence (Genzel et al., 2015; Tacconi et al., 2018), with the ΔsSFR dependence implying that galaxies in a starburst phase consume their gas more quickly (Hodge & da Cunha, 2020). We flag that t_{dep} and ΔsSFR are both ratios involving SFR, suggesting that the more fundamental factor may be the ratio of the independent terms used in those parameters, M_{gas} and M_*: the gas fraction, $\mu_{gas} = M_{gas}/M_*$ (discussed in §3.3.5).
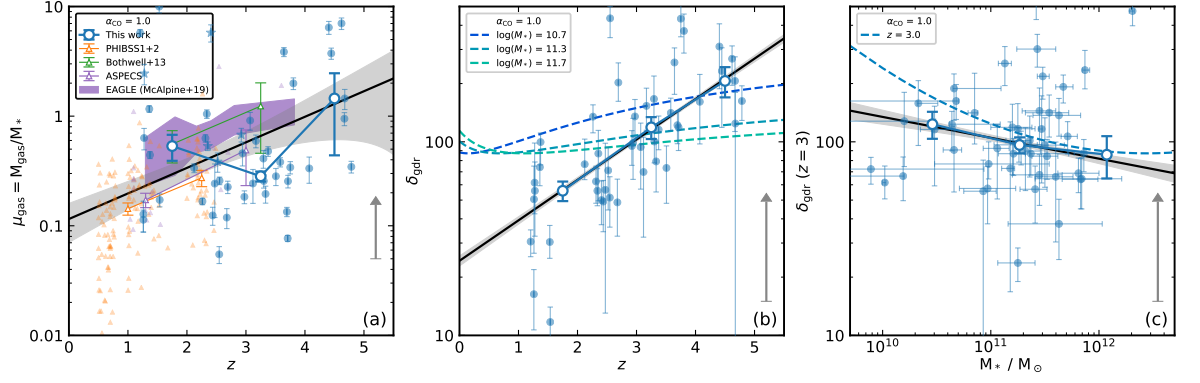
Figure 3.6: **(a)** Gas fraction $\mu_{\mathrm{gas}} = M_{\mathrm{gas}}/M_*$ versus redshift for the SMGs in our sample compared to the SMG survey of Bothwell et al. (2013) and the typically lower-redshift PHIBSS surveys (Tacconi et al., 2018). We show medians of our sample binned by redshift (large points). The data show an increase in gas fraction with redshift that is described by the model $\log_{10}(\mu_{\mathrm{gas}}) = 0.23 \times (z - \langle z \rangle) - 0.41$. **(b)** Evolution of the gas-to-dust ratio, δ_{gdr}, with redshift for our CO-detected sample. Our data are fit with the model $\log_{10}(\delta_{\mathrm{gdr}}) = 0.17 \times (z - \langle z \rangle) + 1.97$ which is consistent with a factor of ~ 4 increase in δ_{gdr} across $z = 2$–5. We overlay tracks of the Tacconi et al. (2018) prediction for the evolution of the gas-to-dust ratio with redshift at the 16th, 50th and 84th percentile stellar masses of our sample, although we note that these are not corrected to $\alpha_{\mathrm{CO}} = 1$. **(c)** Gas-to-dust ratio versus stellar mass, where we have adjusted δ_{gdr} for all sources to a fiducial $z = 3$ according to the redshift evolution measured in **(b)**. We again indicate the Tacconi et al. (2018) prediction for the evolution of the gas-to-dust ratio, but this time we only include the $z = 3$ result and we again note that is not normalised to $\alpha_{\mathrm{CO}} = 1$. Given the significant scatter, we conclude that either no variation in δ_{gdr} with stellar mass, or behaviour similar to that predicted by the model could be consistent with the observations. Our binned data are well-fit by the model $\log_{10}(\delta_{\mathrm{gdr}}) = -0.16 \times \log_{10}(M_*/M_{*,\mathrm{med}}) + 1.92$. In all three panels we show a vector indicating by how much the points move if we were to adopt $\alpha_{\mathrm{CO}} = 3.6$ instead of $\alpha_{\mathrm{CO}} = 1$.

In the main sequence paradigm, determining how the depletion timescale evolves leads to a better understanding of how the molecular gas fractions evolve, and is therefore the starting point for deriving scaling relations. As noted earlier, we caution that there has been shown to be considerable variation in galaxy physical properties on and off the main sequence, which may indicate that the paradigm is less fundamental than presented.

Our sample displays a median $t_{\mathrm{dep}} = 210 \pm 40\,\mathrm{Myr}$. This compares to $t_{\mathrm{dep}} = 292 \pm 10\,\mathrm{Myr}$ estimated from the dust masses, using a fixed gas-to-dust ratio of 100, for the 707 AS2UDS SMGs by Dudzevičiūtė et al. (2020) (after correcting for their adoption of a 50 per cent efficiency conversion factor when estimating the depletion timescale). The modest difference between these two estimates reflects the $\sim 1.5 \times$ higher dust (and hence gas) masses for the SMGs in our sample compared to those in AS2UDS, $M_{\mathrm{dust}} = (10.5 \pm 0.8) \times 10^8\,\mathrm{M_\odot}$ versus $(6.8 \pm 0.3) \times 10^8\,\mathrm{M_\odot}$, but a larger ($\sim 1.7 \times$) difference in star-formation rate, $\mathrm{SFR} = 400 \pm 50\,\mathrm{M_\odot\,yr^{-1}}$ versus $\mathrm{SFR} = 235 \pm 8\,\mathrm{M_\odot\,yr^{-1}}$.

In Fig. 3.5 we show the dependence of t_{dep} on both ΔsSFR (b) and redshift (c) separately. We find no discernible evolution of the depletion timescale with ΔsSFR in the sample as a whole, and in fact the high-sSFR "starbursts" in our sample have relatively long timescales. As they are lower-redshift sources this likely reflects the evolution of the gas depletion timescale with redshift, which we also investigate in Fig. 3.5(c). The depletion timescale decreases with redshift in the range $z \sim 1$–5, however our data are consistent with no evolution across $z \sim 2.5$–5. We fit the form $t_{\mathrm{dep}} \propto (1 + z)^a$ to our data alone, finding $a = -1.1 \pm 0.3$, a much shallower dependence than the $a = -1.5$ proposed by (Davé et al., 2012). Additionally, when compared to the PHIBSS (Tacconi et al., 2018) and ASPECS (Walter et al., 2016) samples we see that our sources exhibit longer depletion timescales, although the SMGs appear to be consistent with the [Cii]-detected ALPINE galaxies (Le Fèvre et al., 2019). The scatter in our data is likely to be driven in part by variations in the SLEDs of individual sources (see Fig. 3.2(a)), by the broad range in ΔsSFR spanned by our sample and by the fact that rapidly evolving systems may naturally exhibit a wider range in t_{dep}.

Tacconi et al. (2018) suggest that the variation of the depletion time can be separated into the product of redshift, stellar mass and specific star-formation rate, providing an *Ansatz* of the form:

$$\log(t_{\mathrm{dep}}) = A + B \log(1 + z) + C \log(\Delta\text{sSFR}) + D \log(\Delta M_*), \qquad (3.3.9)$$

where ΔM_* is defined as $M_* / 5 \times 10^{10}\,\mathrm{M_\odot}$ ($5 \times 10^{10}\,\mathrm{M_\odot}$ is chosen as a fiducial stellar mass), and the coefficients A, B, C and D are fitted for. Tacconi et al. (2018) also include an optical half-light radius term, but given that they find this term to be of negligible importance, and optical sizes are not useful measures of the physical sizes of high-redshift dust-obscured galaxies (e.g., Gullberg et al., 2019), we choose to ignore this term.

Given the modest size of our small sample, we choose not to determine a free fit to all four parameters, instead we focus on comparing the redshift behaviour and so opt to fix C and D to the values found by Tacconi et al. (2018): specifically $C = -0.43$ and $D = 0.17$. From fitting this model to our dataset, we determine coefficients of $A = 0.05 \pm 0.06$ and $B = -1.12 \pm 0.10$. Hence in our sample, the gas depletion timescale decreases almost exponentially with redshift. In comparison, Tacconi et al. (2018) find values for their sample of $A = 0.06 \pm 0.03$ and $B = -0.44 \pm 0.13$, thus we see a sharper decrease in the depletion timescale with redshift for our SMGs than their sample, which consists mainly of main-sequence star-forming galaxies. In Fig. 3.5(b) we also show the $t_{\mathrm{dep}} \propto \Delta\text{sSFR}^{-0.43}$ behaviour described above (Tacconi et al., 2018). This does not appear to be supported by our SMGs, which are consistent with

no evolution, however given the uncertainties on the binned data we cannot rule out the $t_{\mathrm{dep}} \propto \Delta\mathrm{sSFR}^{-0.43}$ behaviour.

Gas fraction

In addition to the gas depletion timescale, we can derive the gas fraction

$$\mu_{\mathrm{gas}} = \frac{M_{\mathrm{gas}}}{M_*} \tag{3.3.10}$$

for our sources using our CO-based mass estimates and stellar masses from MAGPHYS. The gas fraction is also expected to be a key property in galaxy evolution, following from the gas depletion timescale, describing the fraction of baryons available for star formation (Tacconi et al., 2018). Fig. 3.6(a) shows the evolution of μ_{gas} with redshift, where we have included all of our CO-detected sources in addition to PHIBSS sources. The gas fraction increases with redshift (e.g Daddi et al., 2010; Genzel et al., 2010; Geach et al., 2011; Tacconi et al., 2018; Liu et al., 2019b), but as with Fig. 3.5 we see a large amount of scatter, and by separately examining the gas and stellar masses in our sample we conclude that the trend we see in μ_{gas} with redshift is driven mainly by sources at higher redshift having more massive gas reservoirs. An additional explanation for the scatter could then be that these galaxies are consuming gas on short timescales leading to wider variations in the gas fraction within the observed population.

We fit a model $\log_{10}(\mu_{\mathrm{gas}}) = a \times (z - \langle z \rangle) + b$ to our binned data, along with the sources from Bothwell et al. (2013) and binned data from PHIBSS to anchor the low-redshift end. This results in best-fit parameters of $a = 0.23 \pm 0.08$ and $b = -0.41 \pm 0.08$, and we plot this fit in Fig. 3.6(a), although we note that there is considerable scatter at all redshifts. Nevertheless, for the combined dataset we conclude that there is a gradual increase in gas fraction with a median of $\mu_{\mathrm{gas}} \sim 0.4$ at $z \sim 2.5$. This trend is similar to that seen for the model SMGs in the EAGLE simulation (McAlpine et al., 2019) which we show in Fig. 3.6(a), although we note that the individual gas phases are not resolved in EAGLE, and therefore the gas fractions reflect contributions from both the atomic and molecular gas phases.. These galaxies are consistent with our $z \sim 1.5$–2 sources, and if the observed trend were to continue we would also expect them to be consistent with our $z \sim 4$ sources. However, in the $z \sim 2.5$–4 range our sources appear to be below the trend, but this is related to our usage of the Eyelash SLED for converting to CO(1–0). In this region many of the sources are detected in CO(4–3), and the $J_{\mathrm{up}} = 4$ line ratio measured from the Eyelash ($r_{41} = 0.50 \pm 0.04$) is higher than that measured
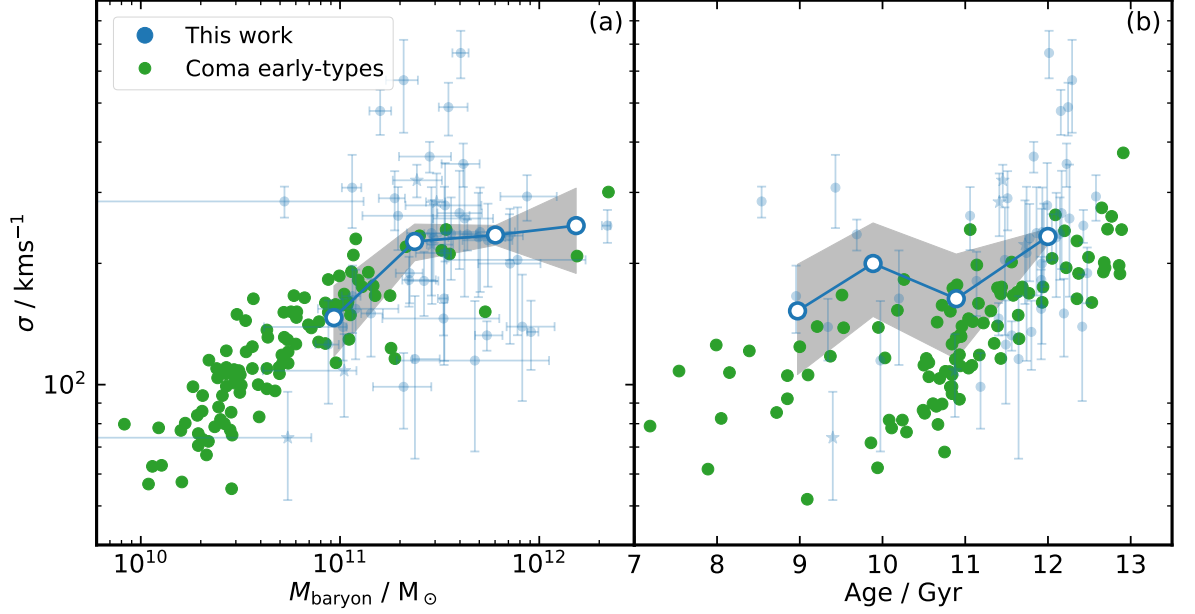
Figure 3.7: **(a)** The Baryonic mass–σ relation for CO-detected SMGs in our sample compared to early-type galaxies in the Coma cluster from Shetty et al. (2020). The open points and grey region represent the median of our sample in M_* bins and its bootstrapped uncertainty, respectively. The SMGs are consistent with the trend shown in the Coma early-type population, providing further circumstantial evidence that the SMGs could represent progenitors of such systems. We interpret the scatter in our data as primarily due to the effect of random inclination angles on the measured CO line widths, which we are unable to correct for on a case-by-case basis. **(b)** The variation in estimated stellar age as a function of velocity dispersion of the early-type galaxies in Coma from Shetty et al. (2020), compared to the estimated formation ages of the SMGs in our sample, derived from the lookback time to their observed redshift and the estimate of their expected age from the MAGPHYS SED fitting. We see that the trend in the SMGs roughly delineates the high-mass boundary as a function of age estimated for the early-type galaxies.

from our composite SLED ($r_{41} = 0.34 \pm 0.04$; also see Table 3.1 and Fig. 3.2), suggesting that we underestimate the gas fraction in Fig. 3.6(a).

Gas-to-dust ratio

The relationship between the molecular gas in a galaxy and its dust content is encoded in the gas-to-dust ratio, δ_{gdr}. As discussed in §3.3.4, it is expected that the gas-to-dust ratio depends on metallicity, with more massive (and therefore potentially more metal-rich) galaxies containing proportionally more dust and thus having a lower δ_{gdr} (Li et al., 2019). Here we wish to investigate any potential variation of δ_{gdr} in our sample with redshift and stellar mass. In Fig. 3.6 we show the gas-to-dust ratio of our sources adopting $\alpha_{CO} = 1\,M_\odot$ $(K\,km\,s^{-1}\,pc^2)^{-1}$ and using dust masses estimated from MAGPHYS SED fitting. The SMGs

display an increase in the gas-to-dust ratio by a factor ~ 4 across the redshift range $z \sim 1$–5. Our binned data are fit with a model of the form $\log_{10}(\delta_{\mathrm{gdr}}) = a \times (z - \langle z \rangle) + b$ from which we obtain the best-fit parameters $a = 0.17 \pm 0.02$ and $b = 1.97 \pm 0.03$. For comparison, we overlay in Fig. 3.6(b) the model for the evolution of the gas-to-dust ratio with redshift proposed by Tacconi et al. (2018), for the 16th, 50th and 84th percentile stellar masses of our sample. This model assumes that δ_{gdr} is approximately linearly correlated with metallicity, and uses the mass-metallicity relation from Genzel et al. (2015), for this reason it is hard to simply rescale the model to match our adopted $\alpha_{\mathrm{CO}} = 1$ and so we can only make a qualitative comparison. The trend expected for the median mass is much flatter than the evolution we see.

Finally, we turn to the variation of the gas-to-dust ratio with stellar mass in Fig. 3.6(c). Here we use the fit from Fig. 3.6(b) to adjust all sources to a fiducial redshift of $z = 3$. We see that the gas-to-dust ratios for SMGs decrease slightly with stellar mass, although there is considerable scatter in the population. Moreover, we note that we have adopted a fixed α_{CO} value for our sample, and that if we instead used a CO–H_2 conversion factor that decreases with higher metallicity (and thus stellar mass), this would strengthen the trend in the δ_{gdr} we see. We also overlay in Fig. 3.6(c) the Tacconi et al. (2018) δ_{gdr} model corresponding to the fiducial redshift, $z = 3$. In this case we see that the behaviour expected in the model is broadly consistent with our observations, given the large dispersion in δ_{gdr} we observe. However, we note that the model adopted by Tacconi et al. (2018) is determined assuming a CO-H_2 conversion factor of 4.36, and the model normalisation would be lower if it was corrected to our $\alpha_{\mathrm{CO}} = 1$.

3.3.6 Implications for galaxy evolution

It has been suggested since their discovery that submillimetre galaxies are connected to the progenitors of massive and compact early-type galaxies in the local Universe (e.g. Lilly et al., 1999; Simpson et al., 2014; Toft et al., 2014), potentially following an evolutionary pathway through a QSO phase (Blain et al., 2002; Swinbank et al., 2006; Hopkins et al., 2008). Simpson et al. (2014) showed that SMGs would evolve to have $z \sim 0$ stellar masses comparable to massive early-types (see also Dudzevičiūtė et al. 2020), while Hodge et al. (2016) demonstrated that the implied effective radii and gas surface densities of SMGs are consistent with those of the most compact massive early-type galaxies.

We can now apply an additional test of this hypothesis using the kinematic information from our CO survey in the context of the M_{baryon}–σ and σ–Age relations for local early-

type galaxies. We plot these in Fig. 3.7, where we compare the properties of the SMGs to early-type galaxies in the Coma cluster from Shetty et al. (2020). For this comparison the baryonic masses of the SMGs comprises the sum of their stellar and gas masses, while for the (generally gas-poor) local early-types we only consider their stellar masses. For the ages of the SMGs we convert their redshifts into a lookback time and add to this the estimated ages of the systems from the MAGPHYS SED fits to determine a crude "formation" age, to compare to the locally derived stellar ages from Shetty et al. (2020). We adopt σ derived from the CO line width as our measure of the expected velocity dispersion of the descendent galaxies and, because we lack individual inclination estimates for the galaxies, we have to average over the population to remove the sensitivity to inclination. We therefore plot the binned median velocity dispersions as a function of stellar mass or age for the SMGs and a bootstrap estimate of the uncertainty on this in Fig. 3.7. We note here that we are making the simplistic assumption that the SMGs lose no kinetic energy during their evolution to $z = 0$. If they are to undergo gas-rich mergers they would in fact lose energy due to friction which would result in lower velocity dispersions at $z = 0$ than those plotted in Fig. 3.7.

We see that the trend in M_{baryon}–σ for the SMGs is a good match for the distribution of the most massive early-type galaxies from Shetty et al. (2020), not only in normalisation but also showing hints of flattening in σ seen at the highest masses which arises from the so-called Zone of Exclusion (Bender et al., 1992; Shetty et al., 2020). As Shetty et al. (2020) highlight the inflection point at masses of $\sim 2 \times 10^{11}\,\mathrm{M}_\odot$ corresponds to the point separating low-mass, fast-rotator early-type galaxies with discs, from the more massive, round slow-rotators. Our SMG population at $z \sim 3$ straddle this transition, with an 870-μm flux of $S_{870} \sim 5\,\mathrm{mJy}$ roughly corresponding to the boundary. This flux also roughly marks the break in the number counts of SMGs (e.g., Stach et al., 2018) suggesting that the physical origin of this difference in the properties of early-type galaxies in the local Universe may be reflected in the properties and evolution of SMGs above and below this flux. SMGs with $S_{870} \gtrsim 5\,\mathrm{mJy}$ typically lie at higher redshifts (Fig. 3.1), have higher gas masses and gas fractions, and shorter depletion timescales (Fig. 3.4 and 3.6), which may also link to the structural differences of the two descendant populations.

In terms of the σ–Age plot in Fig. 3.7, we see that our rough estimates of the formation ages of the SMGs tend to follow the boundary of the distribution derived for the Coma sample (although we caution that there are potentially systematic uncertainties in such a comparison). This is a result of our sample being dominated by the most massive systems as a result of our selection on dust mass. We therefore pick out the most massive galaxies formed

at any epoch and so our median line tracks the upper boundary of the Coma population in this plot.

We also note that as our CO survey is predominantly limited to the most massive gas-rich galaxies, a more sensitive survey for less luminous SMGs would likely extend to lower baryonic masses and so lower velocity dispersions, expanding the overlap with the parameter space populated by the Coma early-type galaxies in both mass and possibly age. Nevertheless, we conclude that our CO observations indicate that the most massive SMGs are dynamically consistent with them being the progenitors of most massive compact early-type galaxies in the local Universe. We stress that this does not preclude further, dry, merging of these systems as that is expected to predominantly influence the sizes of the galaxies, while leaving σ relatively unaffected (e.g. Naab et al., 2009). We will return to this analysis with spatially resolved kinematics of SMGs in Chapter 5.

3.4 Conclusions

We have undertaken a spectroscopic survey of 61 ALMA-located SMGs in the 3-mm band ($\nu \sim 82$–$114\,\mathrm{GHz}$) using ALMA and NOEMA to search for emission lines from the rotational transitions of molecular CO gas. Our sample roughly divides in two: with 31 submillimetre bright, but typically optically faint/K-faint, SMGs lacking existing spectroscopic redshifts, and a complementary sample of 30 typically submillimetre-fainter SMGs that have optical/UV spectroscopic redshifts. For our survey we obtained complete spectral scans of the 3-mm window for the former sample, but more targeted spectral coverage of the latter. Our strategy of combining these two sample selections has allowed us to efficiently probe a wide parameter space to identify trends in the properties of the SMG population. Our main findings are as follows:

- CO line emission is detected in 45 of the targets, 26 of which come from blind spectral scans and 19 of which come from the targeted observations of sources with optical/UV spectroscopic redshifts, with a further five serendipitous CO detections: two in nearby ALMA-detected SMGs and three in apparently unrelated galaxies. This provides a large sample of high-S/N CO detections in massive dust-selected, high-redshift galaxies for our analysis. The non-detection of CO emission in the remaining SMGs arises from two factors: for those SMGs with existing spectroscopic redshifts we suggest that the CO line emission is missed due to inaccuracies in those redshifts, whereas we suggest

non-detections of CO emission in the spectral scans are due to these sources being predominantly CO faint due to their low gas masses.

- 38 ± 9 per cent of our CO lines are better fit by double-Gaussian profiles, compared to single Gaussians. By simulating the line profiles from spatially unresolved observations of rotating discs we show this to be consistent with the expectations for a population of randomly oriented discs. This is strong circumstantial evidence that the CO kinematics of most SMGs are dominated by the motion of gas in a rotating disc, although we stress that such discs can form rapidly during dynamical interactions and mergers.

- The median redshift of our sample is $z = 2.9 \pm 0.2$. We compare the variation in redshift of our sources with their 870-μm flux, finding that brighter sources are typically found at higher redshifts, confirming previous claims of a correlation between 870-μm flux density and redshift in this population. We measure a gradient for this trend of $0.07 \pm 0.01 \, \mathrm{mJy}^{-1}$, in agreement with Stach et al. (2019) and Simpson et al. (2020). This represents potential evidence for galaxy downsizing, the phenomenon where more massive galaxies, with higher gas fractions, form earlier.

- We study the average ISM excitation properties of SMGs by constructing a composite CO spectral line energy distribution from our own data and archival observations, finding that excitation increases with J_{up} up to $J_{\mathrm{up}} = 6$. We derive line ratios for this composite SLED that are consistent with that of SMM J2135$-$0102 (the "Cosmic Eyelash") measured in Danielson et al. (2011). Using these line ratios to convert from $L'_{\mathrm{CO,J}}$ to $L'_{\mathrm{CO(1-0)}}$ we find that, as expected, our sources lie at the bright end of the L'_{CO}–L_{IR} relation, with median $L'_{\mathrm{CO(1-0)}} = (6.7 \pm 0.5) \times 10^{10} \, \mathrm{K \, km \, s^{-1} \, pc^2}$ and $L_{\mathrm{IR}} = (4.6 \pm 0.8) \times 10^{12} \, \mathrm{L_\odot}$.

- Adopting a CO–H_2 conversion factor of $\alpha_{\mathrm{CO}} = 1$, our estimated median CO(1–0) line luminosity corresponds to a median gas mass of $M_{\mathrm{gas}} = (9.1 \pm 0.7) \times 10^{10} \, \mathrm{M_\odot}$ for our SMG sample. We also find a correlation between the CO line luminosity and the line width with a power law index of 2, consistent with that expected for disc-dominated kinematics.

- We compare the inferred CO(1–0) luminosities of our SMGs with two independent tracers of their molecular gas masses: their dust masses and [CI] luminosities (where available), finding all three to correlate well. Given the difficulty in detecting [CI] emission with high significance, we suggest that the CO luminosity and dust mass, as

estimated from the *rest-frame* 870-μm continuum measured in the 3-mm band, are the best correlated measures and hence the preferable choices for estimating H_2 masses. We use our data to estimate the average ratio between the gas-to-dust ratio and CO–H_2 conversion factor finding $\delta_{gdr}/\alpha_{CO} = 59 \pm 6$ where the rest-frame 870-μm luminosities are used to estimate the dust mass, and $\delta_{gdr}/\alpha_{CO} = 63 \pm 9$ where the dust masses from MAGPHYS are used. However, to make reliable use of the dust mass method to estimate the gas mass also requires tighter constraints on α_{CO}.

- We find that the bulk of the SMGs in our survey have estimated specific star-formation rates which place them within the scatter of the main sequence at their respective redshifts, with the exception of a few lower-redshift starbursts. We study the properties of our sources in the context of scaling relations of the gas depletion timescale and gas fraction, proposed for the main-sequence population. We estimate the median gas depletion time scale of our sample is $t_{dep} = 210 \pm 40\,$Myr, and find no significant evidence for any evolution in depletion time with offset from the main sequence, as found by Tacconi et al. (2018), but a sharper decrease with redshift than that work.

- We use the CO line kinematics along with the estimated stellar and gas masses for our sample to demonstrate that the distribution of SMGs in the M_{baryon}–σ plane is similar to that of the most massive early-type galaxies in the local Universe, both in normalisation and shape. Our selection of galaxies with the highest dust masses also suggests that the expected age distribution of their descendants at $z \sim 0$ matches the high-mass boundary of the distribution of Coma galaxies on the σ–Age plane. These two results provide further circumstantial evidence of a link between SMGs and the progenitors of massive early-type galaxies. Moreover, the median trend in the SMGs spans the characteristic mass where the properties of local early-type galaxies transition from fast-rotating at lower masses to slow-rotating at higher masses. In the SMG population this mass corresponds roughly to an 870-μm flux of $\sim 5\,$mJy suggesting that the origin of this difference in the properties of ellipticals may be reflected in the properties and evolution of SMGs above and below this flux (which also marks a break in the SMG counts, Stach et al. 2018).

Source ID	$J_{\rm up}$	Frequency [GHz]	$I_{\rm CO}$ [Jy kms^{-1}]	$z_{\rm CO}$	FWHM$_{\rm CO}$ [kms^{-1}]	$S_{\rm 3mm}$ [μJy]	$L'_{{\rm CO},J_{\rm up}}$ [10^{10} K kms^{-1} pc^{-2}]	S/N	Q
AS2COS0006.1†	5	102.55	2.4 ± 0.3	4.620	1150 ± 170	300 ± 30	7.9 ± 0.9	8.7	…
AS2COS0008.1†	4	100.65	2.1 ± 0.2	3.581	550 ± 70	340 ± 30	7.2 ± 0.7	11.2	…
AS2COS0011.1	5	99.60	1.7 ± 0.2	4.786	690 ± 90	425 ± 13	5.7 ± 0.7	9.0	…
AS2COS0014.1	3	88.19	1.4 ± 0.2	2.921	670 ± 120	180 ± 40	6.2 ± 0.9	8.1	…
AS2COS0031.1†	4	99.29	1.84 ± 0.17	3.643	430 ± 60	260 ± 40	6.5 ± 0.6	12.0	…
AS2UDS009.0†	3	87.73	1.2 ± 0.3	2.942	$nan\pm200$	80 ± 20	5 ± 1	5.8	…
AS2UDS010.0	3	82.95	2.1 ± 0.3	3.169	540 ± 120	140 ± 40	10 ± 1	8.9	…
AS2UDS011.0	4	90.88	0.9 ± 0.2	4.073	600 ± 200	120 ± 20	4 ± 1	4.0	…
AS2UDS012.0	3	98.23	1.2 ± 0.2	2.520	520 ± 150	50 ± 20	4.0 ± 0.8	6.0	…
AS2UDS014.0	4	95.96	2.6 ± 0.3	3.804	1600 ± 200	190 ± 20	10 ± 1	8.2	…
AS2UDS026.0	4	107.33	1.4 ± 0.3	3.296	630 ± 170	110 ± 30	4.3 ± 0.8	6.0	…
AS2UDS029.0†	2	91.12	2.1 ± 0.3	1.530	720 ± 150	180 ± 30	6.5 ± 0.8	9.4	…
AS2UDS072.0	3	101.52	1.4 ± 0.3	2.406	250 ± 60	80 ± 40	4.5 ± 0.8	6.1	…
AS2UDS112.0	2	101.98	1.4 ± 0.3	1.260	270 ± 110	43 ± 11	3.0 ± 0.7	5.8	…
AS2UDS126.0	3	100.63	1.4 ± 0.3	2.436	480 ± 170	170 ± 40	4.3 ± 0.8	6.4	…
AS2UDS231.0	4	111.95	1.3 ± 0.4	3.119	550 ± 160	46 ± 20	4 ± 1	2.9	…
AS2UDS345.0	2	101.91	1.1 ± 0.3	1.262	380 ± 120	60 ± 20	2.3 ± 0.7	4.1	…
AS2UDS492.0	2	101.21	1.1 ± 0.2	1.278	170 ± 50	46 ± 6	2.4 ± 0.5	5.6	…
AS2UDS562.0	3	99.60	0.6 ± 0.3	2.472	680 ± 110	70 ± 40	1.8 ± 0.9	0.1	…
AS2UDS627.0	2	101.39	1.3 ± 0.3	1.274	390 ± 70	40 ± 17	2.8 ± 0.6	4.5	…

Table 3.3: Line properties for CO-detected SMGs. The frequency given here is the frequency measured from a Gaussian fit to each source. The quoted values of the velocity-integrated line intensity $I_{\rm CO}$, the redshift $z_{\rm CO}$ and the linewidth FWHM$_{\rm CO}$ are calculated from the zeroth, first and second moments of the line as described in §2.5.3. 3 mm continuum flux densities $S_{\rm 3mm}$ are measured from the line fit. We also quote the CO line luminosity $L'_{\rm CO}$, measured for the detected transition, which is indicated by the $J_{\rm up}$ column. Q is the spectroscopic redshift quality flag from Danielson et al. (2017). † Source displays a double-peaked line profile.

Source ID	$J_{\rm up}$	Frequency [GHz]	$I_{\rm CO}$ [Jy kms^{-1}]	$z_{\rm CO}$	FWHM$_{\rm CO}$ [kms^{-1}]	$S_{\rm 3\,mm}$ [μJy]	$L'_{{\rm CO},J_{\rm up}}$ [10^{10} K kms^{-1} pc^{-2}]	S/N	Q
ALESS001.1†	5	101.55	1.0 ± 0.2	4.674	1300 ± 300	170 ± 5	3.2 ± 0.7	5.1	3
ALESS001.2	5	101.66	0.84 ± 0.11	4.669	440 ± 70	98 ± 16	2.8 ± 0.4	8.0	3
ALESS003.1†	4	105.39	1.08 ± 0.11	3.375	870 ± 80	134 ± 4	3.3 ± 0.3	10.1	3
ALESS005.1†	4	107.15	0.74 ± 0.10	3.303	540 ± 120	79 ± 12	2.2 ± 0.3	8.2	...
ALESS006.1†	3	103.63	1.69 ± 0.15	2.337	620 ± 110	300 ± 50	5.0 ± 0.4	13.5	1
ALESS007.1	3	93.66	2.2 ± 0.3	2.692	320 ± 60	180 ± 40	8 ± 1	8.8	1
ALESS009.1	4	98.22	0.99 ± 0.10	3.694	330 ± 110	155 ± 8	3.6 ± 0.3	13.5	...
ALESS017.1	2	90.82	0.61 ± 0.08	1.538	230 ± 50	70 ± 20	1.9 ± 0.3	8.5	1
ALESS019.1	4	97.04	0.92 ± 0.12	3.751	560 ± 130	37 ± 7	3.4 ± 0.4	8.8	...
ALESS022.1†	3	105.99	1.40 ± 0.10	2.263	310 ± 30	55 ± 6	3.9 ± 0.3	16.4	...
ALESS023.1†	4	106.42	0.67 ± 0.12	3.332	650 ± 180	113 ± 5	2.0 ± 0.4	6.6	...
ALESS031.1†	4	97.83	0.86 ± 0.11	3.712	830 ± 100	133 ± 9	3.1 ± 0.4	8.3	...
ALESS034.1	3	84.95	0.44 ± 0.08	3.071	300 ± 80	34 ± 12	2.1 ± 0.4	6.0	2
ALESS035.1	3	87.03	0.88 ± 0.12	2.974	560 ± 160	79 ± 12	3.9 ± 0.5	9.7	4
ALESS041.1†	3	97.48	0.54 ± 0.09	2.547	470 ± 170	64 ± 8	1.9 ± 0.3	7.2	2
ALESS061.1	4	85.30	1.07 ± 0.14	4.405	1120 ± 140	90 ± 30	5.1 ± 0.7	7.6	...
ALESS062.2†	2	97.61	1.39 ± 0.09	1.362	330 ± 60	70 ± 30	3.4 ± 0.2	18.6	1
ALESS065.1	4	84.67	0.86 ± 0.10	4.445	350 ± 80	120 ± 20	4.1 ± 0.5	10.2	...
ALESS066.1	3	97.34	0.98 ± 0.08	2.553	340 ± 30	18 ± 5	3.4 ± 0.3	14.0	1
ALESS067.1†	3	110.78	1.20 ± 0.11	2.122	270 ± 120	31 ± 14	3.0 ± 0.3	13.8	1
ALESS068.1	4	102.28	0.29 ± 0.05	3.507	360 ± 90	66 ± 10	0.97 ± 0.17	5.7	...
ALESS071.1†	4	97.94	1.59 ± 0.10	3.707	580 ± 50	24 ± 11	5.8 ± 0.4	17.4	2
ALESS079.1	4	94.08	0.42 ± 0.09	3.901	560 ± 170	50 ± 10	1.7 ± 0.3	5.1	...
ALESS088.1	2	104.48	1.42 ± 0.10	1.206	670 ± 60	29 ± 13	2.8 ± 0.2	15.4	1
ALESS098.1†	2	97.11	3.3 ± 0.2	1.374	550 ± 50	240 ± 60	8.2 ± 0.6	15.0	1
ALESS101.1	3	103.13	2.0 ± 0.2	2.353	760 ± 70	140 ± 30	4.2 ± 0.4	15.6	2
ALESS112.1†	3	104.36	1.75 ± 0.14	2.314	430 ± 80	90 ± 20	5.1 ± 0.4	15.9	1

Table 3.4: Table 3.3 continued.

A near-infrared spectroscopic survey of dust-obscured star-forming galaxies at $z \sim 2$

Preamble

In this chapter we introduce our ongoing VLT/KMOS Large Programme, KAOSS, which has been designed to perform a blind emission line redshift survey of the high-redshift submillimetre galaxy (SMG) population, and to study the spatially resolved kinematics of sources with bright extended emission lines. We provide a description of the target selection, observing strategy and data reduction, before presenting integrated Hα and [OIII]$\lambda5007$ line properties. These properties are then combined with a multi-wavelength SED analysis to study the AGN prevalence in the spectroscopically detected population, the mass-metallicity relation and BPT diagram for our sample, and also to compare the Hα, optical/NIR and dust sizes where available. The spatially resolved properties of bright line sources from KAOSS are presented in Chapter 5.

4.1 Introduction

The global star-formation rate density (SFRD) has been shown to increase with redshift out to $z \sim 2$, so-called "cosmic noon", where many of the stars in massive galaxies in the local Universe were formed (e.g. Madau & Dickinson, 2014; Förster Schreiber & Wuyts, 2020). At this epoch there is a significant contribution from dust-obscured star-forming galaxies (DSFGs; Barger et al., 2000; Swinbank et al., 2014), many of which are sub-millimetre galaxies (SMGs; Smail et al., 1997) which have typical star-formation rates (SFRs) of 100–1000 $M_\odot yr^{-1}$ (e.g. Magnelli et al., 2013; Dudzevičiūtė et al., 2020, also see Chapters 2 and 3). Such rapid star formation in large numbers of massive galaxies at these early times requires large reservoirs of cold gas to be supplied on short dynamical timescales, and as a result this population provides an important test of galaxy formation models (e.g. Lagos et al., 2020; Hayward et al., 2021; Lovell et al., 2021b).

Rest-frame optical emission lines, most prominently Hα and [OIII], are a powerful tool for studying the SMG population (e.g. Swinbank et al., 2004). Galaxies at $z \sim 1$–2 display redshifted Hα emission in the H and K bands which are covered by near-infrared (NIR) integral field spectrographs (IFSs) such as KMOS, OSIRIS and SINFONI, and for more distant sources the [OIII]$\lambda 5007$ emission line is covered up to $z \sim 3.5$. As discussed in previous chapters, the proportion of SMGs with spectroscopic redshifts in the literature is low, and if we are to further our understanding of the properties of these systems, their contribution to the star-formation rate density (Chapman et al., 2005) and how they fit into the broader picture of galaxy evolution, this proportion must be significantly increased.

The Hα emission line is also a useful tracer of the star-formation rate in galaxies as it directly probes the ionisation arising predominantly from young OB stars (e.g. Kewley et al., 2002; Erb et al., 2006; Kennicutt & Evans, 2012). The intensity of the Hα emission line is affected by dust attenuation however, which can lead to underestimates of the SFR in galaxies which are heavily dust-enshrouded, such as SMGs (e.g. Dopita et al., 2002; Swinbank et al., 2004; Hogan et al., 2021). Comparing Hα- and infrared-derived SFRs thus allows us to investigate the level of dust attenuation in the population (e.g. Swinbank et al., 2004; Hogan et al., 2021) and compare it to that of local galaxies and less active star-forming galaxies. Additionally, instruments such as SINFONI and KMOS allow us to spatially resolve the Hα emission in galaxies that are both bright enough and have extended emission, in which case we can begin to address questions about their kinematics.

A number of rest-frame optical spectroscopic studies of more typical "main-sequence" star-forming galaxies at $z \sim 1$–2 have been undertaken with instruments such as SINFONI, KMOS and the Multi-Object Spectrometer for Infra-Red Exploration (MOSFIRE; McLean et al., 2008). Examples of such surveys include the Spectroscopic Imaging survey in the near-infrared with SINFONI (SINS/zC-SINF; Förster Schreiber et al., 2009; Mancini et al., 2011), the MOSFIRE Deep Evolution Field (MOSFIRE; Sanders et al., 2015), the KMOS Redshift One Spectroscopic Survey (KROSS; Stott et al., 2016); the KMOS^{3D} survey (Wisnioski et al., 2015) and the KMOS Galaxy Evolution Survey (KGES; Tiley et al., 2021). These surveys have covered hundreds of galaxies spanning a wide range in stellar mass, and generally show that the majority of galaxies at the high-mass end appear to be rotationally supported, with baryon fractions that are high, and increasing with redshift (e.g. Wuyts et al., 2016b; Genzel et al., 2017; Tiley et al., 2021). However, the number of SMGs currently covered by NIR IFU surveys is low (but see e.g. Swinbank et al., 2004; Alaghband-Zadeh et al., 2012). Whether or not the above conclusions apply to the SMG population thus remains unclear.

We are therefore attempting to significantly increase the NIR IFU coverage of the SMG population by taking advantage of the multiplex capabilities of KMOS on the VLT (Sharples et al., 2013), which allows for 24 integral fields units (IFUs) to observe targets simultaneously. As previously discussed there are over 1000 ALMA-identified SMGs in the COSMOS, UDS and ECDFS fields, and this makes KMOS is an efficient facility for carrying out large scale surveys of SMGs to obtain spectroscopic redshifts, through the Hα and [O III] emission lines, and potentially resolved kinematics of a subset.

This chapter presents our ongoing KMOS/VLT Large Programme "KMOS+ALMA Observations of Submillimetre Sources", KAOSS (Programme ID: 1103.A-0182). KAOSS will ultimately observe ~ 400 SMGs in the COSMOS, UDS and ECDFS fields, and boost the number of SMGs with secure redshifts, while simultaneously studying the spatially resolved kinematics of the brightest and most extended sources. The outline of this chapter is as follows: in §4.2 we describe the sample selection and observations carried out, before discussing our data reduction and analysis methods. In §4.3 we present the analysis of our results and their implications. In §4.4 we conclude with our findings and discuss future work. We then present the spatially resolved Hα and [O III] kinematics of a subset of KAOSS sources in Chapter 5. Throughout this chapter we adopt a flat Λ-CDM cosmology defined by $(\Omega_{\mathrm{m}}, \Omega_{\Lambda}, \mathrm{H_0}) = (0.3, 0.7, 70\,\mathrm{km\,s^{-1}\,Mpc^{-1}})$.

	COSMOS	UDS	ECDFS	Total
Targets	73	260	74	407
Fully/partially observed	55/55	115/94	74/74	244/223
Redshifts	10	18	15	43
Resolved maps	7	15	14	36

Table 4.1: Summary of the number of the sources targeted in the three survey fields covered by the KAOSS LP, along with how much sources have been partially and fully observed, how many have yielded spectroscopic redshifts and how many have yielded resolved maps. We note here that of the 74 sources in the ECDFS field, 62 are taken from the SUPER GOODS survey which is focused on the smaller GOODS-S region of ECDFS. Of the 12 sources outside this region, none were detected by KMOS, therefore all of the detected sources in ECDFS reside in the GOODS-S survey field.

4.2 Observations and data

4.2.1 Sample

The ongoing KAOSS survey has been designed to provide spectroscopic redshifts for a large sample of SMGs in the COSMOS, UDS and ECDFS fields, while obtaining spatially resolved kinematic information for brighter line sources. The latter is typically only achievable for sources with $K \lesssim 22.5$ (Swinbank priv. comm.), and we therefore prioritise $K \lesssim 22.5$ sources when designing KMOS pointings to try to maximise the yield of sources with kinematic information. In Table 4.1 we present a summary of the number of targets selected in each field, along with how many have currently been observed and how many of these have detected/undetected emission lines. The survey is approximately 60% complete at this time.

The majority of sources in the KAOSS sample have pre-existing physical properties derived from MAGPHYS SED fitting, using the photo-z extension of the code (Battisti et al., 2019), i.e. with the redshift left as a free parameter in the fitting, and we use these here to place the KAOSS sample in context. We note that later in this chapter we will use the high-redshift extension of MAGPHYS together with the spectroscopic redshifts to improve the constraints on these physical parameters for emission line-detected sources (as we did in Chapter 2), but when selecting targets the photo-z MAGPHYS parameters can provide a good assessment of the bulk properties of the sample.

In Fig. 4.1 we show the distributions of photometric redshift ($z_{\rm phot}$), 870 μm flux (S_{870}), K-band magnitude, star-formation rate (SFR), stellar mass (M_*) and dust mass ($M_{\rm dust}$) for the KAOSS sample, along with the AS2UDS sample for comparison (Stach et al., 2019;
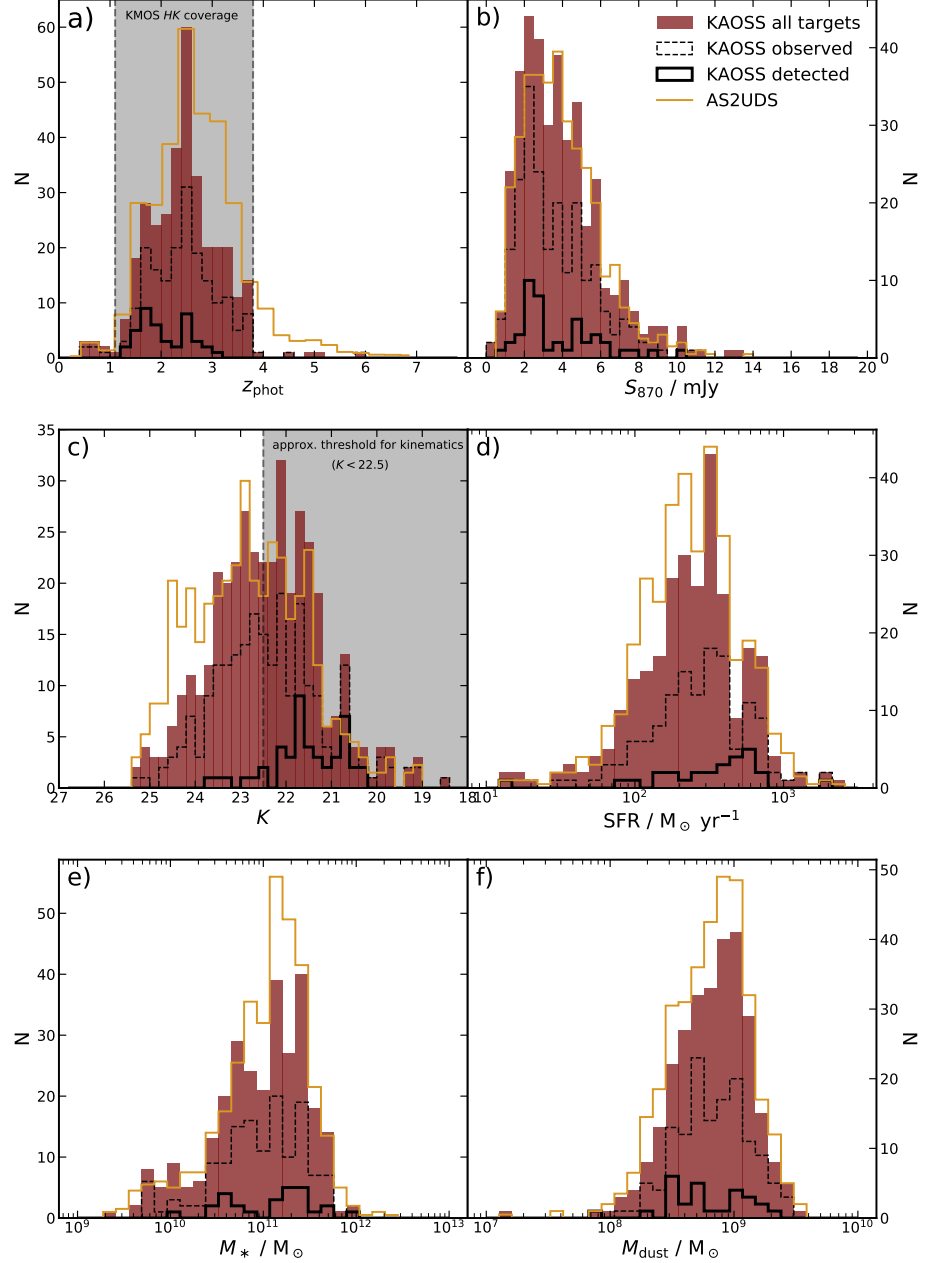
Figure 4.1: Histograms of photometric redshift (z_{phot}), $870\,\mu$m flux density (S_{870}), K-band magnitude, star-formation rate (SFR), stellar mass (M_*) and dust mass (M_{dust}) for the KAOSS sample (where estimates of the corresponding property are available), along with its most representative parent sample, AS2UDS, for comparison (normalised arbitrarily to match KAOSS). In **a)** we shade the range of redshifts $z \sim 1.1$–3.8 for which the Hα and/or [O III] emission lines are covered by the KAOSS HK band, therefore we do not expect to be able to detect sources outside of this region (Only 14 of the 333 sources (4 percent) with available photometric redshifts do not lie in this region). In **c)** we shade the region $K < 22.5$ for which we expect to be able to obtain spatially resolved kinematics. The distributions show that KAOSS is generally representative of the AS2UDS sample, and therefore of the $870\,\mu$m-selected star-forming population.

Dudzevičiūtė et al., 2020). The latter is comprised of 707 ALMA-identified SMGs in the UDS field, and is thus one of the largest samples of its kind. 260 of the 407 KAOSS targets are drawn from this sample and it therefore broadly represents the parent sample of KAOSS. All AS2UDS sources have ALMA-identified counterparts (Stach et al., 2019) to 850 μm sources detected by SCUBA-2 (Geach et al., 2017), K-band magnitudes measured from UKIRT WFCAM imaging (Almaini et al. in prep.), along with z_{phot} and other physical properties estimated from SED fitting with MAGPHYS by Dudzevičiūtė et al. (2020).

In the COSMOS field we draw targets from the AS2COSMOS survey (Simpson et al., 2020), an ongoing ALMA 870 μm survey which will eventually observe > 1000 SMGs selected from the SCUBA-2 850 μm survey of the COSMOS field (S2COSMOS; Simpson et al., 2019), of which the brightest 260 have been observed thus far. We also select targets from the A3COSMOS survey (Liu et al., 2019a), an automated pipeline designed to detect SMGs in archival ALMA data of sources lying in the COSMOS field. All COSMOS sources have K-band coverage from the Visible & Infrared Survey Telescope for Astronomy (VISTA; Emerson et al., 2004), and all AS2COSMOS sources have MAGPHYS SED fitting which provides photometric redshifts and physical properties such as stellar masses and SFRs.

In ECDFS we select 12 targets from the ALESS sample – all of which have MAGPHYS SED fitting available (da Cunha et al., 2015; Danielson et al., 2017), and K coverage from the Taiwan ECDFS Near-Infrared Survey (TENIS; Hsieh et al., 2012). We also select 62 sources from the SUPER GOODS survey (Cowie et al., 2018), an ALMA survey of SMGs in the GOODS-S field. All 62 sources have 870 μm fluxes and K coverage – but none have published physical properties derived from SED fitting, and these sources are therefore not included in Figs. 4.1 and 4.2. We note here however, that the SUPER GOODS sources in our sample have a median 870 μm flux of $S_{870} = 2.5 \pm 0.2 \, \mathrm{mJy}$, whereas A3COSMOS sources have a median of $S_{870} = 4.0 \pm 0.5 \, \mathrm{mJy}$. Compared to the whole sample which has a median $S_{870} = 3.6 \pm 0.2 \, \mathrm{mJy}$, the A3COSMOS sources are comparable, but the SUPER GOODS sources are marginally fainter at submillimetre wavelengths, and therefore are likely to be among the less dust obscured and less actively star-forming sources.

Fig. 4.1 shows that the majority of KAOSS targets lie in the (photometric) redshift range $z_{\mathrm{phot}} = 1.1$–3.8 where rest-frame optical emission lines are expected to fall within the HK coverage of KMOS. Of the sources observed so far the majority lie in the range $z_{\mathrm{phot}} = 1$–3, indicating a bias towards sources in the lower-redshift end of this coverage. This corresponds to mostly sources brighter than the threshold of $K < 22.5$, which is also indicated in Fig. 4.1.
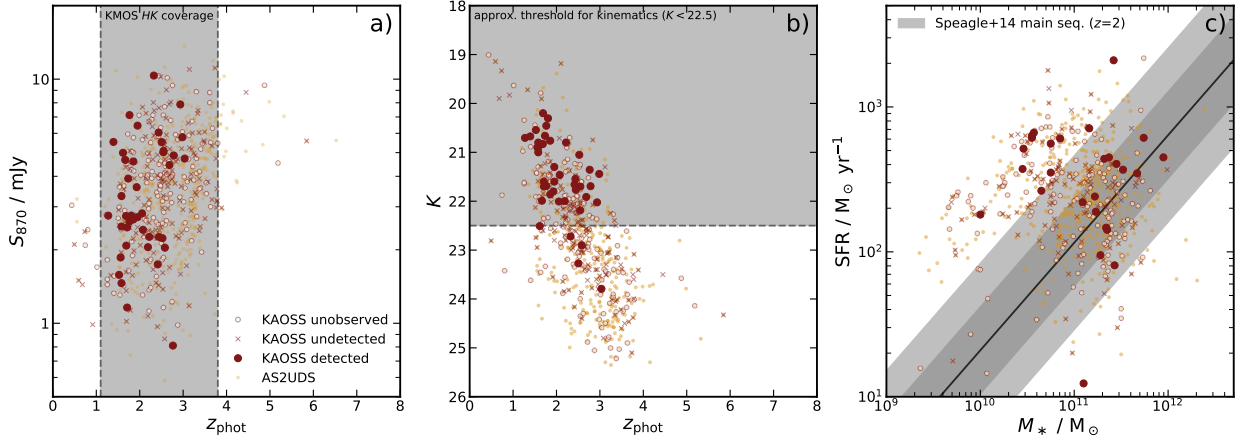
Figure 4.2: Key parameters for the KAOSS sample and its most representative parent sample, the AS2UDS sample. In all panels we indicate which KAOSS targets have not yet been observed, which have been observed but have no detected line emission, and which display line emission. **a)** $870\,\mu$m flux versus photometric redshift. We indicate the redshift coverage of the HK band of KMOS, and see that we preferentially detect sources at the lower-redshift end of this region. **b)** K-band magnitude versus z_{phot}. We indicate the approximate threshold of $K < 22.5$ which we expect to require in order to measure spatially resolved kinematics. All but five of the 43 detected sources in the current survey lie above this threshold. This panel also shows the trend of optically brighter sources residing at lower redshifts for the SMG population **c)** SFR versus stellar mass (the star-forming "main sequence"). We show the main sequence prescription of Speagle et al. (2014), calculated at $z \sim 2$, and indicate regions of $\pm\,0.3\,$dex and $\pm\,0.6\,$dex from the main sequence value, the former roughly representing the main-sequence scatter and the latter representing the boundary between "starburst" and "main-sequence" galaxies. Our detected sources span the range of the SFR and M_* within the AS2UDS sample, and therefore the $870\,\mu$m-selected SMG population. Approximately half of the detected sample lie within $0.6\,$dex of the $z \sim 2$ main sequence.

On average, the KAOSS targets have SFRs of $\sim 300\,\mathrm{M_\odot\,yr^{-1}}$, stellar masses of $\sim 10^{11}\,\mathrm{M_\odot}$ and dust masses of $\sim 10^9\,\mathrm{M_\odot}$, although Fig. 4.1 shows that with KMOS we are preferentially detecting sources with higher SFRs and stellar masses, which make them brighter in the observed-frame NIR and therefore more likely to be detected. We highlight again that physical parameters derived with the photometric redshift extension of MAGPHYS are likely to be less precise than those where a spectroscopic redshift is available. However, from our analysis of the CO-detected sources in Chapter 2 we find that the photometric and spectroscopic redshift-derived parameters are generally consistent within their uncertainties, and including the spectroscopic redshift mainly improves the precision of the parameter estimates.

Fig. 4.2 shows $870\,\mu$m flux and K-band magnitude against photometric redshift, and star-formation rate against stellar mass for the KAOSS targets (where estimates of the properties are available) and the AS2UDS comparison sample. This results in similar conclusions to

those drawn from Fig. 4.1, however we can also see in Fig. 4.2 that there is a correlation between photometric redshift and K – sources which are NIR-brighter are normally found at lower redshifts (also see Dudzevičiūtė et al., 2020), hence why we detect lower-redshift sources with KMOS.

4.2.2   Observing strategy

KMOS is a near-infrared multi-object spectrograph mounted at the Nasmyth focus of Unit Telescope 1 on the Very Large Telescope (VLT). It is comprised of 24 IFUs that patrol a field of $7.2'$ diameter area of the sky, with each IFU covering a $2.8'' \times 2.8''$ field of view sampled by 14×14 spaxels ($0.2''$ per pixel). In our survey fields KMOS pointings typically contain ~ 10 SMGs, and as KMOS has 24 IFUs available we choose to pair IFUs on our targets and a matched blank sky region where possible, thus maximising the on-target time, given the need for sky offsets. A schematic of our observing setup is shown in Fig. 4.3. When observing, the instrument nods back and forth between the target (position 1) and a sky position (position 2) in order to assist sky subtraction. By creating sky positions offset relative to the corresponding target position by a similar fixed vector, we can ensure that the target is observed by either the primary or secondary (sky) IFU (A or B in Fig. 4.3) at all times.

Once the data is reduced, the frames corresponding to the target in both IFUs can be combined to increase the signal-to-noise ratio (S/N). This pairing of object and sky IFUs is not *always* possible given the positioning of targets within the field of view, but we prioritise this approach for sources with $K < 22.5$ that are most likely to yield spatially resolved kinematics. We also reserve one IFU to be placed on a bright ($H \sim 12$–15) star, allowing us to monitor the telescope pointing and the point spread function (PSF). Key observational parameters for the KAOSS survey, such as exposure times and seeing, are given in Table 4.2.

Each observing block (OB) takes approximately one hour of telescope time yielding $2.7\,\mathrm{ks}$ of on-source integration time, and to obtain our desired sensitivity we observe each OB five times, resulting in a total exposure time of $13.5\,\mathrm{ks}$ for each pointing. Observations are carried out in the combined HK grating which covers the wavelength range $\lambda \sim 1.4$–$2.4\,\mu\mathrm{m}$, sufficient to cover the Hα or [OIII] lines for sources at $z \sim 1.1$–3.8, where the majority of our targets are expected to lie (see Fig. 4.1). This choice of grating was motivated by the desire to obtain a large number of spectroscopic redshifts for the sample. The combined grating gives us greater redshift coverage than had we used the H grating, at the cost of halving the

	COSMOS	UDS	ECDFS
Exposure time / ks	13.5	13.5	13.5
Seeing / ″	~ 0.6	~ 0.6	~ 0.6
Number of pointings	8	26	8
Number of completed pointings	6	9	8

Table 4.2: Summary of KAOSS observational parameters, by survey field.

resolving power, which ultimately means our observations suffer more from sky lines along with greater uncertainties on velocity estimates (see Chapter 5). In particular, the resolving power of KMOS in the HK band is 1514 and 2538 at the short- and long-wavelength edges of the band, and 1985 at the band centre, therefore the instrumental resolution is expected to vary between $\sigma_{\mathrm{instr}} \sim 50\text{–}84\,\mathrm{km\,s^{-1}}$. Given that the primary goal of KAOSS is to obtain spectroscopic redshifts, we view this as an acceptable compromise, and this instrumental resolution is still expected to be sufficient to resolve the Hα emission in our targets.

4.2.3 KMOS data reduction

In this section we provide a brief description of the processes taken to produce fully reduced data cubes from the raw KMOS data, from the calibration frames used, to sky subtraction and cube alignment/stacking. A flowchart summarising the data reduction steps is presented in Fig. 4.4.

Calibration frames

Although the KMOS detectors are cooled to $35\,\mathrm{K}$, observations are still affected by the thermal excitation of electrons, known as dark current. To correct for this, dark frames are taken with the shutter closed and subtracted from the calibration frames. For our HK KAOSS observations we use dark frames with exposure times of $60\,\mathrm{s}$. In addition to subtracting dark frames we divide by a flat field frame (taken during the day) to correct for the non-uniform spatial response of the detector. To create a wavelength solution for the observed data we use arc frames which are taken from arc lamps emitting a known set of spectral lines – one Argon and the other Neon. This also corrects for potential spectral curvature. The telluric features from the atmosphere are corrected for by observing a standard star at the same airmass as the science target, which is also subsequently used for flux calibration.

All calibration frames are taken from as near in time to the science frames as possible to ensure the calibration is as accurate as possible. Calibration of the raw data products proceeds
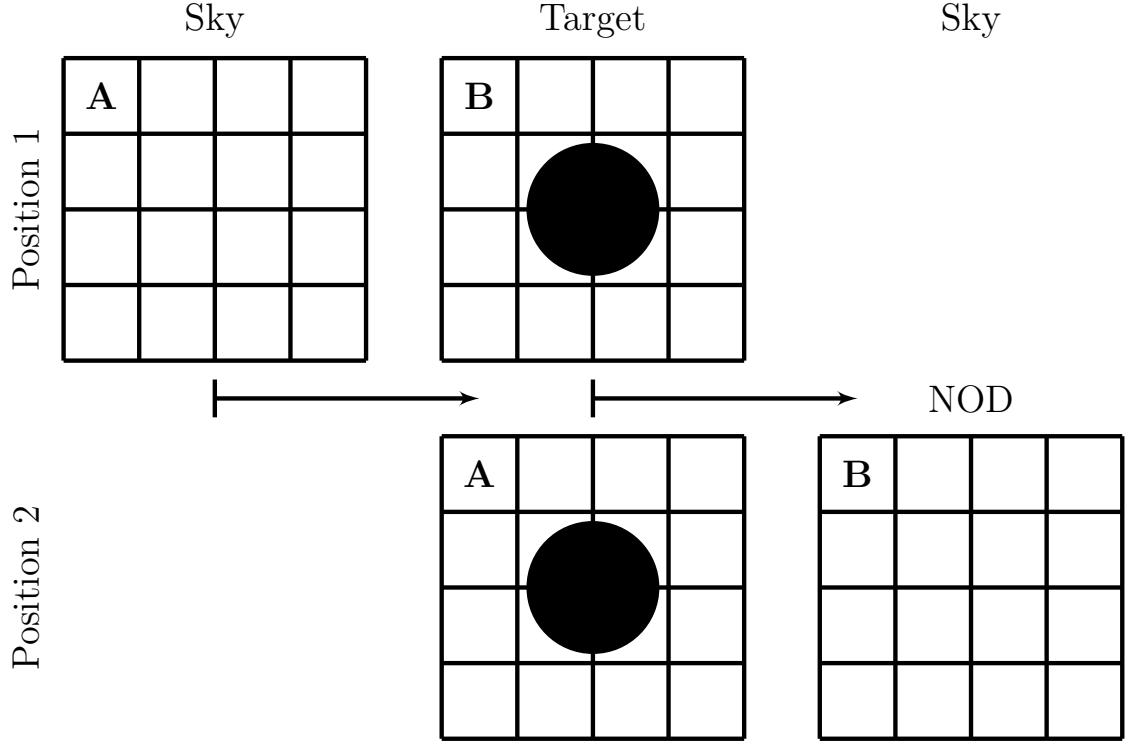
Figure 4.3: Schematic showing the setup of our KMOS observations. In both positions one IFU is centred on the target (black circle), initially IFU B in position 1 and subsequently IFU A after the instrument nods to position 2.

via the European Southern Observatory (ESO) Recipe Execution Tool (ESOREX; ESO CPL Development Team, 2015), a library of functions that take as an input the raw data and produce reduced 3D cubes.

Sky subtraction

In the H and K bands, observations suffer from contamination caused by OH emission from the Earth's atmosphere, a systematic that must be corrected for in order to obtain any meaningful results, particularly for NIR-faint galaxies such as those in our survey. While the standard ESOREX pipeline carries out a basic A-B sky subtraction, this is often poor in the HK band of KMOS, therefore we employ a more sophisticated technique based on the Zurich Atmospheric Purge (ZAP; Soto et al., 2016) method initially developed for the MUSE instrument, with optimisations made for KMOS observations. The ZAP method is based on principal component analysis (PCA), using filtering and data segmentation to reduce sky emission residuals while preserving flux from the astronomical target. This KMOS-adapted method is encapsulated in the PYSPARK code (Mendel et al. in prep.).

```
┌─────────────────────────────────────────┐
│       All science frames − DARK          │
└─────────────────────────────────────────┘
┌─────────────────────────────────────────┐
│        All science frames / FLAT         │
└─────────────────────────────────────────┘
┌─────────────────────────────────────────┐
│     λ calibrate all science frames       │
└─────────────────────────────────────────┘
┌──────────────────────┐  ┌──────────────────────┐
│   A−B for position 1 │  │  B−A for position 2  │
└──────────────────────┘  └──────────────────────┘
┌─────────────────────────────────────────┐
│           PYSPARK correction             │
└─────────────────────────────────────────┘
┌─────────────────────────────────────────┐
│  Check astrometry using PSF star and centre │
└─────────────────────────────────────────┘
┌─────────────────────────────────────────┐
│        Stack A−B and B−A pairs           │
└─────────────────────────────────────────┘
┌─────────────────────────────────────────┐
│        Check alignment and stack all     │
│     OBs in a field to give final cubes   │
└─────────────────────────────────────────┘
```
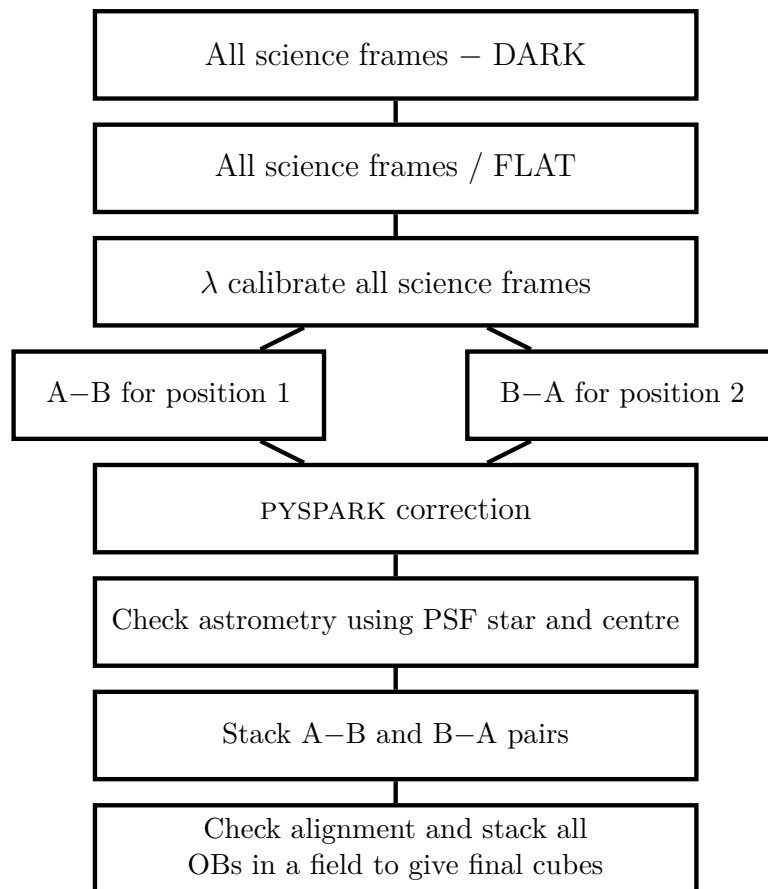
Figure 4.4: Flowchart showing the steps taken to reduce KMOS data.

PYSPARK requires a sky cube to model the sky background. To generate a skycube, data from each spectrograph are median-combined (eight frames per spectrograph and three spectrographs per observation) to remove line emission from individual galaxies, which should lie at different redshifts. However, some stellar continuum emission from both the galaxy IFUs and the star IFU can remain in the cubes. We thus collapse each cube and visually inspect it for any prominent continuum emission, then generate masks manually, such that the masked spaxels are not included in the median-combination to yield the sky modelling. The PYSPARK-modelled sky emission is then subtracted from the cubes to remove residual sky contamination.

Cube alignment and stacking

As previously stated, in every OB we assign at least one IFU to a bright star, one of the primary purposes of which is to centre the data cubes between OBs. Therefore, for each set of AB pairs we obtain a reduced cube of a bright star, and we measure the centroid of the emission in this cube by collapsing it and fitting a 2-D Gaussian profile to the spatial emission. We then shift all observations of that field to a common centre using the measured centroid from the star.

We also check for any significant offset in the final cubes between individual observations. This allows us to be confident that we are not losing S/N in our combined cubes, as a result of misalignment. Small perturbations can affect the alignment of the telescope, and while in theory these should be corrected for in the acquisition and data reduction, we check each $\sim 1\,\mathrm{hr}$ observing block for offsets by comparing the measured position of any sources bright enough in their continuum or line emission to be detected. Once the reduced cubes have been produced and aligned, we stack each object individually by taking the mean of the individual frames and applying a 3σ clip.

4.2.4 Spectral extraction and line identification

Having reduced the KMOS data we "unwrap" the cubes into a 2-D spectrum (see Fig. 4.5 for examples) and visually inspect the data cubes, noting any potential line emission and cross-referencing with pre-existing photometric and/or spectroscopic redshifts to assist in identifying the emission lines. For sources where we believe a line to be present we collapse the cube around the approximate wavelength of the observed emission line and visually inspect the resultant line map, then extract a 1-D spectrum at the position of the emission
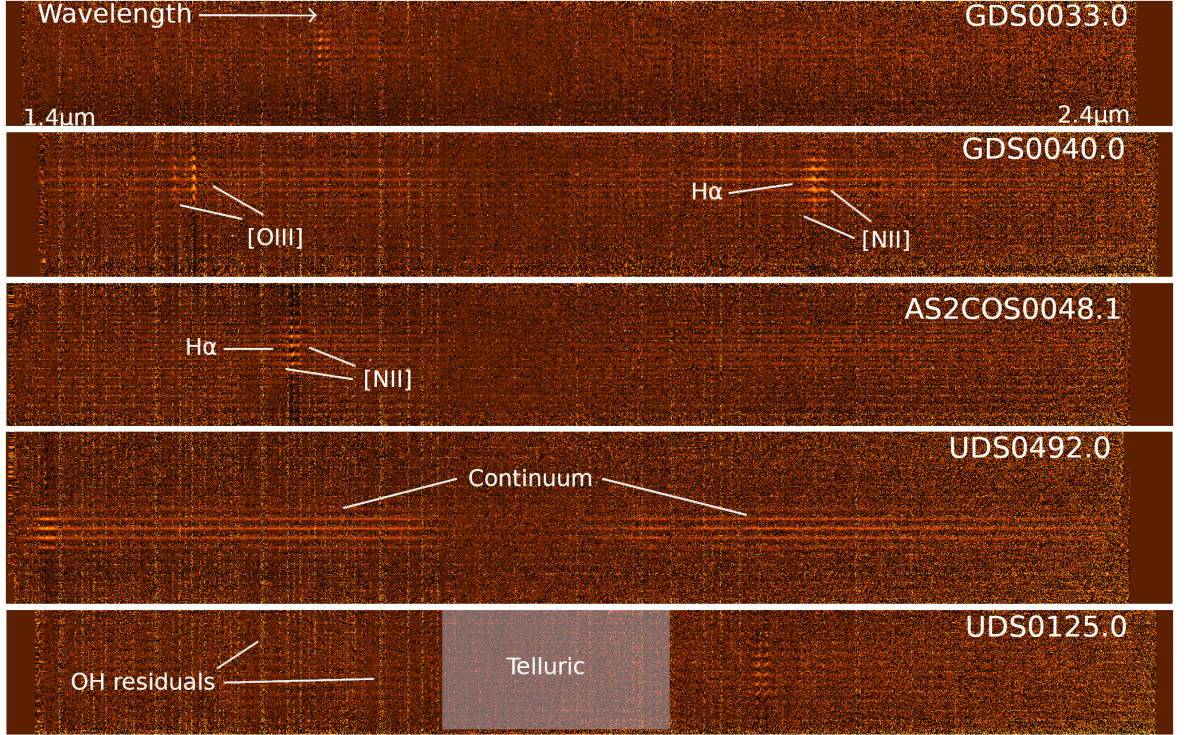
Figure 4.5: Reduced 2-D spectra of five KAOSS sources: GDS0033.0, GDS0040.0, AS2COS0048.1, UDS0492.0 and UDS0125.0 (from top to bottom), with wavelength increasing from left to right ($\lambda \sim 1.4$–$2.4\,\mu m$). Emission lines can be clearly seen in all five examples, with GDS0040.0 and UDS0492.0 displaying strong continuum emission. We highlight some of these emission lines and continuum, along with residuals of OH sky emission and the telluric region of the spectra where the atmosphere absorbs the majority of emission (most clearly seen in the continuum of UDS0492.0).

(shown in Figs. 4.6–4.8). Spectra are extracted in an aperture of radius $0.6''$, selected by analysing a subset of five sources and performing a curve-of-growth analysis to determine the aperture which results in the maximum S/N. In cases where the line ID is ambiguous we also use the emission line profile to identify the line.

4.2.5   Emission line fitting

To determine the redshifts and integrated line properties of our sources we model the observed emission lines in the spectra extracted in §4.2.4, using a χ^2 minimisation. For Hα emission lines we attempt to fit a three-component Gaussian profile to the H$\alpha\lambda6563$ line and [NII]$\lambda6583$ doublet, coupling their wavelengths and linewidths while leaving the Hα/[NII]$\lambda6583$ flux ratio to vary as a free parameter, with the [NII]$\lambda6583$/[NII]$\lambda6548$ flux ratio fixed to a value of 2.8 (Osterbrock & Ferland, 2006). We determine the instrumental resolution σ_{instr} to be $\sim 50\,\mathrm{km\,s^{-1}}$ (which is reasonable given the resolving power $R \sim 2000$ for the HK grating) by fitting several sky lines over the HK band, and include this in our fitting as $\sigma_{\mathrm{obs}}^2 = \sigma^2 + \sigma_{\mathrm{instr}}^2$.

It should be noted that we fix $\sigma_{\mathrm{instr}} = 50\,\mathrm{km\,s^{-1}}$ for simplicity, whereas in practice this value is wavelength dependent, and therefore redshift dependent. As discussed in §4.2.2 the nominal instrumental resolution is expected to vary between $\sigma_{\mathrm{instr}} \sim 50$–$84\,\mathrm{km\,s^{-1}}$, however we expect our assumption of a fixed value to translate to insignificant differences in our measurements, relative to their uncertainties.

For [OIII] emission lines we attempt to fit a two-component Gaussian profile to the two emission lines at rest-frame wavelengths of 4959 Å and 5007 Å, again coupling their wavelengths and linewidths and leaving the [OIII]λ4959/[OIII]λ5007 flux ratio to vary as a free parameter.

In all cases we fit a constant continuum component, and only fit to the region within $\pm 0.02\,\mu\mathrm{m}$ of the emission line as opposed to the entire KMOS spectrum (as the continuum emission can vary strongly across the wide HK band, see Fig. 4.5). As some of our sample appear to display very broad ($> 1000\,\mathrm{km\,s^{-1}}$) lines, for both the H$\alpha$ and [OIII]λ5007 emission lines we separately attempt to fit a broad component in addition to the components described above. We compute the Akaike Information Criterion (AIC; Akaike, 1974), which takes into account the number of parameters, for the models with and without broad components, and use the model with the lowest AIC in the final fit. We fit broad components for four sources, the properties of which are shown in Table 4.9.

4.2.6   Spectral energy distribution fitting

Our KAOSS observations are supplemented by a wealth of photometric coverage in all three fields, which we utilise here to estimate the physical properties of our sample, such as star-formation rates, stellar masses and dust masses. In the analysis of this chapter and Chapter 5 we will study how the Hα emission properties vary with these physical properties. To derive these we fit spectral energy distributions (SEDs) to our sources with the high-redshift version of MAGPHYS (as described in Section 2.5.2), fixing the redshift to be that derived from the Hα or [OIII] emission line fitting. The photometry used is listed in Table 4.3:

We refer to the reader to Chapter 2 for a more comprehensive discussion of our method of SED fitting with MAGPHYS (also see da Cunha et al., 2015; Dudzevičiūtė et al., 2020). The observed flux measurements/limits and the corresponding best-fit MAGPHYS SEDs for the 43 sources are displayed in Figs. 4.10 and 4.11, showing that MAGPHYS provides a good fit to the observed photometry in the majority of cases. Some SED fits appear to miss one or more of the IRAC data points – this occurs in sources displaying a mid-infrared power law component potentially associated with hot dust heated by an AGN (Hainline et al., 2009),
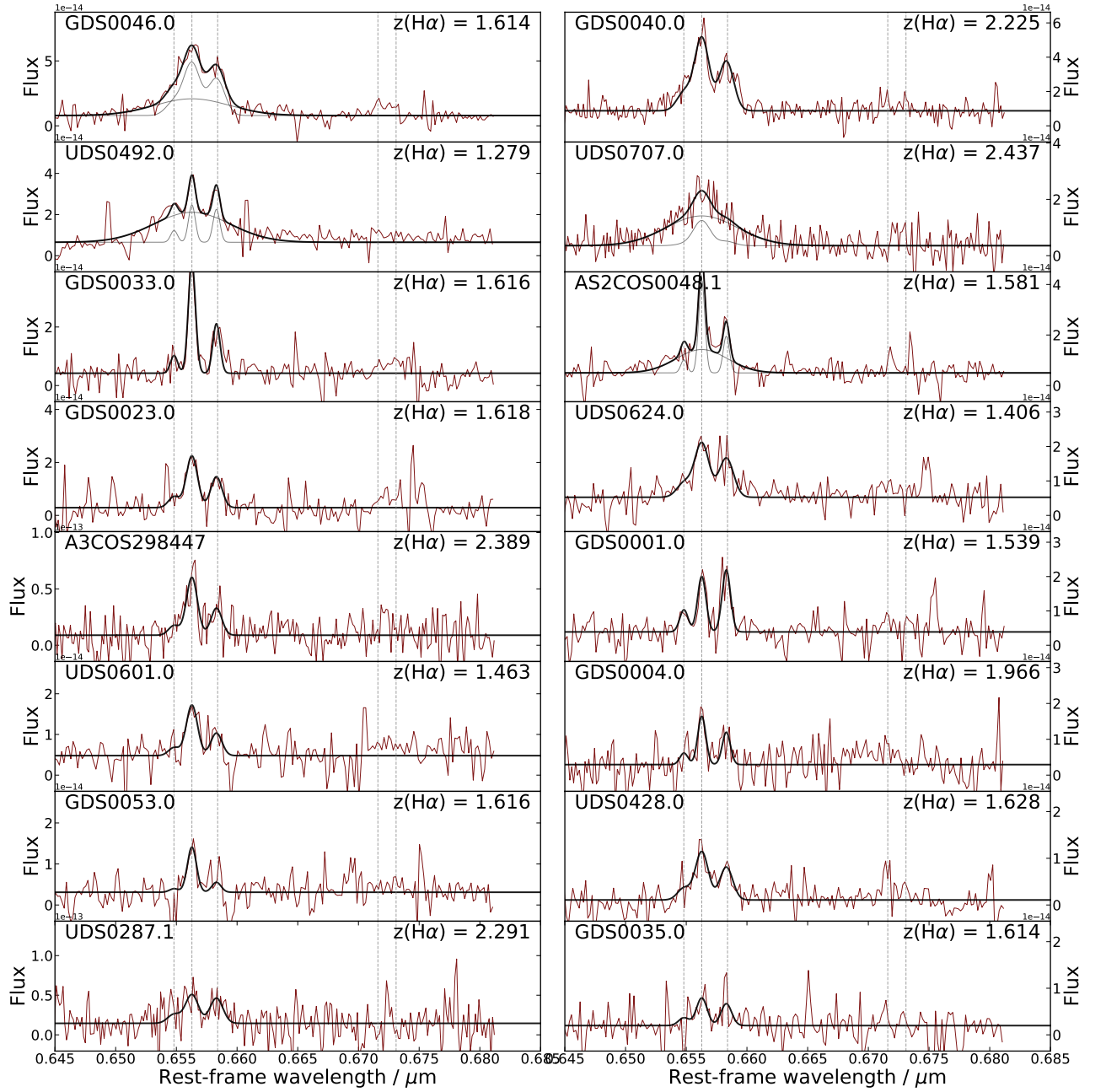
Figure 4.6: Rest-frame 1-D Hα line emission spectra of KAOSS SMGs (red), with Gaussian plus constant continuum fits overlaid (black). Sources are ordered by descending S/N of the Hα emission line (see Table 4.7). In each panel we indicate the measured redshift of the source, along with the redshift of key rest-frame optical emission lines. All flux densities are in units of $\mathrm{erg\,s^{-1}\,cm^2\,\mu m^{-1}}$, and we show as vertical dashed lines the key emission lines [O I] (0.63 μm), Hα (0.6563 μm), [N II] (0.6548 μm and 0.6583 μm) and [S II] (0.6716 μm and 0.6731 μm). The sources display a range of Hα profiles with some sources, such as GDS0001.0 and UDS0125.0, displaying strong [N II]λ6583 emission. Broad Hα emission is seen in sources such as GDS0046.0 and UDS0492.0, potentially indicating the presence of an AGN. We discuss the line properties and their implications in §4.3.2 Continued in Figs. 4.7–4.8.
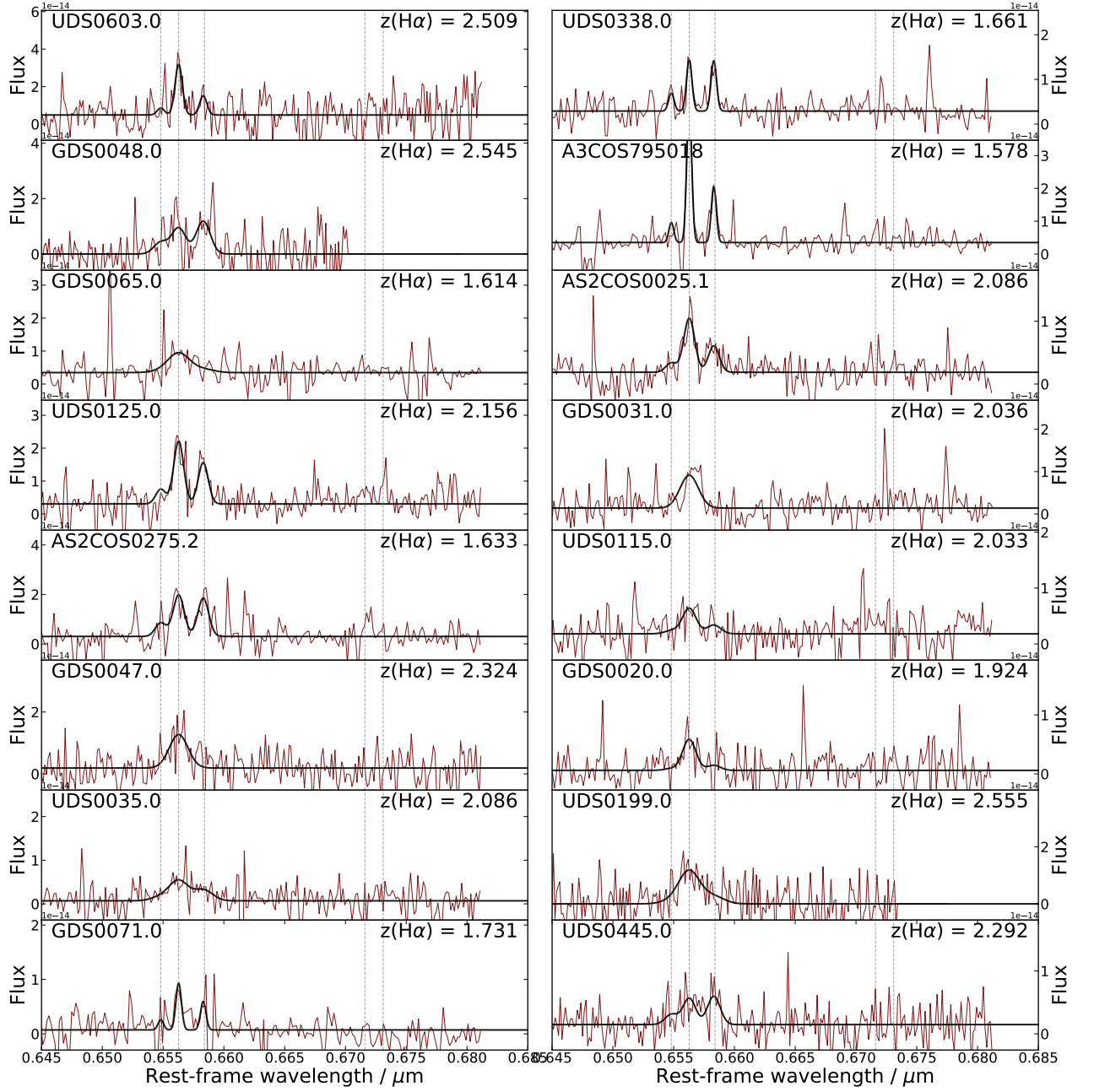
Figure 4.7: Fig. 4.6 continued.
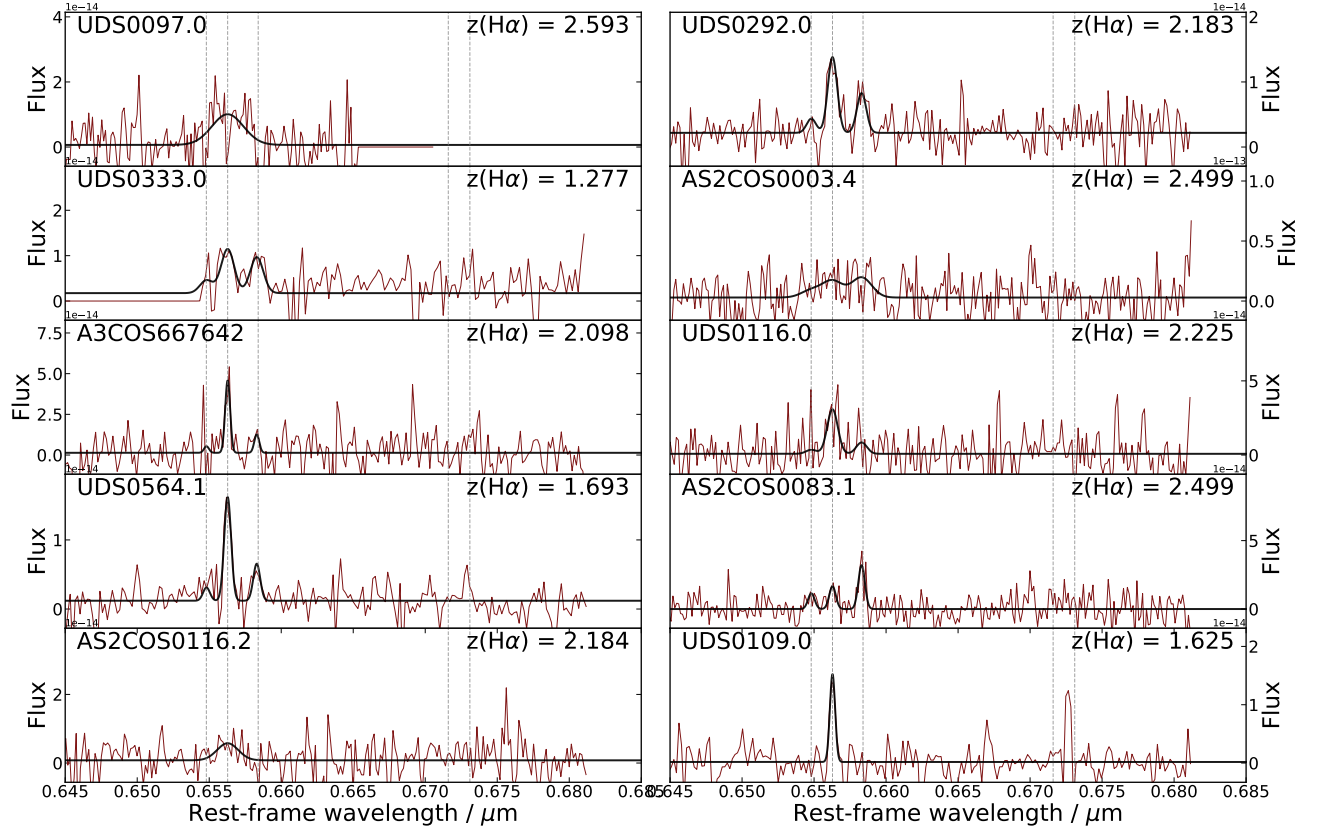
Figure 4.8: Fig. 4.6 continued.
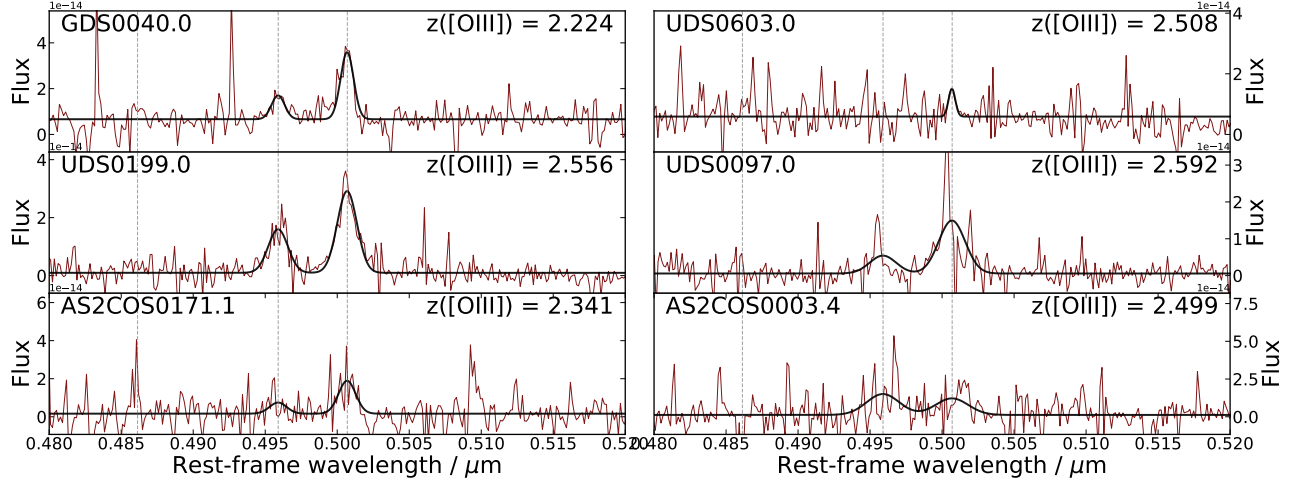
Figure 4.9: Same as Figs. 4.6–4.8, but here displaying [OIII] emission lines and Gaussian plus constant continuum fits. Sources are ordered by descending S/N of the [OIII] emission line (see Table 4.8). In general, the [OIII] is weaker than the Hα line for most of our sample, and therefore the S/N in the displayed emission is lower than our brightest Hα emission lines (see Fig. 4.6). We show as dashed vertical lines the key emission lines Hβ (0.486 μm) and [OIII] (0.4959 μm and 0.5007 μm).

COSMOS	UDS	GOODS-S
CFHT Megacam U (Laigle et al., 2016)	CFHT Megacam U (Lawrence et al., 2007)	VIMOS U (Guo et al., 2013)
Subaru SuprimeCam $BVRIz$ (Laigle et al., 2016)	Subaru SuprimeCam $BVRIz$ (Lawrence et al., 2007)	*HST* ACS F435W, F606W, F775W, F814W, F850LP (Guo et al., 2013)
Subaru HSC Y (Laigle et al., 2016)	VISTA Y (Lawrence et al., 2007)	*HST* WFC3 F098M, F105W, F125W, F160W (Guo et al., 2013)
VISTA HK_s (Laigle et al., 2016)	UKIRT WFCAM JHK (Lawrence et al., 2007)	VLT/HAWK-I K_s (Guo et al., 2013)
Spitzer IRAC1-4 (Laigle et al., 2016)	*Spitzer* IRAC1-4 (Kim et al., 2011)	*Spitzer* IRAC1-4 (Guo et al., 2013)
Spitzer MIPS 24μm (Jin et al., 2018)	*Spitzer* MIPS 24μm (Kim et al., 2011)	*Spitzer* MIPS 24μm (Giavalisco et al., 2004)
Herschel PACS 100μm, 160μm (Jin et al., 2018)	*Herschel* PACS 100μm, 160μm (Oliver et al., 2012)	*Herschel* PACS 70μm, 100μm, 160μm (Elbaz et al., 2011)
Herschel SPIRE 250μm, 350μm, 500μm (Jin et al., 2018)	*Herschel* SPIRE 250μm, 350μm, 500μm (Oliver et al., 2012)	*Herschel* SPIRE 250μm, 350μm, 500μm (Elbaz et al., 2011)
ALMA 870μm (Simpson et al., 2020)	ALMA 870μm (Stach et al., 2019)	ALMA 870μm (Cowie et al., 2018)
VLA 3 GHz (Smolčić et al., 2017)	VLA 1.4 GHz (Simpson et al., 2013)	VLA 1.4 GHz (Miller et al., 2013)

Table 4.3: Photometry used in MAGPHYS SED fitting of the KAOSS sources. Note that we list GOODS-S rather than ECDFS, as none of the sources in the wider ECDFS field were detected, therefore we only require photometry from the smaller GOODS-S region.
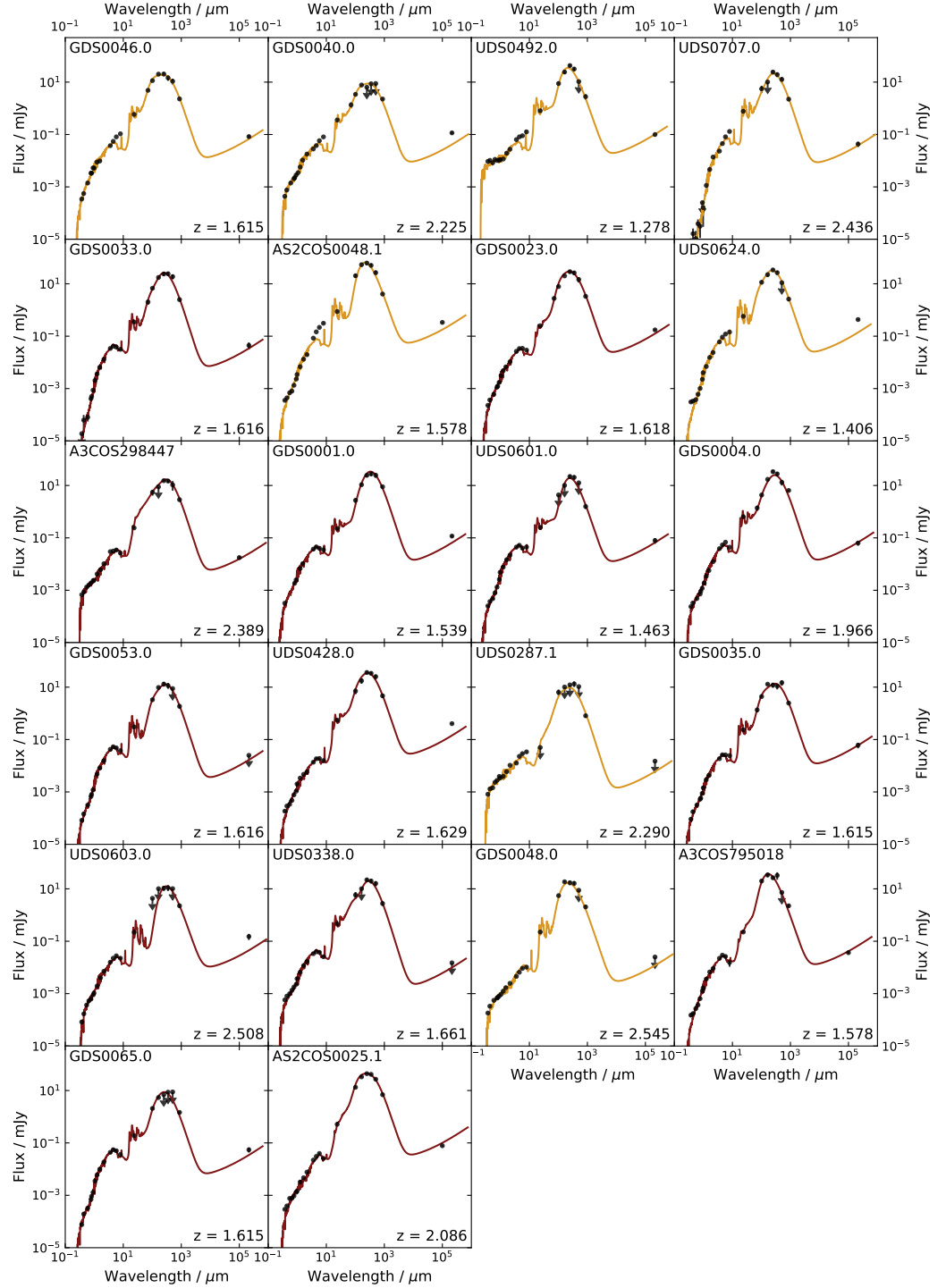
Figure 4.10: MAGPHYS SED fits to optical-UV photometry for the 43 emission line-detected KAOSS SMGs. The data are well fit in most cases, with the exception of a handful of sources displaying mid-infrared power laws, and some in which the fit underestimates the radio flux. These sources (flagged in yellow, 13 out of 43) are likely to be AGN hosts. Continued in Fig. 4.11.

Figure 4.11: Fig. 4.10 continued.

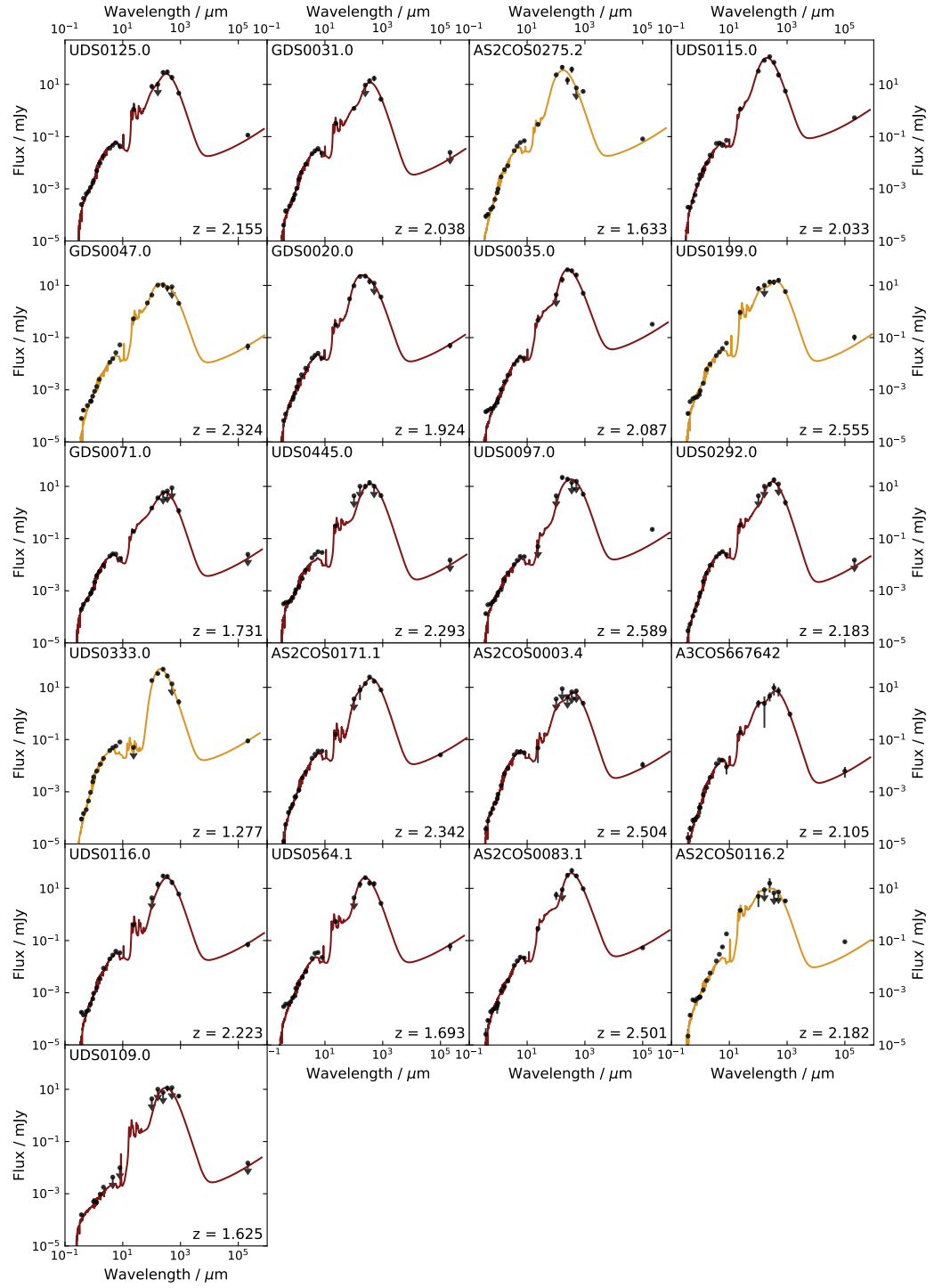| ID	$\log_{10}\left(\dfrac{M_*}{\mathrm{M_\odot}}\right)$	$\log_{10}\left(\dfrac{\mathrm{SFR}}{\mathrm{M_\odot yr^{-1}}}\right)$	$\log_{10}\left(\dfrac{M_{\mathrm{dust}}}{\mathrm{M_\odot}}\right)$	$\log_{10}\left(\dfrac{L_{\mathrm{IR}}}{\mathrm{L_\odot}}\right)$	A_V
GDS0046.0	$11.06^{+0.08}_{-0.07}$	$2.44^{+0.03}_{-0.02}$	$8.6^{+0.2}_{-0.12}$	$12.47^{+0.03}_{-0.010}$	$1.86^{+0.10}_{-0.05}$
GDS0040.0	$11.26^{+0.08}_{-0.07}$	$2.33^{+0.06}_{-0.05}$	$8.7^{+0.3}_{-0.16}$	$12.36^{+0.05}_{-0.05}$	$1.14^{+0.08}_{-0.10}$
UDS0492.0	$10.20^{+0.010}_{-0.010}$	$1.99^{+0.08}_{-0.010}$	$8.71^{+0.13}_{-0.06}$	$12.30^{+0.010}_{-0.05}$	$0.99^{+0.03}_{-0.05}$
UDS0707.0	$12.07^{+0.09}_{-0.07}$	$2.3^{+0.2}_{-0.18}$	$8.43^{+0.11}_{-0.09}$	$12.71^{+0.05}_{-0.04}$	$3.21^{+0.10}_{-0.17}$
GDS0033.0	$11.49^{+0.10}_{-0.07}$	$2.14^{+0.11}_{-0.08}$	$8.68^{+0.13}_{-0.09}$	$12.37^{+0.04}_{-0.03}$	$2.96^{+0.12}_{-0.05}$
AS2COS0048.1	$11.4^{+0.4}_{-0.2}$	$2.73^{+0.09}_{-0.16}$	$8.83^{+0.11}_{-0.09}$	$12.79^{+0.05}_{-0.06}$	$2.69^{+0.15}_{-0.2}$
GDS0023.0	$10.82^{+0.11}_{-0.11}$	$2.43^{+0.02}_{-0.04}$	$8.78^{+0.14}_{-0.14}$	$12.46^{+0.010}_{-0.03}$	$2.31^{+0.05}_{-0.05}$
A3COS298447	$11.11^{+0.02}_{-0.10}$	$2.38^{+0.16}_{-0.14}$	$8.69^{+0.18}_{-0.12}$	$12.6^{+0.13}_{-0.05}$	$1.44^{+0.18}_{-0.10}$
GDS0001.0	$11.12^{+0.18}_{-0.11}$	$2.19^{+0.06}_{-0.06}$	$9.38^{+0.11}_{-0.14}$	$12.27^{+0.02}_{-0.03}$	$1.89^{+0.08}_{-0.10}$
UDS0601.0	$11.25^{+0.09}_{-0.06}$	$1.98^{+0.06}_{-0.06}$	$8.55^{+0.10}_{-0.09}$	$12.1^{+0.05}_{-0.05}$	$1.79^{+0.10}_{-0.10}$
GDS0004.0	$11.51^{+0.010}_{-0.010}$	$2.182^{+0.005}_{-0.010}$	$9.0^{+0.3}_{-0.15}$	$12.53^{+0.010}_{-0.010}$	$1.89^{+0.09}_{-0.10}$
GDS0053.0	$11.38^{+0.06}_{-0.07}$	$1.97^{+0.06}_{-0.04}$	$8.5^{+0.2}_{-0.14}$	$12.13^{+0.03}_{-0.05}$	$2.01^{+0.08}_{-0.10}$
UDS0428.0	$10.47^{+0.15}_{-0.06}$	$2.42^{+0.03}_{-0.06}$	$9.08^{+0.10}_{-0.10}$	$12.49^{+0.03}_{-0.05}$	$2.69^{+0.08}_{-0.12}$
UDS0287.1	$10.58^{+0.10}_{-0.08}$	$2.36^{+0.06}_{-0.16}$	$8.09^{+0.09}_{-0.13}$	$12.38^{+0.05}_{-0.12}$	$1.16^{+0.10}_{-0.2}$
GDS0035.0	$11.15^{+0.10}_{-0.2}$	$2.00^{+0.11}_{-0.005}$	$8.88^{+0.08}_{-0.14}$	$12.17^{+0.010}_{-0.010}$	$2.19^{+0.10}_{-0.12}$
UDS0603.0	$11.09^{+0.13}_{-0.09}$	$2.34^{+0.09}_{-0.08}$	$8.53^{+0.17}_{-0.13}$	$12.39^{+0.08}_{-0.06}$	$1.61^{+0.10}_{-0.12}$
UDS0338.0	$11.0^{+0.3}_{-0.10}$	$2.22^{+0.08}_{-0.07}$	$8.90^{+0.13}_{-0.11}$	$12.28^{+0.04}_{-0.03}$	$1.64^{+0.08}_{-0.15}$
GDS0048.0	$10.16^{+0.18}_{-0.010}$	$2.20^{+0.10}_{-0.010}$	$8.3^{+0.2}_{-0.10}$	$12.68^{+0.18}_{-0.010}$	$2.61^{+0.10}_{-0.14}$
A3COS795018	$10.85^{+0.11}_{-0.08}$	$2.43^{+0.07}_{-0.07}$	$8.3^{+0.3}_{-0.06}$	$12.48^{+0.06}_{-0.06}$	$2.76^{+0.10}_{-0.12}$
GDS0065.0	$11.46^{+0.05}_{-0.09}$	$1.71^{+0.06}_{-0.07}$	$8.4^{+0.3}_{-0.15}$	$11.93^{+0.04}_{-0.03}$	$1.61^{+0.07}_{-0.08}$
AS2COS0025.1	$10.65^{+0.14}_{-0.010}$	$2.71^{+0.09}_{-0.11}$	$9.11^{+0.15}_{-0.17}$	$12.95^{+0.02}_{-0.10}$	$2.86^{+0.08}_{-0.4}$
UDS0125.0	$11.5^{+0.3}_{-0.13}$	$2.62^{+0.06}_{-0.12}$	$8.98^{+0.12}_{-0.11}$	$12.7^{+0.05}_{-0.03}$	$1.94^{+0.12}_{-0.10}$
GDS0031.0	$11.28^{+0.08}_{-0.06}$	$2.03^{+0.09}_{-0.07}$	$8.92^{+0.17}_{-0.11}$	$12.15^{+0.06}_{-0.05}$	$1.86^{+0.10}_{-0.10}$
AS2COS0275.2	$11.15^{+0.10}_{-0.06}$	$2.49^{+0.06}_{-0.06}$	$8.2^{+0.3}_{-0.13}$	$12.55^{+0.06}_{-0.05}$	$3.11^{+0.08}_{-0.15}$
UDS0115.0	$11.29^{+0.13}_{-0.06}$	$3.15^{+0.04}_{-0.04}$	$8.77^{+0.09}_{-0.03}$	$13.23^{+0.03}_{-0.04}$	$2.96^{+0.10}_{-0.08}$
GDS0047.0	$10.8^{+0.2}_{-0.11}$	$2.50^{+0.04}_{-0.04}$	$8.5^{+0.3}_{-0.18}$	$12.54^{+0.05}_{-0.03}$	$2.36^{+0.10}_{-0.05}$
GDS0020.0	$10.86^{+0.11}_{-0.13}$	$2.50^{+0.05}_{-0.06}$	$8.6^{+0.3}_{-0.2}$	$12.55^{+0.05}_{-0.05}$	$2.61^{+0.15}_{-0.07}$
UDS0199.0	$11.45^{+0.08}_{-0.08}$	$2.66^{+0.08}_{-0.08}$	$9.1^{+0.2}_{-0.14}$	$12.75^{+0.08}_{-0.05}$	$2.14^{+0.15}_{-0.12}$
GDS0071.0	$10.96^{+0.11}_{-0.10}$	$1.74^{+0.06}_{-0.04}$	$8.4^{+0.3}_{-0.2}$	$11.83^{+0.04}_{-0.04}$	$1.36^{+0.05}_{-0.12}$
UDS0445.0	$11.0^{+0.08}_{-0.15}$	$2.24^{+0.14}_{-0.13}$	$9.0^{+0.2}_{-0.16}$	$12.31^{+0.10}_{-0.06}$	$1.7^{+0.2}_{-0.2}$
UDS0097.0	$10.8^{+0.06}_{-0.15}$	$2.57^{+0.06}_{-0.06}$	$9.05^{+0.05}_{-0.2}$	$12.63^{+0.04}_{-0.06}$	$2.16^{+0.15}_{-0.10}$
UDS0292.0	$11.4^{+0.09}_{-0.06}$	$2.19^{+0.10}_{-0.10}$	$8.64^{+0.19}_{-0.13}$	$12.34^{+0.08}_{-0.06}$	$2.16^{+0.12}_{-0.12}$
UDS0333.0	$11.25^{+0.09}_{-0.07}$	$2.63^{+0.06}_{-0.2}$	$8.4^{+0.2}_{-0.13}$	$12.33^{+0.02}_{-0.07}$	$3.26^{+0.15}_{-0.3}$
AS2COS0003.4	$11.47^{+0.06}_{-0.04}$	$1.90^{+0.16}_{-0.11}$	$8.8^{+0.2}_{-0.17}$	$12.09^{+0.10}_{-0.11}$	$1.36^{+0.12}_{-0.18}$
UDS0564.1	$10.68^{+0.15}_{-0.15}$	$2.34^{+0.04}_{-0.09}$	$8.71^{+0.13}_{-0.09}$	$12.37^{+0.02}_{-0.07}$	$2.49^{+0.03}_{-0.17}$
AS2COS0083.1	$10.68^{+0.08}_{-0.08}$	$2.74^{+0.04}_{-0.05}$	$9.30^{+0.13}_{-0.07}$	$12.84^{+0.04}_{-0.03}$	$2.89^{+0.12}_{-0.03}$

Table 4.4: MAGPHYS-derived stellar masses, star-formation rates, dust masses, infrared luminosities and dust attenuation. The lower and upper bounds presented are taken as the 16th and 84th percentiles of the probability distribution function for the relevant parameter.

which is not captured as MAGPHYS does not include an AGN component. As the MAGPHYS SED libraries do not contain models with mid-infrared power laws, and therefore there are few models which fit the data well, the physical parameters from the fit still have relatively low uncertainties (e.g. in the case of AS2COS0048.1; see §4.3.1 for a discussion of the AGN properties of the sample).

For the SED fitting parameters we adopt the median of the probability distribution function from MAGPHYS, and for their uncertainties we adopt the 16th and 84th percentile values as the 1σ lower and upper bounds, respectively. In some cases this leads to lower and/or upper uncertainties of zero (implying that only one model has been found which fits the photometry within the uncertainties), in which cases we adopt the median fractional lower/upper uncertainty of the remainder of the sample. These median fractional uncertainties are $\sim15\%$ for star-formation rates, $\sim20\%$ for stellar masses, $\sim10\%$ for infrared luminosities and $\sim35\%$ for dust masses. We also compare the values of L_{IR} and M_* for the AS2UDS and AS2COSMOS sources with those derived from the photo-z version of MAGPHYS (Battisti et al., 2019) in Dudzevičiūtė et al. (2020) and Ikarashi et al. (in prep.) respectively, finding both sets of values to agree within their uncertainties.

We note that one of the sources in our sample, UDS0445.0, is not unambiguous in the identification of Hα as the detected emission line. From the 1-D and 2-D spectra the brighter [NII]$\lambda6583$ emission line appears to be present (see Fig. 4.6), but the S/N is too low to be confident that the line is not instead [OIII]. The SED fitting (see Fig. 4.11) does provide some diagnostic information, and indeed the photometry does appear to be better fit at the redshift corresponding to the emission line being [OIII]$\lambda5007$, hence it is possible that the line identification is incorrect.

The best-fit SED parameters and their uncertainties are shown in Table 4.4. Our sample of 43 SMGs has median values of $M_* = (1.2 \pm 0.2) \times 10^{11}\,\mathrm{M}_{\odot}$, $M_{\mathrm{dust}} = (5.1 \pm 0.8) \times 10^{8}\,\mathrm{M}_{\odot}$, $\mathrm{SFR} = 210 \pm 20\,\mathrm{M}_{\odot}\,\mathrm{yr}^{-1}$, $L_{\mathrm{IR}} = (2.5 \pm 0.4) \times 10^{12}\,\mathrm{L}_{\odot}$ and $A_V = 2.31 \pm 0.17$.

To compare with the AS2UDS SMGs we select the 283 sources in the range $z = 1.25$–2.6, which encompasses all the KAOSS sources (apart from one [OIII]-only source). The median photometric redshift of the AS2UDS subsample is $z_{\mathrm{phot}} = 2.1 \pm 0.03$, consistent with our the median for the KAOSS sample (see §4.3.4). These sources have corresponding median values of $M_* = (1.44 \pm 0.01) \times 10^{11}\,\mathrm{M}_{\odot}$, $M_{\mathrm{dust}} = (6.3 \pm 0.4) \times 10^{8}\,\mathrm{M}_{\odot}$, $\mathrm{SFR} = 173 \pm 6\,\mathrm{M}_{\odot}\,\mathrm{yr}^{-1}$, $L_{\mathrm{IR}} = (2.14 \pm 0.08) \times 10^{12}\,\mathrm{L}_{\odot}$ and $A_V = 2.6 \pm 0.09$. In other words, the sample we present in this chapter is representative of the AS2UDS sources at similar redshifts in terms of stel-

lar masses, dust masses and infrared luminosities, but has marginally higher SFRs, and marginally lower dust extinctions.

4.2.7 Size measurements

A key property of galaxies is the extent of the emission in different components. For example, $870\,\mu$m-selected galaxies are observed to be very compact in the dust emission relative to the stellar component, suggesting intense star formation in a compact region which may be linked to the formation of spheroids (Ikarashi et al., 2015; Simpson et al., 2015; Gullberg et al., 2019). A number of sources in the KAOSS sample have been observed at $870\,\mu$m with high enough spatial resolution to derive cold dust sizes (Gullberg et al., 2019), and we can supplement this with our Hα imaging and optical/NIR imaging to investigate and compare the extent of KAOSS sources in three different components: Hα, stellar continuum and cold dust continuum. Determining the extent and apparent axial ratio of the stellar emission is also necessary for deriving inclination angles and correcting observed rotational velocities, also a critical step in calculating accurate dynamical masses, which we will present in Chapter 5.

To measure optical sizes and inclinations we fit the 2-D H/K-band continuum with Sérsic profiles using the GALFIT code (Peng et al., 2010). This is also necessary for deriving inclination angles for correcting observed velocities (see Chapter 5). Where possible we use HST/F160W imaging, but this is only available for 19 of the 43 KAOSS sources, and so we also use ground-based K-band imaging from VISTA (McCracken et al., 2012; Jarvis et al., 2013, seeing $\sim 0.8''$) for the remaining 24 sources.

As a test of the suitability of lower-resolution ground-based K-band imaging we compare measurements of R_e and b/a from VISTA and HST/F160W for the 18 sources with coverage in both bands, fitting a fixed $n = 1$ profile in both cases. Fig. 4.12 shows that the two are consistent for these sources, and we therefore suggest that size and b/a measurements from ground-based K-band imaging are acceptable in the absence of HST/F160W imaging.

When fitting we constrain the Sérsic index n to be between 0.5 and 4 and allow all other parameters to vary. We visually inspect all fits and flag sources where we are unable to find a model that reproduces source structure, or where the best-fit parameters are unphysical (for example, sizes of $\ll 1$ pixel), although this is only necessary for three sources (GDS0046.0, UDS0707.0 and UDS0287.1, see Table 4.5). The median Sérsic index of the entire sample is
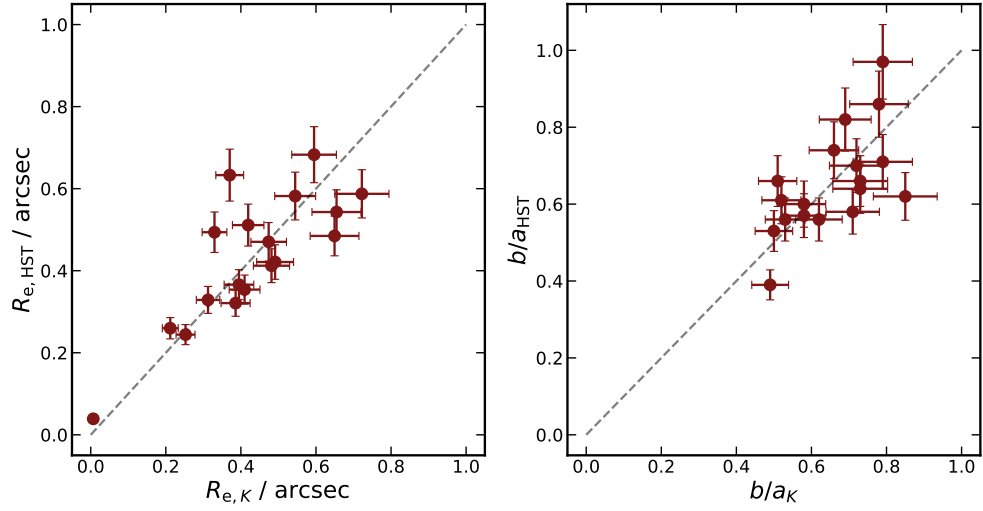
Figure 4.12: Comparison of effective radii R_e and axis ratios b/a measured from ground-based K-band and *HST* imaging for the same sources, assuming $n = 1$ in both cases. We find the two sets of values to be generally consistent within the 1σ uncertainties, and we therefore suggest that size and b/a measurements from ground-based K-band imaging are acceptable for sources without *HST*/F160W coverage in this study.

$n = 0.97 \pm 0.14$ from the fits with n as a free parameter, i.e. consistent with an exponential profile, and we therefore repeat the fitting fixing $n = 1$, following Gullberg et al. (2019).

In order to estimate uncertainties we simulate Sérsic profiles with known properties at different signal-to-noise ratios. We do this for two cases, one with PSFs comparable to the K-band imaging and one comparable to the *HST*/F160W imaging. We then calculate the dispersion in the measurements at different S/N. Fig. 4.13 shows our uncertainties estimated from these simulations with the S/N of the individual galaxies marked as ticks on the abscissa. However, the values plotted in Fig. 4.13 do not take into account other sources of uncertainty such as the fact that we have fixed $n = 1$, and that there is structure in the *HST* imaging that is not reproduced by the model profiles. We therefore elect to adopt a constant 10% uncertainty for all measurements of R_e and b/a, which from Fig. 4.13 we see is generally conservative.

In Chapter 5 we will use the dynamics to derive rotational velocities and subsequently dynamical masses. To measure the inclination we exploit the GALFIT parameters as follows:

$$\cos(i) = \sqrt{\frac{(b/a)^2 - (b/a)_0^2}{1 - (b/a)_0^2}} \tag{4.2.1}$$

where $(b/a)_0$ accounts for the fact that the discs have a finite thickness – we adopt $(b/a)_0 = 0.2$, following Gillman et al. (2019) and other similar surveys such as KROSS (Stott et al., 2016) and KGES (Gillman et al., 2020) for consistency.
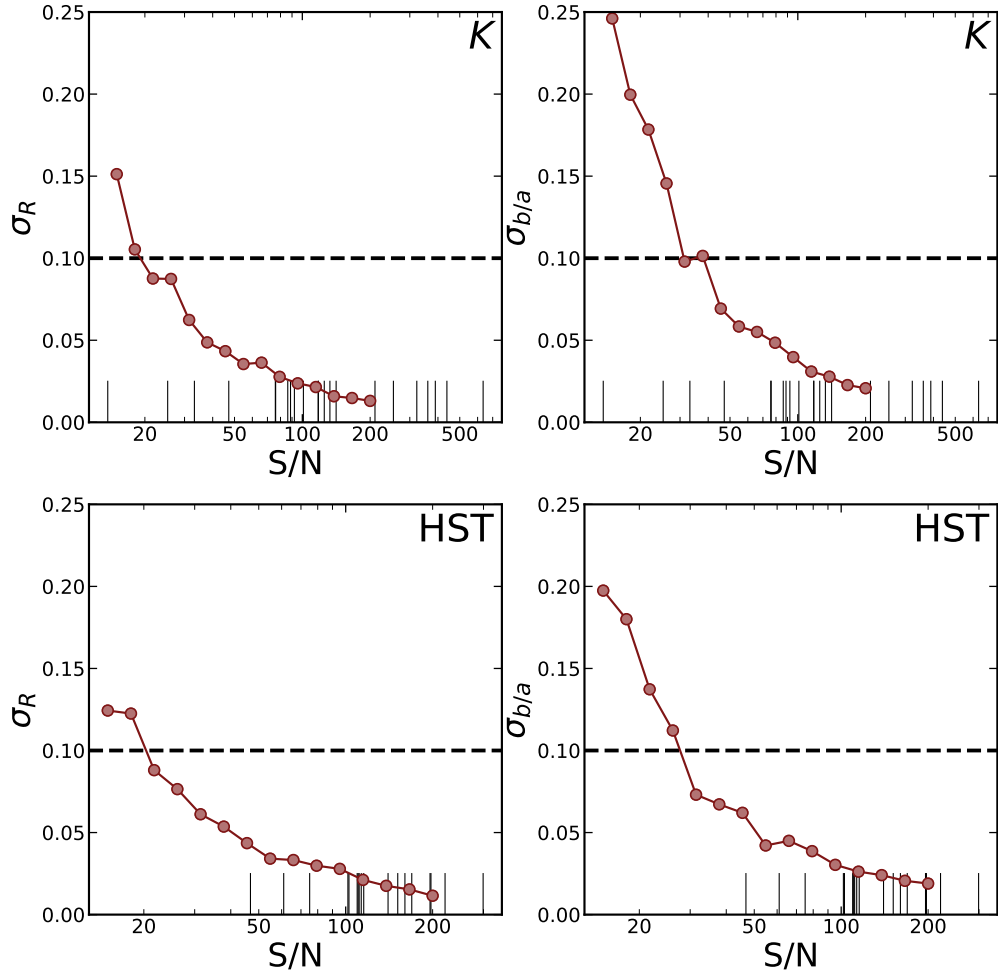
Figure 4.13: Fractional uncertainties on the effective radii (σ_R) and axial ratios ($\sigma_{b/a}$) for simulated Sérsic profiles fixing $n = 1$, as a function of signal-to-noise ratio (S/N). The top row displays the uncertainties measured from PSF sizes comparable to our ground-based imaging, and the bottom row displays the uncertainties measured from PSF sizes comparable to our *HST* F160W imaging. We indicate the S/N of the images of our KAOSS sources as ticks on the x-axis, and the 10% uncertainty adopted in our analysis (dashed). The vast majority of our sources have S/Ns which indicate that a 10% fractional uncertainty is conservative.

ID	Band	n_{free}	$b/a_{n=1}$	$R^{n=1}_{\text{optical}}$ [kpc]	$R^{n=1}_{\text{H}\alpha}$ [kpc]	$R^{n=1}_{\text{dust}}$ [kpc]
GDS0046.0	K	...	...	...	3.7 ± 0.2	...
GDS0040.0	F160W	2.1	0.6	2.1	5.4 ± 0.4	...
UDS0492.0	K	3.8	0.6	1.2	5.4 ± 0.5	...
UDS0707.0	K	...	...	...	3.0 ± 0.3	...
GDS0033.0	F160W	0.5	0.8	3.6	5 ± 2	...
AS2COS0048.1	K	2.4	0.8	3.2	3.7 ± 0.8	$1.8^{+0.2}_{-0.2}$
GDS0023.0	F160W	0.5	0.5	5.0	4.2 ± 0.3	...
UDS0624.0	K	4.0	0.8	1.3	...	...
A3COS298447	K	4.0	0.5	2.9	5.0 ± 1.0	...
GDS0001.0	F160W	1.6	0.9	2.7	3.8 ± 0.8	...
UDS0601.0	K	3.6	0.8	3.8	3.2 ± 0.7	...
GDS0004.0	F160W	0.5	0.6	4.6	4.7 ± 0.4	...
GDS0053.0	F160W	1.0	0.6	4.9	...	...
UDS0428.0	K	3.4	0.3	5.7	...	$0.4^{+0.3}_{-0.3}$
UDS0287.1	F160W	...	...	...	...	...
GDS0035.0	K	0.8	0.3	5.4	...	...
UDS0603.0	K	1.1	0.4	2.9	...	...
UDS0338.0	K	1.3	0.7	3.6	...	...
GDS0048.0	F160W	0.8	0.7	2.0	2.4 ± 0.6	...
A3COS795018	K	1.0	0.9	2.7	4 ± 1	...
GDS0065.0	F160W	1.3	0.7	5.4	...	...
AS2COS0025.1	F160W	0.7	0.6	3.4	4.8 ± 0.6	$1.78^{+0.13}_{-0.18}$
UDS0125.0	F160W	0.6	0.7	5.7	6 ± 2	$1.8^{+0.3}_{-0.2}$
GDS0031.0	F160W	0.6	0.6	3.9	6 ± 1	...
AS2COS0275.2	K	1.1	0.7	2.2	2.6 ± 0.4	$1.4^{+0.3}_{-0.3}$
UDS0115.0	K	0.9	0.3	5.0	2 ± 1	$0.9^{+0.2}_{-0.2}$
GDS0047.0	F160W	0.9	0.6	2.9	3.8 ± 0.5	...
GDS0020.0	F160W	0.6	0.7	3.1	...	...
UDS0035.0	K	1.2	0.9	2.7	...	$0.6^{+0.2}_{-0.3}$
UDS0199.0	K	0.5	0.7	6.3	...	$0.82^{+0.18}_{-0.2}$
GDS0071.0	F160W	0.5	0.6	4.3	...	...
UDS0445.0	K	1.8	0.6	3.3	1 ± 2	...
UDS0097.0	K	0.9	0.4	6.8	6.1 ± 0.3	...
UDS0292.0	F160W	0.8	1.0	2.7	4.2 ± 0.4	...
UDS0333.0	K	0.6	0.7	2.4	...	...
AS2COS0171.1	K	2.94	0.5	3.5	...	...
AS2COS0003.4	K	4.0	0.6	5.5	...	...
A3COS667642	F160W	0.5	0.4	4.0	...	...
UDS0116.0	F160W	0.52	0.6	4.1	...	...
UDS0564.1	K	0.5	0.2	6.5	...	...
AS2COS0083.1	K	0.5	0.4	7.5	...	$1.2^{+0.2}_{-0.2}$
AS2COS0116.2	K	4.0	0.8	3.6	...	...
UDS0109.0	K	0.7	0.1	7.9	...	...

Table 4.5: Sérsic indices n, axial ratios b/a, optical sizes, Hα sizes and dust sizes for the KAOSS sample. Sérsic indices n are derived from a free fit with GALFIT to either the VISTA K or HST/F160W imaging (constraining n to be between 0.5 and 4). b/a and R_{optical} are estimated from GALFIT modelling of the same images but with fixed $n = 1$. $R_{\text{H}\alpha}$ are derived from $n = 1$ Sérsic fits to the Hα imaging of spatially resolved sources (see Chapter 5), and dust sizes are measured from Sérsic fits to the $870\,\mu$m continuum emission (Gullberg et al., 2019, Ikarashi et al. in prep.). All values without quoted errors have a nominal 10% uncertainty.

We measure Hα sizes by fitting 2-D Sérsic profiles to the Hα emission in spatially resolved sources (see Chapter 5), with uncertainties derived by randomly sampling from the Hα flux error map and calculating the RMS in the derived values. We note here that while GALFIT was used to fit the optical/NIR data, we chose to instead use our own PYTHON routines to fit the Hα imaging. This choice was driven by the lower S/N in the Hα maps which we found to work less well with GALFIT, and creating our own PYTHON routines gave us more control over the fitting. Best fit values for the profile parameters are reported in Table 4.5, and we discuss the results further in §4.3.7.

4.3   Results and analysis

Having reduced and analysed the KMOS data currently available from KAOSS and estimated the source physical properties from SED fitting, we now move on to analysing their Hα and [OIII] integrated properties. We first identify the sources that are likely to be AGN hosts as determined from their rest-frame optical spectra along with their IRAC and X-ray photometry, so that we can flag these sources in subsequent analysis. We then discuss the integrated Hα and [OIII] line properties of the individual sources in the sample, along with the properties of composite spectra from the sample. We briefly discuss the redshift distribution of the sample, followed by a comparison of the Hα- and infrared-derived star-formation rates. Using measurements of the [NII]λ6583/Hα flux ratio we place our sources on the fundamental metallicity relation, the BPT diagram, and we finally discuss the galaxy sizes and shapes derived from GALFIT modelling.

4.3.1   Identifying potential AGN emission

To place our results in context it is important to first understand the fraction of sources with active galactic nuclei (AGN) in our sample. We expect this to be non-negligible – the largest sample of $870\,\mu$m-selected SMGs (also the main parent sample of KAOSS), the AS2UDS sample, contains an estimated 8–28% sources with AGN components (Stach et al., 2019). In addition to the wealth of photometric data available for our sources, our rest-frame optical spectra allows us to search for indications of AGN. Therefore to provide a census of AGN in our sample we assess how many sources meet the following criteria:

- Flux ratio [NII]λ6583/Hα > 0.8 (e.g. Wisnioski et al., 2018)

- Hα emission displays a broad component with a linewidth of FWHM $> 1000\,\mathrm{km\,s^{-1}}$ (e.g. Genzel et al., 2014)

- Presence of a luminous X-ray counterpart ($L_X \geq 10^{42}\,\mathrm{erg\,s^{-1}}$) matched within $1''$ (Civano et al., 2016; Luo et al., 2017; Franco et al., 2018; Kocevski et al., 2018)

- IRAC colours indicating an AGN according to the criteria of Donley et al. (2012)

Table 4.6 shows a summary of the AGN diagnostics for the emission line-detected KAOSS sources. In total 23 out of the sample of 43 sources fit one or more of these criteria, indicating an AGN fraction of $53 \pm 11\,\%$. This is significantly higher than the range quoted for the AS2UDS sample in Stach et al. (2019), but we expect a bias towards detecting AGN in our sample given the fact that such sources display stronger emission lines. Additionally, this should be treated as an upper limit given that some sources may meet the criteria for other reasons, for example high [NII]/Hα ratios may also arise from high metallicities (e.g. Allen et al., 2008; Kewley & Ellison, 2008). Only two sources meet all four criteria, these are UDS0492.0 and UDS0287.1. We also note here that the presence of AGN in these sources does not necessarily mean that the AGN are energetically important, and we do not attempt to estimate the fractional contribution of the AGN to the total luminosity.

We separate potential AGN host sources into two categories: those that are classified as AGN based on their rest-frame optical spectra, and those that are classified as AGN based on their X-ray and/or IRAC properties. In the former case we include the 14 sources ($33 \pm 9\%$ of the sample) which either [NII]/Hα > 0.8 and $\mathrm{FWHM_{H\alpha}} > 1000\,\mathrm{km\,s^{-1}}$. In the latter category we find 18 sources ($42 \pm 10\%$) including eight that are also in the spectral AGN sample. The only source we classify as AGN hosts based on its spectral properties without finding an X-ray counterpart or AGN-like IRAC colours is AS2COS0003.4 (In §4.3.2 we note that the fit to this line is likely to be unreliable). In all plots that follow we flag AGN-classified SMGs as stars, with the remaining 21 star-forming sources (49 ± 11) shown as circular points.

4.3.2 Emission line properties

From our inspection of the 2D cubes we identify 43 sources with robust line detections and secure line IDs, 42 of which display Hα emission and six of which display [OIII] emission (five display both Hα and [OIII] emission). Figs. 4.6–4.8 show 1-D spectra of the Hα-detected sources, and Fig. 4.9 shows 1-D spectra of the [OIII]-detected sources. We overlay the fits to the data (as described in §4.2.5) and indicate by dashed lines the wavelengths of key emission

ID	z_{KAOSS}	[NII]/Hα	Hα FWHM [km s^{-1}]	X-ray counterpart	IRAC colours	AGN?
GDS0046.0	1.6153	0.7 ± 0.4	$\mathbf{3300 \pm 1100}^{\dagger}$	✗	✓	✓
GDS0040.0	2.2254	0.68 ± 0.08	630 ± 40	✓	✓	✓
UDS0492.0	1.2785	$\mathbf{0.9 \pm 0.6}$	$\mathbf{3400 \pm 700}^{\dagger}$	✓	✓	✓
UDS0707.0	2.4358	0.2 ± 0.5	$\mathbf{3200 \pm 1600}^{\dagger}$	✗	✓	✓
GDS0033.0	1.6157	0.45 ± 0.10	300 ± 40	✗	✗	✗
AS2COS0048.1	1.5775	0.40 ± 0.10	$\mathbf{2300 \pm 1600}^{\dagger}$	✓	✓	✓
GDS0023.0	1.6178	0.60 ± 0.09	480 ± 40	✗	✗	✗
UDS0624.0	1.4063	0.7 ± 0.2	630 ± 160	✗	✓	✓
A3COS298447	2.3886	0.47 ± 0.12	470 ± 130	✗	✗	✗
GDS0001.0	1.5393	$\mathbf{1.1 \pm 0.3}$	360 ± 40	✓	✗	✓
UDS0601.0	1.4629	0.45 ± 0.13	480 ± 70	✗	✗	✗
GDS0004.0	1.9658	0.7 ± 0.2	340 ± 110	✗	✗	✗
GDS0053.0	1.6158	0.2 ± 0.2	390 ± 120	✓	✗	✓
UDS0428.0	1.6285	0.68 ± 0.11	560 ± 50	✗	✗	✗
UDS0287.1	2.2904	$\mathbf{0.9 \pm 0.3}$	560 ± 100	✓	✓	✓
GDS0035.0	1.6152	0.8 ± 0.5	460 ± 120	✗	✗	✗
UDS0603.0	2.5084	0.38 ± 0.14	300 ± 90	✗	✗	✗
UDS0338.0	1.6609	$\mathbf{1.0 \pm 0.3}$	210 ± 110	✗	✗	✓
GDS0048.0	2.5451	$\mathbf{1.3 \pm 0.7}$	600 ± 200	✗	✓	✓
A3COS795018	1.5780	0.41 ± 0.05	190 ± 20	✗	✗	✗
GDS0065.0	1.6151	0.2 ± 0.2	900 ± 200	✓	✗	✓
AS2COS0025.1	2.0860	0.49 ± 0.12	470 ± 70	✗	✗	✗
UDS0125.0	2.1553	0.66 ± 0.08	430 ± 50	✗	✗	✗
GDS0031.0	2.0381	0.0 ± 0.0	810 ± 130	✗	✗	✗
AS2COS0275.2	1.6333	$\mathbf{0.9 \pm 0.3}$	470 ± 70	✓	✓	✓
UDS0115.0	2.0334	0.3 ± 0.3	590 ± 130	✗	✗	✗
GDS0047.0	2.3239	0.0 ± 0.3	820 ± 180	✓	✓	✓
GDS0020.0	1.9240	0.2 ± 0.2	570 ± 180	✗	✗	✗
UDS0035.0	2.0874	0.5 ± 0.2	800 ± 300	✗	✗	✗
UDS0199.0	2.5547	0.22 ± 0.13	920 ± 140	✗	✓	✓
GDS0071.0	1.7313	0.6 ± 0.6	200 ± 300	✗	✗	✗
UDS0445.0	2.2928	$\mathbf{1.1 \pm 0.5}$	550 ± 120	✓	✗	✓
UDS0097.0	2.5890	0.0 ± 0.0	$\mathbf{1170 \pm 190}$	✗	✗	✓
UDS0292.0	2.1829	0.52 ± 0.09	330 ± 50	✓	✗	✓
UDS0333.0	1.2775	$\mathbf{0.82 \pm 0.17}$	480 ± 90	✗	✓	✓
AS2COS0171.1	2.3416	...	...	✗	✗	✗
AS2COS0003.4	2.5038	$\mathbf{1.2 \pm 0.6}$	700 ± 200	✗	✗	✓
A3COS667642	2.1052	0.3 ± 0.2	140 ± 120	✗	✗	✗
UDS0116.0	2.2233	0.3 ± 0.2	380 ± 150	✗	✗	✗
UDS0564.1	1.6927	0.36 ± 0.08	230 ± 70	✗	✗	✗
AS2COS0083.1	2.5010	$\mathbf{1.9 \pm 0.6}$	220 ± 100	✗	✗	✓
AS2COS0116.2	2.1822	0.000 ± 0.014	800 ± 200	✗	✓	✓
UDS0109.0	1.6249	0.000 ± 0.005	160 ± 90	✗	✗	✗

Table 4.6: Four AGN diagnostics for our KAOSS sources. For [NII]/Hα ratios and line widths we highlight values which satisfy our criteria for AGN ([NII]/H$\alpha > 0.8$ and FWHM $> 1000 \, \text{km s}^{-1}$) in bold. A $\dagger$ indicates that the line width shown is for a broad component. For the "IRAC colours" criterion we show a tick or cross to indicate whether or not the source is classified as an AGN according to the Donley et al. (2012) criteria.
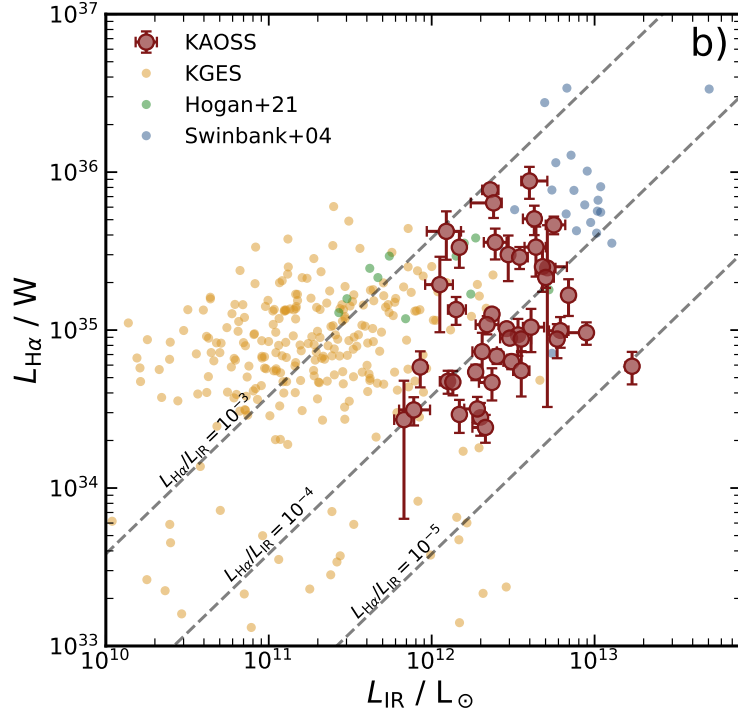
Figure 4.14: Hα luminosity $L_{\text{H}\alpha}$ versus infrared luminosity L_{IR} for Hα-detected KAOSS SMGs, $z \sim 1.5$ KGES galaxies (Tiley et al., 2021), $z \sim 2.5$ ULIRGs (Hogan et al., 2021) and $z \sim 2.5$ SMGs (Swinbank et al., 2004). Our sample has comparable Hα luminosities to the $z \sim 2.5$ ULIRGs, but is fainter in both the Hα and infrared than the Swinbank et al. (2004) SMGs. The KAOSS SMGs have a ratio of $L_{\text{H}\alpha}/L_{\text{IR}} \sim 10^{-4}$. When compared to $z \sim 1.5$ KGES galaxies our sources are much brighter in the infrared, but of comparable luminosity in the Hα emission. This is a result of much heavier dust obscuration in our sample – which has a median dust extinction from MAGPHYS SED fitting of $A_V = 2.31 \pm 0.17$ compared to $A_V = 0.71 \pm 0.04$ for the KGES sample.

lines. We note that in the cases of AS2COS0003.4 and AS2COS0171.1, the fits to the data are poor. In the former case the S/N is low, and the fit is very broad (see Table 4.9), therefore this line may not be real. In the latter case, we fit an [O III] doublet, but at the [O III] redshift the Hα line appears to be absent, suggesting that the line ID may be inaccurate.

For sources where the emission was determined by its AIC to be more appropriately modelled with a narrow and broad component, we also show these two components separately. The measured properties of the detected Hα and [O III] emission lines are presented in Tables 4.7 and 4.8 respectively. In the remainder of this section we will briefly discuss the best-fit line luminosities and widths, and compare to them to other samples, and we will discuss the measured [N II]/Hα flux ratios in §4.3.6.

In Fig. 4.14 we show the Hα luminosity of our sample (uncorrected for dust extinction; $L_{\text{H}\alpha}$)

ID	R.A. (J2000)	Dec. (J2000)	$z_{H\alpha}$	$S/N_{H\alpha}$	$F_{H\alpha}/10^{-19}$ [W m^{-2}]	FWHM$_{H\alpha}$ [km s^{-1}]	[NII]/Hα	Cont./10^{-15} [erg cm^{-2} μm^{-1}]
GDS0046.0	53.1049	-27.7053	1.6142	101.7	1.8 ± 0.6	710 ± 130	0.7 ± 0.4	7.9 ± 0.6
GDS0040.0	53.1311	-27.7732	2.2254	93.9	2.06 ± 0.13	630 ± 40	0.68 ± 0.08	8.8 ± 0.3
UDS0492.0	34.5398	-5.0334	1.2787	74.4	0.29 ± 0.07	280 ± 50	0.9 ± 0.6	6.5 ± 0.6
UDS0707.0	34.7984	-5.2526	2.4367	55.7	0.5 ± 0.5	700 ± 400	0.2 ± 0.5	3.6 ± 0.4
GDS0033.0	53.0727	-27.8343	1.6155	45.9	0.74 ± 0.06	300 ± 40	0.45 ± 0.10	4.2 ± 0.2
AS2COS0048.1	150.2885	2.3819	1.5813	34.7	0.61 ± 0.13	250 ± 70	0.40 ± 0.10	5.0 ± 0.5
GDS0023.0	53.1572	-27.8335	1.6177	31.4	0.59 ± 0.04	480 ± 40	0.60 ± 0.09	2.9 ± 0.4
UDS0624.0	34.1012	-5.2103	1.4058	26.6	0.56 ± 0.06	630 ± 160	0.7 ± 0.2	5.3 ± 0.3
A3COS298447	149.9483	1.7386	2.3889	26.4	2.0 ± 0.5	470 ± 130	0.47 ± 0.12	8.9 ± 0.7
GDS0001.0	53.0304	-27.8558	1.5390	24.7	0.36 ± 0.04	360 ± 40	1.1 ± 0.3	3.9 ± 0.3
UDS0601.0	34.8179	-5.2796	1.4628	22.1	0.35 ± 0.06	480 ± 70	0.45 ± 0.13	4.8 ± 0.3
GDS0004.0	53.0204	-27.7799	1.9657	22.1	0.34 ± 0.09	340 ± 110	0.7 ± 0.2	2.9 ± 0.3
GDS0053.0	53.1989	-27.8439	1.6157	20.6	0.27 ± 0.05	390 ± 120	0.2 ± 0.2	3.1 ± 0.3
UDS0428.0	34.7962	-4.9427	1.6284	19.6	0.36 ± 0.04	560 ± 50	0.68 ± 0.11	1.1 ± 0.2
UDS0287.1	34.3653	-5.2508	2.2907	18.9	1.6 ± 0.3	560 ± 100	0.9 ± 0.3	14 ± 1
GDS0035.0	53.0917	-27.7121	1.6145	18.4	0.17 ± 0.04	460 ± 120	0.8 ± 0.5	2.0 ± 0.2
UDS0603.0	34.8121	-5.2893	2.5086	18.3	0.72 ± 0.16	300 ± 90	0.38 ± 0.14	4.9 ± 0.5
UDS0338.0	34.0932	-5.0805	1.6612	18.1	0.17 ± 0.03	210 ± 110	1.0 ± 0.3	2.9 ± 0.2
GDS0048.0	53.1606	-27.7763	2.5453	17.0	0.48 ± 0.15	600 ± 200	1.3 ± 0.7	0.00 ± 0.08
A3COS795018	149.5035	2.5070	1.5780	16.8	0.55 ± 0.04	190 ± 20	0.41 ± 0.05	3.51 ± 0.18
GDS0065.0	53.1315	-27.8414	1.6140	16.6	0.34 ± 0.09	900 ± 200	0.2 ± 0.2	3.5 ± 0.4
AS2COS0025.1	150.1635	2.3725	2.0859	16.3	0.30 ± 0.05	470 ± 70	0.49 ± 0.12	1.87 ± 0.15
UDS0125.0	34.3633	-5.1994	2.1556	15.7	0.62 ± 0.09	430 ± 50	0.66 ± 0.08	3.0 ± 0.2
GDS0031.0	53.0774	-27.8596	2.0360	15.7	0.45 ± 0.09	810 ± 130	0.0 ± 0.0	1.4 ± 0.2
AS2COS0275.2	149.9517	1.7440	1.6334	14.9	0.50 ± 0.08	470 ± 70	0.9 ± 0.3	3.0 ± 0.4
UDS0115.0	34.5119	-5.0086	2.0335	14.9	0.20 ± 0.05	590 ± 130	0.3 ± 0.3	1.8 ± 0.2
GDS0047.0	53.1635	-27.8906	2.3237	14.0	0.69 ± 0.11	820 ± 180	0.0 ± 0.3	1.9 ± 0.3
GDS0020.0	53.1983	-27.7479	1.9236	12.2	0.21 ± 0.07	570 ± 180	0.2 ± 0.2	0.60 ± 0.17
UDS0035.0	34.1691	-5.1831	2.0863	10.8	0.27 ± 0.07	800 ± 300	0.5 ± 0.2	0.7 ± 0.3
UDS0199.0	34.8455	-5.2497	2.5553	10.6	0.88 ± 0.11	920 ± 140	0.22 ± 0.13	0.00 ± 0.17
GDS0071.0	53.0568	-27.7984	1.7313	9.7	0.13 ± 0.10	200 ± 300	0.6 ± 0.6	0.71 ± 0.18
UDS0445.0	34.4759	-5.0255	2.2922	9.6	0.18 ± 0.06	550 ± 120	1.1 ± 0.5	1.47 ± 0.14
UDS0097.0	34.8680	-5.2059	2.5928	8.8	0.9 ± 0.2	1170 ± 190	0.0 ± 0.0	0.6 ± 0.3
UDS0292.0	34.3226	-5.2301	2.1829	8.5	0.30 ± 0.04	330 ± 50	0.52 ± 0.09	2.18 ± 0.18
UDS0333.0	34.5285	-4.9882	1.2773	8.3	0.25 ± 0.05	480 ± 90	0.82 ± 0.17	1.7 ± 0.2
AS2COS0003.4	150.2369	2.3358	2.4991	7.9	0.8 ± 0.3	700 ± 200	1.2 ± 0.6	2.9 ± 0.9
A3COS667642	150.1121	2.3140	2.0984	7.9	0.6 ± 0.3	140 ± 120	0.3 ± 0.2	1.4 ± 0.8
UDS0116.0	34.3335	-5.2182	2.2251	7.6	0.9 ± 0.3	380 ± 150	0.3 ± 0.2	0.8 ± 0.7
UDS0564.1	34.7234	-4.9923	1.6929	7.4	0.24 ± 0.06	230 ± 70	0.36 ± 0.08	1.20 ± 0.15
AS2COS0083.1	149.9157	1.7868	2.4987	6.1	0.33 ± 0.09	220 ± 100	1.9 ± 0.6	0.0 ± 0.3
AS2COS0116.2	150.4904	1.7464	2.1839	5.4	0.29 ± 0.09	800 ± 200	0.000 ± 0.014	0.8 ± 0.4
UDS0109.0	34.0766	-5.3723	1.6249	4.7	0.18 ± 0.04	160 ± 90	0.000 ± 0.005	0.2 ± 0.2

Table 4.7: Integrated Hα emission line properties of KAOSS SMGs. The median fractional error on the redshifts is 0.0002, or $60 \, \mathrm{km \, s^{-1}}$. For sources with broad Hα components the linewidths and fluxes shown here are for the narrow component, with the broad component properties shown in Table 4.9.

ID	R.A. (J2000)	Dec. (J2000)	$z_{[\mathrm{OIII}]}$	S/N$_{[\mathrm{OIII}]}$	$F_{[\mathrm{OIII}]}/10^{-19}$ [W m^{-2}]	FWHM$_{[\mathrm{OIII}]}$ [km s^{-1}]	$\frac{[\mathrm{OIII}]_{4959}}{[\mathrm{OIII}]_{5007}}$	Cont./10^{-15} [erg cm^{-2} μm^{-1}]
UDS0199.0	34.8455	−5.2497	2.5560	47.9	1.72 ± 0.10	960 ± 90	0.53 ± 0.07	1.0 ± 0.2
GDS0040.0	53.1311	−27.7732	2.2244	44.1	1.08 ± 0.12	630 ± 100	0.36 ± 0.05	6.6 ± 0.4
UDS0603.0	34.8121	−5.2893	2.5085	28.5	0.19 ± 0.06	310 ± 140	0.00 ± 0.10	5.9 ± 0.3
UDS0097.0	34.8680	−5.2059	2.5924	20.2	1.2 ± 0.3	1290 ± 170	0.34 ± 0.14	0.57 ± 0.18
AS2COS0003.4	150.2369	2.3358	2.4991	7.3	1.1 ± 0.3	1590 ± 200	1.3 ± 0.5	1.2 ± 0.8
AS2COS0171.1	149.9721	1.7141	2.3406	7.2	0.9 ± 0.2	830 ± 170	0.3 ± 0.2	1.6 ± 0.5

Table 4.8: Integrated [OIII]λ5007 emission line properties of KAOSS SMGs.

ID	Line	z	$F_{\mathrm{broad}}/F_{\mathrm{narrow}}$	FWHM$_{\mathrm{broad}}$ [km s^{-1}]
GDS0046.0	Hα	1.6142	5 ± 2	3300 ± 1100
UDS0492.0	Hα	1.2787	12 ± 3	3400 ± 700
UDS0707.0	Hα	2.4367	4 ± 4	3200 ± 1600
AS2COS0048.1	Hα	1.5813	9 ± 7	2300 ± 1600

Table 4.9: Broad Hα line properties of four KAOSS sources. These were determined to be better fit by including a broad Hα component in addition to the narrow Hα+[NII] triplet.

versus their linewidths (FWHM$_{\mathrm{H}\alpha}$). We also indicate in Fig. 4.14 lines of constant $L_{\mathrm{H}\alpha}/L_{\mathrm{IR}}$, and we see that the H$\alpha$ luminosities of the SMGs are approximately 10^4 times lower than their IR luminosities. The 43 Hα-detected KAOSS sources have a median Hα luminosity of $L_{\mathrm{H}\alpha} = (10 \pm 2) \times 10^{34}$ W, with medians of $L_{\mathrm{H}\alpha} = (9.3 \pm 1.8) \times 10^{34}$ W for the star-forming sample and $L_{\mathrm{H}\alpha} = (11 \pm 6) \times 10^{34}$ W for the AGN sample. Thus, the star-forming sources and the AGN hosts have consistent Hα luminosities. In contrast, the $z \sim 2.5$ ULIRGs detected in Hα by Hogan et al. (2021) have a higher median of $L_{\mathrm{H}\alpha} = (23 \pm 3) \times 10^{34}$ W, which is more comparable to the AGN-classified sources in the KAOSS sample. From the KMOS^{3D} survey (Wisnioski et al., 2019) the median Hα luminosity is $L_{\mathrm{H}\alpha} = (16 \pm 2) \times 10^{34}$ W, again higher than the KAOSS SMGs, although these sources have lower dust extinctions than the KAOSS SMGs (median $A_V = 0.8 \pm 0.05$ for KMOS^{3D}; Wisnioski et al., 2019, compared to 2.31 ± 0.17 for KAOSS).

Within the sample KAOSS sample we measure a median Hα full width at half maximum (FWHM) of FWHM$_{\mathrm{H}\alpha} = 480 \pm 50$ km s^{-1}, with medians of FWHM$_{\mathrm{H}\alpha} = 460 \pm 50$ km s^{-1} for the star-forming sample and FWHM$_{\mathrm{H}\alpha} = 590 \pm 80$ km s^{-1} for the AGN sample. Therefore, the AGN host galaxies in our sample have broader Hα emission lines than the star-formation-dominated sources, although this is largely due to the fact that we have used broad emission lines as a diagnostic for identifying AGN. Comparing with Hogan et al. (2021), they find a median of FWHM$_{\mathrm{H}\alpha} = 280 \pm 50$ km s^{-1}, significantly lower than our sample, although this is

partially driven by the AGN in our sample, whereas the Hogan et al. (2021) sample is unlikely to have as much AGN contamination as KAOSS as their [NII]/Hα flux ratios are lower than ours (see §4.3.6).

Comparing the Hα and [OIII] emission lines, we find a median [OIII] linewidth of FWHM$_{[OIII]}$ = 900 ± 200 km s^{-1}, broader that than of the Hα, but among the sources with detections of both lines, the Hα and [OIII] linewidths are comparable, except for AS2COS0003.4 which displays much broader [OIII] emission FWHM$_{[OIII]}$ = 1600 ± 200 km s^{-1} versus FWHM$_{H\alpha}$ = 700 ± 200 km s^{-1}. As noted in §4.3.2 however, the fit to this line is poor, and it is possible that the line is not real.

4.3.3 Composite spectra

To assess the general properties of the sample and search for evidence of weaker emission lines (e.g. Hβ) that do not appear as significant detections in individual spectra we also generate composite spectra of the following four sub-samples:

1. 21 sources with no indication of AGN activity, which we label the *star-forming* composite.

2. 14 sources with evidence of AGN activity from the rest-frame optical spectra, which we label the *spectral AGN* composite (see Table 4.6).

3. 18 sources with evidence of AGN activity from a luminous X-ray counterpart or AGN-like IRAC colours (Donley et al., 2012), which we label the *X-ray/IRAC AGN* composite (see Table 4.6).

4. A composite of all 43 galaxies in the sample.

These composites are created by continuum subtracting the spectra with a running median (using a window large enough to avoid subtracting from the emission line flux), de-redshifting, normalising by the Hα flux and taking a median at each wavelength. The four resultant composites are shown in Fig. 4.15. In all four composites we see a strong detection of the Hα emission line, albeit much broader in the spectral AGN composite (FWHM $\sim$ 840 km s^{-1} in the rest-frame compared to FWHM $\sim$ 200 km s^{-1} for the other three samples). Additionally, the *star-forming* composite shows little evidence of [OIII] emission, but a 5σ detection of the [SII] doublet at λ = 0.6716 μm and 0.6731 μm, which is only detected at 3.5σ in the *X-ray/IRAC AGN* composite and not at all in the *spectral AGN* composite. There is also weak

evidence for NaD absorption at $\lambda = 0.5892\,\mu$m (which was also found by Swinbank et al. (2004) for submillimetre-selected galaxies) in the *star-forming* composite. The line ratios of these four composites are discussed in the context of the BPT diagram in §4.3.6. Although not attempted here, we note that the relative strengths of the Hα and Hβ fluxes (the Balmer decrement) could be used to estimate the extinction directly from the gas, rather than from the stellar emission via the SED fits.

4.3.4 Redshift distribution

We now present the spectroscopic redshifts of the 43 KAOSS SMGs, which are shown in Tables 4.7 and 4.8. As previously discussed the number of SMGs with robust redshifts is low, and therefore the KAOSS sample presents a significant increase on what is currently available. Fig. 4.16 shows the redshift distribution of the 43 emission line-detected KAOSS sources. For comparison we also show the distribution of photometric redshifts from the AS2UDS sample. The median redshift of the KAOSS sources is $z = 2.03 \pm 0.16$, significantly lower than the median of $z = 2.61 \pm 0.08$ for the AS2UDS sample, with a median uncertainty on the KAOSS redshifts of 0.0002, or $60\,\mathrm{km\,s^{-1}}$. We also split the KAOSS redshift distribution by survey field, and find that sources are detected at marginally lower redshifts in the ECDFS field than in COSMOS and UDS – with a median of $z = 1.67 \pm 0.14$ for ECDFS compared to $z = 2.1 \pm 0.2$ for UDS and $z = 2.1 \pm 0.2$ for COSMOS. This is likely because the SCUBA-2 $850\,\mu$m coverage of this field (Cowie et al., 2018) is deeper than the other two fields, meaning that the targets are fainter at $870\,\mu$m and therefore more likely to be found at lower redshifts due to the $S_{870} - z$ correlation (Chapter 3; Birkin et al., 2021).

There is a noticeable spike in the redshift distribution at $z \sim 1.6$ in the GOODS-S field, and investigating further we find that there are five sources in the GOODS-S field which lie within $\sim 150\,\mathrm{km\,s^{-1}}$ of each other at $z \sim 1.615$ – GDS0033.0, GDS0035.0, GDS0046.0, GDS0053.0 and GDS0065.0. These are found in two groups on the sky: GDS0035.0 and GDS0046.0 are separated by a projected distance of $0.8\,'$ ($\sim 400\,$kpc), and the remaining three sources are in a patch $\sim 3\,'$ across ($\sim 1.6\,$Mpc). The two groups are separated by $\sim 4\,$Mpc. We conclude that these SMGs are located within the same large-scale structure in the GOODS-S field, representing a similar finding to the work of Mitsuhashi et al. (2021) who found six SMGs in a structure at $z \sim 4.6$ in the COSMOS field.
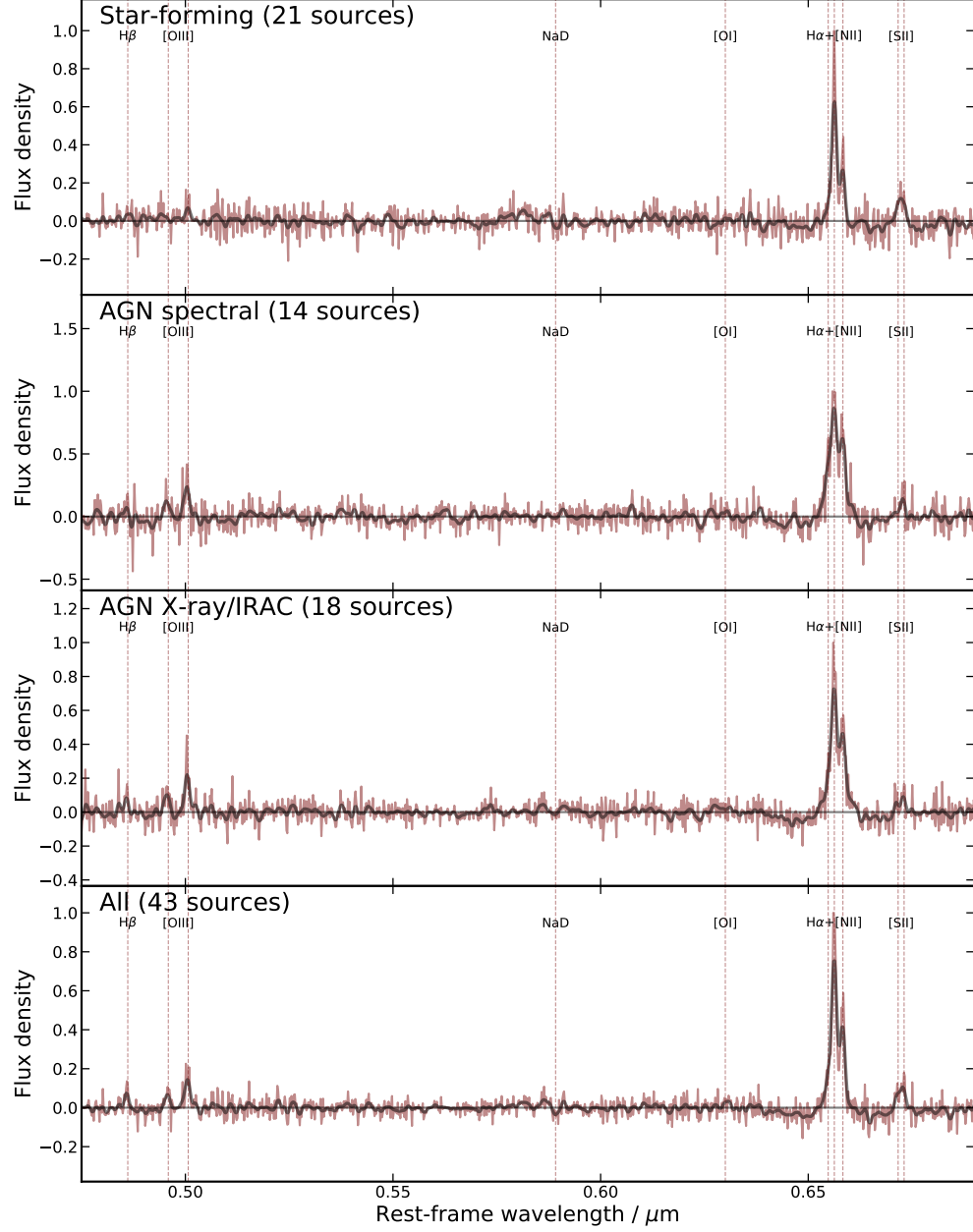
Figure 4.15: Median stack of SMG spectra from four subsets of the KAOSS sample (red), where each panel is labelled to identify the relevant subset (also see §4.3.2 for more details) We smooth the spectra with a Gaussian filter to more clearly show the line emission (black), and indicate by dashed vertical lines key rest-frame optical emission lines: Hβ (0.486 μm), [OIII] (0.4959 μm and 0.5007 μm), [OI] (0.63 μm), Hα (0.6563 μm), [NII] (0.6548 μm and 0.6583 μm) and [SII] (0.6716 μm and 0.6731 μm). We also indicate the wavelength of the NaD absorption line (0.5892 μm), for which there is weak evidence in the star-forming composite. We detect Hβ emission in the AGN subsets, and [SII] emission in the star-forming subset.
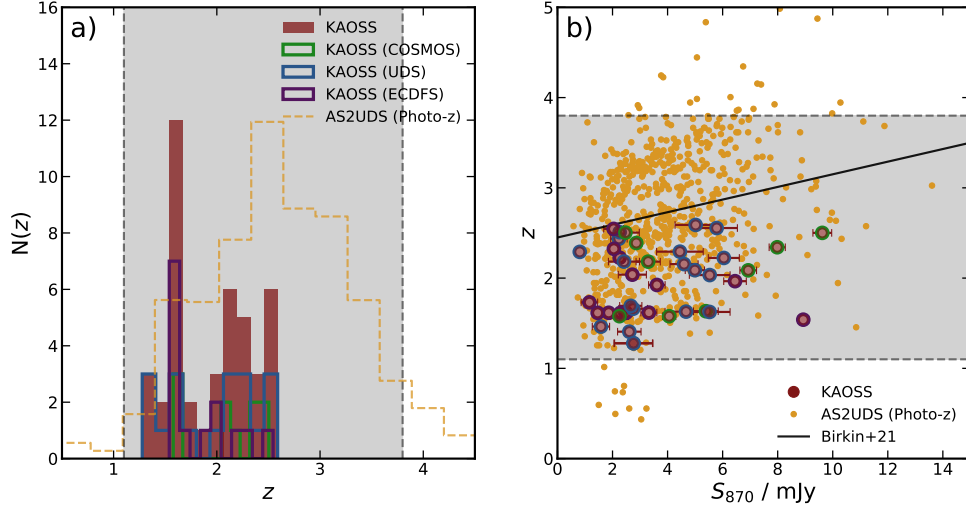
Figure 4.16: **a)** Redshift distribution of the KAOSS sample compared with the AS2UDS sample. The spectroscopically confirmed KAOSS sources have a median redshift of $z = 2.03 \pm 0.16$. We also split the sample by survey field, which shows that we detect sources typically at lower redshifts in the ECDFS field than in COSMOS and UDS – a consequence of the $870\,\mu$m coverage of this field being deeper (see the text for more details). **b)** Redshift versus $870\,\mu$m flux for emission line-detected sources in KAOSS and also AS2UDS SMGs. While there is evidence for a positive trend between the two quantities plotted (we show as a black line the trend derived in Chapter 3), the KAOSS sources in this figure do not follow this trend. However, this is likely due to the fact that we sample only a modest range in redshift, limited by the need to detect strong emission lines in the KMOS HK band.

4.3.5   Obscured and unobscured star-formation rates

Hα emission is a tracer of recent star formation, as in star-forming galaxies young O- and B-type stars provide the majority of ionising radiation that produces it, unless a luminous AGN is present (Kennicutt & Evans, 2012). The Hα luminosity can therefore be used to estimate the star-formation rate, which we do according to (Kennicutt, 1998a):

$$\mathrm{SFR}_{\mathrm{H}\alpha} = C_{\mathrm{IMF}} X_{\mathrm{H}\alpha} L_{\mathrm{H}\alpha}, \tag{4.3.1}$$

where $C_{\mathrm{IMF}} = 10^{-0.201}$ is the factor used to convert to a Chabrier (2003) IMF (Madau & Dickinson, 2014), $X_{\mathrm{H}\alpha} = 7.9 \times 10^{-42}\,\mathrm{M}_\odot\,\mathrm{yr}^{-1}\,\mathrm{erg}\,\mathrm{s}^{-1}$ is the conversion between $L_{\mathrm{H}\alpha}$ and SFR assuming a Salpeter (1955) initial mass function (IMF) and the observed Hα luminosity $L_{\mathrm{H}\alpha}$ is measured in $\mathrm{erg}\,\mathrm{s}^{-1}$.

Our sources are heavily dust obscured (median dust extinction $A_V = 2.31 \pm 0.17$ from the MAGPHYS analysis; see §4.2.6), and so the Hα emission is likely to underestimate the SFR in relation to the IR emission, potentially by orders of magnitude as is seen in compact star-forming galaxies (Swinbank et al., 2004; Rodríguez-Zaurín et al., 2011). We therefore
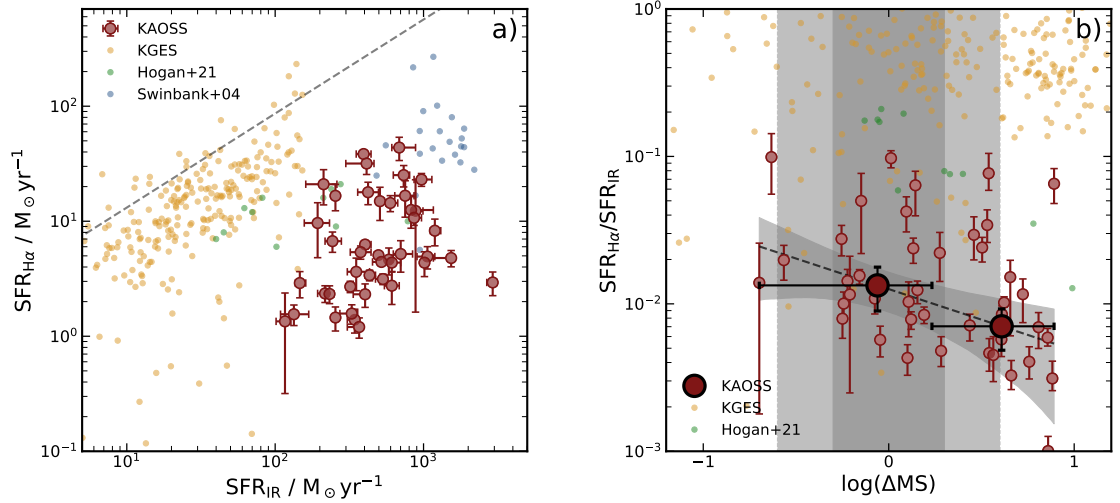
Figure 4.17: **a)** SFR derived from the Hα emission versus SFR derived from the infrared emission for Hα-detected KAOSS SMGs, $z \sim 1.5$ KGES galaxies (Tiley et al., 2021), $z \sim 2.5$ ULIRGs (Hogan et al., 2021) and $z \sim 2.5$ SMGs (Swinbank et al., 2004). In our sample and the other ULIRG/SMG samples we see that the Hα emission underestimates the SFR when compared to the IR emission. We interpret this result as confirming that KAOSS SMGs are more heavily dust-obscured than less active galaxies such as those in the KGES sample. **b)** SFR$_{\mathrm{H}\alpha}$/SFR$_{\mathrm{IR}}$ versus the logarithm of the offset from the star-forming main sequence ΔMS, calculated using the prescription of Speagle et al. (2014). Approximately half of the KAOSS sample lie within the 0.3 dex scatter of the main sequence at their redshift. We find no evidence for more sources with higher ΔMS experiencing stronger dust obscuration in the KAOSS sample.

also estimate SFRs from the IR emission, which we will compare with the Hα-derived SFRs, according to (Kennicutt, 1998a):

$$\mathrm{SFR_{IR}} = 4.5 \times 10^{-37} L_{\mathrm{IR}}, \tag{4.3.2}$$

where L_{IR}, as derived from SED fitting (see §4.2.6), is measured in W. The median infrared-derived SFR of our sample is $\mathrm{SFR_{IR}} = 430 \pm 60\,\mathrm{M_\odot\,yr^{-1}}$, which is much higher than the median Hα-derived $\mathrm{SFR_{H\alpha}} = 4.9 \pm 0.9\,\mathrm{M_\odot\,yr^{-1}}$. Therefore as we would expect for SMGs, the star-formation rate is significantly underestimated by the Hα (by a factor of ~ 90 in this case).

As the infrared and Hα emission trace obscured and relatively unobscured star formation respectively we can use the ratio $\mathrm{SFR_{H\alpha}/SFR_{IR}}$ to study how dust obscured our SMGs are when compared to other samples. Fig. 4.17 shows the SFR derived from the Hα emission according to Eq. 4.3.1 as a function of the SFR derived from the infrared emission according to Eq. 4.3.2. While $\mathrm{SFR_{H\alpha}}$ is approximately $100\times$ lower than $\mathrm{SFR_{IR}}$ for KAOSS, many of the less active galaxies in the KGES sample lie close to or on the 1:1 line. We interpret this result as an indication that our sources are more heavily dust-obscured than the less actively star-forming KGES galaxies. Indeed, comparing the dust extinctions A_V derived from MAGPHYS SED fitting for the two samples we find a median $A_V = 2.31 \pm 0.17$ for KAOSS compared to $A_V = 0.71 \pm 0.04$ for KGES. We conclude that KAOSS galaxies are experiencing far more dust obscuration than their less active counterparts.

We also wish to test whether sources that are more "starburst"-like in the main-sequence paradigm are likely to experience stronger dust obscuration, and we therefore show in Fig. 4.17 the ratio $\mathrm{SFR_{H\alpha}/SFR_{IR}}$ versus offset from the star-forming main sequence, $\delta\mathrm{MS}$, which is defined according to the prescription of Speagle et al. (2014) at the redshift of each source individually. We indicate the $\pm 0.3\,\mathrm{dex}$ and $\pm 0.6\,\mathrm{dex}$ regions which define the scatter of the main sequence, and the starburst boundary. 30 of the 43 sources are located within $0.6\,\mathrm{dex}$ of the main sequence, and 13 lie above it, where they would be defined as starbursts. The "main-sequence" SMGs and "starbursts" in our sample have median redshifts of $z = 2.06 \pm 0.14$ and $z = 1.7 \pm 0.2$. This result reflects the fact that the main sequence evolves to higher SFRs at higher redshifts, meaning that higher-redshift SMGs are more similar to typical galaxies than their lower-redshift counterparts. We divide KAOSS into two bins and fit the trend, finding it to be significant at only the 1.6σ level. There is therefore no evidence to suggest a negative correlation between $\mathrm{SFR_{H\alpha}/SFR_{IR}}$ and $\Delta\mathrm{MS}$ in the KAOSS sample.

4.3.6 Emission line diagnostics

For star-forming galaxies exhibiting Hα emission lines, the flux ratio of [NII]λ6583/Hα (also known as the N2 index; see Maiolino & Mannucci, 2019, for a review) can be used to estimate the proportion of metals in the ISM, typically expressed in the form $12 + \log_{10}(O/H)$ where O and H are the Oxygen and Hydrogen abundance, respectively, as Oxygen is usually the most abundant heavy element in the ISM (e.g. Maiolino & Mannucci, 2019). N2 is also used as a tracer of AGN activity (e.g. Wisnioski et al., 2018), and indeed, we have already used the criterion [NII]/H$\alpha > 0.8$ to flag sources as potential AGN in §4.3.1.

The median [NII]/Hα flux ratio of our sample is [NII]/H$\alpha = 0.49 \pm 0.09$, and median values for the star-forming and AGN samples of [NII]/H$\alpha = 0.45 \pm 0.07$ and [NII]/H$\alpha = 0.72 \pm 0.16$, respectively. Both are higher than the $z \sim 2.5$ ULIRGs observed with KMOS by Hogan et al. (2021), who detected [NII] emission in only four of the 14 Hα-detected sources, with a median [NII]/H$\alpha = 0.32 \pm 0.04$. As previously discussed, Hogan et al. (2021) claim that this sample is unlikely to be contaminated by AGN emission, and therefore this lower value is unsurprising.

It has been shown that the metallicity of galaxies on the main sequence depends on the stellar mass content, the so-called Mass-Metallicity Relation (MZR; e.g. Tremonti et al., 2004), which generally shows an evolution with redshift – high-mass galaxies are typically fully enriched by $z \sim 1$ whereas the metallicity evolves quickly for low-mass galaxies at low redshifts. Galaxies are also believed to follow a "three-dimensional" relation between mass, metallicity and SFR, named the Fundamental Metallicity Relation (FMR; Mannucci et al., 2010), whereby more highly star-forming sources have lower metallicites. This relation is claimed to be constant, with very little scatter, up to $z > 2.5$, and the origin of the relation has been suggested to be a varying star-formation efficiency (SFE) by Ellison et al. (2008), whereas Mannucci et al. (2010) proposed the link between infalling, metal-poor gas, and star formation, may be important in shaping this role.

We can combine the [NII]/Hα flux ratios with the stellar mass and SFRs of our sources to study the SMG population in the context of the fundamental metallicity relation. To derive metallicities for the star-forming KAOSS sources, in the form $12 + \log(O/H)$, we use the empirical relation from Pettini & Pagel (2004):

$$12 + \log(O/H) = 9.37 + 2.03 \times N2 + 1.26 \times N2^2 + 0.32 \times N2^3, \qquad (4.3.3)$$

where $N2 \equiv$ [NII]/Hα. Fig. 4.18 shows $12 + \log(O/H)$ for the star-forming KAOSS sources, along with $z \sim 2.5$ ULIRGs from Hogan et al. (2021) and KMOS^{3D} galaxies (Wuyts et al.,
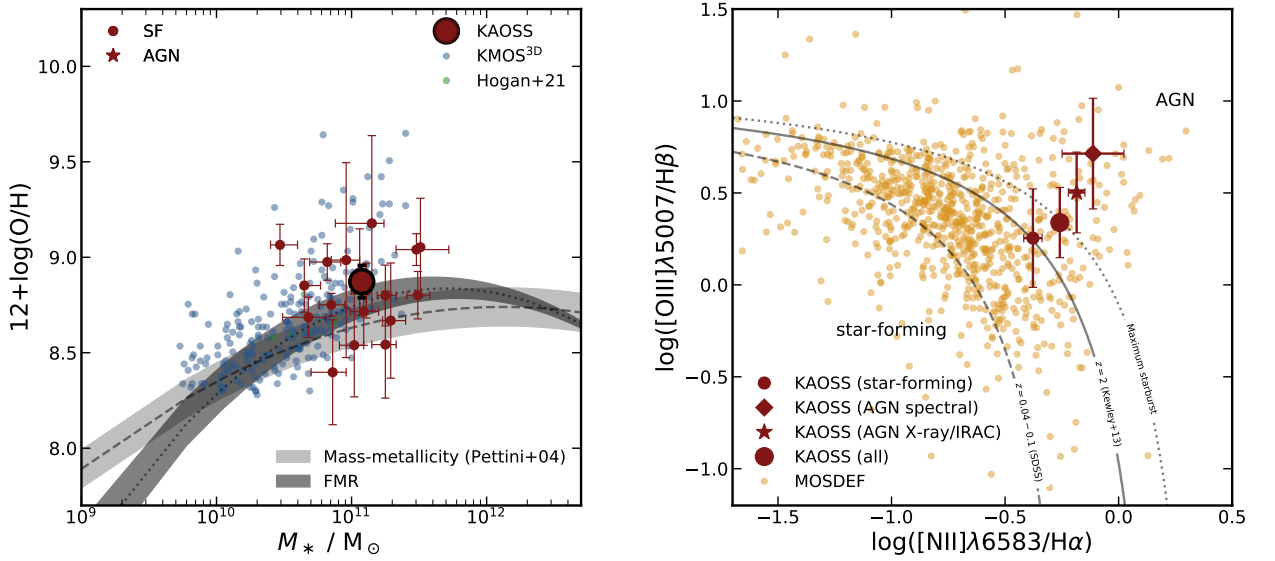
Figure 4.18: **a)** Metallicity-stellar mass relation for star-forming KAOSS sources, along with galaxies from the KMOS^{3D} survey and Hogan et al. (2021). Values of $12 + \log(\mathrm{O/H})$ are derived from $[\mathrm{N\textsc{ii}}]\lambda6583/\mathrm{H}\alpha$ flux ratios using the relation from (Pettini & Pagel, 2004). The large red point indicates our binned median, which lie systematically above both the mass-metallicity diagram and fundamental metallicity relation. This is partially driven by the large number of AGN in our sample, but even the star-forming sources are more metal rich than expected using both relations. **b)** $[\mathrm{N\textsc{ii}}]/\mathrm{H}\alpha$–$[\mathrm{O\textsc{iii}}]/\mathrm{H}\beta$ BPT diagram showing the position of KAOSS composites and MOSDEF galaxies (Shapley et al., 2015). We also show star-forming/AGN dividing lines as measured from $z \sim 0.04$–0.1 from SDSS galaxies, and theoretical predictions for $z \sim 2$ SFGs with hard ionisation fields (both from Kewley et al., 2013), along with the "maximum starburst" prediction from (Kewley et al., 2001). Like the $z \sim 2.3$ MOSDEF sample our sources are offset from the local relation, with all four composites are consistent with being classified as AGN within the uncertainties according to this relation. With the AGN hosts in our sample removed, the SMGs still have high $[\mathrm{N\textsc{ii}}]/\mathrm{H}\alpha$ flux ratios that are close to the maximum starburst limit.

2016a). We also show the mass-metallicity relation from Genzel et al. (2015), computed for $z \sim 2$ and the fundamental metallicity relation from Mannucci et al. (2010). Star-forming KAOSS sources are consistent with the fundamental metallicity relation and marginally above the mass-metallicity relation, with similar scatter to the most massive $z \sim 1$ KMOS^{3D} galaxies. Therefore the highly star-forming KAOSS SMGs are not typically more metal-enriched than other star-forming galaxies at similar masses and SFRs.

As a further test of the rest-frame optical emission lines, we study our sources in the context of the Baldwin, Phillips & Terlevich (BPT; Baldwin et al., 1981; Veilleux & Osterbrock, 1987) diagram, a commonly used tool to classify galaxies. It uses the ratios of $[\mathrm{O\textsc{iii}}]\lambda5007/\mathrm{H}\beta$ and $[\mathrm{N\textsc{ii}}]\lambda6583/\mathrm{H}\alpha$ to estimate whether the emission line properties of a galaxy indicate that it

Subset	N_{source}	$FWHM_{H\alpha}$ [km s^{-1}]	$FWHM_{[OIII]}$ [km s^{-1}]	[NII]/Hα	[OIII]/Hβ
Star-forming	21	185 ± 2	720 ± 50	-0.38 ± 0.05	0.3 ± 0.2
AGN spectral	14	294 ± 3	212 ± 5	-0.11 ± 0.19	0.7 ± 0.4
AGN X-ray/IRAC	18	266 ± 1	243 ± 10	-0.18 ± 0.04	0.5 ± 0.2
All	43	224 ± 1	331 ± 6	-0.26 ± 0.03	0.34 ± 0.16

Table 4.10: Emission line properties of four KAOSS composites. The [NII]/Hα and [OIII]/Hβ flux ratios for the composites are shown in Fig. 4.18.

is e.g. star-forming, or an AGN host (e.g. Garg et al., 2022). While Hβ is faint and therefore highly difficult to detect in SMGs, it is detected in our composite spectra (see Fig. 4.15), and therefore we can place these subsets onto the BPT diagram to classify them on average. The emission line properties of the composite samples are shown in Table 4.10.

Fig. 4.18 shows the BPT diagram with our four composite points along with a comparison sample of $z \sim 2.3$ galaxies from the MOSDEF survey, which is comparable in redshift but composed of less actively star-forming systems (4–180 M$_\odot$ yr^{-1} corrected for dust attenuation) We show the classification of star-forming galaxies and AGN as measured by Kewley et al. (2006) for 85,224 emission-line galaxies from the Sloan Digital Sky Survey (SDSS) at $z \sim 0.04$– 0.1, along with the theoretical prediction by Kewley et al. (2013) for the boundary between star-forming galaxies and AGN at $z = 2$, under the assumption of a hard radiation field. As our sources are highly star forming, this assumption is not unreasonable, however our star-forming sources fall on the star-forming-AGN boundary according to the $z = 2$ prediction, and are generally offset towards higher [NII]λ6583/Hα ratios compared to the MOSDEF sample. However, the maximum starburst model of Kewley et al. (2001) can account for the high [NII]/Hα flux ratios in our sample, and we suggest that our SMGs are close to the theoretical limit for ionising radiation in starburst galaxies (see Chapter 3 for a brief discussion of the radiation field properties of SMGs as traced by the [CI] emission). Alternatively, this may suggest that the prevalence of low-luminosity AGN is higher in SMGs than in less active galaxies, even in sources which are star-formation dominated.

4.3.7   Galaxy sizes and shapes

In this chapter we have presented early integrated results from KAOSS SMGs with Hα and/or [OIII] emission line detections. To conclude this section we discuss the resolved optical, Hα and dust sizes of the KAOSS sample, along with their Sérsic indices n, which will form part of the analysis we will present in Chapter 5. We have described the 2-D modelling with which

we derive optical and Hα sizes in §4.2.7. As a measure of the dust sizes we use measurements of 870 μm continuum sizes for five AS2UDS sources and four AS2COSMOS sources for which high-resolution ALMA imaging is available (Ikarashi et al. in prep.). All three sets of values are listed in Table 4.5.

The median sizes of the KAOSS sources are as follows: $R_e = 3.6 \pm 0.3$ kpc, $R_{H\alpha} = 4.2 \pm 0.4$ kpc and $R_{dust} = 1.2 \pm 0.3$ kpc. If we limit this to the five sources with all three sizes available we find medians of $R_e = 3.4 \pm 0.9$ kpc, $R_{H\alpha} = 3.7 \pm 1.0$ kpc and $R_{dust} = 1.8 \pm 0.3$ kpc. Therefore, our sources show much more compact emission in the dust than in the optical or Hα components, consistent with previous studies of SMGs (Ikarashi et al., 2015; Simpson et al., 2015; Gullberg et al., 2019). This also suggests that the Hα emission is marginally more extended than the stellar emission (Chen et al., 2015). We confirm this for individual sources by plotting the three sizes against one other in Fig. 4.19. As a comparison sample we include a compilation from Bellocchi et al. (2022), comprised of star-forming galaxies at $z \sim 1$–3, along with sources from the KMOS^{3D} survey (Wilman et al., 2020). We see good agreement between the Hα sizes and optical sizes, similar to the KMOS^{3D} and Bellocchi et al. (2022) data, and the dust size is lower than both the Hα and optical sizes for all galaxies where both measurements are available. This is in agreement with previous results that the dust component of SMGs is much more compact than the stellar emission region, which has been presented as evidence for bulge growth (e.g. Chen et al., 2017)

The axial ratios (b/a) estimated from GALFIT modelling of the HST/K-band imaging (see §4.2.7) can provide diagnostic information about the population of galaxies we are observing when combined with the assumption that our sources are randomly inclined. For example, for a collection of thin circular discs at random orientation angles, the probability of viewing the disc at an angle i should be proportional to $\cos(i)$, with the peak of the probability distribution function at $i = 57.3°$ (Law et al., 2009). Our sample has a median axial ratio of $b/a = 0.64 \pm 0.03$ and a median derived inclination of $i = 52 \pm 2°$, marginally lower than the prediction for thin discs, but we expect our sources to be thick given previous kinematic studies of SMGs (e.g. Alaghband-Zadeh et al., 2012).

Fig. 4.20 shows the distribution of axis ratios b/a for KAOSS, along with early- and late-type galaxies in the Galaxy and Mass Assembly (GAMA; Driver et al., 2009) survey (Kelvin et al., 2014). We show the KAOSS distribution as a whole, but also the b/a distribution of only the sources identified as AGN. The KAOSS sample appears to be consistent with the early-type galaxies in GAMA, whereas in comparison to the late-types we appear to be
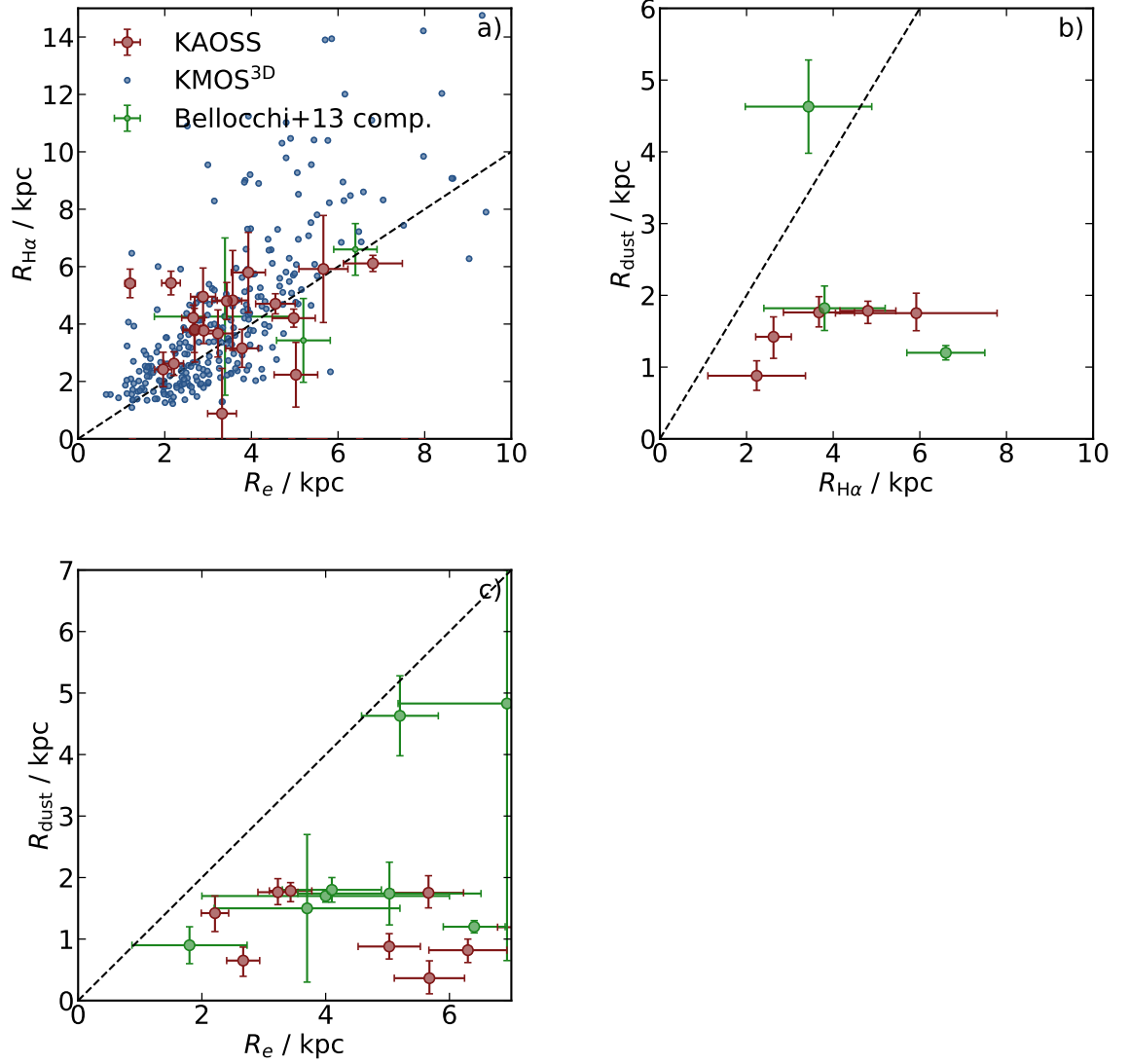
Figure 4.19: Optical, Hα and dust sizes for the KAOSS resolved subset. In all panels we include a 1:1 line (dashed), and for comparison a compilation of sizes from Bellocchi et al. (2022). **a)** Hα size versus optical size (*HST*/F160W or *K*) for the KAOSS resolved subset and for galaxies from the KMOS^{3D} survey (Wilman et al., 2020) **b)** 870 μm dust size versus Hα size for the KAOSS resolved subset with available high-resolution ALMA imaging. Our KAOSS SMGs are typically more compact in the dust emission when compared to the Hα component. **c)** 870 μm dust size versus optical size (*HST*/F160W or *K*) for the KAOSS resolved subset with available high-resolution ALMA imaging. Our KAOSS SMGs are typically more compact in the dust emission when compared to the optical component.
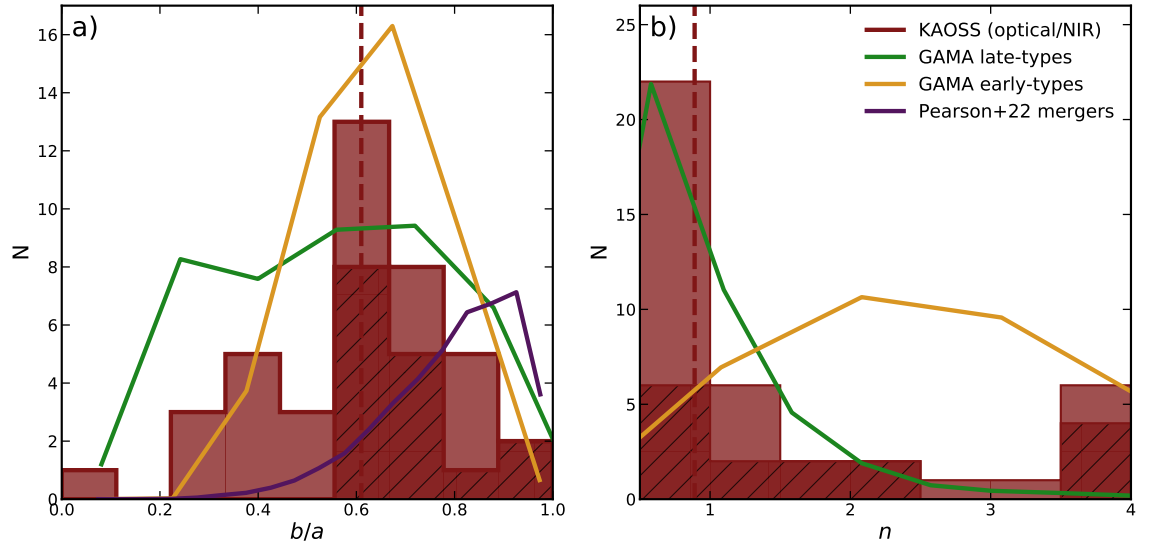
Figure 4.20: **a)** Axis ratio b/a distributions measured from optical/NIR imaging from the KAOSS sample of SMGs, with the entire sample shown as a solid histogram, and the AGN subset shown as a hatched histogram. We also include distributions measured from GAMA early- and late-type galaxies (Kelvin et al., 2014), and local mergers (Pearson et al., 2022). **b)** Sérsic indices n derived from GALFIT modelling of VISTA K/HSTF160w imaging for KAOSS sources, with the entire sample shown as a solid histogram, and the AGN subset shown as a hatched histogram. This panel also shows the expected distributions for GAMA early- and late-galaxies. Our sample is consistent with that of the GAMA late-types apart from a small peak of sources at $n \sim 4$. However, we see that the majority of these are identified as AGN hosts.

"missing" sources with low axis ratios. Gullberg et al. (2019) explained this discrepancy by invoking bars – however as we are probing the stellar component this is not a feasible explanation, because bars are unlikely to be found on scales comparable to our Hα sizes. It is possible that we are biased against observing systems that are close to edge-on, as in these cases the dust obscuration would cause the system to be much fainter than if the system were closer to face-on, and therefore less likely to be detected. However, if our sample is representative of the Pearson et al. (2022) local mergers, it is less likely that we would experience a similar bias against systems that are close to face-on. Lovell et al. (2021a) also used simulated submillimetre galaxies in the SIMBA cosmological simulation to suggest that flux-limited single-dish surveys may be biased towards detecting face-on SMGs, which could also explain our lack of edge-on sources compared to the GAMA late-types.

Fig. 4.20 also shows the distribution of Sérsic indices n measured for both the full KAOSS sample and only the AGN hosts. As discussed in §4.2.7, we derive a median n from the free fits of $n = 0.97 \pm 0.14$ for the KAOSS sources. Additionally, the distribution appears to be in agreement with the GAMA late-types, and this is particularly true if the AGN hosts are removed. We conclude that the Sérsic index distribution of the star-forming KAOSS sample is consistent with that of late-type galaxies, and the axis ratio b/a distribution is close to being consistent with the same population apart from a lack of sources of with low b/a. We suggest that this could be the result of a bias due to dust obscuration, or an orientation bias in single-dish surveys of SMGs as predicted by (Lovell et al., 2021b).

4.4 Conclusions

In this chapter we have presented the ongoing project KAOSS, a KMOS Large Programme designed to obtain spectroscopic redshifts for a large number of SMGs and to study spatially resolved kinematics in the population. We summarised our target selection, which results in a sample of 407 targets in the COSMOS, UDS and ECDFS fields, and our observing strategy and data reduction methods. The survey is ongoing, and over 50% of the KMOS pointings have been at least partially observed, and analysed, from which we draw the following preliminary conclusions:

- We detect line emission in 43 sources – 42 of which display Hα emission and six of which display [OIII] emission (five display both). Some sources display hints of [SII] emission but we find little evidence of Hβ in any SMGs where the line is covered, until we stack

the 43 sources with redshifts and detect the Hβ at low S/N. The median redshift of the sample is $z = 2.03 \pm 0.16$, significantly lower than the median of $z = 2.61 \pm 0.08$ found for the AS2UDS sample of SMGs, partly as a result of our limited coverage of the Hα emission and partly due to a bias towards optically bright SMGs, which generally reside a lower redshifts.

- We study four tracers of AGN activity in our sample and find that up to $53 \pm 11\%$ of our sources may contain an AGN according to their spectral properties, X-ray counterparts or IRAC colours, with $33 \pm 9\%$ of these being classified according to their spectral properties, and $44 \pm 10\%$ of these being classified according to their X-ray/IRAC properties. We make no attempt, however, to determine the fractional contribution of the AGN to the total luminosity in these sources. For the $49 \pm 11\%$ of KAOSS SMGs that we deem to be star-formation dominated we convert the [N$\textsc{ii}$]/Hα ratios to $12 + \log(\text{O/H})$ as a proxy for the metallicity and find them to be consistent with the Fundamental Metallicity Relation.

- Using the composite spectra we place our sample onto the [N$\textsc{ii}$]/Hα–[O$\textsc{iii}$]/Hβ BPT diagram. All the subsets are offset from the local relation, and from less star-forming $z \sim 2.3$ MOSDEF galaxies, and we suggest that KAOSS SMGs are close to the "maximum starburst" limit for ionising radiation due to their high star-formation rates, or that subdominant AGN may be present in the majority of our sample.

- Modelling the optical and Hα sizes as Sérsic profiles using GALFIT we estimate median effective radii of $R_e = 3.6 \pm 0.3\,\text{kpc}$, $R_{\text{H}\alpha} = 4.2 \pm 0.4\,\text{kpc}$, both much more extended than the median dust radii of $R_{\text{dust}} = 1.2 \pm 0.3\,\text{kpc}$. The SMGs are consistent with a median Sérsic index of $n = 1$. i.e. with an exponential disc-like light profile, and their distributions of n and axial ratios b/a when excluding AGN are apparently consistent with late-type galaxies from the GAMA survey.

Resolved kinematics of high-redshift dust-obscured galaxies

Preamble

In Chapter 4 we introduced the KAOSS Large Programme and presented the spectroscopic redshifts and integrated Hα/[OIII] properties of a sample of 43 870 μm-selected SMGs. One of the main science goals of KAOSS, which we did not address in Chapter 4, is to study the kinematics of the SMG population. To that end, in this chapter we present spatially resolved Hα/[OIII] maps of 36 SMGs at $z \sim 1.5$–2.5, from which we derive and model rotation curves to estimate the rotational velocities ($v_{\rm rot}$) of the SMGs, along with their intrinsic velocity dispersions (σ_0). We then quantify the proportion of sources in our sample that are rotationally supported by measuring their ratios of rotational velocity to velocity dispersion $v_{\rm rot}/\sigma_0$. We measure the normalisation of the Tully-Fisher relation for our sample and search for offsets to the local relation, and estimate stellar-to-dynamical mass ratios which we compare with galaxies at similar redshifts that are less massive and have lower star-formation rates. Proceeding to compare the KAOSS SMGs with star-forming galaxies selected from the EAGLE simulation, we estimate their halo masses in an attempt to understand the mechanisms through which they are supplied with gas for star formation.

5.1   Introduction

We have shown in previous chapters that dust-obscured star-forming galaxies (DSFGs), particularly submillimetre galaxies (SMGs), at the peak of cosmic star formation ($z \sim 2$) are massive, gas rich and highly star forming (also see e.g. Tacconi et al., 2006; Magnelli et al., 2012b; Bothwell et al., 2013; Swinbank et al., 2014; Miettinen et al., 2017; Dudzevičiūtė et al., 2020; Shim et al., 2022), but we have not yet investigated the kinematic nature of these sources. Are they predominantly turbulent merger-driven (e.g. Narayanan et al., 2009, 2010; Lagos et al., 2020) sources, like their local counterparts the Ultra Luminous Infrared Galaxy (ULIRG) population (e.g. Bellocchi et al., 2016)? Or do they more closely resemble regular gas discs that are smoothly accreting gas from the intergalactic medium (IGM; Kereš et al., 2005; Dekel & Birnboim, 2006; Narayanan et al., 2015; Tacconi et al., 2020)?

One of the most promising routes to test these competing theories is through integral field spectroscopy (IFS) in the rest-frame optical, which enables two-dimensional (2-D) mapping of the spatially resolved kinematics via the nebular emission lines, such as Hα (e.g. Cresci et al., 2009; Förster Schreiber et al., 2009; Alaghband-Zadeh et al., 2012; Wisnioski et al., 2015, 2019; Tiley et al., 2021). These maps can then be used to measure the rotational velocity $v_{\rm rot}$ and velocity dispersion σ (e.g. Förster Schreiber et al., 2009; Wisnioski et al., 2015, 2019; Johnson et al., 2018).

In the local Universe there are several comprehensive studies, with surveys such as CALIFA, SAMI and MANGA providing statistical data sets of thousands of $z \sim 0$ galaxies spanning a range of properties. These surveys have studied scaling relations in local galaxies, such as the Schmidt-Kennicutt law (e.g. Leroy et al., 2008), the resolved star-forming main sequence (e.g. Sánchez et al., 2013; Wuyts et al., 2013) and the mass-metallicity relation (e.g. Barrera-Ballesteros et al., 2016; Erroz-Ferrer et al., 2019), and verified these down to $\sim$ kpc scales (see Sánchez, 2020, for a review).

At $z \sim 2$, the rest frame-optical nebular emission lines such as Hα and [O III] are redshifted into the near-infrared (NIR) and into the coverage of instruments such as KMOS and SINFONI. However, dynamical analyses at this epoch are much harder because of the limited spatial resolution – KMOS achieves a resolution of $\sim 0.6''$ (FWHM) which corresponds to a physical size of $\sim 5\,$kpc at $z \sim 2$ (although the 2-D coverage of an integral field unit means finer spatial scales can be sampled if the sources exhibit velocity gradients). Therefore NIR integral field unit (IFU) surveys of $z \sim 2$ galaxies are less able to probe galaxies on the same scales as

their local counterparts. Additionally, the H and K bands which cover the redshifted Hα and [O$_{\text{III}}$] emission suffer from strong sky contamination (Soto et al., 2016; Tiley et al., 2021) which increases the noise level and is challenging to fully model and remove.

As a result, the tools used to study kinematics at high redshifts are different. We instead use measurements of the ratio of rotational velocity to intrinsic velocity dispersion v_{rot}/σ_0 (Weiner et al., 2006; Newman et al., 2013; Wisnioski et al., 2015), along with morphologies (dust attenuation makes this unreliable, however) to quantify the kinematics. For example, galaxies that have $v_{\text{rot}}/\sigma_0 > 1.5$ have been considered to be rotationally supported (e.g. Stott et al., 2016; Tiley et al., 2021), whereas a galaxy with $v_{\text{rot}}/\sigma_0 < 1.5$ would conversely be dominated by turbulent motions that may indicate an ongoing/completed merger (e.g. Alaghband-Zadeh et al., 2012).

Progress in NIR integral field spectrograph technology has allowed IFU studies of large numbers of sources in recent years, and as in the local Universe there are now several large surveys of spatially resolved kinematics with KMOS and SINFONI including SINS/zC-SINF, KROSS, KMOS$^{\text{3D}}$, KDS and KGES. These surveys cover the epoch where the star-formation rate density (SFRD) is at its peak, and where the majority of the stellar mass we see in the local Universe was assembled. They have revealed that high-redshift star-forming galaxies appear dynamically "hot" compared to local galaxies (e.g Förster Schreiber et al., 2009; Wisnioski et al., 2015, 2019; Stott et al., 2016; Johnson et al., 2018). Some of the above have also used the Tully-Fisher relation (Tully & Fisher, 1977) – the relationship between galaxy luminosity and rotational velocity – to study the evolution of star-forming galaxies between $z \sim 2$ and $z \sim 0$. For example, some authors have found variations in the evolution of the TFR (e.g. Kassin et al., 2007; Förster Schreiber et al., 2009; Swinbank et al., 2012; Übler et al., 2017), whereas some find no evolution at all (e.g. Tiley et al., 2019), the latter indicating a close link between the build up of stellar mass and dark matter in $z \sim 2$ SFGs.

Spatially resolved kinematic studies of SMGs however, have been much more limited in scope. Among the few examples include Alaghband-Zadeh et al. (2012), who observed nine SMGs at $z \sim 2.0$–2.7 with SINFONI and the Gemini-North/Near-Infrared Integral Field Spectrograph (NIFS), measuring an average Hα velocity dispersion of $\sigma = 220 \pm 80 \, \text{km s}^{-1}$, indicating large amounts of turbulence in these sources. Additionally, they found that six of the nine sources showed multiple kinematically distinct components, and they classified all nine sources as mergers based on kinemetry of the velocity and velocity dispersion maps. Swinbank et al. (2006) had previously come to a similar conclusion, finding four of their sample of six SMGs

to contain multiple components. Menéndez-Delmestre et al. (2013) observed three SMGs with the OH-Suppressing Infrared Imaging Spectrograph (OSIRIS) on the Keck telescope, finding the systems to contain multiple clumps which they suggested to be in the process of merging, and thus driving high SFRs.

Studying the kinematics of high-redshift SMGs is one of the main goals of KAOSS (see Chapter 4). We targeted 407 SMGs with KMOS in the HK filter, which covers the Hα and/or [O III] emission lines at z $\sim$ 1–3, and in this chapter we will exploit KAOSS to map the Hα/[O III] emission in the optically bright, extended sources and extract velocity fields/rotation curves. We will significantly increase the sample of SMGs with spatially resolved measurements of rotational velocities and intrinsic velocity dispersions, along with $v_{\rm rot}/\sigma_0$, the latter of which has been claimed to be a key diagnostic of the level of rotational support in galaxies (e.g. Wisnioski et al., 2019).

In this chapter, we present the properties of a subset of 36 KAOSS sources in the COSMOS, UDS and GOODS-S fields with sufficiently bright and extended Hα and/or [O III] detections to yield 2-D kinematic information. The outline of this chapter is as follows: in §5.2 and §5.3 we describe the sample studied and the observations carried out, along with our data reduction and analysis methods, before discussing the measurements made. In §5.4 we discuss the results and their implications. In §5.5 we summarise our findings. Throughout this chapter we adopt a flat Λ-CDM cosmology defined by $(\Omega_{\rm m}, \Omega_\Lambda, {\rm H}_0) = (0.3, 0.7, 70\,{\rm km\,s^{-1}\,Mpc^{-1}})$.

5.2   Sample selection

In this chapter we exploit data from the KAOSS Large Programme (Programme ID: 1103.A-0182). As detailed in Chapter 4, these are 13.5 ks exposure observations of SMGs in the HK grating ($\sim$ 1.4–2.5 μm) with KMOS (Sharples et al., 2013) on the Very Large Telescope, designed to obtain spatially resolved Hα and/or [O III] detections. For this chapter we select KAOSS sources with Hα or [O III] detections that are bright enough to search for resolved velocity structure from the Hα or [O III] emission line. The selection of this sample is based on a visual inspection of the velocity fields derived from the fitting as described in §5.3.1. We deem a source to be "resolved" if the fits recover information in a significant number of adjacent pixels, which we require to carry out the majority of analysis in this chapter. We identify 36 Hα sources, which have $f_{\rm H\alpha} > 1.3 \times 10^{-20}\,{\rm W\,m^{-2}}$ and five [O III] sources, which have $f_{\rm [OIII]} > 1.9 \times 10^{-20}\,{\rm W\,m^{-2}}$. All sources have detections with a signal-to-noise ratio of S/N $>$ 5 for the emission line in the integrated spectrum.

Before discussing the resolved kinematics, we place our sample in context with samples from other galaxy surveys. In Chapter 4 we provided a detailed description of the KAOSS sample, and therefore in this section we focus on comparing to other resolved kinematic studies at similar redshifts. In Fig. 5.1 we show the $870\,\mu$m fluxes of the resolved sample versus their K-band magnitudes. Four sources are not shown here as they have no K-band coverage, but all four of these sources are resolved. We also plot sources that are detected but unresolved, and these sources are mostly fainter in the K-band – the resolved and unresolved sources have median K-band magnitudes of $K = 21.3 \pm 0.2$ and $K = 22.0 \pm 0.4$ respectively. The opposite is true at $870\,\mu$m – the resolved and unresolved sources have median $870\,\mu$m flux densities of $S_{870} = 2.7 \pm 0.3\,$mJy and $S_{870} = 5.3 \pm 0.9\,$mJy respectively. This is likely to be the result of SMGs with higher S_{870} fluxes having higher dust masses (Dudzevičiūtė et al., 2020), potentially leading to stronger dust obscuration, therefore the Hα/[O III] emission lines are fainter and more difficult to resolve. The median redshifts of the resolved and unresolved samples are comparable – $z = 1.94 \pm 0.17$ and $z = 2.11 \pm 0.16$ respectively.

As a comparison sample we show 707 SMGs from the ALMA-SCUBA-2 Ultra Deep Survey (AS2UDS; Stach et al., 2019; Dudzevičiūtė et al., 2020), which is the largest sample of submillimetre galaxies (SMGs) and therefore provides a good indicator of the properties of the general $870\,\mu$m-selected population. Our KAOSS sample spans the range of $870\,\mu$m fluxes in AS2UDS, although the resolved subset only samples sources with $K \lesssim 22.9$. This is caused by heavy dust obscuration in the NIR – the resolved KAOSS sources have median dust extinctions from MAGPHYS SED fitting of $A_V = 2.15 \pm 0.16$ (see §4.2.6) – and therefore the brighter sources are more likely to be detected by KMOS.

In Fig. 5.1 we also show $z \sim 1.5$ star-forming galaxies from the KMOS Galaxy Evolution Survey (KGES; Tiley et al., 2021). $870\,\mu$m fluxes are not available for these sources, but they do have MAGPHYS-derived dust mass estimates, which we convert to S_{870} estimates using the M_{dust}–S_{870} relation derived by Dudzevičiūtė et al. (2020). These are therefore approximate values, but they highlight the region of the parameter space probed by the KGES sample: they have lower submillimetre fluxes than KAOSS, but similar comparable rest-frame optical fluxes.

In Fig. 5.1 we also show star-formation rates (SFRs) versus stellar masses (M_*) derived from MAGPHYS SED fitting for our sample (see §4.2.6). Open circles represent sources that are detected, and therefore studied in Chapter 4, but unresolved and therefore not presented in this chapter. We show the star-forming main sequence at $z = 2$ according
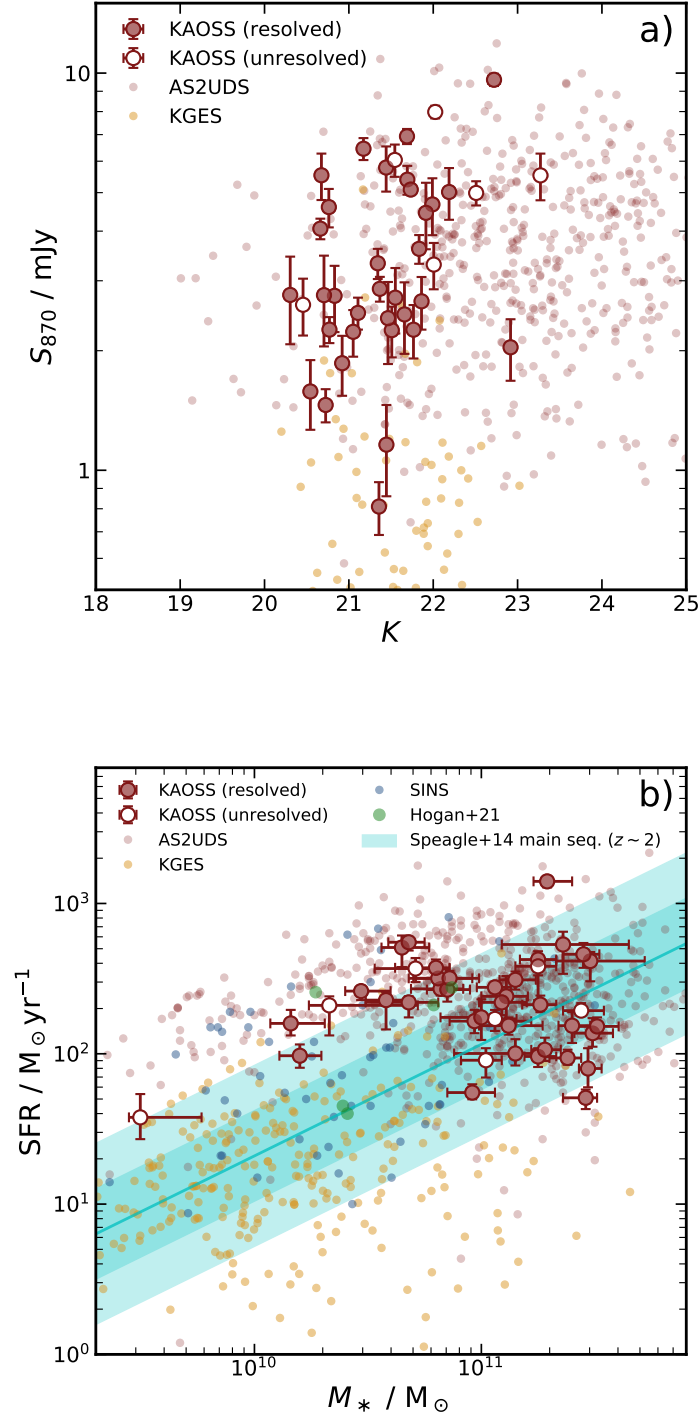
Figure 5.1: **a)** K-band magnitude versus $870\,\mu$m flux (S_{870}) for the KAOSS resolved sample compared with the 707 AS2UDS SMGs (Dudzevičiūtė et al., 2020) and $z \sim 1.5$ star-forming galaxies from KGES (Tiley et al., 2021). The KAOSS resolved sample is generally representative of the range of S_{870} in the SMG population, but biased towards near-infrared-brighter sources. For the KGES sample we indicate the region containing the K-band magnitudes of the sample and the expected $870\,\mu$m fluxes, as the latter are not available for this sample. KGES extends the range to less active sources than KAOSS. **b)** Star-formation rate versus M_* for the same samples, now also including six $z \sim 2.5$ ULIRGs from Hogan et al. (2021). KAOSS probes sources that are approximately an order of magnitude more massive than KGES, and overlaps with the parameter range of the *Herschel*-selected ULIRGs in Hogan et al. (2021).

to the prescription of Speagle et al. (2014). The 36 KAOSS sources have median stellar masses and SFRs of $M_* = (1.3 \pm 0.2) \times 10^{11}\,\mathrm{M}_\odot$ and $\mathrm{SFR} = 220 \pm 30\,\mathrm{M}_\odot\mathrm{yr}^{-1}$, compared to $M_* = (1.44 \pm 0.01) \times 10^{11}\,\mathrm{M}_\odot$ and $\mathrm{SFR} = 173 \pm 6\,\mathrm{M}_\odot\mathrm{yr}^{-1}$ for the redshift-matched AS2UDS sample that we used in Chapter 4. Hence in this analysis we are probing SMGs that are generally representative of the stellar masses in the $870\,\mu$m-selected population, but slightly more active in terms of star-formation rate.

Fig. 5.1 shows that the KGES sample is complementary to KAOSS as it probes much less massive and less actively star-forming sources, with median stellar masses and SFRs of $M_* = (1.3 \pm 0.1) \times 10^{10}\,\mathrm{M}_\odot$ and $\mathrm{SFR} = 16 \pm 1\,\mathrm{M}_\odot\mathrm{yr}^{-1}$ respectively, approximately an order of magnitude lower than the KAOSS resolved sample in both cases. Therefore, by supplementing our results with those from KGES we will be able to study the variation of kinematic properties across a wider range in stellar mass and star-formation rate.

As a further comparison sample in Fig. 5.1 we include data from KMOS observations of six $z \sim 2.5$ *Herschel*-selected ULIRGs with kinematical information estimated by Hogan et al. (2021). While these sources are selected based on shorter wavelengths than our SMGs, they are gas-rich star-forming galaxies at comparable redshifts to the most distant sources in our resolved sample, which spans the range $z \sim 1.5$–2.5. Indeed, the six sources from Hogan et al. (2021) have median stellar masses and SFRs of $M_* = (2.5 \pm 1.5) \times 10^{11}\,\mathrm{M}_\odot$ and $\mathrm{SFR} = 130 \pm 90\,\mathrm{M}_\odot\,\mathrm{yr}^{-1}$, consistent with the KAOSS resolved sample. Where possible we compare our results with both the KGES and Hogan et al. (2021) ULIRG samples throughout this chapter.

5.3 Data reduction and analysis

Details on the reduction of KAOSS data are provided in Chapter 4. We do not repeat the description of this process in this chapter, instead we describe the additional steps taken to analyse the spatially resolved sample.

5.3.1 Hα and [OIII] line fitting

To determine the kinematics of our sources we model the Hα and [OIII] emission in each spaxel. By fitting the emission line we can derive resolved maps of the velocity and velocity dispersion from which we will extraction rotation curves and measure rotational velocities.
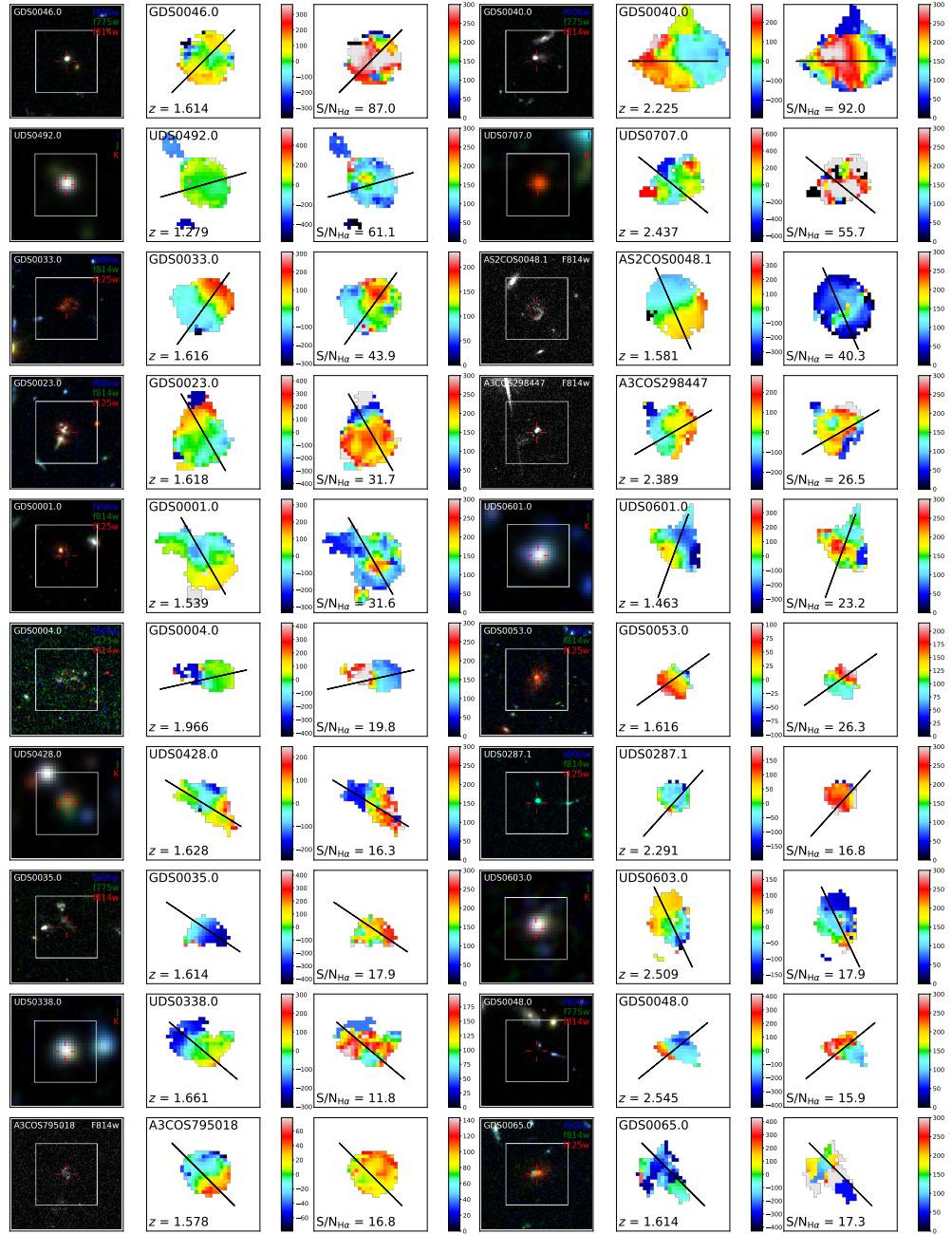
Figure 5.2: *HST* or ground-based images (left), velocity fields (middle) and velocity dispersion profiles (right) for our sample of 36 resolved KAOSS SMGs. Sources are ordered by the S/N of the Hα emission line (shown in the bottom left corner of the middle panels) and we indicate the inclination angle derived for the source from GALFIT modelling. The black lines on the centre and right panels indicate the kinematic position angle along which rotation curves are measured. For the left panels we indicate the three filters that make up the RGB colour image, or the single filter in cases where the image is greyscale.
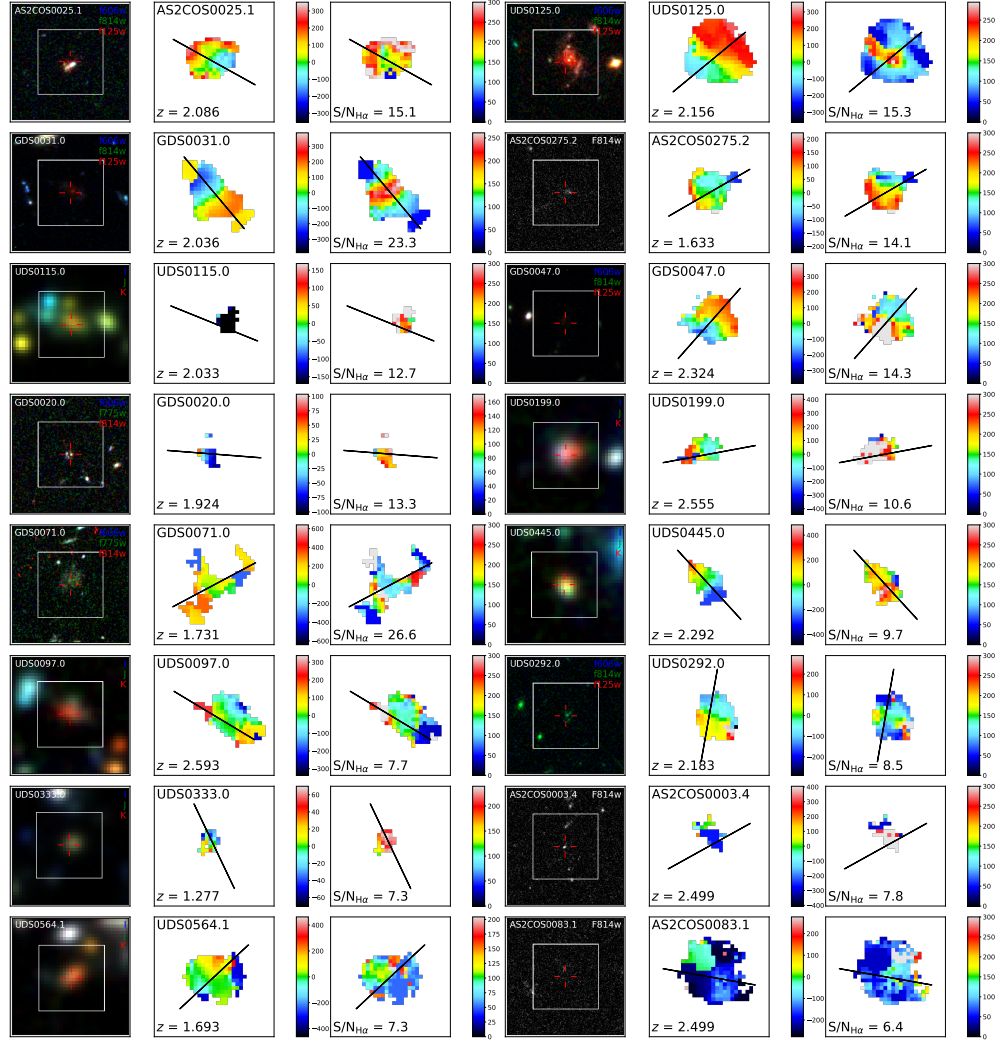
Figure 5.3: Fig. 5.2 continued.
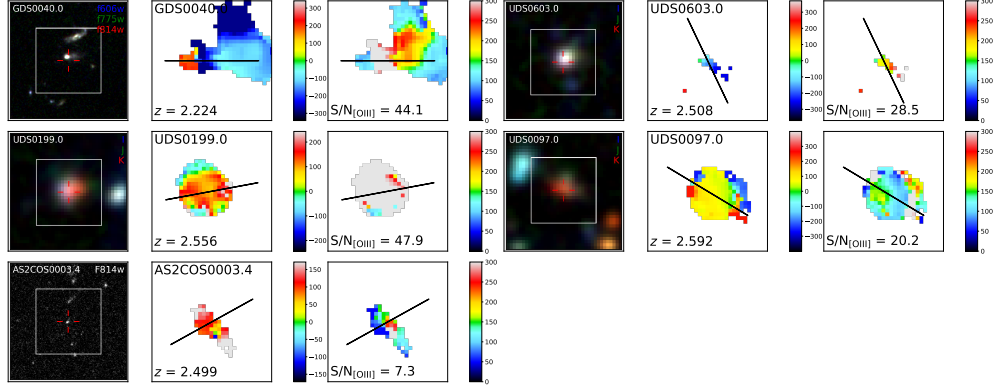
Figure 5.4: Same as Fig. 5.2 but now with resolved [OIII] maps instead of Hα.

As discussed in §4.2.5 we fit a three-component Gaussian profile to the Hα line and [NII] doublet, coupling their wavelengths and linewidths, with the Hα/[NII] flux ratio as a free parameter, and fixing the [NII]λ6583/[NII]λ6548 flux ratio to a value of 2.8 (Osterbrock & Ferland, 2006). We account for the instrumental resolution as described in §4.2.5. For the [OIII] doublet we fit a two-component Gaussian profile, again coupling the wavelengths and linewidths and allowing the [OIII]λ4959/[OIII]λ5007 flux ratio to vary. In all cases we fit a constant continuum component. In this chapter, however, we perform the fitting on a pixel-by-pixel basis. We first resample the velocity fields from a pixel scale of $0.2''$ to $0.1''$ to improve the sampling. For each pixel we attempt to fit the emission lines, and if the fit does not achieve a threshold of $S/N = 5$ we bin with neighbouring pixels, increasing the bin size and repeating up to a maximum bin size of 5 ($0.5''$) or until the S/N threshold is achieved. For the systemic redshifts we use the integrated values derived in Chapter 4.

Velocity and velocity dispersion maps for all the galaxies in the resolved sample are shown in Figs. 5.2–5.4 alongside colour images of the sources. For the colour images we include high-resolution *HST* imaging where possible, otherwise we use ground-based imaging. Sources are ordered by the integrated S/N of the Hα emission line which generally correlates with the quality of the kinematic information from the fitting. Many of the sources appear to display velocity gradients, with some sources such as AS2COS0048.1 showing apparently simple kinematic structure and potentially ordered rotation. Some sources, such as GDS0001.0, display
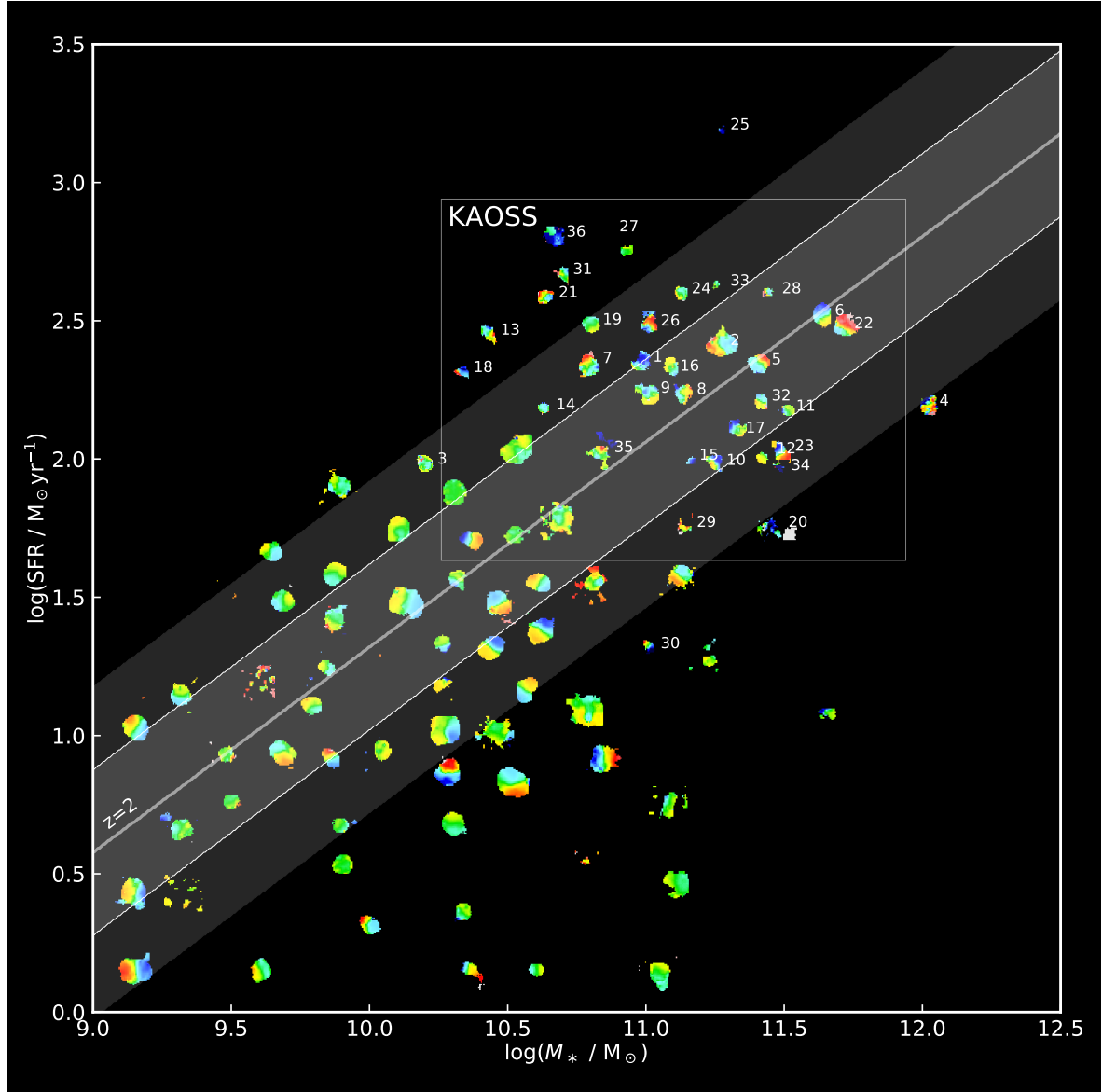
Figure 5.5: Hα velocity fields for the resolved KAOSS galaxies (numbered by rank of Hα S/N) displayed in the star-formation rate versus stellar mass ("main sequence") plane, along with a representative selection of KGES galaxies (not numbered). Red and blue indicate positive and negative velocities, respectively, scaled from 300 to $-300\,\mathrm{km s^{-1}}$, as in Figs. 5.2–5.3. The KAOSS sources appear less extended than the typically lower-redshift KGES galaxies, and the KGES sources display more ordered structure.

more turbulent, complex velocity structures and morphologies. The source AS2UDS0492.0 is unique in our sample as we detect velocity structure from a separate component to the north west within the 2.8″ field of the KMOS IFU – this component is detected in the ground-based near-infrared imaging (see Fig. 5.2) and corresponds to a companion. This particular source also displays a broad component in the Hα emission, AGN-like IRAC colours and has an X-ray component (see §4.3.1). The fit to the Hα emission in UDS0707.0 is poor despite the high S/N of the integrated emission (S/N$_{H\alpha} \sim 56$). Like AS2UDS0492.0, this source displays broad Hα emission, but it also has a very low Hα/[NII] flux ratio.

The five [OIII] velocity and velocity dispersion maps display less ordered structure than the Hα maps, and in the remainder of this analysis for deriving rotational velocities and velocity dispersions we focus on analysing the Hα maps.

The velocity dispersion maps in Figs. 5.2–5.4 generally appear complex or noisy, even for the sources with the most significant detections, for example UDS0707.0, AS2COS0025.1 and UDS0338.0. Given the compact sizes of our sources (median $R_e \sim 0.4''$) relative to the KMOS PSF (FWHM $\sim 0.6''$) our observations are susceptible to the effects of beam smearing leading to increased observed velocity dispersions in the centre of the galaxy (e.g. Johnson et al., 2018). It can be seen in sources such as AS2COS0048.1 and UDS0125.0 that we resolve the Hα emission on scales large enough to reach the outskirts of the velocity dispersion profile, and therefore measure an intrinsic velocity dispersion that is less affected by beam smearing. We provide a discussion of beam smearing in our sample and the methods with which we correct for it in §5.4.2.

Given the structure in the velocity fields, which even affects some of the brighter, more extended sources (see Figs. 5.2–5.4), we choose to perform a visual classification of the sample. We divide the sample into two classes, those that exhibit a velocity gradient and those that do not. We identify 28 sources with velocity gradients from the sample of 36, a fraction of $78 \pm 15\,\%$. In the remainder of this analysis we refer to this as the *ordered* subset, and the remaining eight sources we term the *disordered* subset, and in figures we distinguish the two samples using closed and open symbols, respectively.

A simple question we can address is whether the *ordered* and *disordered* are intrinsically different in any way. We first check their integrated signal-to-noise ratios, finding the *ordered* and *disordered* samples to have median S/N$_{H\alpha} = 18 \pm 2$ and S/N$_{H\alpha} = 12 \pm 3$ respectively. Therefore, the fact that we are unable to recover kinematic information from the *disordered* sample may partially reflect their lower integrated S/N values. This difference is only marginal how-

ever, and we do not expect that the noise should vary strongly across the sample as the exposure times are similar for all sources, therefore this should not significantly affect the classifications. To assess this, we perform a simple test, degrading the S/N of some of the *ordered* velocity fields by adding random Gaussian noise. Four examples of *ordered* velocity fields at degraded S/N values are shown in Fig. 5.6. In the cases of GDS0046.0 and AS2COS0048.1 we see that velocity gradients are still visible (and would still be classified as *ordered*) below a S/N of ~ 15, whereas for GDS0033.0 most of the velocity information has been lost at this S/N. We therefore suggest that the S/N of the observations at least partially accounts for the differences in the *ordered* and *disordered* samples, possibly in combination with the degree of dust extinction, although we note that the examples shown are four of the strongest Hα detections in the sample. A more robust analysis would require accounting for the structured noise in the spectra due to e.g. sky emission, and carrying out this test on all of the *ordered* sample, but we leave this for future work.

The two samples also have consistent stellar masses, $M_* = (1.3 \pm 0.2) \times 10^{11}\,\mathrm{M}_\odot$ for the *ordered* subset and $M_* = (2.3 \pm 0.9) \times 10^{11}\,\mathrm{M}_\odot$ for the *disordered* subset, consistent star-formation rates, $\mathrm{SFR} = 220 \pm 30\,\mathrm{M}_\odot\,\mathrm{yr}^{-1}$ for the *ordered* subset and $\mathrm{SFR} = 210 \pm 80\,\mathrm{M}_\odot\,\mathrm{yr}^{-1}$ for the *disordered* subset, and consistent dust extinctions $A_V = 2.09 \pm 0.15$ and for the *ordered* subset and $A_V = 2.4 \pm 0.4$ for the *disordered* subset. We therefore find little significant difference between the two subsets in terms of their physical properties, and suggest that low line-integrated S/N is their main distinguishing feature.

As a visual comparison between the KAOSS velocity fields and those of less active (and more typical) SFGs, in Fig. 5.5 we shows the 36 KAOSS Hα velocity fields plotted at their positions in the SFR–M_* (main sequence) plane compared to a selection of galaxies from KGES. Our sources are numbered according to their rank in Hα S/N, with 1 representing the most significant detection. We also include velocity fields of a subset of high-quality maps from the KGES sample selected to have comparable signal-to-noise ratios, which are plotted without numerical labels. All velocity fields are plotted with a colour scale of $\pm 300\,\mathrm{km\,s}^{-1}$ (blue to red). We indicate the main sequence and $\pm 0.3\,\mathrm{dex}$ spread according to the prescription of Speagle et al. (2014) at $z = 2$. Like the $z \sim 1.5$ KGES galaxies, KAOSS galaxies lie mostly within the spread of the main sequence, but at stellar masses and SFRs over an order of magnitude higher (see §5.3). Visually the KAOSS velocity fields appear more compact than the KGES sample, and also typically display more turbulent structure and higher rotation velocities.
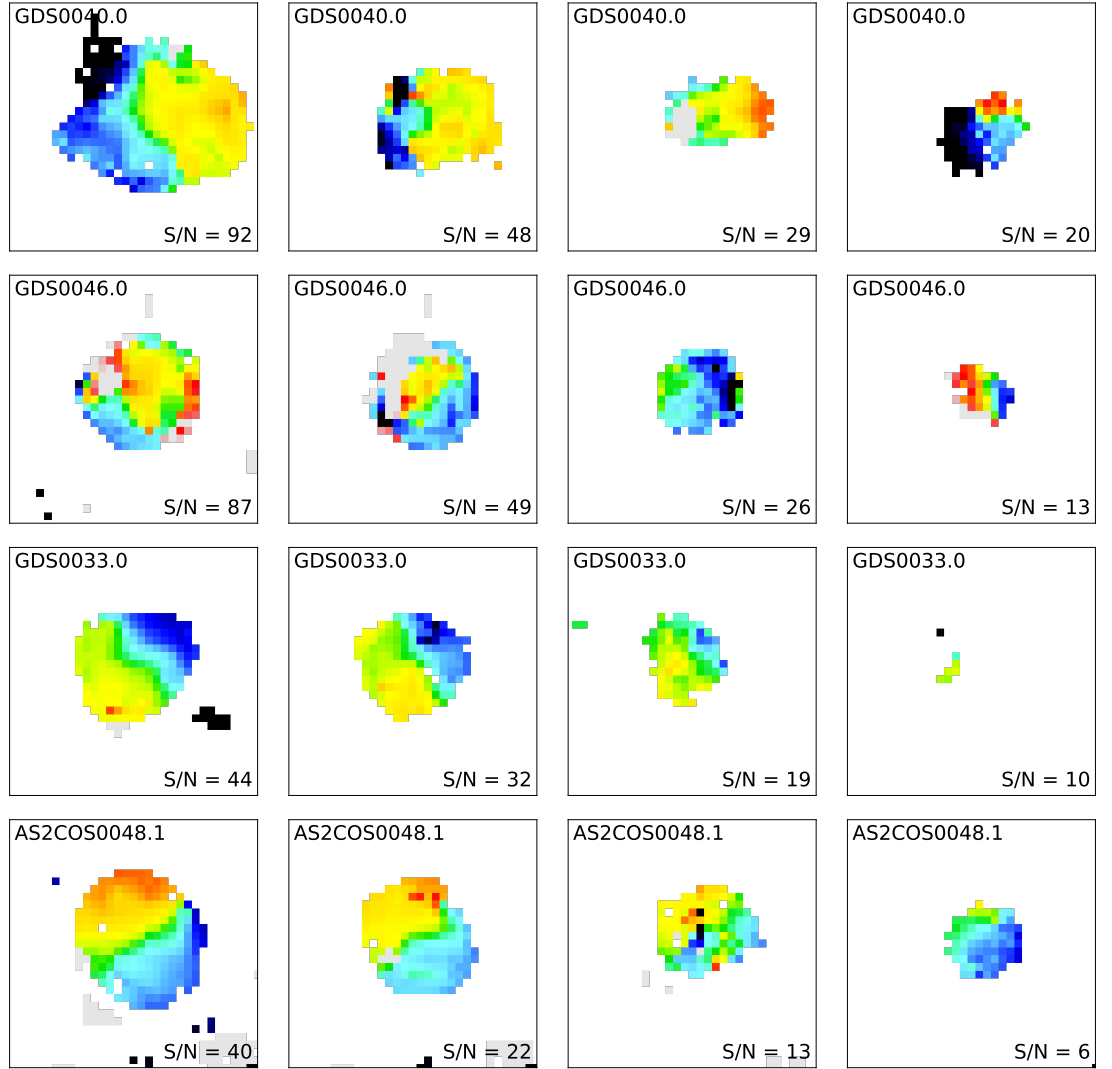
Figure 5.6: Velocity fields of four sources from the *ordered* sample after degrading the S/N to lower values. In all cases the degradation leads to smaller velocity fields due to the outer pixels no longer meeting the S/N threshold in the fitting procedure. We see in the cases of GDS0046.0 and AS2COS0048.1 that in the right-hand panel the velocity fields display noticeable gradients, and would be classified as *ordered*. However, for GDS0033.0 the majority of the velocity information has been lost at S/N ~ 10, and would therefore be classified as *disordered*. We leave a thorough examination of this effect for future work, but tentatively conclude that S/N is a significant distinguishing factor between the *ordered* and *disordered* samples.

5.3.2 Determining rotation axes

To quantify the kinematic structure of our sample we need to parametrise the dynamics, which we will do through measurements of the rotational velocity, $v_{2.2R_d}$, and velocity dispersion, $\sigma_{\rm obs}$. These quantities can be estimated from the rotation curves and velocity dispersion profiles, which we will extract from the kinematic maps derived in §5.3.1, but we must first determine the axes across which our sources have the largest velocity gradient. One way to assess this axis is to use the morphological major axis derived in §4.2.7, $\rm PA_{morph}$. Alternatively we can use the velocity field itself to estimate a kinematic axis, $\rm PA_{kin}$.

To determine $\rm PA_{kin}$ it is necessary to ensure that the velocity fields are appropriately centred, for which we employ the following method. First, we attempt to measure a centroid from the continuum image of the source constructed from the collapsed KMOS cube. If the continuum is not detected, we next measure a centroid from the Hα image. In the event that both of these methods are unsuccessful (i.e. if the Hα S/N is low) we centre the velocity field by eye. In total we measure centroids for 25, 6 and 5 sources for the three methods, respectively. We then shift the velocity field to align it with the chosen centroid, corresponding to a median shift of $0.39'' \pm 0.05''$.

Having centred our velocity fields we now determine their rotational axes (or kinematic position axes; $\rm PA_{kin}$), i.e. the axis across which the velocity gradient is the largest. This will enable us to extract rotation curves in such a way that the measured velocity is as close as possible to the true value. To determine the $\rm PA_{kin}$ we use two methods. First, we place a pseudo-slit across the velocity field and measure the peak-to-peak difference in velocity, Δv. We then rotate the pseudo-slit by $1°$ and repeat the process, determining Δv as a function of θ, from which we find the angles that both maximise and minimise Δv: $\theta_{\Delta v_{\max}}$ and $\theta_{\Delta v_{\min}}$. Finally we use

$$\rm PA_{kin} = \frac{\theta_{\Delta v_{\max}} + (\theta_{\Delta v_{\min}} + 90°)}{2} \tag{5.3.1}$$

to derive the $\rm PA_{kin}$. To estimate uncertainties on the $\rm PA_{kin}$ we use a Monte Carlo technique where we randomly resample the velocity fields using the measurement uncertainties 100 times and measure the spread in the distribution of the resultant 100 values.

When the S/N of the emission is low, this method is noisy and the resulting $\rm PA_{kin}$ may not appear to correlate well with the velocity field. Hence, in all cases we also identify a maximum velocity gradient $\rm PA_{kin}$ by eye, and where the $\rm PA_{kin}$ chosen by the algorithm described above does not appear to be a good fit to the velocity field (which we assess visually) we simply
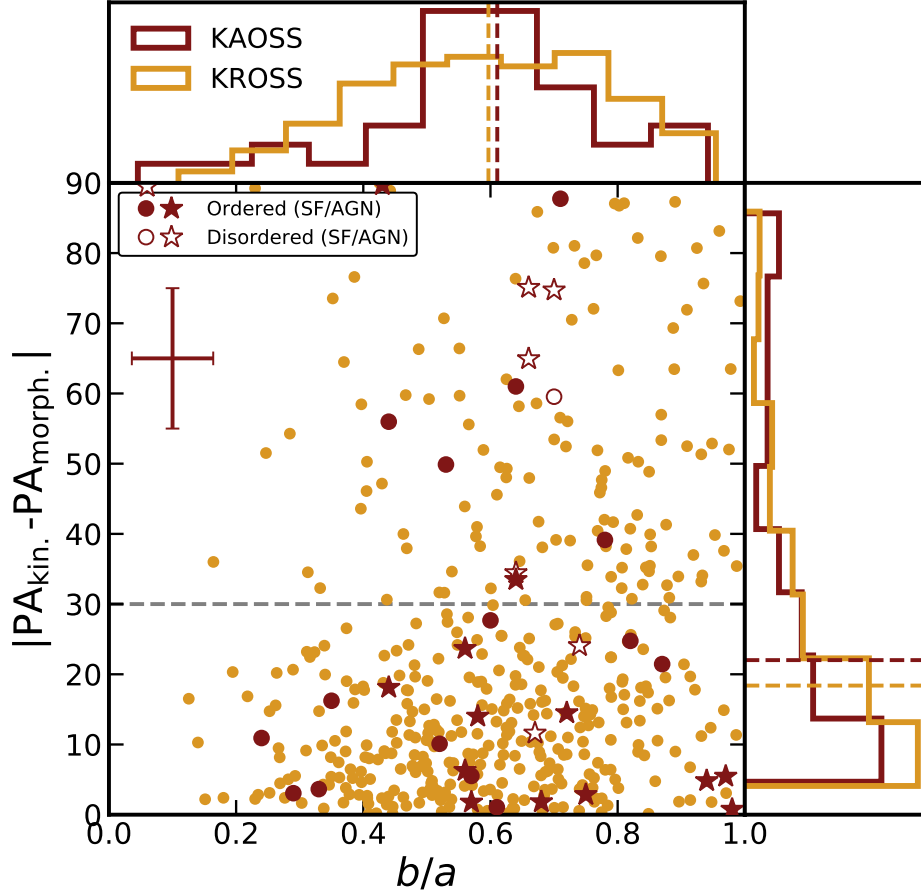
Figure 5.7: Misalignment between the position angle derived from Hα kinematics (PA$_{\text{kin}}$) and the position angle derived from optical/NIR imaging (PA$_{\text{morph}}$), versus axis ratio b/a. PA$_{\text{morph}}$ and b/a are both measured from GALFIT modelling of high-resolution optical/NIR imaging (see §4.2.7). The horizontal dashed line indicates a misalignment of 30°, less than which we take to be reasonable agreement between the two PAs. In the top-left corner we show a representative error bar for KAOSS galaxies, and as a comparison sample we plot results from the KROSS survey of SFGs at $z \sim 1$ (Harrison et al., 2017). A K-S test shows that the two distributions are consistent with having been drawn from the same parent sample at the 95 % confidence level, indicating that the KAOSS resolved sample shows similar levels of kinematic misalignment to "main-sequence" galaxies at $z \sim 1$.

use the "by eye" PA_{kin}. For context, we use the visual estimate of PA_{kin} for 15 (typically lower S/N) out of the 36 sources in the sample. For these sources we adopt an uncertainty of $\pm 5°$, which is comparable to the median uncertainty estimated from the 21 sources with Monte Carlo-derived uncertainties as described above. Our best-estimated values of the PA are tabulated in Table 5.2, and in Figs. 5.2 and 5.3 we overlay PA_{kin} on both the velocity and velocity dispersion maps.

For galaxies that are highly inclined, the kinematic and morphological position angles should be consistent (i.e. $PA_{kin} = PA_{morph}$), however in systems that are kinematically and morphologically complex this is not necessarily true. Comparing the two position angles therefore provides another metric for identifying disturbed systems (e.g. Wisnioski et al., 2015; Harrison et al., 2017). In Fig. 5.7 we show the misalignment between the kinematic position angle PA_{kin} and the morphological position angle measured from the GALFIT modelling of the optical/NIR imaging, PA_{morph} (see §4.2.7), as a function of the major-to-minor axis ratio b/a (also derived from GALFIT, see §4.2.7). We indicate a misalignment of 30° following Wisnioski et al. (2015), which would constitute reasonable agreement between the kinematic and morphological position axes based on the uncertainties. 13 lie above this threshold and 23 below it, therefore $36 \pm 10\%$ of the resolved KAOSS SMGs sample display kinematic and morphological axes which are misaligned. Six of the eight sources in the *disordered* subset (75%) have misaligned kinematic and morphological axes, which is unsurprising as these sources have low-quality velocity maps from which it is hard to estimate the PA accurately, although it is also possible that these systems are intrinsically more disturbed kinematically. For the typical S/N of this subset it is very difficult to distinguish the true cause.

As a comparison sample we also show the distribution of galaxies from the $z \sim 1$ KROSS star-forming galaxy sample (Harrison et al., 2017), with histograms of the distributions shown on both axes. We perform a two-sample Kolmogorov-Smirmov (K–S) test between the distributions of both the PA offsets and the axial ratios from KAOSS and KROSS, finding them to be consistent with being drawn from the same parent population at the 95% confidence level. The KROSS sample is comprised of main-sequence star-forming galaxies at $z \sim 1$, with typical star-formation rates of $\sim 7\,M_\odot\,yr^{-1}$, and this indicates that our sample is no more kinematically complex than much less-active SFGs, in terms of the axial misalignment. Later in this chapter we will further test this by comparing the star-formation rates and velocity dispersions of different samples.

5.4   Results and discussion

5.4.1   Rotation curves and rotational velocities

From our derived resolved velocity maps we now extract rotation curves and velocity dispersions profiles: velocities and velocity dispersions as a function of position along the rotation axis ($\mathrm{PA_{kin}}$). Rotation curves are extracted from the velocity field within a $0.5''$ wide ($N = 5$ pixels in the rebinned cube) pseudo-slit along the $\mathrm{PA_{kin}}$ from the velocity field, taking the median of the pixels across the slit. Velocity dispersion profiles are extracted from the velocity dispersion maps using the same slit, and uncertainties are extracted from the corresponding uncertainty maps.

The resultant rotation curves are shown in the left panels of Figs. 5.8–5.12. We note that the velocities plotted are those directly measured from the velocity maps, and no inclination corrections are applied at this stage. The rotation curves are ordered by descending Hα S/N, and we colour code the points depending on whether the source is in the *ordered* (red) or *disordered* (yellow) subset, as determined in §5.3.1.

In order to derive rotational velocities we fit the rotation curves with a model of the form (Freeman, 1970):

$$(v(r) - v_{\mathrm{off}})^2 = \frac{(r - r_{\mathrm{off}})^2 \pi G \mu_0}{h}(I_0 K_0 - I_1 K_1), \tag{5.4.1}$$

following Harrison et al. (2017) and Tiley et al. (2021), where v is the velocity in $\mathrm{km\,s^{-1}}$, r is the radial distance from the centre along the rotation axis in kpc, v_{off} if the velocity offset of the rotation curve from $0\,\mathrm{km\,s^{-1}}$, r_{off} is the spatial offset selected centroid the spatial position of the systemic velocity point on the rotation curve from $0\,\mathrm{kpc}$, μ_0 is the peak mass surface density, h is the disc scale radius and $I_n K_n$ are Bessel functions evaluated at $0.5r/h$. The best-fit v_{off} and r_{off} are shown in Tables 5.2. Then, as a measure of the rotational velocity of each galaxy we evaluate $v_{\mathrm{rot}} = v_{2.2R_d} / \sin i$, where $v_{2.2R_d}$ is the observed velocity at $2.2\,\mathrm{R}_d$[1] according to the model fits and the factor of $1/\sin i$ corrects for the observed inclination of the source. i is measured from GALFIT modelling (see §4.2.7, and Table 5.2). We note that in Chapter 4 we found that our sample may be inconsistent with the expected axial ratios b/a for late-type disc galaxies. Given that our inclination angles are estimated under the assumption that the SMGs are thick discs, this may be introducing an additional source of uncertainty into our velocity calculations.

---

[1]R_d is also convolved with $\sigma_{\mathrm{PSF}} \sim 2\,\mathrm{kpc}$.

	ID	R.A. (J2000)	Dec. (J2000)	$z_{\mathrm{H}\alpha}$	Ordered?	$\mathrm{PA_{kin}}$ [°]	$v_{2.2R_d}$ [km s^{-1}]	σ Sample	$\sigma_{\mathrm{obs.}}$ [km s^{-1}]
1	GDS0046.0	53.1049	-27.7053	1.6142	✓	135 ± 7	44 ± 7	O	120 ± 30
2	GDS0040.0	53.1311	-27.7732	2.2254	✓	90 ± 5	109 ± 3	O	78 ± 5
3	UDS0492.0	34.5398	-5.0334	1.2787	✓	106 ± 5	57 ± 13	O	88 ± 9
4	UDS0707.0	34.7984	-5.2526	2.4367	✗	50 ± 30	87 ± 9	M	280 ± 60
5	GDS0033.0	53.0727	-27.8343	1.6155	✓	144 ± 7	145 ± 15	O	90 ± 4
6	AS2COS0048.1	150.2885	2.3819	1.5813	✓	24 ± 1	113 ± 8	O	34 ± 3
7	GDS0023.0	53.1572	-27.8335	1.6177	✓	30 ± 5	137 ± 14	O	53 ± 3
8	A3COS298447	149.9483	1.7386	2.3889	✓	120 ± 6	82 ± 13	M	183 ± 9
9	GDS0001.0	53.0304	-27.8558	1.5390	✓	30 ± 5	88 ± 8	O	93 ± 5
10	UDS0601.0	34.8179	-5.2796	1.4628	✓	160 ± 8	84 ± 7	O	113 ± 7
11	GDS0004.0	53.0204	-27.7799	1.9657	✓	102 ± 5	200 ± 50	M	140 ± 50
12	GDS0053.0	53.1989	-27.8439	1.6157	✓	126 ± 18	250 ± 20	O	111 ± 6
13	UDS0428.0	34.7962	-4.9427	1.6284	✓	60 ± 20	32 ± 6	M	180 ± 40
14	UDS0287.1	34.3653	-5.2508	2.2907	✗	138 ± 7	220 ± 20	M	220 ± 50
15	GDS0035.0	53.0917	-27.7121	1.6145	✓	60 ± 30	180 ± 40	M	191 ± 10
16	UDS0603.0	34.8121	-5.2893	2.5086	✓	26 ± 1	131 ± 18	M	110 ± 20
17	UDS0338.0	34.0932	-5.0805	1.6612	✓	50 ± 5	151 ± 12	M	145 ± 16
18	GDS0048.0	53.1606	-27.7763	2.5453	✗	129 ± 6	240 ± 20	M	220 ± 30
19	A3COS795018	149.5035	2.5070	1.5780	✓	45 ± 5	26 ± 5	O	81 ± 4
20	GDS0065.0	53.1315	-27.8414	1.6140	✗	45 ± 2	330 ± 30	M	210 ± 70
21	AS2COS0025.1	150.1635	2.3725	2.0859	✓	60 ± 20	240 ± 100	M	176 ± 11
22	UDS0125.0	34.3633	-5.1994	2.1556	✓	130 ± 6	195 ± 16	O	84 ± 8
23	GDS0031.0	53.0774	-27.8596	2.0360	✓	40 ± 17	164 ± 8	M	160 ± 30
24	AS2COS0275.2	149.9517	1.7440	1.6334	✓	120 ± 30	100 ± 60	M	187 ± 14
25	UDS0115.0	34.5119	-5.0086	2.0335	✓	68 ± 5	156 ± 11	M	270 ± 60
26	GDS0047.0	53.1635	-27.8906	2.3237	✓	140 ± 50	172 ± 9	O	56 ± 5
27	GDS0020.0	53.1983	-27.7479	1.9236	✗	86 ± 5	62 ± 6	M	113 ± 11
28	UDS0199.0	34.8455	-5.2497	2.5553	✗	100 ± 5	250 ± 20	M	290 ± 60
29	GDS0071.0	53.0568	-27.7984	1.7313	✓	118 ± 6	160 ± 9	M	124 ± 13
30	UDS0445.0	34.4759	-5.0255	2.2922	✓	42 ± 2	280 ± 30	O	191 ± 10
31	UDS0097.0	34.8680	-5.2059	2.5928	✓	59 ± 5	73 ± 7	O	57 ± 10
32	UDS0292.0	34.3226	-5.2301	2.1829	✓	170 ± 8	85 ± 16	O	52 ± 6
33	UDS0333.0	34.5285	-4.9882	1.2773	✗	26 ± 5	28 ± 3	M	110 ± 40
34	AS2COS0003.4	150.2369	2.3358	2.4991	✗	119 ± 17	260 ± 20	M	290 ± 40
35	UDS0564.1	34.7234	-4.9923	1.6929	✓	130 ± 40	302 ± 19	O	51 ± 7
36	AS2COS0083.1	149.9157	1.7868	2.4987	✓	80 ± 5	26 ± 2	O	39 ± 2

Table 5.1: Properties of the resolved KAOSS sample. Sources are ordered by descending S/N of the integrated Hα detection, with the rank shown in the leftmost column, corresponding to the numbered velocity fields in Fig. 5.5. "Sample" indicates how the velocity dispersion was measured: "O" meaning outskirts and "M" meaning median (see §5.4.2) for more details. The median fractional error on the redshifts is 0.0002 or 60 km s^{-1} (see Chapter 4).

ID	i [°]	$v_{\rm rot}$ [km s^{-1}]	σ_0 [km s^{-1}]	$v_{\rm rot}/\sigma_0$	$v_{\rm circ}$ [km s^{-1}]	$v_{\rm off}$ [km s^{-1}]	$r_{\rm off}$ [kpc]
			Ordered				
GDS0046.0	12 ± 17	136 ± 20	120 ± 30	1.1 ± 0.3	220 ± 30	76	2.04
GDS0040.0	58 ± 4	141 ± 4	75 ± 4	1.88 ± 0.13	177 ± 5	36	-0.73
UDS0492.0	52 ± 5	82 ± 16	87 ± 9	0.9 ± 0.2	148 ± 14	47	4.38
GDS0033.0	36 ± 9	260 ± 30	86 ± 4	3.0 ± 0.3	290 ± 30	-74	-3.74
AS2COS0048.1	42 ± 7	178 ± 14	32 ± 3	5.5 ± 0.7	184 ± 14	-3	-0.05
GDS0023.0	60 ± 4	164 ± 16	52 ± 3	3.2 ± 0.3	180 ± 14	100	2.86
A3COS298447	61 ± 4	100 ± 14	116 ± 6	0.86 ± 0.12	193 ± 9	-20	-0.26
GDS0001.0	20 ± 13	270 ± 50	90 ± 4	3.0 ± 0.6	300 ± 40	-1	-2.09
UDS0601.0	40 ± 8	138 ± 12	109 ± 6	1.27 ± 0.14	207 ± 10	-42	-2.99
GDS0004.0	54 ± 5	260 ± 60	70 ± 7	3.7 ± 0.9	270 ± 50	175	0.06
GDS0053.0	58 ± 4	310 ± 30	102 ± 5	3.0 ± 0.3	340 ± 20	-183	-5.33
UDS0428.0	78 ± 2	34 ± 6	140 ± 30	0.24 ± 0.07	200 ± 40	-41	-3.61
GDS0035.0	73 ± 3	190 ± 50	121 ± 6	1.6 ± 0.4	260 ± 40	-188	-0.39
UDS0603.0	66 ± 3	153 ± 19	87 ± 16	1.8 ± 0.4	200 ± 20	-116	-4.08
UDS0338.0	45 ± 6	224 ± 19	92 ± 10	2.4 ± 0.3	259 ± 17	87	3.27
A3COS795018	30 ± 11	57 ± 11	81 ± 4	0.69 ± 0.13	128 ± 5	-12	-1.38
AS2COS0025.1	52 ± 5	320 ± 90	89 ± 5	4 ± 1	340 ± 80	168	4.43
UDS0125.0	46 ± 6	280 ± 20	78 ± 7	3.6 ± 0.4	300 ± 20	-70	-1.99
GDS0031.0	55 ± 5	210 ± 10	81 ± 15	2.6 ± 0.5	239 ± 13	13	-0.17
AS2COS0275.2	48 ± 6	150 ± 40	118 ± 9	1.3 ± 0.4	230 ± 30	77	2.68
UDS0115.0	74 ± 3	167 ± 12	170 ± 40	1.0 ± 0.2	300 ± 50	-8	-0.11
GDS0047.0	56 ± 4	222 ± 11	51 ± 4	4.3 ± 0.4	233 ± 11	-38	-1.60
GDS0071.0	57 ± 4	199 ± 12	63 ± 7	3.2 ± 0.4	218 ± 11	140	0.93
UDS0445.0	57 ± 4	350 ± 40	176 ± 9	2.0 ± 0.2	430 ± 30	-71	0.30
UDS0097.0	66 ± 3	81 ± 7	52 ± 9	1.6 ± 0.3	110 ± 10	141	0.76
UDS0292.0	14 ± 15	270 ± 50	52 ± 6	5 ± 1	280 ± 50	-29	-1.84
UDS0564.1	82 ± 3	311 ± 19	47 ± 7	7 ± 1	318 ± 18	183	4.39
AS2COS0083.1	67 ± 3	29 ± 2	39 ± 2	0.75 ± 0.05	62.0 ± 1.0	-192	0.56
			Disordered				
UDS0707.0	...	130 ± 40	220 ± 50	0.6 ± 0.2	340 ± 60	...	...
UDS0287.1	43 ± 7	330 ± 30	140 ± 30	2.4 ± 0.6	390 ± 40	...	...
GDS0048.0	50 ± 5	350 ± 30	109 ± 13	3.2 ± 0.5	380 ± 30	...	...
GDS0065.0	50 ± 5	440 ± 40	108 ± 10	4.1 ± 0.6	460 ± 40	...	...
GDS0020.0	47 ± 6	90 ± 8	87 ± 8	1.03 ± 0.13	153 ± 11	...	...
UDS0199.0	49 ± 5	340 ± 30	150 ± 30	2.3 ± 0.5	400 ± 40	...	...
UDS0333.0	47 ± 6	41 ± 4	54 ± 5	0.76 ± 0.10	87 ± 7	...	...
AS2COS0003.4	52 ± 5	340 ± 30	230 ± 30	1.5 ± 0.2	470 ± 40	...	...

Table 5.2: Kinematic properties of the KAOSS sample. Sources are ordered by their integrated Hα signal-to-noise ratio, and we also separate the *ordered* and *disordered* subsets. The latter have less robust velocity measurements due to their less regular rotation curves, and so we use Δv as a proxy for $v_{2.2R_d}$ (see §5.4.1). For sources where we have identified the kinematic position angle PA$_{\rm kin}$ by eye we set a nominal uncertainty of 10°.

ID	σ_{eff} [km s^{-1}]	M_{baryon} [10^{11} M$_\odot$]	M_{dyn} [10^{11} M$_\odot$]	M_{halo} [10^{12} M$_\odot$]
		Ordered		
GDS0046.0	410 ± 30	1.4 ± 0.2	2.6 ± 0.2	160 ± 50
GDS0040.0	125 ± 4	2.1 ± 0.3	0.58 ± 0.03	3.0 ± 0.8
UDS0492.0	129 ± 10	0.49 ± 0.07	0.58 ± 0.04	6 ± 2
GDS0033.0	204 ± 19	3.4 ± 0.6	2.0 ± 0.3	12 ± 4
AS2COS0048.1	149 ± 9	3 ± 2	0.85 ± 0.11	4 ± 1
GDS0023.0	127 ± 10	1.1 ± 0.2	1.05 ± 0.14	2.4 ± 0.8
A3COS298447	136 ± 6	1.6 ± 0.2	1.37 ± 0.07	6 ± 2
GDS0001.0	210 ± 30	2.9 ± 0.6	1.6 ± 0.4	13 ± 6
UDS0601.0	147 ± 8	2.0 ± 0.3	1.76 ± 0.11	7 ± 2
GDS0004.0	190 ± 40	3.8 ± 0.3	2.1 ± 0.6	9 ± 5
GDS0053.0	240 ± 17	2.6 ± 0.4	3.8 ± 0.5	20 ± 6
UDS0428.0	140 ± 30	1.1 ± 0.2	3.4 ± 0.4	9 ± 6
GDS0035.0	180 ± 20	1.9 ± 0.3	3.4 ± 0.5	12 ± 5
UDS0603.0	138 ± 15	1.5 ± 0.3	0.99 ± 0.12	4 ± 2
UDS0338.0	183 ± 13	1.5 ± 0.5	1.79 ± 0.19	9 ± 3
A3COS795018	91 ± 4	0.83 ± 0.16	0.61 ± 0.03	1.8 ± 0.4
AS2COS0025.1	240 ± 60	1.3 ± 0.3	2.5 ± 1.0	19 ± 15
UDS0125.0	211 ± 15	4 ± 2	3.1 ± 0.4	12 ± 4
GDS0031.0	169 ± 10	2.4 ± 0.3	1.61 ± 0.16	7 ± 2
AS2COS0275.2	159 ± 20	1.5 ± 0.3	1.21 ± 0.14	9 ± 3
UDS0115.0	210 ± 30	2.3 ± 0.4	5.4 ± 0.7	25 ± 16
GDS0047.0	165 ± 8	0.8 ± 0.3	0.90 ± 0.10	5 ± 1
GDS0071.0	154 ± 8	1.1 ± 0.2	1.34 ± 0.13	4 ± 1
UDS0445.0	300 ± 20	1.7 ± 0.4	5.1 ± 0.5	55 ± 17
UDS0097.0	78 ± 7	1.4 ± 0.3	0.80 ± 0.08	0.7 ± 0.3
UDS0292.0	200 ± 30	2.8 ± 0.4	1.1 ± 0.3	9 ± 5
UDS0564.1	225 ± 13	0.81 ± 0.19	3.4 ± 0.5	13 ± 4
AS2COS0083.1	43.9 ± 0.7	1.8 ± 0.3	0.387 ± 0.014	0.15 ± 0.03
		Disordered		
UDS0707.0	380 ± 30	12 ± 2	0.195 ± 0.015	150 ± 50
UDS0287.1	270 ± 30	0.46 ± 0.08	0.36 ± 0.05	35 ± 16
GDS0048.0	270 ± 20	0.28 ± 0.05	1.8 ± 0.2	28 ± 10
GDS0065.0	330 ± 30	3.0 ± 0.5	7 ± 1	50 ± 17
GDS0020.0	108 ± 7	1.0 ± 0.3	0.86 ± 0.06	2.7 ± 0.9
UDS0199.0	280 ± 30	3.7 ± 0.6	7.7 ± 1.0	40 ± 16
UDS0333.0	61 ± 4	1.9 ± 0.3	0.244 ± 0.014	0.47 ± 0.16
AS2COS0003.4	330 ± 30	3.3 ± 0.4	12 ± 1	90 ± 40

Table 5.3: Further properties of the KAOSS sample. σ_{eff} is the effective linewidth if all of the SMG kinetic energy was translated into turbulent motions (see §5.4.8). M_{baryon} is the combined mass of the gas and stellar components and M_{dyn} is the entire matter content estimated within $2R_e$. M_{halo} is the estimated mass of the halo in which the SMG resides.
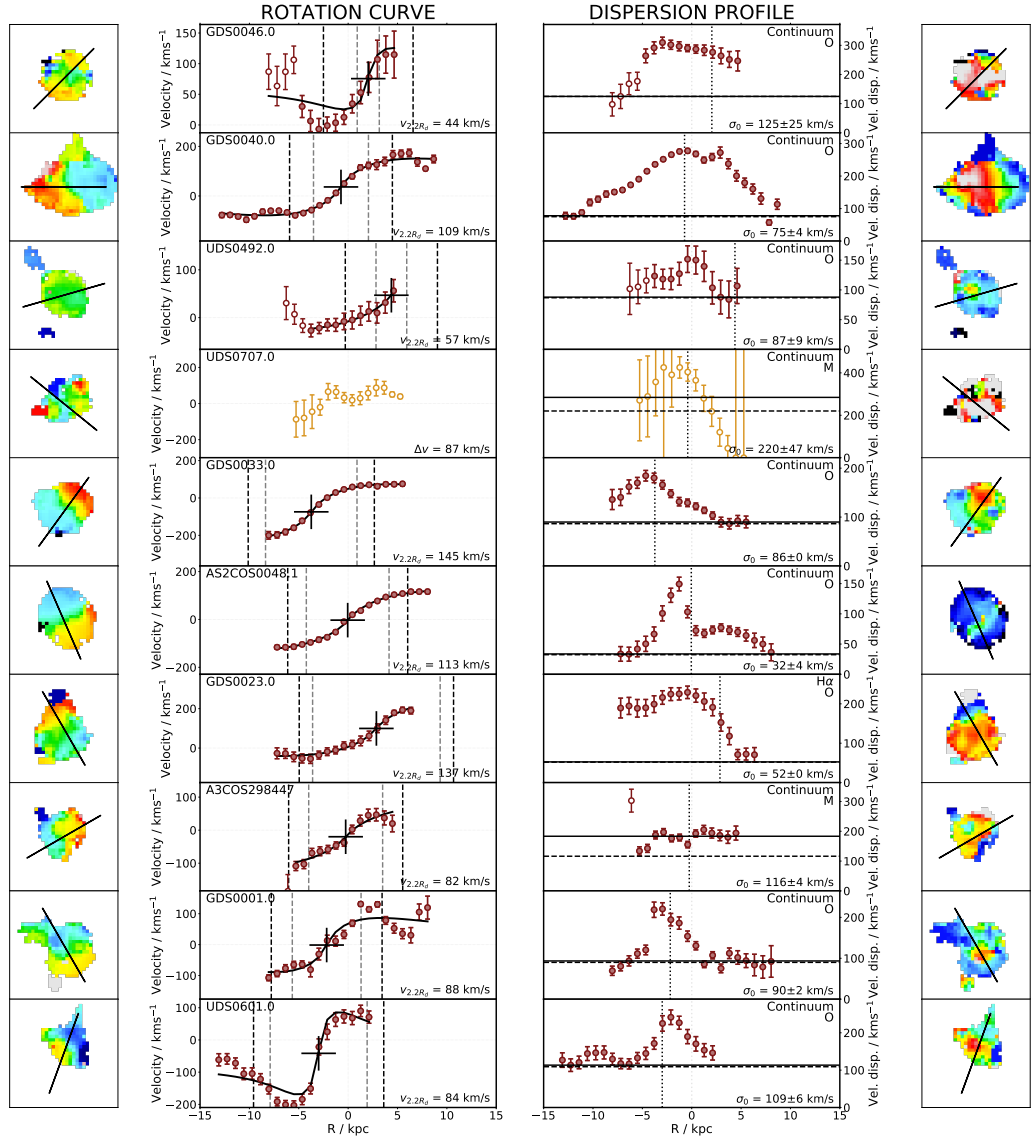
Figure 5.8: Hα rotation curves (left) and velocity dispersion profiles (right) for the resolved KAOSS sample. Sources are ordered by the S/N of the Hα emission line as in Figs. 5.2–5.4, and we colour code sources in the *ordered* subset in red and those in the *disordered* subset in yellow. For the same sources, the solid black lines indicate Freeman disc model fits to the data, the vertical dashed lines indicate ±2.2 times the disc radius (thin) and ±2.2 times the disc radius convolved with $\sigma_{\rm PSF}$ (thick), the latter at which we measure the velocity, and the cross indicates the original source centroid. Points that are plotted as open circles are masked in the fitting procedure. For the dispersion profiles we indicate the observed sigma, $\sigma_{\rm obs}$ (horizontal black solid line), along with the method used to measure it (top right), and the beam smearing-corrected intrinsic velocity dispersion (horizontal black dashed line). We also indicate the method used to centre the velocity field in the top right corner of the dispersion profile panels.
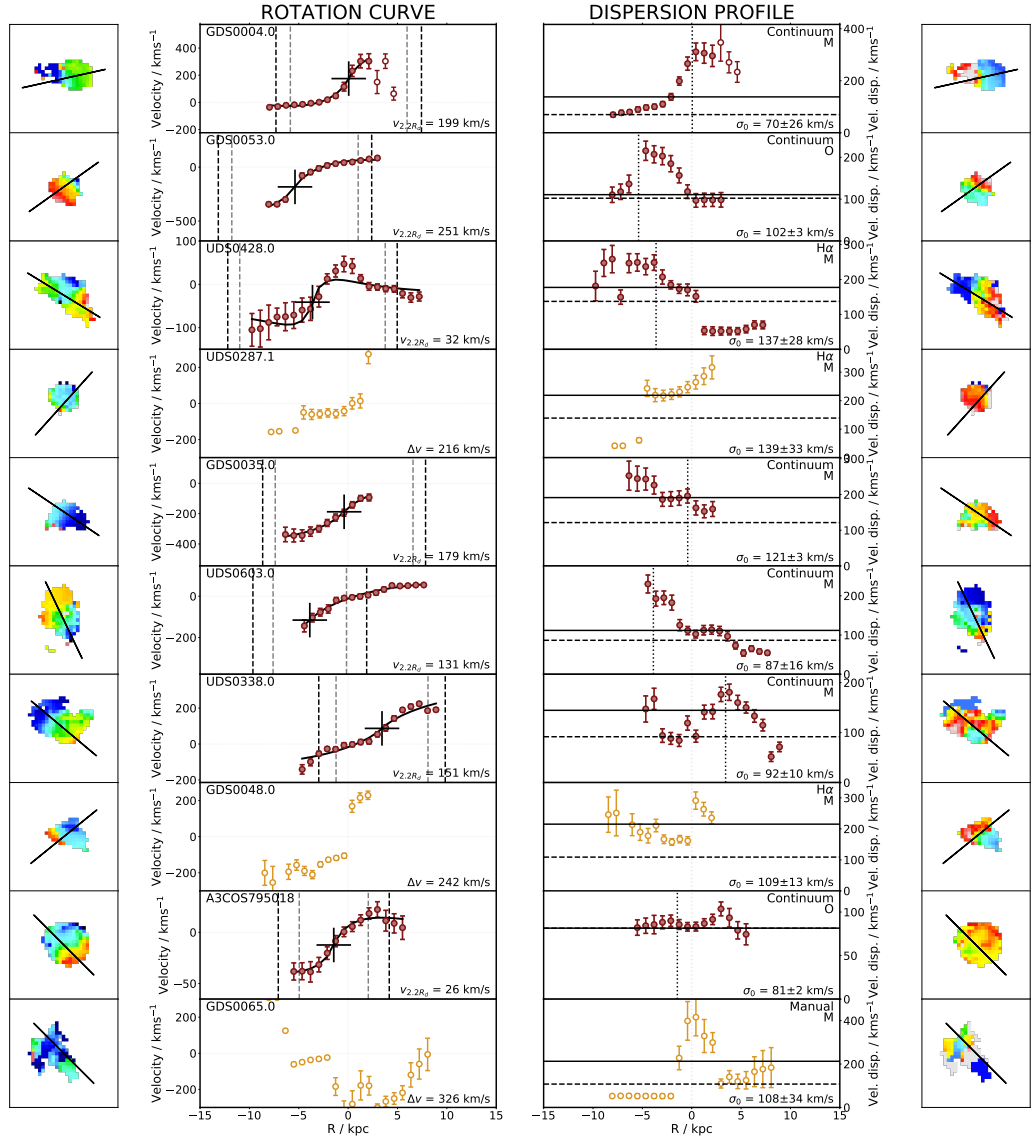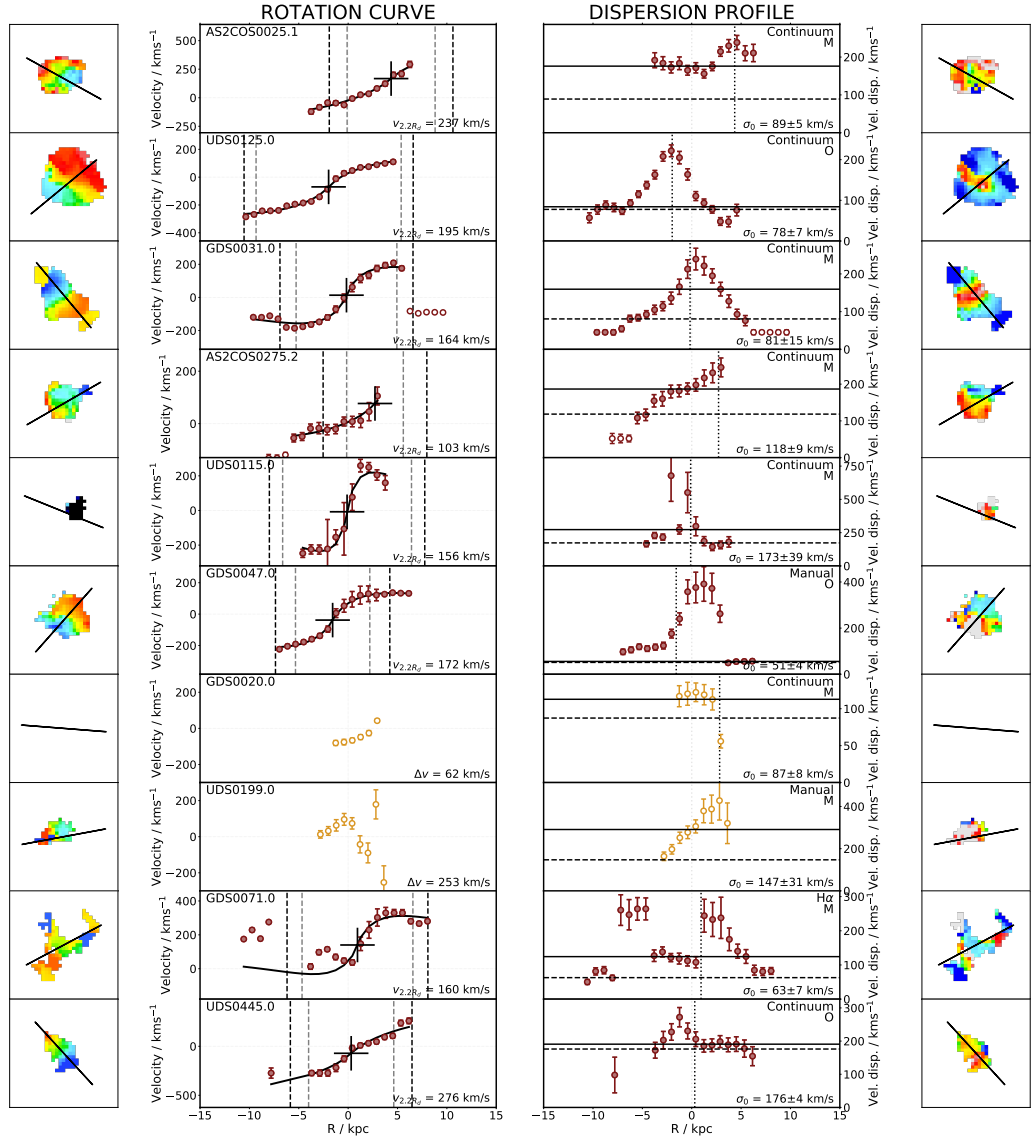
Figure 5.9: Fig. 5.8 continued.
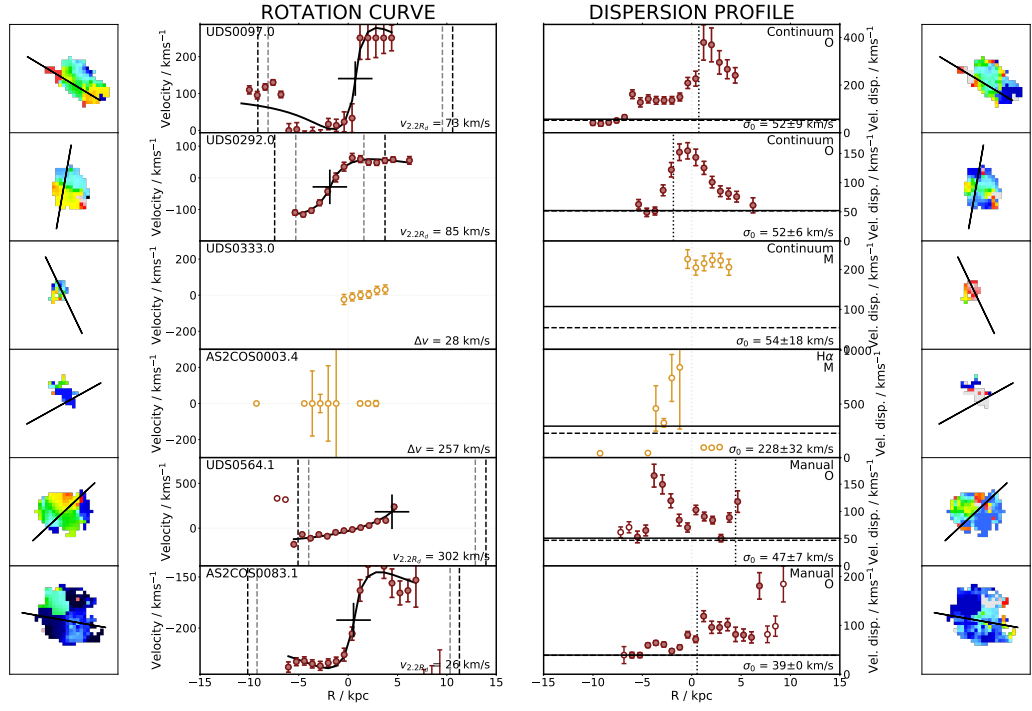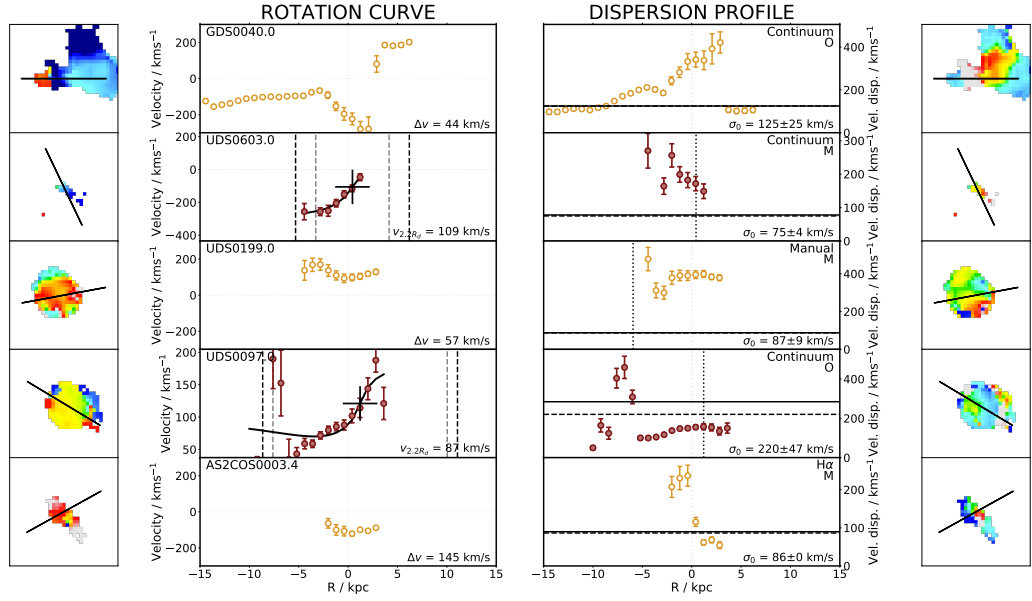
Figure 5.10: Fig. 5.8 continued.

Figure 5.11: Fig. 5.8 continued.

Figure 5.12: Same as Fig. 5.8 but now with [OIII] rotation curves instead of Hα.

The offsets r_{off} and v_{off} are plotted as crosses in Figs. 5.8–5.12. In some cases the velocity offsets are as large as $|v_{\mathrm{off}}| > 100\,\mathrm{km\,s^{-1}}$ and the spatial offsets can be over $|r_{\mathrm{off}}| > 4\,\mathrm{kpc}$. As we take the redshift measured from the integrated emission in Chapter 4 this suggests that there are significant asymmetries in the Hα intensity which may be an indicator of turbulent structure in our sample. A similar argument can be made for the spatial offsets, as the initial centres are in most cases derived from the rest-frame optical continuum emission. For the 28 sources in the *ordered* subset we inspect the histograms of both r_{off} and v_{off} (not shown), finding them to be consistent with Gaussian distributions with widths of $100\,\mathrm{km\,s^{-1}}$ and $0.3''$ ($\sim 2.5\,\mathrm{kpc}$) respectively.

For the eight sources in the *disordered* subset we calculate as an alternative measure of the rotational velocity:

$$v'_{\mathrm{rot}} = \frac{\Delta v}{2 \sin i} = \frac{v_{\mathrm{max}} - v_{\mathrm{min}}}{2 \sin i}, \tag{5.4.2}$$

where v_{min} and v_{max} are the minimum and maximum velocities of the rotation curve, respectively. For these eight sources we find a median v_{rot} of $230 \pm 60\,\mathrm{km\,s^{-1}}$ compared to a median v_{rot} of $130 \pm 20\,\mathrm{km\,s^{-1}}$ for the *ordered* subset. In all plots that follow where v_{rot} is used we plot these eight sources as open symbols, to highlight values that are less robust than those measured from rotation curve fits.

We note that as some of the derived inclination angles are apparently small ($< 20°$), we set a minimum inclination of $i = 20°$ to avoid significant extrapolations (given the simple models we are adopting). This only affects two sources, GDS0046.0 and UDS0292.0, that have GALFIT-derived inclinations of $i = 12° \pm 17°$ and $i = 14° \pm 15°$ respectively. Both are consistent with our chosen minimum inclination ($20°$) within their large uncertainties. Additionally, the axis ratio measured from GALFIT for UDS0707.0 is less than $(b/a)_0$ (for which we adopted a value of 0.2, see §4.2.7), resulting in an unphysical inclination angle, and we also set a minimum inclination of $i = 20°$ for this source.

After applying inclination corrections we derive median rotational velocities of $v_{\mathrm{rot}} = 190 \pm 20\,\mathrm{km\,s^{-1}}$ for the *ordered* subset and $v_{\mathrm{rot}} = 330 \pm 60\,\mathrm{km\,s^{-1}}$ for the *disordered* subset. For context, the $z \sim 1.5$ KGES sample has a median velocity at 2.2 times the disc radius ($2.2\,R_d$) of $47 \pm 4\,\mathrm{km\,s^{-1}}$, increasing to $61 \pm 5\,\mathrm{km\,s^{-1}}$ for inclination-corrected velocities. The $z \sim 1$ KROSS sample has a median inclination-corrected velocity at $2.2\,R_d$ of $105 \pm 4\,\mathrm{km\,s^{-1}}$, also lower than KAOSS. We conclude that KAOSS galaxies have much higher rotational velocities than less active (and apparently lower mass) galaxies that have been observed with KMOS. This is likely a consequence of the higher gas fractions in these sources (Chapter 3

Birkin et al., 2021), which leads to higher star-formation rates and therefore higher stellar masses (as described by the star-forming "main sequence". We explore this idea further in §5.4.1.

Comparing to other ULIRG samples, the six $z \sim 2.5$ sources observed by Hogan et al. (2021) have a median $v_{\max} = 310 \pm 50$, significantly higher than the KAOSS sample, however this is partly reflected by the fact that $v_{\max}$ samples the rotation curve at its maximum value, whereas our measure, at 2.2 times the disc radius, may not reach the maximum of the rotation curves. Alaghband-Zadeh et al. (2012) measure the quantity V_{obs} as the maximum difference in velocity in the velocity fields, finding an average value of $V_{\mathrm{obs}} = 330 \pm 80 \, \mathrm{km \, s^{-1}}$. This is not directly comparable to our median v_{rot}, but if we were to compare against their V_{obs} we would find that our sources are rotating faster.

5.4.2 Observed velocity dispersions and beam smearing corrections

We now turn to measuring the velocity dispersions in our sources, which will allow us to assess the degree of turbulent motion in SMGs. Figs. 5.8–5.12 shows velocity dispersion profiles for the resolved KAOSS sources. We see that in most cases, particularly for sources in the *ordered* subset, that the dispersion profiles rise strongly into the centre of the galaxy, the result of beam smearing.

To measure the observed velocity dispersion, σ_{obs}, we inspect the velocity dispersion profiles and divide them into two groups, following Johnson et al. (2018): where the velocity dispersion appears to have flattened in the outskirts we measure σ_{obs} as the median of the three outer points (spanning $0.3''$ or $\sim 2.5 \, \mathrm{kpc}$) on both sides and take the lower value of the two sides, and in all other cases we simply measure σ_{obs} as the median of the profile. As in Johnson et al. (2018) we label the sources "O" and "M" (see Figs. 5.8–5.12) to indicate that the intrinsic velocity dispersion has been measured from the "outskirts" or "median", respectively. From the 36 resolved sources, we measure σ_{obs} from the outskirts in 17 cases, and from the median in the remaining 19 cases.

Our observations with KMOS are seeing limited, with $\mathrm{FWHM_{PSF}} \sim 0.6''$ (compared to a median effective radius of $R_e \sim 0.4''$ for the resolved sample) and the convolution of our observations with the seeing causes information from adjacent pixels to be combined – this effect is referred to as "beam smearing" (e.g. Johnson et al., 2018). The main effects of this are flattening of the observed rotation curve and increasing the observed velocity dispersion (e.g. Epinat et al., 2010; Burkert et al., 2016; Johnson et al., 2018). To correct for beam

smearing and estimate the intrinsic velocity dispersion σ_0 we use the prescriptions of Johnson et al. (2018), who derived correction factors from mock KMOS observations for the KROSS survey. We adopt the median R_d of our sample from the GALFIT measurements for all sources, $R_d = 0.42''$, and use $v_{2.2R_d}$ (i.e. not corrected for inclination) as an estimate of the rotational velocity. We list the observed velocity dispersions, σ_{obs}, in Table 5.1 and the intrinsic velocity dispersions, σ_0, in Table 5.2.

For the 19 sources in the "M" subset the median beam smearing correction is $\xi_\sigma = 0.63 \pm 0.09$, and for the 17 sources in the "O" subset the median beam smearing correction is $\xi_\sigma = 0.96 \pm 0.02$. The latter is comparable to the corrections used for KROSS by Johnson et al. (2018) who find $\xi_\sigma = 0.96^{+0.02}_{-0.06}$ for outskirt corrections, but they apply a much smaller correction than we do, $\xi_\sigma = 0.8^{+0.1}_{-0.3}$ for median corrections. The two variables which affect the beam smearing according to the model we use are the disc radius relative to the PSF size, and the rotational velocity. From Chapter 4, we see that the KAOSS sources are marginally larger than the KROSS sources, median $R_e = 3.6 \pm 0.3\,\mathrm{kpc}$ for KAOSS compared to median $R_e = 2.9^{+1.8}_{-1.5}\,\mathrm{kpc}$ (Harrison et al., 2017) for KROSS (both surveys have comparable seeing). However, the KAOSS galaxies have much higher rotational velocities, median $v_{\mathrm{rot}} = 190 \pm 20\,\mathrm{km\,s^{-1}}$ compared to median $v_{\mathrm{rot}} = 109 \pm 5\,\mathrm{km\,s^{-1}}$ from KROSS (Harrison et al., 2017). Therefore the KAOSS sources experience stronger beam smearing than KROSS due to the much larger rotational velocities of the galaxies.

We also apply beam smearing corrections to the rotation velocities, ξ_v, following Johnson et al. (2018), although these corrections are generally much smaller. Our sample has a median correction of $\xi_v = 1.06 \pm 0.01$, increasing the median v_{rot} by $\sim 11\,\mathrm{km\,s^{-1}}$. This is also consistent with the corrections applied by Johnson et al. (2018) to the KROSS sample, who found a median $\xi_v = 1.07 \pm 0.03$.

We caution that our use of the beam smearing corrections from Johnson et al. (2018) are based on the assumption that the resolved KAOSS sources can be described by rotating discs, which is a simplistic assumption for SMGs given that they may be kinematically more complex as discussed earlier (see also e.g. Alaghband-Zadeh et al., 2012). We therefore add vectors to all figures that show quantities derived using σ_0 to illustrate how the plotted values would change if we had applied no beam-smearing correction. The "true" intrinsic velocity dispersions are likely to lie somewhere between no correction and the full correction. As the corrections to v_{rot} are small ($\sim 5\,\%$) we do not add similar vectors to plots of v_{rot}.
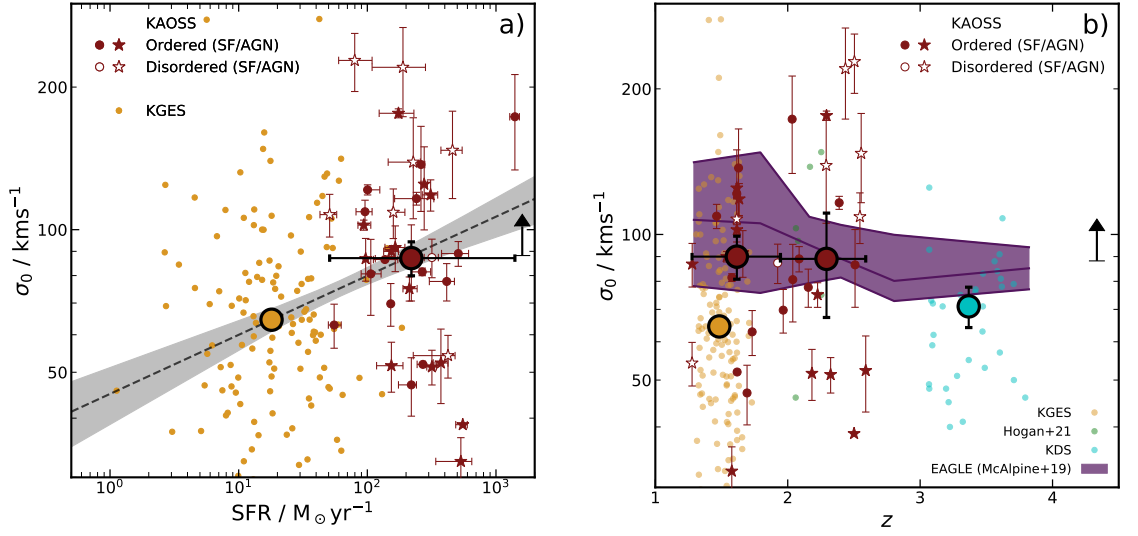
Figure 5.13: **a)** Intrinsic velocity dispersion σ_0 versus SFR for the KAOSS and KGES samples, all of which are estimated from MAGPHYS SED fitting. The KAOSS resolved sample has SFRs that are roughly an order of magnitude higher than those of the less actively star forming KGES sample, and we see a modest positive trend in σ_0 with SFR (and hence that more actively star forming galaxies are more turbulent) which is significant at $4\,\sigma$. **b)** Intrinsic velocity dispersion σ_0 versus redshift for the resolved KAOSS sample, along with $z \sim 1.5$ KGES galaxies, $z \sim 2.5$ ULIRGs (Hogan et al., 2021), and $z \sim 3.5$ star-forming galaxies (Turner et al., 2017). We also compare our sources with submillimetre-bright galaxies from the EAGLE simulations (McAlpine et al., 2019), finding agreement with the resolved KAOSS subset, but we find no evidence for any evolution of σ_0 with redshift.

5.4.3 Intrinsic velocity dispersions

Intrinsic velocity dispersions provide a measure of the turbulence in galaxies, and so we can compare our values to those measured from other galaxy populations to determine the relative level of turbulence as a function of galaxy parameters such as star-formation rate and redshift.

Our sample has a median $\sigma_{\mathrm{obs}} = 120 \pm 20\,\mathrm{km\,s}^{-1}$, and a median $\sigma_0 = 88 \pm 7\,\mathrm{km\,s}^{-1}$. The Hogan et al. (2021) and Alaghband-Zadeh et al. (2012) samples have median intrinsic velocity dispersions of $\sigma_0 = 100 \pm 20\,\mathrm{km\,s}^{-1}$ and $\sigma_0 = 160 \pm 60\,\mathrm{km\,s}^{-1}$ respectively, both comparable with the KAOSS sample. On the other hand the KGES sample has a median beam smearing-corrected velocity dispersion of $\sigma_0 = 46 \pm 2\,\mathrm{km\,s}^{-1}$ (Tiley et al., 2021). Hence the dust-obscured KAOSS sources have systematically higher intrinsic velocity dispersions, and are therefore apparently more turbulent than the KGES galaxies. This result supports the idea that more highly star-forming galaxies experience greater turbulence in the ISM.

To quantify this further, in Fig. 5.13 we show σ_0 versus star-formation rate, as measured from

MAGPHYS SED fitting. The KAOSS SMGs have an order of magnitude higher star-formations rates than the KGES sample, and we again see that KAOSS galaxies display higher velocity dispersions, whether corrected or uncorrected for beam smearing. We fit the median KAOSS and KGES points (with bootstrap uncertainties), finding a 4σ correlation between σ_0 and SFR, indicating a mild link between the two quantities.

Previous kinematic studies of star-forming galaxies suggest that high-redshift galaxies are more turbulent than galaxies in the local Universe, with much higher velocity dispersions (e.g. Förster Schreiber et al., 2009; Wisnioski et al., 2015; Johnson et al., 2018). We therefore exploit our sample, along with other literature samples, to search for a trend between velocity dispersion and redshift. Fig. 5.13 shows the beam smearing-corrected velocity dispersions of our sample versus redshift. As a comparison with simulations we show results from McAlpine et al. (2019), who studied submillimetre-bright galaxies in the EAGLE simulations. We divide the resolved KAOSS sample into two bins in redshift, with median values of $z \sim 1.6$ and $z \sim 2.3$, and the two bins have median intrinsic velocity dispersions of $\sigma_0 = 90 \pm 9\,\mathrm{km\,s^{-1}}$ and $\sigma_0 = 89 \pm 20\,\mathrm{km\,s^{-1}}$ respectively, showing no trend across the redshift range covered by the resolved KAOSS sample. Both medians are consistent within the uncertainties with the EAGLE predictions (McAlpine et al., 2019), but higher than both the $z \sim 1.5$ KGES and $z \sim 3.5$ KDS samples. We conclude from these results that our sources are likely to be more turbulent on average than "normal" star-forming galaxies at similar redshifts, in line with previous observational studies (e.g. Alaghband-Zadeh et al., 2012), but we see no evidence for a systematic trend with redshift. Identifying such a trend robustly would require similarly selected samples across a wide redshift range.

5.4.4   Rotational support

Having determined that KAOSS SMGs are apparently turbulent and massive sources we now assess whether turbulence is the dominant source of motion. One of the simplest methods of doing this is to calculate the ratio of rotation velocity to intrinsic velocity dispersion $v_{\rm rot}/\sigma_0$ (e.g. Weiner et al., 2006; Wisnioski et al., 2015), and if a galaxy has a much larger rotation velocity than its velocity dispersion then it is considered to be "rotationally supported". Alternatively a galaxy that appears to be dominated by turbulent motions may be displaying inclination/projection effects, and/or may be supported through ongoing interactions/mergers.

Before deriving $v_{\rm rot}/\sigma_0$ we show the intrinsic velocity dispersion σ_0 as a function of the ro-

tational velocity v_{rot} for the resolved KAOSS sources in Fig. 5.14, alongside galaxies from the KGES sample and Hogan et al. (2021). This demonstrates the elevated rotational velocities and velocity dispersions of the KAOSS sources compared to the KGES sample that were discussed in §5.4.1 and §5.4.3. We remind the reader that we are flagging sources in the *disordered* subset, for which the measurements of rotational velocity are likely to be less robust, by open symbols. These values are likely to be biased high compared to our measured values of $v_{2.2R_d}$ from the *ordered* subset, as 2.2 times the disc radius (~ 4.5 kpc) may not be far out enough to reach the peak of the rotation curve in some cases.

For the remainder of this chapter we also flag sources which have been identified as AGN hosts (see §4.3.1) as stars, in order to test whether these sources are kinematically distinct from star-forming sources. We measure median v_{rot} for the AGN and star-forming subsamples of $v_{rot} = 180 \pm 40 \,\mathrm{km\,s^{-1}}$ and $v_{rot} = 190 \pm 30 \,\mathrm{km\,s^{-1}}$, when only using measurements from the *ordered* sources. Median intrinsic velocity dispersions for the two subsamples are $\sigma_0 = 97 \pm 12 \,\mathrm{km\,s^{-1}}$ and $\sigma_0 = 87 \pm 8 \,\mathrm{km\,s^{-1}}$. Therefore, the AGN in our sample have marginally higher rotational velocities and velocity dispersions (although still consistent within the uncertainties in both cases).

In Fig. 5.14 we show lines indicating $v_{rot}/\sigma_0 = 1$ and 3, in accordance with the criteria described above. Among the sources in our sample with robust v_{rot} measurements, 22 of the 28 sources ($79 \pm 17\,\%$) fit the criterion for rotationally dominated sources of $v_{rot}/\sigma_0 > 1.5$, dropping to 12 out of 28 ($43 \pm 12\,\%$) if we instead adopt the criterion of $v_{rot}/\sigma_0 > 3$. The median value of our sample is $v_{rot}/\sigma_0 = 2.2 \pm 0.4$, with medians of $v_{rot}/\sigma_0 = 2.6 \pm 0.7$ and $v_{rot}/\sigma_0 = 2.0 \pm 0.6$ for the star-forming and AGN samples respectively. This is consistent with the KROSS sample (Stott et al., 2016), which has an average $v_{rot}/\sigma_0 = 2.2 \pm 1.4$ (where the uncertainty is the standard deviation of the distribution), and the KGES sample which has a median $v_{rot}/\sigma_0 = 1.6 \pm 0.1$. We suggest that the resolved KAOSS SMGs are likely to be rotationally supported, yet highly turbulent systems.

Our SMGs are among the more actively star-forming systems at $z \sim 2$, with a median SFR of $220 \pm 30 \,\mathrm{M_\odot yr^{-1}}$. As such, we are interested in understanding the implications of this fact for the kinematics of the sources, and we showed earlier in this section that KAOSS sources appear to be more turbulent than the $z \sim 1.5$ "main sequence" KGES galaxies, as traced by their Hα velocity dispersions. We are also interested in whether v_{rot}/σ_0 varies similarly with SFR, and we show these two quantities in Fig. 5.15. To search for a trend between v_{rot}/σ_0 and SFR we bin the KAOSS and KGES sources in SFR, but we see little evidence
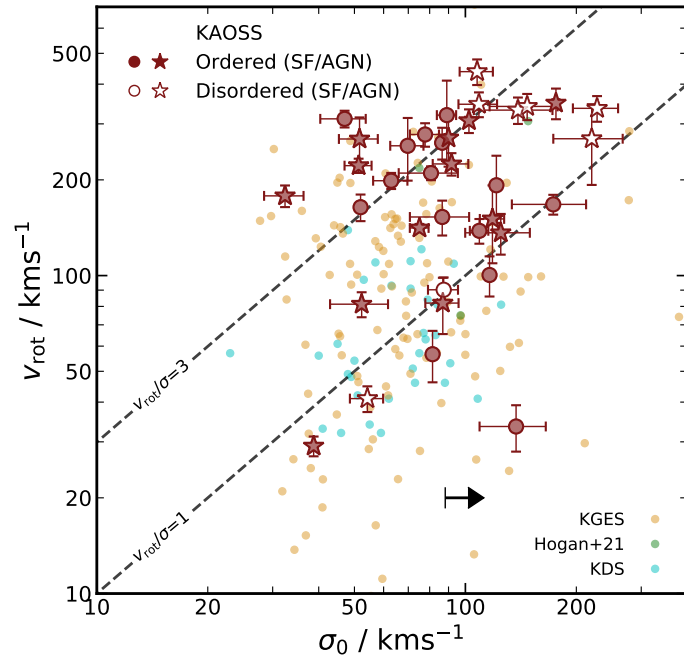
Figure 5.14: **a)** Intrinsic velocity dispersion σ_0 versus $v_{\rm rot}$ for the resolved KAOSS sample, along with $z \sim 1.5$ KGES galaxies, $z \sim 2.5$ ULIRGs (Hogan et al., 2021) and $z \sim 3.5$ KDS galaxies (Turner et al., 2017). Star-forming/AGN sources are plotted as circles/stars, and *ordered/disordered* sources are plotted as open/closed symbols. We indicate lines of constant $v_{\rm rot}/\sigma_0 = 1$ and 3, two commonly adopted criteria for identifying rotation-dominated galaxies. KAOSS galaxies have higher rotational velocities and velocity dispersions than the other samples, and $79 \pm 1\,\%$ of the *ordered* sample are consistent with having rotation-dominated motions.
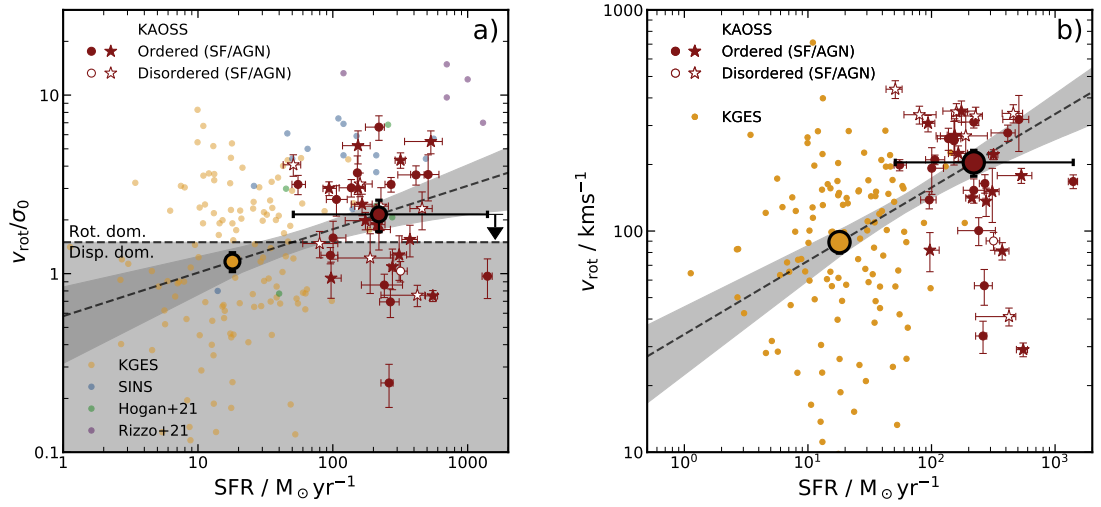
Figure 5.15: **a)** Ratio of rotational velocity to velocity dispersion $v_{\rm rot}/\sigma_0$ versus SFR. Also shown are $z \sim 1.5$ galaxies from the KGES survey, $z \sim 3.5$ galaxies from the KMOS Deep Survey (Turner et al., 2017) and $z \sim 4.5$ DSFGs from Rizzo et al. (2021). We fit the binned KAOSS and KGES median points (large circles with black outline), finding a weak (2.4σ) correlation between $v_{\rm rot}/\sigma_0$ and SFR (black dashed line with grey uncertainty region). The arrow shows how far the points would move down if we were to remove the beam smearing corrections to the velocity dispersions. **b)** Rotational velocity $v_{\rm rot}$ versus SFR for the KAOSS and KGES samples. We measure a 4.3σ correlation between $v_{\rm rot}$ and SFR from the fit to the binned data (black dashed line with grey uncertainty region), which we suggest is driven by the "main-sequence" correlation between SFR and stellar mass, leading to higher SFRs in galaxies with greater stellar masses and therefore faster rotation velocities.
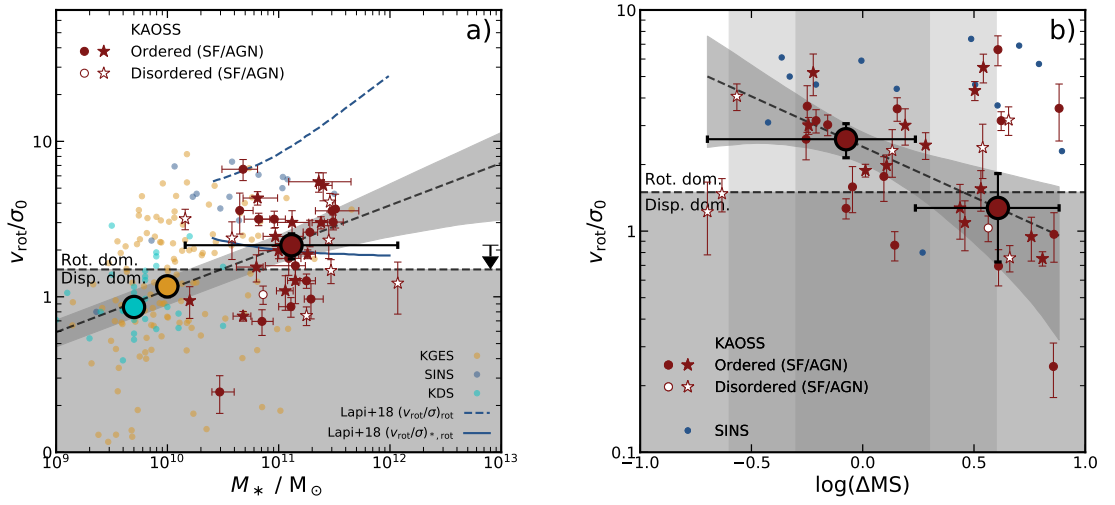
Figure 5.16: **a)** Ratio of rotational velocity to velocity dispersion $v_{\rm rot}/\sigma_0$ versus stellar mass. We include two tracks from simulations of early-type galaxy progenitors (Lapi et al., 2018), with $v_{\rm rot}/\sigma_0$ measured at the centrifugal size of the gas (dashed) and stellar (solid) components. Our data is in reasonable agreement with the latter and is therefore consistent with the predictions of $v_{\rm rot}/\sigma_0$ for early-type progenitors. **b)** Ratio of rotational velocity to velocity dispersion $v_{\rm rot}/\sigma_0$ offset from the main sequence (ΔMS) for KAOSS and SINS sources. The dark grey region shows the ± 0.3 dex scatter of the main sequence. We fit our binned data (black dashed line), which shows a weak (1.3σ) negative correlation between the two properties, hinting at "starburst"-like sources having more dispersion support, although there is not enough evidence to claim this from the available data.

for more highly star-forming sources being significantly more or less rotation dominated, and fitting the binned points reveals a positive trend that is only marginally significant at the 2.4σ level. To test the driver of this relation we study the $v_{\rm rot}$ versus SFR (in Fig. 5.15) and σ_0 versus SFR (in Fig. 5.13, discussed in §5.4.3) trends. We find the $v_{\rm rot}$–SFR and σ_0–SFR relations to have $\sim 4.3\sigma$ and $\sim 4\sigma$ positive correlations respectively. Therefore, we find that rotational velocity and intrinsic velocity dispersion both increase with star-formation rate, which effectively cancels out any significant evolution in $v_{\rm rot}/\sigma_0$ with star-formation rate.

The $v_{\rm rot}$–SFR correlation likely reflects the so-called "main sequence" trend whereby galaxies with larger stellar masses have higher star-formation rates (e.g. Brinchmann et al., 2004; Elbaz et al., 2007; Noeske et al., 2007; Whitaker et al., 2012; Schreiber et al., 2015), and therefore as a result of their higher stellar masses, also higher rotational velocities. In conclusion, we have little evidence to suggest that KAOSS SMGs are more or less rotation dominated than less active SFGs, and they may simply be scaled-up versions of such sources, which are more massive *and* more turbulent.

One of the predictions from the observed "main-sequence" is that galaxies within its spread are secularly evolving, whereas sources significantly above the main-sequence SFRs are such because of a different mechanism driving star formation, such as mergers or interactions. Therefore, we may expect sources above the main sequence to have lower $v_{\rm rot}/\sigma_0$. To test this, with show $v_{\rm rot}/\sigma_0$ versus ΔMS, i.e. the specific star-formation rate (sSFR) normalised by the main-sequence sSFR (for a given mass and redshift). Galaxies with higher ΔMS are more "starburst"-like. We adopt the Speagle et al. (2014) prescription of the main sequence. Fig. 5.16 shows $v_{\rm rot}/\sigma_0$ versus $\log(\Delta$MS$)$ for KAOSS and SINS galaxies, and we divide our data into two bins, $\log_{10}(\Delta$MS$) = -0.7$–0.3 and $\log_{10}(\Delta$MS$) = 0.3$–0.9, which show a very weak (1.3σ) negative correlation with $v_{\rm rot}/\sigma_0$. We therefore see little-to-no evidence to suggest that the main-sequence-normalised sSFRs of our sources correlate with rotational support.

We also test for the expected main-sequence correlation between $v_{\rm rot}/\sigma_0$ and stellar mass, which is shown in Fig. 5.16, along with KDS and KGES galaxies. We fit the binned medians of these samples, finding a 3.8σ positive correlation between the two quantities, suggesting that galaxies with higher stellar masses are more rotation dominated as expected. In Fig. 5.16 we also include theoretical predictions by Lapi et al. (2018) for the progenitors of the local early-type galaxy (ETG) population. These predictions include $v_{\rm rot}/\sigma_0$ measured at several different radii, and we include here only the values at the gas and stellar centrifugal sizes. Our data are consistent with their $v_{\rm rot}/\sigma_0$ measured at the stellar centrifugal size.

On the whole we suggest that $v_{\rm rot}/\sigma_0$ is not a useful parameter to describe the kinematics of our sources. While over 80 % of the sample is consistent with $v_{\rm rot}/\sigma_0 > 1$, these sources are not dynamically "cold" discs – they are very turbulent, with intrinsic velocity dispersions of $\sigma_0 \sim 90\,{\rm km\,s}^{-1}$. On the other hand, they also have high rotational velocities $v_{\rm rot} \sim 200\,{\rm km\,s}^{-1}$ which provide strong rotational support leading to relatively high $v_{\rm rot}/\sigma_0$ ratios. At the S/N of our KMOS observations, the KAOSS SMGs appear to be rotation-dominated, and we find little evidence of major mergers and or strong interactions, which have been suggested to be the triggers of star formation in the highly star-forming SMG population, although we cannot rule out more minor mergers and perturbations as a trigger for their activity (McAlpine et al., 2019).

5.4.5   Tully-Fisher relation

The Tully–Fisher relation (TFR; Tully & Fisher, 1977) connects the baryonic matter content of a galaxy to its dark matter. Our sample, which is one of the largest with estimates of kinematic information for SMGs, allows us to probe the TFR relation for this massive galaxy population at $z \sim 1.5$–2.5. The TFR uses the rotational velocity of the interstellar medium as a proxy for the potential of the dark matter halo. This proxy is valid if the gas rotates in circular orbits, however as we have shown in §5.4.3 star-forming disc galaxies at high redshift are generally more turbulent systems than local galaxies (Wisnioski et al., 2015; Gillman et al., 2019), and these turbulent motions contribute to the dynamical support of the system (see §5.4.4), which reduces the necessary rotational support for a stable orbit. Before studying the TFR for KAOSS SMGs we therefore estimate the circularised velocity $v_{\rm circ}$ according to:

$$v_{\rm circ} = \sqrt{v_{2.2R_d}^2 + 2\sigma_0^2 \left(\frac{R}{R_d} \right)}, \tag{5.4.3}$$

where the pressure contribution to the rotational velocity is encapsulated by the σ_0 term, and we take $R = 2.2\,R_d$ (Burkert et al., 2010). Among the sources in our *ordered* subset we find a median $v_{\rm circ} = 229 \pm 16\,{\rm km\,s}^{-1}$.

Fig. 5.17 shows the estimated circular velocity $v_{\rm circ}$ for the KAOSS resolved subset versus their stellar masses as estimated from MAGPHYS SED fitting (see §4.2.6). We also include similar measurements for KGES galaxies (Tiley et al., 2021) and *Herschel*-selected $z \sim 2.5$ ULIRGs from Hogan et al. (2021). In order to quantify the TFR for our $z \sim 2$ sources, we fit to our data points the model $\log_{10}(v_{\rm circ}) = a \log_{10}(M_*) + b$ where a and b are constant parameters, using an orthogonal distance regression (ODR) method which takes both the
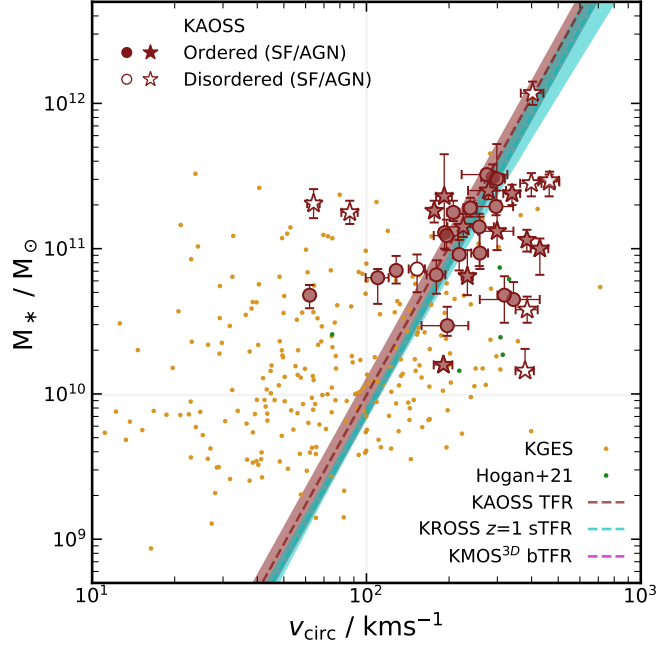
Figure 5.17: Stellar Tully-Fisher relation (sTFR): v_{circ} versus stellar mass for the KAOSS and KGES samples, along with $z \sim 2.5$ ULIRGs from Hogan et al. (2021). We fit for the normalisation of the Tully-Fisher relation, fixing the slope to be $a = 3.4$ (Tiley et al., 2019) and finding a best-fit normalisation of $\log_{10}(M_*/\mathrm{M}_\odot) = 10.03 \pm 0.13$ at $v_{\mathrm{circ}} = 100\,\mathrm{km\,s^{-1}}$, consistent with the value found by Tiley et al. (2019) for $z = 0$ SAMI galaxies, $\log_{10}(M_*/\mathrm{M}_\odot) = 9.87 \pm 0.04$, indicating a close link between the growth of stellar mass and dark matter from $z \sim 2$ to $z \sim 0$.

errors in M_* and v_{circ} into account. Following Tiley et al. (2019) we measure the value of $\log_{10}(M_*)$ at $v_{\mathrm{circ}} = 100\,\mathrm{km\,s^{-1}}$, finding a value of $\log_{10}(M_*/\mathrm{M}_\odot)_{v_{2.2}=100} = 10.03 \pm 0.13$ from the fit to our data. This is consistent with the values measured by Tiley et al. (2019) for both the $z \sim 1$ KROSS and $z \sim 0$ SAMI samples, indicating that the stellar mass and dark matter components in galaxies grow at similar rates from $z \sim 2$ to the present day.

5.4.6 Dynamical masses

Another important quantity which is not yet well-measured for many SMGs is the dynamical mass, i.e. the total matter content contributing to the motions of the galaxy. The kinematic information from our sample provides a diagnostic of the total matter content within the galaxies, and we estimate dynamical masses within twice the effective radius, $2R_e$ (which is typically $\sim 7\,\mathrm{kpc}$) for our sample according to:

$$M_{\mathrm{dyn}}(< 2R_e) = \frac{2R_e v_{\mathrm{circ}}^2}{G} \tag{5.4.4}$$
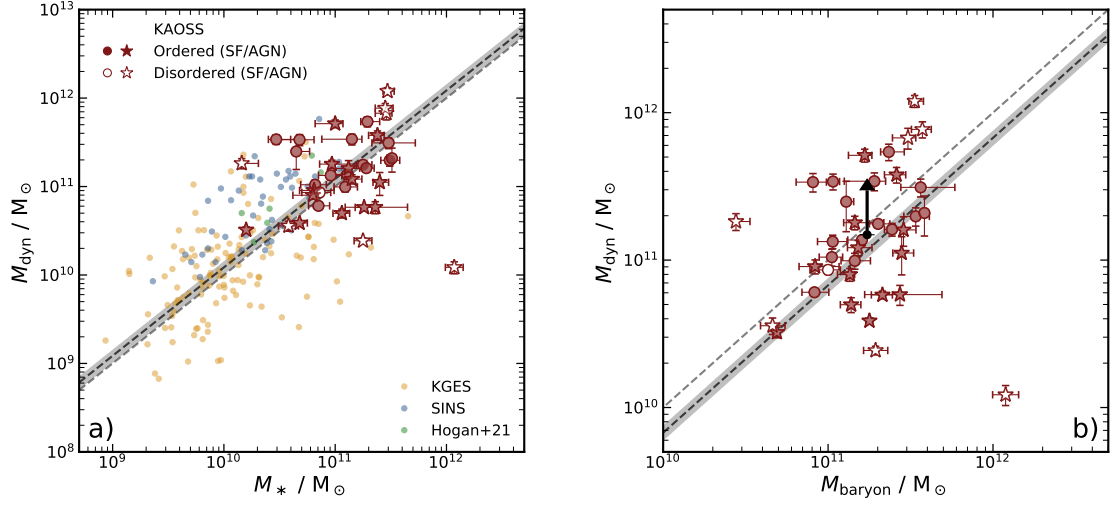
Figure 5.18: **a)** Dynamical masses of the resolved KAOSS sample, estimated from the Hα kinematics, plotted against stellar masses. Velocity dispersions are not corrected for beam smearing. Plotted as a comparison are $z \sim 1.5$ KGES galaxies (Tiley et al., 2021), $z \sim 2$ SINS galaxies (Förster Schreiber et al., 2009) and $z \sim 2.5$ ULIRGs from Hogan et al. (2021). **b)** The same as **a)** except here we plot $v_{\rm circ}$ against baryonic mass, adding a gas component to the stellar mass by converting the MAGPHYS dust masses to gas masses using a gas-to-dust ratio of $\delta_{\rm gdr} = 65$ (Birkin et al., 2021).

following Burkert et al. (2010), where $v_{\rm circ}$ is calculated using Eq. 5.4.3, with $R = 2R_e$. As we have shown, our SMGs appear to be rotationally supported, but turbulence is still a significant contributor to their support, and therefore we must include the σ_0 term in $v_{\rm circ}$. In Fig. 5.18 we show the dynamical mass estimates for our sample plotted against their stellar masses M_*. For sources in the KAOSS resolved sample with robust velocity measurements the median dynamical mass is $M_{\rm dyn} = (2.0 \pm 0.5) \times 10^{11}\,{\rm M}_\odot$ for the star-forming sample and $M_{\rm dyn} = (0.9 \pm 0.3) \times 10^{11}\,{\rm M}_\odot$ for the AGN sample. The median $M_*/M_{\rm dyn}$ ratios for the two samples are 0.9 ± 0.2 and 0.8 ± 0.4, respectively. This would indicate that there is very little dark matter within $R \sim 7\,{\rm kpc}$ for our sources.

We also show in Fig. 5.18 the KAOSS dynamical masses versus baryonic masses derived according to:

$$M_{\rm baryon} = M_* + \delta_{\rm gdr} M_{\rm dust}, \tag{5.4.5}$$

where $\delta_{\rm gdr}$ is the gas-to-dust ratio (see §3.3.5) for which we adopt a value of 65, using the fit of Birkin et al. (2021) at $z \sim 2$ (see Chapter 3). We also note here that adopting $\delta_{\rm gdr} = 65$ to derive the molecular gas mass $M_{\rm gas}$ results in a gas fraction $\mu_{\rm gas} = M_{\rm gas}/M_* \sim 0.3$, which is consistent with the predictions of Birkin et al. (2021) at $z \sim 2$ (see Fig. 3.6). Dynamical and baryonic masses are tabulated in Table 5.3. In the star-forming sample and AGN samples
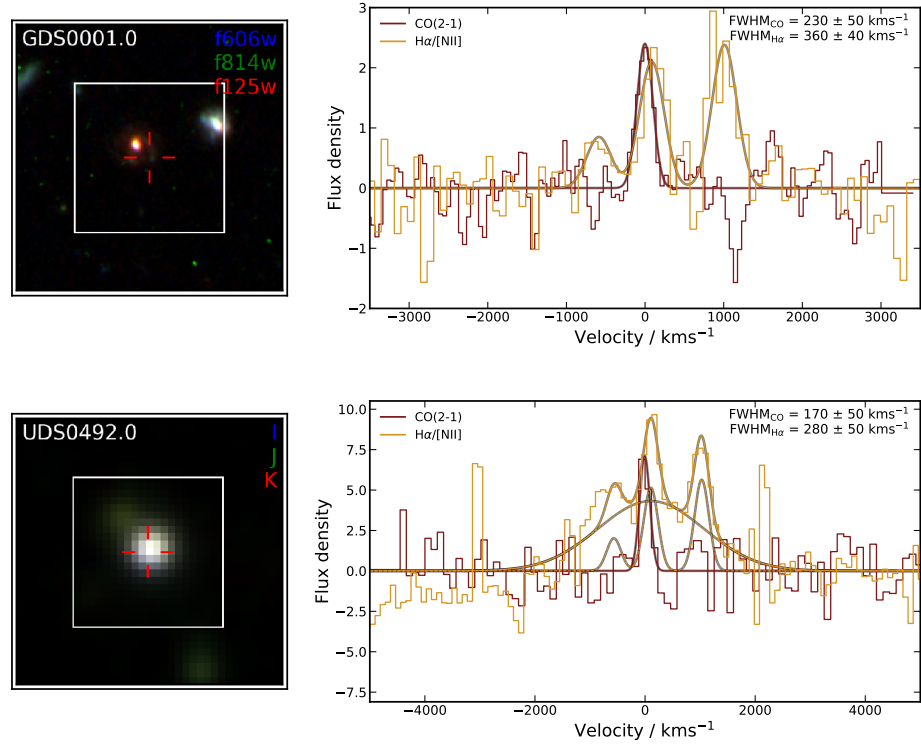
Figure 5.19: CO(2–1) and Hα line profiles of GDS0001.0 and UDS0492.0. The spectra are continuum subtracted and normalised to the peak flux of the Hα line. In both cases the Hα line is marginally broader than the CO(2–1), while the Hα emission in UDS0492.0 (which displays several AGN features; see §4.3.1) displays a broad component not seen in the CO(2–1) emission.

respectively we calculate median $M_{\mathrm{baryon}}/M_{\mathrm{dyn}}$ ratios of 1.1 ± 0.2 and 1.7 ± 0.6, consistent with no dark matter content in these sources $R \sim 7\,\mathrm{kpc}$, or potentially suggesting that the bulk of the gas is not located within this radius.

5.4.7   Comparison of CO and Hα line profiles

We briefly compare the kinematic information from Hα to that obtained from molecular gas to understand different tracers. To date, few studies have combined resolved observations of both CO and Hα (but see e.g. Chen et al., 2017), and unfortunately there is currently little overlap between the CO sample studied in Chapters 2 and 3 and the KAOSS sample. However, two sources in our KAOSS resolved sample are covered as part of the CO survey: GDS0001.0 (also known as ALESS017.1) at $z_{\mathrm{H}\alpha} = 1.5393$ and AS2UDS0492.0 (for which we identified a companion source in the KMOS IFU) at $z_{\mathrm{H}\alpha} = 1.2785$. In Figs. 5.19 we overlay the CO(2–1) and Hα line profiles of ALESS017.1 and AS2UDS0492.0 respectively.

For ALESS017.1 we find linewidths (FWHM) of $230 \pm 50\,\mathrm{km\,s^{-1}}$ for the CO(2–1) (Birkin

et al., 2021) compared to $360 \pm 40 \, \mathrm{km \, s^{-1}}$ for the Hα. For AS2UDS0492.0 we find a FWHM of $170 \pm 50 \, \mathrm{km \, s^{-1}}$ for the CO(2–1) (Chapter 3; Birkin et al., 2021) compared to $280 \pm 50 \, \mathrm{km \, s^{-1}}$ for the Hα. Hence in both cases we find the velocity dispersion to be greater in the molecular gas component than in the ionised gas. In the latter case of AS2UDS0492.0, however, the Hα emission displays a broad component not seen in the molecular emission. In §4.3.1 we identified this source as an AGN from its spectral properties, the presence of a luminous X-ray counterpart and its IRAC colours, and this likely indicates the broad line emission of the AGN. We search for any velocity offset between the two components for both sources, finding that the CO component is slightly blueshifted compared to the Hα in both cases but still in agreement within 3σ, as found by Chen et al. (2017) for the $z = 2.12$ SMG ALESS067.1.

Finally, we attempt to use independent dynamical mass estimates from the spatially resolved Hα and the integrated CO to constrain the CO-H$_2$ conversion factor α_{CO} for these sources.

$$M_{\mathrm{dyn}} = \frac{M_* + \alpha_{\mathrm{CO}} L'_{\mathrm{CO}}}{1 - f_{\mathrm{DM}}} = \frac{R_e v_{\mathrm{circ}}}{G}, \tag{5.4.6}$$

where L'_{CO} is the CO(1–0) line luminosity in $\mathrm{K \, km^{-1} \, pc^{-2}}$ and f_{DM} is the dark matter fraction.

ALESS017.1 has a stellar mass $M_* = 1.8 \times 10^{11} \, \mathrm{M_\odot}$ and a CO(1–0) luminosity of $L'_{\mathrm{CO}} = 0.2 \times 10^{11} \, \mathrm{K \, km \, s^{-1} \, pc^{-2}}$, with a dynamical mass from KAOSS of $M_{\mathrm{dyn}}(R < 2R_e) = 1.6 \times 10^{11} \, \mathrm{M_\odot}$. Therefore the dynamical and stellar mass estimates are inconsistent with all of the stellar mass being within $2R_e$. If we instead take the 1σ lower limit on the stellar mass of $M_* = 9.8 \times 10^{10} \, \mathrm{M_\odot}$, and a dark matter fraction of $f_{\mathrm{DM}} = 0.15$ this gives an upper limit on the CO-H$_2$ conversion factor of $\alpha_{\mathrm{CO}} < 1.9$, or in the extreme case of no dark matter, $\alpha_{\mathrm{CO}} < 3.1$.

AS2UDS0492.0 has $M_* = 2 \times 10^{10} \, \mathrm{M_\odot}$ and $L'_{\mathrm{CO}} = 3 \times 10^{10} \, \mathrm{K \, km \, s^{-1} \, pc^{-2}}$. From KAOSS it has a dynamical mass of $M_{\mathrm{dyn}}(R < 2R_e) = 3 \times 10^{10} \, \mathrm{M_\odot}$, again inconsistent with all of the stellar mass being within $2R_e$. As before, taking the 1σ lower limit on the stellar mass, $M_* = 1.5 \times 10^{10} \, \mathrm{M_\odot}$, a dark matter fraction of $f_{\mathrm{DM}} = 0.15$ yields $\alpha_{\mathrm{CO}} \sim 0.3$, or $\alpha_{\mathrm{CO}} \sim 0.4$ if no dark matter is present. Therefore ALESS017.1 is consistent with the "starburst" value of $\alpha_{\mathrm{CO}} \sim 1$, in agreement with Chapter 3 (Birkin et al., 2021), whereas the dynamical mass of AS2UDS0492.0 indicates a lower α_{CO}. This could reflect the fact that AS2UDS0492.0 is likely AGN dominated, or it could simply suggest that there is significant scatter of α_{CO} in SMGs. Of course, the sample of two sources we use here is too small to draw any robust conclusions, and highlights the need for high-quality CO and kinematic measurements of the same sources.

5.4.8 Descendants of SMGs

SMGs have been suggested to be connected with the progenitors of local massive and compact early-type galaxies (e.g. Lilly et al., 1999; Simpson et al., 2014; Toft et al., 2014), potentially by evolving through an obscured, and then an unobscured QSO phase (e.g. Sanders et al., 1988; Blain et al., 2002; Swinbank et al., 2006; Hopkins et al., 2008). Simpson et al. (2014) showed that SMGs descendants at $z \sim 0$ would have stellar masses that are comparable to massive early-types (see also Dudzevičiūtė et al. 2020), while Hodge et al. (2016) found that the gas surface densities and implied effective radii of ALESS SMGs are consistent with the high-mass end of compact massive early-type galaxies. In Chapter 3 we compared SMGs with a sample of early-types in the Coma cluster (Shetty et al., 2020) in the M_{baryon}–σ and Age–σ plane, finding the two populations to be consistent. However, as discussed in §3.3.6, the σ used in that Chapter were estimated from the CO linewidths which we were unable to correct for inclination, due to the low spatial resolution of our data.[2]

With our spatially resolved KMOS observations of SMGs we have been able to measure inclination-corrected rotational and circularised velocities (see §5.4.1). We can now estimate σ_{eff} as (Binney & Tremaine, 2008):

$$\sigma_{\mathrm{eff}} = \frac{v_{\mathrm{circ}}}{\sqrt{2}}, \tag{5.4.7}$$

to provide a more robust metric for comparing with the Coma cluster sample, and these values are presented in Table 5.3. Fig. 5.20 shows σ_{eff} plotted against M_{baryon} for the KAOSS resolved subset, along with the CO-detected sources from Chapter 3 and Coma early-type galaxies from Shetty et al. (2020). We divide our sample into two bins in M_{baryon} and plot the median σ_{eff} with bootstrap uncertainties in these two bins, and we see that these bins are consistent with those of the CO sample within the 1σ uncertainties, and appear to closely match the Coma early-types. The scatter among the KAOSS resolved sample is larger than that of the Coma early-types, and roughly comparable to that of the CO sample, which are not inclination corrected, however a lot of this scatter is driven by AGN and sources in the *disordered* subset. We conclude that our spatially resolved observations with KMOS suggest that $z \sim 2$ SMGs are dynamically consistent with them being the progenitors of massive and compact early-type galaxies in the local Universe.

---

[2]We note here that σ in this context is the *effective* linewidth if all the kinetic energy of the galaxy was transformed from rotation-dominated to dispersion-dominated motion. To avoid confusion, from here on in this section we refer to σ as σ_{eff}.
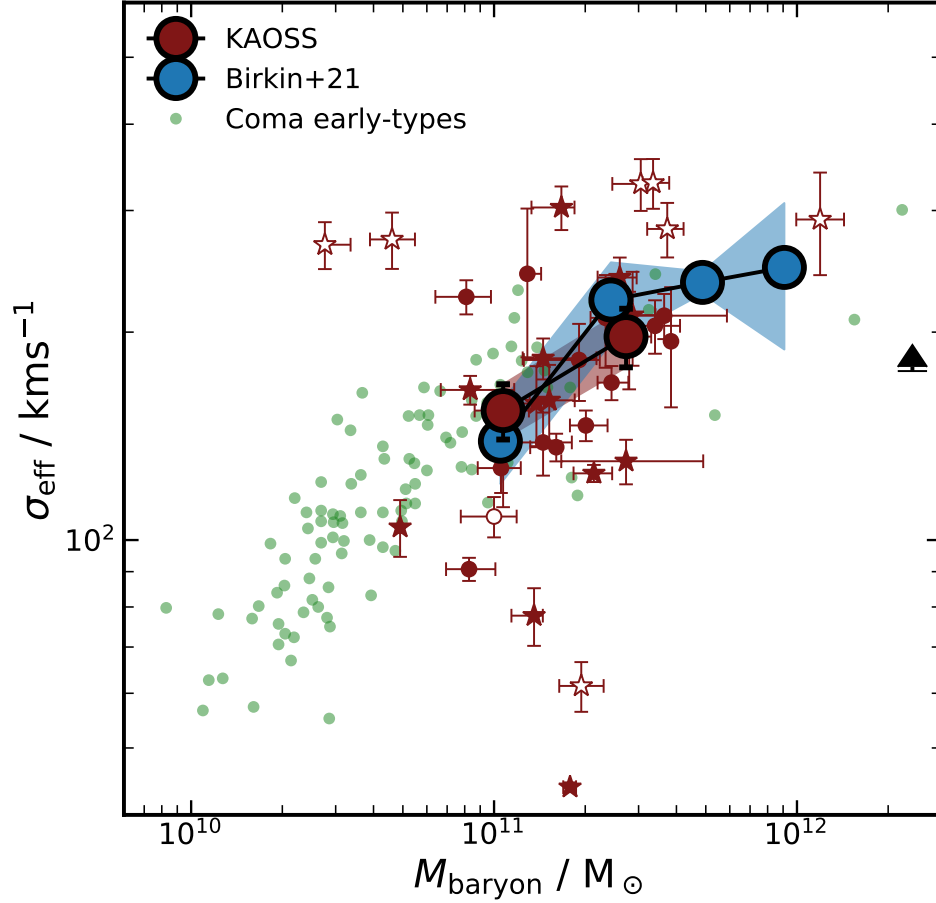
Figure 5.20: The M_{baryon}–σ relation for KAOSS SMGs and CO-detected SMGs from (Chapter 3; Birkin et al., 2021), along with early-type galaxies from the Coma cluster (Shetty et al., 2020). For KAOSS sources M_{baryon} is estimated as the sum of the MAGPHYS-derived stellar and dust masses, with the latter multiplied by a gas-to-dust ratio of 65 (Birkin et al., 2021). We estimate σ_{eff} as $v_c/\sqrt{2}$ (Binney & Tremaine, 2008), and find our sources to have comparable estimated velocity dispersions to the early-types in Coma, which suggests they may plausibly be the descendant population of such sources.

Figure 5.21: M_{200} versus stellar velocity dispersion σ_* for star-forming EAGLE galaxies at $z \sim 1.5$–2.5. We fit the relation in Eq. 5.4.8 (dashed line) to determine a calibration between rotation velocity and halo mass for our KAOSS sources.
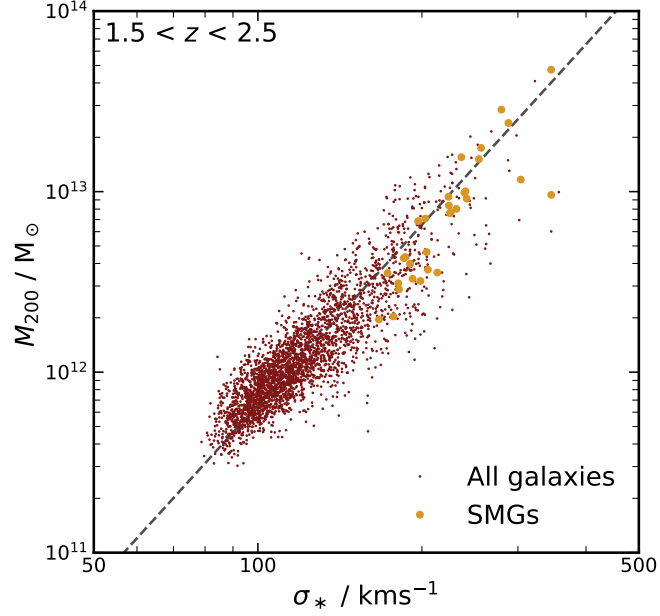
5.4.9 Halo masses

Our kinematic measurements also enable us to estimate the masses of dark matter halos in which our galaxies reside. This is important as the mass of halo affects the processes with which the galaxies can be fed with cold gas for star formation. For example, in less massive halos, discs are fuelled by cool inflows of gas that can fuel star formation, whereas in more massive halos the infalling gas is heated by shocks preventing it from cooling to induce star formation (Dekel & Birnboim, 2006). Therefore estimating halo masses will allow us to determine whether the KAOSS SMGs are likely to be fuelled by cold streams, which has implications for their potential triggering mechanisms.

The properties of submillimetre-bright galaxies in the Evolution and Assembly of GaLaxies and their Environments (EAGLE) simulation (Schaye et al., 2015) have been studied by McAlpine et al. (2019). EAGLE is a suite of hydrodynamical simulations designed to study the formation of galaxies and supermassive black holes in a standard ΛCDM Universe. The simulations include the treatment of stellar and AGN feedback, and has been shown to closely reproduce observables such as the galaxy stellar mass function and Tully-Fisher relation. We can use results from EAGLE to predict halo masses for our SMGs given their stellar velocity dispersions σ_*, which we can relate to our measured rotational velocities. To estimate halo

masses for our sample we select galaxies in EAGLE with $\mathrm{SFR} > 10\,\mathrm{M_\odot yr^{-1}}$ and $z > 1.5$–2.5 and remove satellite galaxies, as SMGs are likely to be central galaxies based on their high SFRs. By fitting the relation between the halo mass, M_{halo}, and the stellar velocity dispersion, σ_*, for the EAGLE galaxies we determine the following calibration:

$$\log(M_{\mathrm{halo}}) = (3.32 \pm 0.03)\log(\sigma_*) + (5.17 \pm 0.07) \quad (z = 1.5 - 2.5,\ 2995\ \mathrm{galaxies}), \quad (5.4.8)$$

from 2995 galaxies at $z \sim 1.5$–2.5. The data are well fit by this model, as shown in Fig. 5.21. We also highlight galaxies with $S_{870} > 1\,\mathrm{mJy}$, i.e. SMGs. Finally, to estimate halo masses from our circularised velocities we adopt $v_{\mathrm{circ}} = 1.33\,\sigma_*$ following Serra et al. (2016), which relates the stellar velocity dispersion to v_{circ}. It should be noted that this relation was derived using H I velocities measured at $6\,R_e$ in early-type galaxies, i.e. using a different tracer and further out from the centre of the galaxy compared to our measurements. This is a crude approximation, but for the purposes of this analysis we do not expect this to be the dominant source of uncertainty, and hence to affect the qualitative conclusions of this section.

The resultant halo masses are tabulated in Table 5.3, and we plot them as a function of redshift in Fig. 5.22. The boundaries divide the parameter space into the regions labelled "cold", where galaxies are being fed by cold streams, "hot" where shock heating suppresses star formation and "cold in hot", where cold streams can still appear despite shock heating, according to the Dekel & Birnboim (2006) model of the thermal properties of gas flows onto galaxies. For the star-forming and AGN samples respectively we derive median halo masses of $M_{\mathrm{halo}} = (9 \pm 2) \times 10^{12}\,\mathrm{M_\odot}$ and $M_{\mathrm{halo}} = (9 \pm 3) \times 10^{12}\,\mathrm{M_\odot}$, respectively. Therefore the star formation-dominated and AGN-dominated sources reside in dark matter halos with masses that are consistent within their 1-σ uncertainties. We see a large scatter in our sample in Fig. 5.22, with most sources occupying the region of the parameter space above the boundary indicating shock heating of some sort, which may be caused by a combination of AGN feedback, a two-phase IGM or dynamical friction feedback (Dekel & Birnboim, 2006).

We also show in Fig. 5.22 halo masses estimated for AS2UDS SMGs by Stach et al. (2021) using a clustering analysis, in redshift bins of $z = 1.5$–2.0, $z = 2.0$–2.5 and $z = 2.5$–3.0. While our data do not cover the latter bin, our median values are consistent with the first two bins within the 1σ uncertainties. Both our binned data and the Stach et al. (2021) measurements are consistent with the predictions of McAlpine et al. (2019) for submillimetre-bright EAGLE galaxies shown in Fig. 5.22. We conclude that KAOSS SMGs reside in halos of masses of $\sim 10^{13}\,\mathrm{M_\odot}$ that are at least partially filled with hot gas. For the $z \sim 2$ sources in our sample
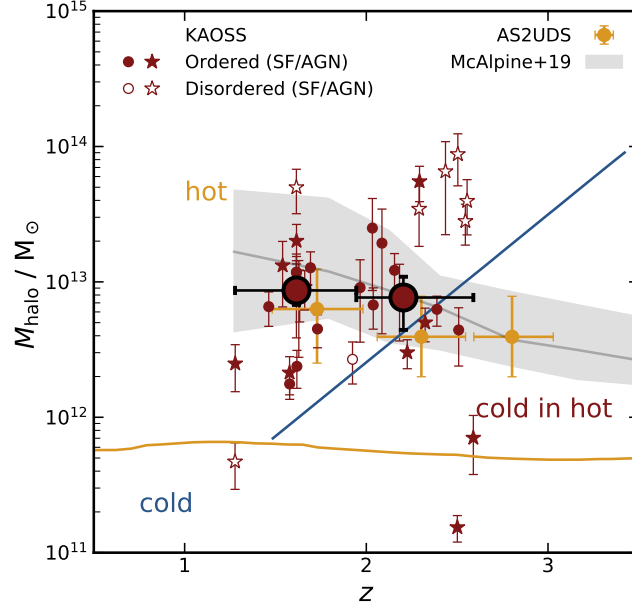
Figure 5.22: Halo mass versus redshift for our resolved KAOSS SMGs. We estimate halo masses for the KAOSS sample by comparing the rotational velocities and velocity dispersions with those of star-forming galaxies in the EAGLE simulations (McAlpine et al., 2019). Also shown are halo masses estimated by Stach et al. (2021) based on a clustering analysis of AS2UDS SMGs. According to the Dekel & Birnboim (2006) model the majority of our galaxies would reside in halos experiencing shock heating which should suppress star formation, and given the high SFRs we suggest this model does not well describe the SMG population.

the implied halo masses suggest that cold streams may still be able to fuel star formation, according to the models of (Dekel & Birnboim, 2006). However for the low-redshift end of our sample these models suggest that cold streams cannot fuel sources in such massive halos, which may suggest that another triggering mechanism is dominant at $z \sim 2$, e.g. mergers and interactions (e.g. Alaghband-Zadeh et al., 2012; Chen et al., 2017).

5.5   Conclusions

In this chapter we have presented results from a subset of sources in the ongoing KMOS+ALMA Observations of Submillimetre Sources (KAOSS) Large Programme. We have measured Hα velocity fields and extracted rotation curves for 36 SMGs in the COS-MOS, UDS and GOODS-S fields, allowing us to derive rotational velocities and dynamical masses as well as $v_{\rm rot}/\sigma_0$ ratios to test the level of rotational support in the SMG population. Our main results are as follows:

- We are able to measure robust rotational velocities for a subsample of 28 out the 36

resolved KAOSS sources from Freeman disc model fitting, which we label the *ordered* subset. For this sample we measure a median inclination-corrected velocity at 2.2 times the disc radius of $v_{\rm rot} = 190 \pm 20 \, {\rm km \, s^{-1}}$. The star-forming and AGN samples, as classified in Chapter 4, have velocities that are on average consistent within their uncertainties, $v_{\rm rot} = 190 \pm 30 \, {\rm km \, s^{-1}}$ and $v_{\rm rot} = 180 \pm 40 \, {\rm km \, s^{-1}}$ respectively.

- The remaining eight sources are labelled the *disordered* subset. These sources have lower integrated signal-to-noise ratios, median $S/N_{\rm H\alpha} = 12 \pm 3$ and $S/N_{\rm H\alpha} = 18 \pm 2$ respectively, which is potentially a driver of the lower-quality velocity maps. This could also be linked to higher dust extinctions, although we find only weak evidence of this in our sample, with median $A_V = 2.4 \pm 0.4$ and $A_V = 2.09 \pm 0.15$ for the *disordered* and *ordered* subsets, respectively.

- We measure observed velocity dispersions, and applying the beam smearing corrections from Johnson et al. (2018) we derive intrinsic velocity dispersions, σ_0. The KAOSS resolved sample has a median $\sigma_0 = 87 \pm 5 \, {\rm km \, s^{-1}}$ for the *ordered* subset and $\sigma_0 = 120 \pm 30 \, {\rm km \, s^{-1}}$ for the *disordered* subset, significantly higher than the samples of less actively star-forming galaxies to which we compare. This indicates high levels of turbulence in SMGs.

- The median ratio of rotational velocity to intrinsic velocity dispersion $v_{\rm rot}/\sigma_0$ is $v_{\rm rot}/\sigma_0 = 2.2 \pm 0.5$ for the *ordered* subset and $v_{\rm rot}/\sigma_0 = 1.9 \pm 0.6$ for the *disordered* subset. We use this information with the above conclusions to suggest that KAOSS SMGs are highly turbulent, yet rotationally supported, star-forming galaxies.

- Our sources follow a trend between stellar mass M_* and rotational velocity $v_{\rm rot}$ (the Tully-Fisher relation), and we find a best-fit zeropoint at $v_{\rm rot} = 100 \, {\rm km \, s^{-1}}$ of $\log_{10}(M_*/{\rm M_\odot}) = 10.03 \pm 0.13$, at a fixed slope of 3.4, which is consistent with the normalisation measured by Tiley et al. (2019) for $z = 0$ SAMI galaxies, $\log_{10}(M_*/{\rm M_\odot}) = 9.87 \pm 0.04$, at the same velocity. This suggests that dark matter and stellar mass growth are closely linked between $z \sim 2$ and the present day.

- Only considering the *ordered* sample, the KAOSS SMGs have a median dynamical mass within $2R_e$ ($\sim 7 \, {\rm kpc}$) of $M_{\rm dyn} = (1.5 \pm 0.3) \times 10^{11} \, {\rm M_\odot}$ and a median stellar-to-dynamical mass ratio of $M_*/M_{\rm dyn} = 0.88 \pm 0.15$. Within the same radius the median baryonic-to-dynamical mass ratio is ${\rm M_{bar}}/M_{\rm dyn} = 1.21 \pm 0.19$, and we suggest the KAOSS SMGs

Property	Description	Equation
Δv	Difference between the minimum and maximum velocities	$v_{\max} - v_{\min}$
$v_{2.2R_d}$	Observed velocity measured at 2.2 times the disc radius R_d	...
v_{rot}	Inclination- and beam smearing-corrected velocity measured at 2.2 R_d	$v_{2.2R_d}/\sin i \times \xi_v$
v_{circ}	Circularised rotation velocity	$\sqrt{v_{2.2R_d}^2 + 2\sigma_0^2\left(\dfrac{R}{R_d}\right)}$
σ_{obs}	Observed velocity dispersion	...
σ_0	Intrinsic (beam smearing-corrected) velocity dispersion	$\sigma_{\mathrm{obs}} \times \xi_\sigma$
σ_{eff}	Effective velocity dispersion if all energy converted to rotation	$v_{\mathrm{circ}}/\sqrt{2}$
σ_*	Stellar velocity dispersion (from EAGLE)	$v_{\mathrm{circ}}/1.33$

Table 5.4: Glossary of dynamical measurements used in this chapter. The disc radius R_d is related to the effective radius R_e of an $n = 1$ Sérsic profile by $R_d = 0.59\,R_e$. i is the observed inclination angle of the galaxy. ξ_σ and ξ_v are the beam smearing corections to the velocity dispersion and rotational velocity, respectively.

have low dark matter fractions, or that the majority of the gas is located outside of $2R_e$.

- By applying calibrations determined from submillimetre-bright galaxies in the EA-GLE simulations we determine halo masses for our sources, finding a median $M_{\mathrm{halo}} = (8.6 \pm 1.3) \times 10^{12}\,\mathrm{M_\odot}$. Based on the redshifts and halo masses of our sample we infer that most sources are located in halos that are shock heated, whereas a small number are potentially being fed by cold streams.

Summary of dynamical quantities

In this chapter we derive and use a variety of dynamical measurements, including several different measures of rotational velocity and velocity dispersion. We have tried to be as clear as possible in the main body of the text when distinguishing these properties, but in Table 5.4 we detail all of them for further clarity:

CHAPTER 6

Conclusions and future work

6.1 Summary of the presented work

This thesis has presented a study of the gas properties of submillimetre galaxies (SMGs), a class of dust-obscured star-forming galaxy (DSFG) at $z \sim$1–4 with significantly higher star-formation rates than typical galaxies. In order to further our understanding of this population we focused first on the integrated molecular gas properties, as traced by the carbon monoxide (CO), and went on to study spatially resolved Hα emission as a tracer of the gas kinematics. Here we summarise the findings presented in Chapters 2–5 before discussing ongoing work and the potential of future and upcoming instrumentation for expanding our knowledge of this galaxy population and its place in the picture of galaxy formation and evolution.

6.1.1 Molecular gas properties of dust-obscured star-forming galaxies

In Chapter 2 we presented a 3 mm survey of 61 SMGs with ALMA and NOEMA. This includes a combination of 30 sources with existing spectroscopic redshifts and 31 sources with only photometric redshifts, for the latter of which we utilise the wide bandwidth of ALMA and NOEMA to perform a blind scan for CO emission. The observations yield CO detections in 47 SMGs, 26 coming from the blind scan sample. This demonstrates the power of ALMA and NOEMA for performing blind scans with no prior knowledge of redshift, which reduces biases arising from the selection of sources with pre-existing redshifts. For the 20

sources with ambiguous (mostly due to single line detections) line identifications we apply a simple technique using the spectral energy distribution (SED) fitting photometric redshift probability distribution functions (PDFs) from MAGPHYS to guide the line ID. We estimate that at most three of the 47 ($\sim 6\%$) line IDs may be incorrect, and determine that this does not affect our conclusions within their uncertainties.

Using the derived spectroscopic redshifts and $3\,\mathrm{mm}$ continuum constraints we updated the existing MAGPHYS SED fits, which were previously carried out with the photometric redshift as a free parameter, in order to obtain more precise constraints on the physical properties of the sample, reducing the fractional uncertainties by a factor of ~ 2–3 in the case of dust masses and far-infrared luminosities. We derive medians for these properties of $L_{\mathrm{IR}} = (4.6 \pm 0.8) \times 10^{12}\,\mathrm{L_\odot}$, $M_* = (2.1 \pm 0.4) \times 10^{11}\,\mathrm{M_\odot}$, $M_{\mathrm{dust}} = (1.05 \pm 0.08) \times 10^9\,\mathrm{M_\odot}$, and $\mathrm{SFR} = 400 \pm 50\,\mathrm{M_\odot\,yr^{-1}}$, which confirms that the SMGs are both massive and highly star-forming, with significant dust masses. We also find from these results that 42 of the 47 CO-detected sources lie within the 0.6 dex spread of the main sequence at their redshifts. Within the main-sequence paradigm this suggests that the majority of the SMGs are secularly evolving systems as opposed to merger-triggered starbursts, an idea we explore further throughout the remaining chapters. Additionally, the five sources classified as "starburst" reside at $z \lesssim 1.5$, reflecting the evolution of the main sequence at higher redshifts, where higher SFRs become more typical for the galaxy population.

Following the data reduction and analysis presented in Chapter 2 we analysed the low- to mid-J CO^{12} properties of these 47 SMGs in Chapter 3. This is one of the largest samples of CO-detected $870\,\mu$m-selected SMGs currently available, representing a more complete sample than that of Bothwell et al. (2013), and that one that is less biased towards low-redshift sources. The sample has spectroscopic redshifts in the range $z_{\mathrm{CO}} \sim 1.2$–4.8, with a median of $z = 2.9 \pm 0.2$, comparable with the median photometric redshift from the largest sample of ALMA-identified SMGs, the AS2UDS sample. We identify the trend between redshift and submillimetre flux density also seen by Stach et al. (2019) and Simpson et al. (2020), with a gradient of $0.07 \pm 0.01\,\mathrm{mJy^{-1}}$ that is consistent with those works. The trend is an indicator of "downsizing" in the SMG population, whereby more massive galaxies form at earlier times.

The median gas mass of the SMG sample is $M_{\mathrm{gas}} = (9.1 \pm 0.7) \times 10^{10}\,\mathrm{M_\odot}$, assuming a CO-$H_2$ conversion factor of $\alpha_{\mathrm{CO}} = 1\,\mathrm{M_\odot}\,(\mathrm{K\,km\,s^{-1}\,pc^2})^{-1}$, and the median gas-to-stellar mass ratio is $\mu_{\mathrm{gas}} \sim 0.4$ at $z \sim 2.5$, which we find to increase with redshift as $\log_{10}(\mu_{\mathrm{gas}}) = 0.23 \times (z - \langle z \rangle) - 0.41$. Our work therefore confirms that SMGs are highly gas-rich systems, and they

also have a median gas depletion timescale of $t_{\mathrm{dep}} = 210 \pm 40\,\mathrm{Myr}$. We find the depletion timescales to decrease modestly towards higher redshifts, as $t_{\mathrm{dep}} \propto (1 + z)^{-1.1}$, but they do not appear to evolve with offset from the main sequence. The latter point is in disagreement with the suggestion that main sequence outliers have higher star-formation efficiencies.

We use the large sample size to attempt to place constraints on the CO-H_2 conversion factor, which is currently not well known for high-redshift galaxies, finding them to be consistent with $\alpha_{\mathrm{CO}} = 1$ assuming an average inclination angle of $i = 57°$, a size of $14\,\mathrm{kpc}$ and dark matter fractions of $35\,\%$. With this expanded sample we also constructed a statistical CO spectral line energy distribution (SLED) and measured line ratios from r_{21} up to r_{71} which will reduce the uncertainty in future gas mass measurements for SMGs. The SLED also shows that SMGs have more highly excited ISM gas than less actively star-forming galaxies, such as the Milky Way.

As a test of the kinematics in our systems we examine the fraction of SMGs with double-peaked emission lines (as determined by using an AIC technique). We find that $38 \pm 9\,\%$ of the CO lines are better fit by double-Gaussian profiles, compared to single Gaussians, and to study this further we generate simple simulations of line profiles from spatially unresolved rotating discs, and find the double-peaked fraction to be consistent with the value in the CO sample. This provides circumstantial evidence that the CO kinematics of SMGs are dominated by the motion of gas in rotating discs, and find that the L'_{CO}–FWHM relation is also consistent with disc kinematics.

We tested the calibration of three different gas mass tracers: the molecular CO, the atomic carbon [CI] and the $3\,\mathrm{mm}$ continuum emission, finding the three to correlate well. Finally, we use the CO linewidths and estimated stellar and gas masses for our sample to demonstrate that the distribution of SMGs in the M_{baryon}–σ plane is comparable with that of the most massive early-type galaxies in the local Universe, providing further circumstantial evidence of a link between SMGs and the progenitors of massive early-type galaxies. We suggest that the descendants of fast- and slow-rotators in the local Universe may correspond to SMGs fainter than, and brighter than $S_{870} \sim 5\,\mathrm{mJy}$.

6.1.2 Near-infrared spectroscopy of dust-obscured star-forming galaxies

Chapter 4 presents the ongoing KAOSS survey, a Large Programme with KMOS designed to observed 407 SMGs in the COSMOS, UDS and GOODS-S fields. We describe the target selection and observing strategy along with the data reduction process, the latter of which is

based on the ESOREX pipeline but has been fully tested and optimised for our sample. The integrated line properties of a sample of 43 sources is presented along with GALFIT modelling of the observed-frame optical/near-infrared emission and MAGPHYS SED fitting.

We find that the KAOSS SMGs experience strong dust obscuration as evidenced by their low $SFR_{H\alpha}/SFR_{IR}$ ratios, median $SFR_{H\alpha}/SFR_{IR} = 0.011 \pm 0.002$. This is significantly higher than for the less actively star-forming galaxies to which we compare, however we find no evidence to suggest that SMGs with greater positive offset from the main sequence, which could represent sources with different triggering mechanisms, show greater dust obscuration.

We investigate the prevalence of AGN in the sample by using four criteria, high [NII]/Hα flux ratios, broad emission lines, the presence of a luminous X-ray counterpart and AGN-like IRAC colours. Within the sample we place an upper limit on the AGN fraction of $53 \pm 11\%$, finding these sources to have comparable dust obscuration and Hα luminosities with the remaining, star-forming, sources. The star-forming KAOSS SMGs are consistent with the Fundamental Metallicity Relation (FMR), but with around half the sample scattering above it. We generate four composite spectra: a star-forming subset, spectral and X-ray/IRAC AGN and an all-galaxy composite – which we place onto the BPT diagram, finding all four subsets to be offset from the local relation, and also offset from $z \sim 2.3$ galaxies from the MOSDEF survey (which are less active than KAOSS SMGs). Using theoretical models by Kewley et al. (2001) we suggest that the KAOSS SMGs may be close to the "maximum starburst" limit based on this offset.

Finally, we model the rest-frame optical and Hα emission as Sérsic profiles, finding the SMGs to be consistent with a median Sérsic index of $n = 1$, i.e. exponential disc-like light profiles. Considering only the star-forming SMGs, the distribution of Sérsic indices is consistent with late-type galaxies, and we find a similar result for the distribution of axial ratios b/a.

6.1.3   Spatially resolved kinematics of dust-obscured star-forming galaxies

The work in Chapter 4 is expanded upon in Chapter 5 which presents a sample of 36 SMGs with spatially resolved Hα and/or [OIII] emission, enabling the study of the kinematics in these sources. When published this will approximately double the sample size of SMGs with spatially resolved Hα kinematics in the literature, which is currently limited mostly to much smaller studies.

We divide the sample into *ordered* and *disordered* subsets through a combination of visually assessing the velocity maps and attempting to model the rotation curves as Freeman discs,

placing 28 and eight sources into the two categories respectively. There is little evidence to suggest that the two samples are intrinsically different, and the lower-quality velocity maps in the *disordered* subset are likely a result of lower signal-to-noise in the integrated Hα flux rather than higher turbulence or any other factor.

For the *ordered* sample we model the rotation curves as Freeman discs, finding a median rotation velocity $v_{\rm rot} = 190 \pm 20\,{\rm km\,s^{-1}}$, much higher than those found in surveys of less-active SFGs such as KROSS and KGES. Similarly, we find much higher intrinsic velocity dispersions than these surveys, with a median $\sigma_0 = 87 \pm 5\,{\rm km\,s^{-1}}$. We suggest that both of these results are driven by the higher star-formation rates in KAOSS SMGs compared to the less-active sources, and we find a median ratio of $v_{\rm rot}/\sigma_0 = 2.2 \pm 0.5$, comparable to KROSS and KGES. From this we conclude that the spatially resolved KAOSS SMGs are turbulent, yet rotationally supported systems.

Using the measured sizes from Chapter 4 we derive dynamical masses, finding a median $M_{\rm dyn} = (1.5 \pm 0.3) \times 10^{11}\,{\rm M_\odot}$ and $M_*/M_{\rm dyn} = 0.88 \pm 0.15$, implying low dark matter fractions in the sample. For two KAOSS SMGs with CO coverage from Chapters 2 and 3 we use the dynamical masses to constrain the CO-H_2 conversion factor $\alpha_{\rm CO}$, finding both to be consistent with $\alpha_{\rm CO} = 1$, as in Chapter 3.

Finally, we exploit the EAGLE simulations to estimate halo masses for our sample, finding a median $M_{\rm halo} = (8.6 \pm 1.3) \times 10^{12}\,M_*$. We study the halo masses in the context of the Dekel & Birnboim (2006) scenario for the thermal properties of gas flows onto galaxies, finding that most of our sample would be experiencing some kind of shock heating. If the majority of our sources were merger-driven then this could still account for the high SFRs, but we see little evidence for this in the kinematics at our S/N, and therefore we suggest that the Dekel & Birnboim (2006) model is not consistent with SMGs.

6.2   Ongoing work and future outlook

6.2.1   Completion of the KAOSS Large Programme

The KAOSS observations presented in Chapters 4 and 5, which were delayed by approximately six months due to the shutdown of VLT during the early stages of the COVID-19 pandemic, are expected to be complete by the end of 2022. This will double the current sample size of KAOSS and allow us to draw more statistical conclusions about the nature

of our sample. Additionally, we have targeted three selected pointings with three times the depth of the rest of the data (15 hr instead of 5 hr). Once obtained, this data will enable us to test whether the resolved sources with low-quality velocity maps are as such because of low signal-to-noise in the data or because they are intrinsically different.

6.2.2 Kinematic studies on (sub-)kiloparsec scales

While providing a large sample of highly active SMGs, the KAOSS observations are seeing limited, with resolutions of $\sim 0.6''$ corresponding to ~ 5 kpc. This is not a high enough resolution to probe the scales on which physical features such as clumps and bars are predicted by theory (Förster Schreiber et al., 2018). Indeed, while many of the spatially resolved KAOSS SMGs appear to have smooth velocity gradients in seeing-limited conditions, this may not be the case when resolving smaller scales. We expect to be able to address this issue soon however, with the expected commissioning of the Enhanced Resolution Imager and Spetrograph (ERIS) on the VLT in 2022. Thanks to adaptive optics (AO) we will be able to use ERIS to follow up Hα-detected KAOSS sources at resolutions of $\sim 0.1''$ corresponding to physical scales of < 1 kpc. Numerical simulations suggest that in a merger the star formation efficiency is enhanced around the point of coalescence, i.e. when the two galactic nuclei are separated by ~ 1 kpc. ERIS AO-assisted observations would allow us to resolve SMGs on these scales and thus look for separate kinematic components and thus indications of merger activity. We will potentially also be able to begin decomposing the rotation curves of SMGs into the stellar and gas components, in order to study dark matter fractions and their evolution with redshift as is currently being done with the KMOS Ultra-deep Rotational Velocity Survey (KURVS; e.g. Gillman et al., 2022, Puglisi et al. in prep.).

Additionally, further into the future (2025 and beyond) the construction of the Extremely Large Telescope (ELT) and the High Angular Resolution Monolithic Optical and Near-infrared Integral field spectrograph (HARMONI; Thatte et al., 2010) will improve on current spatial resolutions by a factor of ~ 5 (Zieleniewski et al., 2015), allowing us to resolve $<$kpc scales.

6.2.3 Spatially resolved molecular gas

As previously discussed, the major benefit to NIR IFU spectroscopy with KMOS is the ability to observe multiple sources simultaneously which makes efficient use of telescope time, but this method has a major drawback in that the Hα structures are prone to dust obscuration and

the influence of outflows and winds. One solution is to use (sub)-millimetre interferometers such as ALMA to spatially resolve the low- to mid-$J_{\rm up}$ CO emission which gives a more accurate picture of the bulk of the cold gas as dust obscuration has relatively little effect on the CO compared to the Hα. In contrast to kinematic studies of Hα, CO and [C$_{\rm II}$] emission lines seem to show more disc-like structures. For example, Hodge et al. (2012) spatially resolved the CO(2–1) emission in the $z \sim 4.05$ SMG GN20, finding a clear velocity gradient and showing the velocity field to be consistent with a rotating disc, with maximum rotational velocity $v_{\rm max} = 575 \pm 100 \, {\rm km \, s^{-1}}$. Similarly, De Breuck et al. (2014) used [C$_{\rm II}$] emission to derive a ratio of rotational velocity to velocity dispersion $v_{\rm rot}/\sigma_0 \sim 3.1$ for the $z = 4.7555$ SMG ALESS073.1. Given that the two systems described here are both at higher redshifts than those mentioned in correspondence with evidence for mergers, it is possible that there are kinematic trends with redshift in the SMG population. It is therefore vital to increase the number of SMGs with spatially resolved kinematic measurements in order to understand any potential variations with properties such as redshift and mass within the population.

The observations we presented in Chapters 2 and 3 were mostly too low resolution to study the kinematics of SMGs in great detail, although we were able to draw some conclusions from the line profiles. However, several of the ALESS SMGs have $\sim 1''$ observations, which Amvrosiadis et al. in prep. are currently analysing, modelling the data in the uv-plane to derive velocity fields. There is little overlap between our KAOSS sample and these ALESS SMGs, but the molecular gas kinematics will provide a useful comparison with the results we presented in Chapter 5. This will also provide more accurate dynamical masses than those we estimated in Chapter 3, and therefore improved constraints on the CO-H$_2$ conversion factor.

6.2.4   Completion of ALMA bands 1 and 2

Additionally, with the completion of ALMA band 1 receivers (expected to be available October 2023) accessing the $J_{\rm up} = 1$ and 2 transitions will be possible at high resolution. This will open up the frequency range $\nu \sim 35$–$84 \, {\rm GHz}$, which means CO(1–0) can be observed out to $z \sim 2.3$, providing more robust gas mass estimates and also improved constraints on the CO SLED, which would then allow us to better calibrate low- to mid-J CO estimates. With more accurate gas masses we would be in a position to better constrain the CO-H$_2$ conversion factor $\alpha_{\rm CO}$, a vital component in accurately measuring gas masses from CO observations. We intend to propose ALMA time to obtain these observations as they will be highly complementary to the work presented in this thesis.

6.2.5 The James Webb Space Telescope

At the time of writing, the first images from the *James Webb Space Telescope* have been released. *JWST* is equipped with four instruments – Near Infrared Camera (NIRCam) and Near Infrared Spectrograph (NIRSpec), an imager and spectrograph respectively operating at $\lambda = 0.6$–$5\,\mu$m, Mid-Infrared Instrument (MIRI), a camera and spectrograph operating at $\lambda = 5$–$27\,\mu$m and Near Infrared Imager and Slitless Spectrograph (NIRISS), a spectrograph operating at the same wavelength as NIRSpec but with lower resolution and a wider field of view.

Operating at the diffraction limit, NIRSpec will provide higher-resolution data than KMOS, out to higher redshifts. For example, at $5\,\mu$m the Hα emission line can be detected out to $z \sim 6.6$, improving significantly on KAOSS which is limited to detecting Hα out to $z \sim 2.6$ ([O{\sc iii}] can be detected out to $z \sim 3.8$ but we found few strong detections of this line in Chapter 4). This will also allow us to measure the AGN fraction for a greater range of redshifts and therefore to search for any evolution over time. In IFU mode, NIRSpec will allow us to resolve SMG kinematics out to higher redshifts, and at a much higher resolution than that of our KAOSS data. As with ERIS we will be able to search for multiple components, and thus for evidence of ongoing mergers in SMGs, on much smaller spatial scales.

Additionally, underpinning some of the results we have given in this thesis are the accurate estimation of stellar masses. The COSMOS and GOODS-S fields (which contain ~ 1000 SMGs) are covered by *JWST* Cycle 1 GTO programs, which will provide high-resolution stellar mass maps yielding reliable measurements for this population for the first time by observing the $1.6\,\mu$m stellar bump, which is not currently covered with *HST*. This will allow us to test and calibrate our SED fitting codes for future studies, and robustly study SMGs in the context of the main sequence.

6.3 Final remarks

On the whole, we have provided two new and relatively large samples of submillimetre galaxies which should form the basis of future studies. We have confirmed that SMGs are massive galaxies when compared to less actively star-forming populations, in terms of their stellar, gas and dynamical content, and they also appear to have higher molecular gas fractions, which seems to be the main driver of the high SFRs in these systems. This is in agreement

with the findings that the molecular gas mass density in galaxies appears to follow the star-formation rate density. We found little evidence for heightened star-formation efficiencies in the population, and from the kinematics SMGs seem to be rotationally supported systems with high turbulence, and an apparently low proportion of the sources showed evidence of interactions and mergers. This would support the idea that SMGs are "scaled-up" versions of galaxies with lower SFRs. We suggest however, that the high star-formation rates could be driven by multiple minor mergers, with smaller companion galaxies being below the detection limits of our current surveys.

However, the samples we have used to draw this conclusion, while being a significant improvement on what already existed, are relatively small, making it difficult to measure trends with e.g. redshift, SFR and stellar mass. Additionally, there is still much improvement to be made on estimates of gas and stellar masses which underpin many of these conclusions. The focus over the next decade will be to obtain high-quality maps of SMG dynamics at different wavelengths. In this thesis we have expanded on the currently available sample of spatially resolved Hα maps, but these need to be pushed to higher resolution and higher signal-to-noise ratios. As the previous section hopefully shows, we are well placed to do this with both current and upcoming facilities such as *JWST*, ALMA, ERIS and ELT.

As discussed in the introduction to this thesis, galaxy evolution is a large field, requiring studies of a variety of interconnected processes. At high redshifts, this poses numerous challenges which can be frustrating to overcome. Twenty-five years ago, when the first submillimetre galaxies were detected by single-dish telescopes, very little was known about their properties and it was nearly impossible to match them with counterparts at other wavelengths. Now, we have observed over a thousand of these sources with ALMA at $870\,\mu$m, and (including the work presented in this thesis) begun to study their kinematic properties. At the current rate of progress the coming decade will almost certainly be fruitful for the study of SMGs, and the wider field of galaxy evolution.

Bibliography

Akaike, H. IEEE Transactions on Automatic Control, **19** (1974), 716.

Alaghband-Zadeh, S., Chapman, S.C., Swinbank, A.M., et al. MNRAS, **424**(3) (2012), 2232. `1205.5452`.

Alaghband-Zadeh, S., Chapman, S.C., Swinbank, A.M., et al. MNRAS, **435**(2) (2013), 1493. `1307.6593`.

Allen, M.G., Groves, B.A., Dopita, M.A., et al. ApJS, **178**(1) (2008), 20. `0805.0204`.

Archibald, E.N., Dunlop, J.S., Hughes, D.H., et al. MNRAS, **323**(2) (2001), 417. `astro-ph/0002083`.

Bakx, T.J.L.C., Dannerbauer, H. arXiv e-prints (2022), arXiv:2204.06011. `2204.06011`.

Baldwin, J.A., Phillips, M.M., Terlevich, R. PASP, **93** (1981), 5.

Barger, A.J., Cowie, L.L., Blair, A.H., et al. arXiv e-prints (2022), arXiv:2205.01114. `2205.01114`.

Barger, A.J., Cowie, L.L., Richards, E.A. AJ, **119**(5) (2000), 2092. `astro-ph/0001096`.

Barger, A.J., Wang, W.H., Cowie, L.L., et al. ApJ, **761**(2) (2012), 89. `1209.1626`.

Barrera-Ballesteros, J.K., Heckman, T.M., Zhu, G.B., et al. MNRAS, **463**(3) (2016), 2513. `1609.01740`.

Battisti, A.J., da Cunha, E., Grasha, K., et al. ApJ, **882**(1) (2019), 61. `1908.00771`.

Bell, E.F., McIntosh, D.H., Katz, N., et al. ApJS, **149**(2) (2003), 289. `astro-ph/0302543`.

Bell, E.F., van der Wel, A., Papovich, C., et al. ApJ, **753**(2) (2012), 167. `1110.3786`.

Bellocchi, E., Arribas, S., Colina, L. A&A, **591** (2016), A85. `1603.03441`.

Bellocchi, E., Pereira-Santaella, M., Colina, L., et al. arXiv e-prints (2022), arXiv:2204.02055. `2204.02055`.

Bender, R., Burstein, D., Faber, S.M. ApJ, **399** (1992), 462.

Binney, J., Tremaine, S. *Galactic Dynamics: Second Edition* (2008).

Birkin, J.E., Weiss, A., Wardlow, J.L., et al. MNRAS, **501**(3) (2021), 3926. `2009.03341`.

Blain, A.W., Smail, I., Ivison, R.J., et al. Phys. Rep., **369**(2) (2002), 111. `astro-ph/0202228`.

Bolatto, A.D., Wolfire, M., Leroy, A.K. ARA&A, **51**(1) (2013), 207. `1301.3498`.

Bonnet, H., Abuter, R., Baker, A., et al. The Messenger, **117** (2004), 17.

Boogaard, L.A., van der Werf, P., Weiss, A., et al. ApJ, **902**(2) (2020), 109. `2009.04348`.

Bothwell, M.S., Aguirre, J.E., Aravena, M., et al. MNRAS, **466**(3) (2017), 2825. `1612.04380`.

Bothwell, M.S., Chapman, S.C., Tacconi, L., et al. MNRAS, **405**(1) (2010), 219. `0912.1598`.

Bothwell, M.S., Smail, I., Chapman, S.C., et al. MNRAS, **429**(4) (2013), 3047. `1205.1511`.

Bournaud, F., Dekel, A., Teyssier, R., et al. ApJ, **741**(2) (2011), L33. `1107.1483`.

Bourne, N., Dunlop, J.S., Merlin, E., et al. MNRAS, **467**(2) (2017), 1360. `1607.04283`.

Bourne, N., Dunlop, J.S., Simpson, J.M., et al. MNRAS, **482**(3) (2019), 3135. `1810.01640`.

Bouwens, R., González-López, J., Aravena, M., et al. ApJ, **902**(2) (2020), 112. `2009.10727`.

Bouwens, R.J., Illingworth, G.D., Oesch, P.A., et al. ApJ, **737**(2) (2011), 90. `1006.4360`.

Bouwens, R.J., Illingworth, G.D., Oesch, P.A., et al. ApJ, **754**(2) (2012), 83. `1109.0994`.

Brinchmann, J., Charlot, S., White, S.D.M., et al. MNRAS, **351**(4) (2004), 1151. `astro-ph/0311060`.

Brisbin, D., Miettinen, O., Aravena, M., et al. A&A, **608** (2017), A15. `1708.05748`.

Bromm, V., Yoshida, N. ARA&A, **49**(1) (2011), 373. 1102.4638.

Bundy, K., Bershady, M.A., Law, D.R., et al. ApJ, **798**(1) (2015), 7. 1412.1482.

Burkert, A., Förster Schreiber, N.M., Genzel, R., et al. ApJ, **826**(2) (2016), 214. 1510.03262.

Burkert, A., Genzel, R., Bouché, N., et al. ApJ, **725**(2) (2010), 2324. 0907.4777.

Cañameras, R., Yang, C., Nesvadba, N.P.H., et al. A&A, **620** (2018), A61. 1811.11215.

Calistro Rivera, G., Hodge, J.A., Smail, I., et al. ApJ, **863**(1) (2018), 56. 1804.06852.

Carilli, C.L., Daddi, E., Riechers, D., et al. ApJ, **714**(2) (2010), 1407. 1002.3838.

Carilli, C.L., Hodge, J., Walter, F., et al. ApJ, **739**(1) (2011), L33. 1105.2451.

Carilli, C.L., Walter, F. ARA&A, **51**(1) (2013), 105. 1301.0371.

Casey, C.M., Narayanan, D., Cooray, A. Phys. Rep., **541**(2) (2014), 45. 1402.1456.

Cassata, P., Liu, D., Groves, B., et al. ApJ, **891**(1) (2020), 83. 2002.04040.

Chabrier, G. PASP, **115**(809) (2003), 763. astro-ph/0304382.

Chapman, S.C., Bertoldi, F., Smail, I., et al. MNRAS, **449** (2015), L68. 1501.02839.

Chapman, S.C., Blain, A.W., Smail, I., et al. ApJ, **622**(2) (2005), 772. astro-ph/0412573.

Chen, C.C., Hodge, J.A., Smail, I., et al. ApJ, **846**(2) (2017), 108. 1708.08937.

Chen, C.C., Liao, C.L., Smail, I., et al. ApJ, **929**(2) (2022), 159. 2112.07430.

Chen, C.C., Smail, I., Swinbank, A.M., et al. ApJ, **799**(2) (2015), 194. 1412.0668.

Civano, F., Marchesi, S., Comastri, A., et al. ApJ, **819**(1) (2016), 62. 1601.00941.

Conroy, C. ARA&A, **51**(1) (2013), 393. 1301.7095.

Coppin, K., Chapin, E.L., Mortier, A.M.J., et al. MNRAS, **372**(4) (2006), 1621. astro-ph/0609039.

Coppin, K., Pope, A., Menéndez-Delmestre, K., et al. ApJ, **713** (2010a), 503. 1003.0447.

Coppin, K.E.K., Chapman, S.C., Smail, I., et al. MNRAS, **407**(1) (2010b), L103. 1004.4001.

Coppin, K.E.K., Swinbank, A.M., Neri, R., et al. MNRAS, **389** (2008), 45. 0806.0618.

Courteau, S. AJ, **114** (1997), 2402. `astro-ph/9709201`.

Cowie, L.L., Barger, A.J., Hsu, L.Y., et al. ApJ, **837**(2) (2017), 139. `1702.03002`.

Cowie, L.L., González-López, J., Barger, A.J., et al. ApJ, **865**(2) (2018), 106. `1805.09424`.

Cowie, L.L., Songaila, A., Hu, E.M., et al. AJ, **112** (1996), 839. `astro-ph/9606079`.

Cresci, G., Hicks, E.K.S., Genzel, R., et al. ApJ, **697**(1) (2009), 115. `0902.4701`.

Croom, S.M., Lawrence, J.S., Bland-Hawthorn, J., et al. MNRAS, **421**(1) (2012), 872. `1112.3367`.

Croton, D.J., Springel, V., White, S.D.M., et al. MNRAS, **365**(1) (2006), 11. `astro-ph/0508046`.

da Cunha, E., Charlot, S., Elbaz, D. MNRAS, **388**(4) (2008), 1595. `0806.1020`.

da Cunha, E., Walter, F., Smail, I.R., et al. ApJ, **806**(1) (2015), 110. `1504.04376`.

Daddi, E., Bournaud, F., Walter, F., et al. ApJ, **713**(1) (2010), 686. `0911.2776`.

Daddi, E., Cimatti, A., Pozzetti, L., et al. A&A, **361** (2000), 535. `astro-ph/0005581`.

Daddi, E., Dannerbauer, H., Elbaz, D., et al. ApJ, **673**(1) (2008), L21. `0711.4995`.

Daddi, E., Dannerbauer, H., Liu, D., et al. A&A, **577** (2015), A46. `1409.8158`.

Daddi, E., Dannerbauer, H., Stern, D., et al. ApJ, **694**(2) (2009), 1517. `0810.3108`.

Dale, D.A., Barlow, R.J., Cohen, S.A., et al. ApJ, **712**(2) (2010), L189. `1003.0463`.

Danielson, A.L.R., Swinbank, A.M., Smail, I., et al. MNRAS, **410**(3) (2011), 1687. `1008.3183`.

Danielson, A.L.R., Swinbank, A.M., Smail, I., et al. MNRAS, **436**(3) (2013), 2793. `1309.5952`.

Danielson, A.L.R., Swinbank, A.M., Smail, I., et al. ApJ, **840**(2) (2017), 78. `1705.03503`.

Dannerbauer, H., Lehnert, M.D., Lutz, D., et al. ApJ, **573**(2) (2002), 473. `astro-ph/0201104`.

Davé, R., Finlator, K., Oppenheimer, B.D. MNRAS, **421**(1) (2012), 98. `1108.0426`.

Davé, R., Finlator, K., Oppenheimer, B.D., et al. MNRAS, **404**(3) (2010), 1355. `0909.4078`.

De Breuck, C., Williams, R.J., Swinbank, M., et al. A&A, **565** (2014), A59. `1404.2295`.

Dekel, A., Birnboim, Y. MNRAS, **368**(1) (2006), 2. `astro-ph/0412300`.

Dessauges-Zavadsky, M., Ginolfi, M., Pozzi, F., et al. arXiv e-prints (2020), arXiv:2004.10771. `2004.10771`.

Dickinson, M., Giavalisco, M., GOODS Team. *The Great Observatories Origins Deep Survey.* In R. Bender, A. Renzini, editors, *The Mass of Galaxies at Low and High Redshift* (2003a), page 324. `astro-ph/0204213`.

Dickinson, M., Papovich, C., Ferguson, H.C., et al. ApJ, **587**(1) (2003b), 25. `astro-ph/0212242`.

Dole, H., Lagache, G., Puget, J.L., et al. A&A, **451**(2) (2006), 417. `astro-ph/0603208`.

Donley, J.L., Koekemoer, A.M., Brusa, M., et al. ApJ, **748**(2) (2012), 142. `1201.3899`.

Dopita, M.A., Pereira, M., Kewley, L.J., et al. ApJS, **143**(1) (2002), 47.

Downes, D., Solomon, P.M. ApJ, **507**(2) (1998), 615. `astro-ph/9806377`.

Driver, S.P., Norberg, P., Baldry, I.K., et al. Astronomy and Geophysics, **50**(5) (2009), 5.12. `0910.5123`.

Dudzevičiūtė, U., Smail, I., Swinbank, A.M., et al. MNRAS, **494**(3) (2020), 3828. `1910.07524`.

Dunne, L., Eales, S., Edmunds, M., et al. MNRAS, **315**(1) (2000), 115. `astro-ph/0002234`.

Elbaz, D., Daddi, E., Le Borgne, D., et al. A&A, **468**(1) (2007), 33. `astro-ph/0703653`.

Elbaz, D., Dickinson, M., Hwang, H.S., et al. A&A, **533** (2011), A119. `1105.2537`.

Elbaz, D., Leiton, R., Nagar, N., et al. A&A, **616** (2018), A110. `1711.10047`.

Ellison, S.L., Patton, D.R., Simard, L., et al. ApJ, **672**(2) (2008), L107. `0711.4833`.

Emerson, J.P., Sutherland, W.J., McPherson, A.M., et al. The Messenger, **117** (2004), 27.

Engel, H., Tacconi, L.J., Davies, R.I., et al. ApJ, **724**(1) (2010), 233.

Epinat, B., Amram, P., Balkowski, C., et al. MNRAS, **401**(4) (2010), 2113. `0904.3891`.

Erb, D.K., Steidel, C.C., Shapley, A.E., et al. ApJ, **646**(1) (2006), 107. `astro-ph/0604041`.

Erroz-Ferrer, S., Carollo, C.M., den Brok, M., et al. MNRAS, **484**(4) (2019), 5009. `1901.04493`.

ESO CPL Development Team. *EsoRex: ESO Recipe Execution Tool* (2015). `1504.003`.

Fixsen, D.J., Bennett, C.L., Mather, J.C. ApJ, **526**(1) (1999), 207.

Foreman-Mackey, D., Hogg, D.W., Lang, D., et al. PASP, **125**(925) (2013), 306. `1202.3665`.

Förster Schreiber, N.M., Genzel, R., Bouché, N., et al. ApJ, **706**(2) (2009), 1364. `0903.1872`.

Förster Schreiber, N.M., Genzel, R., Lehnert, M.D., et al. ApJ, **645**(2) (2006), 1062. `astro-ph/0603559`.

Förster Schreiber, N.M., Renzini, A., Mancini, C., et al. ApJS, **238**(2) (2018), 21. `1802.07276`.

Förster Schreiber, N.M., Wuyts, S. ARA&A, **58** (2020), 661. `2010.10171`.

Franco, M., Elbaz, D., Béthermin, M., et al. A&A, **620** (2018), A152. `1803.00157`.

Frayer, D.T., Ivison, R.J., Scoville, N.Z., et al. ApJ, **506**(1) (1998), L7. `astro-ph/9808109`.

Frayer, D.T., Ivison, R.J., Scoville, N.Z., et al. ApJ, **514**(1) (1999), L13. `astro-ph/9901311`.

Freeman, K.C. ApJ, **160** (1970), 811.

Frias Castillo, M., Rybak, M., Hodge, J., et al. ApJ, **930**(1) (2022), 35. `2203.15811`.

Gaches, B.A.L., Offner, S.S.R., Bisbas, T.G. ApJ, **883**(2) (2019), 190. `1908.06999`.

Gardner, J.P., Mather, J.C., Clampin, M., et al. Space Sci. Rev., **123**(4) (2006), 485. `astro-ph/0606175`.

Garg, P., Narayanan, D., Byler, N., et al. ApJ, **926**(1) (2022), 80. `2201.03564`.

Geach, J.E., Chapin, E.L., Coppin, K.E.K., et al. MNRAS, **432**(1) (2013), 53. `1211.6668`.

Geach, J.E., Dunlop, J.S., Halpern, M., et al. MNRAS, **465**(2) (2017), 1789. `1607.03904`.

Geach, J.E., Smail, I., Best, P.N., et al. MNRAS, **388**(4) (2008), 1473. `0805.2861`.

Geach, J.E., Smail, I., Moran, S.M., et al. ApJ, **730**(2) (2011), L19. `1102.3694`.

Genzel, R., Förster Schreiber, N.M., Rosario, D., et al. ApJ, **796**(1) (2014), 7. 1406.0183.

Genzel, R., Förster Schreiber, N.M., Übler, H., et al. Nature, **543**(7645) (2017), 397. 1703. 04310.

Genzel, R., Tacconi, L.J., Gracia-Carpio, J., et al. MNRAS, **407**(4) (2010), 2091. 1003.5180.

Genzel, R., Tacconi, L.J., Lutz, D., et al. ApJ, **800**(1) (2015), 20. 1409.1171.

Giavalisco, M., Ferguson, H.C., Koekemoer, A.M., et al. ApJ, **600**(2) (2004), L93. astro-ph/ 0309105.

Gillman, S., Puglisi, A., Dudzevičiūtė, U., et al. MNRAS(2022). 2202.12304.

Gillman, S., Swinbank, A.M., Tiley, A.L., et al. MNRAS, **486**(1) (2019), 175. 1903.05148.

Gillman, S., Tiley, A.L., Swinbank, A.M., et al. MNRAS, **492**(1) (2020), 1492. 1911.12375.

Greve, T.R., Bertoldi, F., Smail, I., et al. MNRAS, **359**(3) (2005), 1165. astro-ph/0503055.

Greve, T.R., Leonidaki, I., Xilouris, E.M., et al. ApJ, **794**(2) (2014), 142. 1407.4400.

Gruppioni, C., Pozzi, F., Rodighiero, G., et al. MNRAS, **432**(1) (2013), 23. 1302.5209.

Guilloteau, S., Delannoy, J., Downes, D., et al. A&A, **262** (1992), 624.

Gullberg, B., Smail, I., Swinbank, A.M., et al. MNRAS, **490**(4) (2019), 4956. 1910.01121.

Guo, Y., Ferguson, H.C., Giavalisco, M., et al. ApJS, **207**(2) (2013), 24. 1308.4405.

Hainline, L.J., Blain, A.W., Smail, I., et al. ApJ, **699**(2) (2009), 1610.

Hainline, L.J., Blain, A.W., Smail, I., et al. ApJ, **740**(2) (2011), 96. 1006.0238.

Harris, A.I., Baker, A.J., Frayer, D.T., et al. ApJ, **752**(2) (2012), 152. 1204.4706.

Harrison, C.M., Johnson, H.L., Swinbank, A.M., et al. MNRAS, **467**(2) (2017), 1965. 1701. 05561.

Hatsukade, B., Kohno, K., Umehata, H., et al. PASJ, **68**(3) (2016), 36. 1602.08167.

Hayward, C.C., Sparre, M., Chapman, S.C., et al. MNRAS, **502**(2) (2021), 2922. 2007. 01885.

Hickox, R.C., Alexander, D.M. ARA&A, **56** (2018), 625. 1806.04680.

Hill, R., Chapman, S.C., Scott, D., et al. MNRAS, **477**(2) (2018), 2042. `1710.02231`.

Hodge, J.A., Carilli, C.L., Walter, F., et al. ApJ, **760**(1) (2012), 11. `1209.2418`.

Hodge, J.A., da Cunha, E. arXiv e-prints (2020), arXiv:2004.00934. `2004.00934`.

Hodge, J.A., Karim, A., Smail, I., et al. ApJ, **768**(1) (2013), 91. `1304.4266`.

Hodge, J.A., Smail, I., Walter, F., et al. ApJ, **876**(2) (2019), 130. `1810.12307`.

Hodge, J.A., Swinbank, A.M., Simpson, J.M., et al. ApJ, **833**(1) (2016), 103. `1609.09649`.

Hogan, L., Rigopoulou, D., Magdis, G.E., et al. MNRAS, **503**(4) (2021), 5329.

Holland, W.S., Bintley, D., Chapin, E.L., et al. MNRAS, **430**(4) (2013), 2513. `1301.3650`.

Hopkins, P.F., Hayward, C.C., Narayanan, D., et al. MNRAS, **420**(1) (2012a), 320. `1108.3086`.

Hopkins, P.F., Hernquist, L., Cox, T.J., et al. ApJS, **175**(2) (2008), 356. `0706.1243`.

Hopkins, P.F., Hernquist, L., Hayward, C.C., et al. MNRAS, **425**(2) (2012b), 1121. `1111.1236`.

Hsieh, B.C., Wang, W.H., Hsieh, C.C., et al. ApJS, **203**(2) (2012), 23. `1210.4519`.

Hubble, E.P. *Realm of the Nebulae* (1936).

Hughes, D.H., Serjeant, S., Dunlop, J., et al. Nature, **394** (1998), 241. `astro-ph/9806297`.

Ichikawa, T., Suzuki, R., Tokoku, C., et al. *MOIRCS: multi-object infrared camera and spectrograph for SUBARU*. In I.S. McLean, M. Iye, editors, *Society of Photo-Optical Instrumentation Engineers (SPIE) Conference Series*, volume 6269 of *Society of Photo-Optical Instrumentation Engineers (SPIE) Conference Series* (2006), page 626916.

Ikarashi, S., Ivison, R.J., Caputi, K.I., et al. ApJ, **810**(2) (2015), 133. `1411.5038`.

Iono, D., Peck, A.B., Pope, A., et al. ApJ, **640**(1) (2006), L1. `astro-ph/0602226`.

Ivison, R.J., Greve, T.R., Dunlop, J.S., et al. MNRAS, **380**(1) (2007), 199. `astro-ph/0702544`.

Ivison, R.J., Papadopoulos, P.P., Smail, I., et al. MNRAS, **412**(3) (2011), 1913. `1009.0749`.

Jarvis, M.J., Bonfield, D.G., Bruce, V.A., et al. MNRAS, **428**(2) (2013), 1281. `1206.4263`.

Jin, S., Daddi, E., Liu, D., et al. ApJ, **864**(1) (2018), 56. 1807.04697.

Jin, S., Dannerbauer, H., Emonts, B., et al. A&A, **652** (2021), A11. 2103.08884.

Johnson, H.L., Harrison, C.M., Swinbank, A.M., et al. MNRAS, **474**(4) (2018), 5076. 1707.
02302.

Kassin, S.A., Weiner, B.J., Faber, S.M., et al. ApJ, **660**(1) (2007), L35. astro-ph/0702643.

Kaufman, M.J., Wolfire, M.G., Hollenbach, D.J., et al. ApJ, **527**(2) (1999), 795. astro-ph/
9907255.

Keene, J., Blake, G.A., Phillips, T.G., et al. ApJ, **299** (1985), 967.

Kelvin, L.S., Driver, S.P., Robotham, A.S.G., et al. MNRAS, **439**(2) (2014), 1245. 1401.
1817.

Kennicutt, Robert C., J. ARA&A, **36** (1998a), 189. astro-ph/9807187.

Kennicutt, Robert C., J. ApJ, **498**(2) (1998b), 541. astro-ph/9712213.

Kennicutt, R.C., Evans, N.J. ARA&A, **50** (2012), 531. 1204.3552.

Kereš, D., Katz, N., Weinberg, D.H., et al. MNRAS, **363**(1) (2005), 2. astro-ph/0407095.

Kewley, L.J., Dopita, M.A., Leitherer, C., et al. ApJ, **774**(2) (2013), 100. 1307.0508.

Kewley, L.J., Dopita, M.A., Sutherland, R.S., et al. ApJ, **556**(1) (2001), 121. astro-ph/
0106324.

Kewley, L.J., Ellison, S.L. ApJ, **681**(2) (2008), 1183. 0801.1849.

Kewley, L.J., Geller, M.J., Jansen, R.A., et al. AJ, **124**(6) (2002), 3135. astro-ph/0208508.

Kewley, L.J., Groves, B., Kauffmann, G., et al. MNRAS, **372**(3) (2006), 961. astro-ph/
0605681.

Kim, M., Dunlop, J.S., Lonsdale, C.J., et al. *The Spitzer Public Legacy Survey of the 1
square degree UKIDSS Ultra Deep Survey.* In *American Astronomical Society Meeting
Abstracts #217*, volume 217 of *American Astronomical Society Meeting Abstracts* (2011),
page 335.51.

Kimura, M., Maihara, T., Ohta, K., et al. *Fibre-Multi-Object Spectrograph (FMOS) for Subaru Telescope.* In M. Iye, A.F.M. Moorwood, editors, *Instrument Design and Performance for Optical/Infrared Ground-based Telescopes*, volume 4841 of *Society of Photo-Optical Instrumentation Engineers (SPIE) Conference Series* (2003), pages 974–984.

Kocevski, D.D., Hasinger, G., Brightman, M., et al. ApJS, **236**(2) (2018), 48. `1809.08240`.

Kohandel, M., Pallottini, A., Ferrara, A., et al. MNRAS, **487**(3) (2019), 3007. `1905.11413`.

Koprowski, M.P., Dunlop, J.S., Michałowski, M.J., et al. MNRAS, **458**(4) (2016), 4321. `1509.07144`.

Kormendy, J., Fisher, D.B., Cornell, M.E., et al. ApJS, **182**(1) (2009), 216. `0810.1681`.

Lagos, C.d.P., Bayet, E., Baugh, C.M., et al. MNRAS, **426**(3) (2012), 2142. `1204.0795`.

Lagos, C.d.P., da Cunha, E., Robotham, A.S.G., et al. arXiv e-prints (2020), arXiv:2007.09853. `2007.09853`.

Laigle, C., McCracken, H.J., Ilbert, O., et al. ApJS, **224**(2) (2016), 24. `1604.02350`.

Lang, P., Schinnerer, E., Smail, I., et al. ApJ, **879**(1) (2019), 54. `1905.06960`.

Lapi, A., Pantoni, L., Zanisi, L., et al. ApJ, **857**(1) (2018), 22. `1803.04734`.

Larkin, J., Barczys, M., Krabbe, A., et al. *OSIRIS: a diffraction limited integral field spectrograph for Keck.* In I.S. McLean, M. Iye, editors, *Society of Photo-Optical Instrumentation Engineers (SPIE) Conference Series*, volume 6269 of *Society of Photo-Optical Instrumentation Engineers (SPIE) Conference Series* (2006), page 62691A.

Law, D.R., Steidel, C.C., Erb, D.K., et al. ApJ, **697**(2) (2009), 2057. `0901.2930`.

Lawrence, A., Warren, S.J., Almaini, O., et al. MNRAS, **379**(4) (2007), 1599. `astro-ph/0604426`.

Le Fèvre, O., Béthermin, M., Faisst, A., et al. arXiv e-prints (2019), arXiv:1910.09517. `1910.09517`.

Le Fevre, O., Saisse, M., Mancini, D., et al. *VIMOS and NIRMOS multi-object spectrographs for the ESO VLT.* In M. Iye, A.F. Moorwood, editors, *Optical and IR Telescope Instrumentation and Detectors*, volume 4008 of *Society of Photo-Optical Instrumentation Engineers (SPIE) Conference Series* (2000), pages 546–557.

Lee, S.K., Ferguson, H.C., Somerville, R.S., et al. ApJ, **725**(2) (2010), 1644. 1010.1966.

Lemke, D., Klaas, U., Abolins, J., et al. A&A, **315** (1996), L64.

Leroy, A.K., Bolatto, A., Gordon, K., et al. ApJ, **737**(1) (2011), 12. 1102.4618.

Leroy, A.K., Walter, F., Brinks, E., et al. AJ, **136**(6) (2008), 2782. 0810.2556.

Leslie, S.K., Schinnerer, E., Liu, D., et al. ApJ, **899**(1) (2020), 58. 2006.13937.

Li, Q., Narayanan, D., Davé, R. MNRAS, **490**(1) (2019), 1425. 1906.09277.

Licquia, T.C., Newman, J.A. ApJ, **806**(1) (2015), 96. 1407.1078.

Lilly, S.J., Eales, S.A., Gear, W.K.P., et al. ApJ, **518**(2) (1999), 641. astro-ph/9901047.

Lilly, S.J., Le Fevre, O., Hammer, F., et al. ApJ, **460** (1996), L1. astro-ph/9601050.

Liu, D., Daddi, E., Dickinson, M., et al. ApJ, **853**(2) (2018), 172. 1703.05281.

Liu, D., Lang, P., Magnelli, B., et al. ApJS, **244**(2) (2019a), 40. 1910.12872.

Liu, D., Schinnerer, E., Groves, B., et al. ApJ, **887**(2) (2019b), 235. 1910.12883.

Lotz, J.M., Jonsson, P., Cox, T.J., et al. MNRAS, **391**(3) (2008), 1137. 0805.1246.

Lovell, C.C., Geach, J.E., Davé, R., et al. arXiv e-prints (2021a), arXiv:2106.11588. 2106.11588.

Lovell, C.C., Geach, J.E., Davé, R., et al. MNRAS, **502**(1) (2021b), 772. 2006.15156.

Luo, B., Brandt, W.N., Xue, Y.Q., et al. ApJS, **228**(1) (2017), 2. 1611.03501.

Madau, P., Dickinson, M. ARA&A, **52** (2014), 415. 1403.0007.

Magdis, G.E., Daddi, E., Sargent, M., et al. ApJ, **758**(1) (2012), L9. 1209.1484.

Magnelli, B., Lutz, D., Santini, P., et al. A&A, **539** (2012a), A155. 1202.0761.

Magnelli, B., Lutz, D., Santini, P., et al. A&A, **539** (2012b), A155. 1202.0761.

Magnelli, B., Popesso, P., Berta, S., et al. A&A, **553** (2013), A132. 1303.4436.

Maiolino, R., Mannucci, F. A&A Rev., **27**(1) (2019), 3. 1811.09642.

Mairs, S., Dempsey, J.T., Bell, G.S., et al. AJ, **162**(5) (2021), 191. 2107.13558.

Mancini, C., Förster Schreiber, N.M., Renzini, A., et al. ApJ, **743**(1) (2011), 86. `1109.5952`.

Mannucci, F., Cresci, G., Maiolino, R., et al. MNRAS, **408**(4) (2010), 2115. `1005.0006`.

Martig, M., Bournaud, F., Teyssier, R., et al. ApJ, **707**(1) (2009), 250. `0905.4669`.

McAlpine, S., Smail, I., Bower, R.G., et al. MNRAS, **488**(2) (2019), 2440. `1901.05467`.

McCracken, H.J., Milvang-Jensen, B., Dunlop, J., et al. A&A, **544** (2012), A156. `1204.6586`.

McLean, I.S., Steidel, C.C., Matthews, K., et al. *MOSFIRE: a multi-object near-infrared spectrograph and imager for the Keck Observatory.* In I.S. McLean, M.M. Casali, editors, *Ground-based and Airborne Instrumentation for Astronomy II*, volume 7014 of *Society of Photo-Optical Instrumentation Engineers (SPIE) Conference Series* (2008), page 70142Z.

McMullin, J.P., Waters, B., Schiebel, D., et al. *CASA Architecture and Applications.* In R.A. Shaw, F. Hill, D.J. Bell, editors, *Astronomical Data Analysis Software and Systems XVI*, volume 376 of *Astronomical Society of the Pacific Conference Series* (2007), page 127.

Menéndez-Delmestre, K., Blain, A.W., Swinbank, M., et al. ApJ, **767**(2) (2013), 151. `1302.2145`.

Michałowski, M.J., Dunlop, J.S., Cirasuolo, M., et al. A&A, **541** (2012), A85. `1108.6058`.

Miettinen, O., Delvecchio, I., Smolčić, V., et al. A&A, **606** (2017), A17. `1707.00637`.

Mihos, J.C., Hernquist, L. ApJ, **464** (1996), 641. `astro-ph/9512099`.

Miller, N.A., Bonzini, M., Fomalont, E.B., et al. ApJS, **205**(2) (2013), 13. `1301.7004`.

Mitsuhashi, I., Matsuda, Y., Smail, I., et al. ApJ, **907**(2) (2021), 122. `2011.09917`.

Mortlock, A., Conselice, C.J., Hartley, W.G., et al. MNRAS, **433**(2) (2013), 1185. `1305.2204`.

Naab, T., Johansson, P.H., Ostriker, J.P. ApJ, **699**(2) (2009), L178. `0903.1636`.

Narayanan, D., Cox, T.J., Hayward, C.C., et al. MNRAS, **400**(4) (2009), 1919. `0905.2184`.

Narayanan, D., Hayward, C.C., Cox, T.J., et al. MNRAS, **401**(3) (2010), 1613. `0904.0004`.

Narayanan, D., Turk, M., Feldmann, R., et al. Nature, **525**(7570) (2015), 496. `1509.06377`.

Neugebauer, G., Habing, H.J., van Duinen, R., et al. ApJ, **278** (1984), L1.

Newman, S.F., Genzel, R., Förster Schreiber, N.M., et al. ApJ, **767**(2) (2013), 104. `1211.6160`.

Noeske, K.G., Weiner, B.J., Faber, S.M., et al. ApJ, **660**(1) (2007), L43. `astro-ph/0701924`.

Oliver, S.J., Bock, J., Altieri, B., et al. MNRAS, **424**(3) (2012), 1614. `1203.2562`.

Omont, A. Reports on Progress in Physics, **70**(7) (2007), 1099. `0709.3814`.

Osterbrock, D.E., Ferland, G.J. *Astrophysics of gaseous nebulae and active galactic nuclei* (2006).

Papadopoulos, P.P., Bisbas, T.G., Zhang, Z.Y. MNRAS, **478**(2) (2018), 1716. `1804.09654`.

Papadopoulos, P.P., Greve, T.R. ApJ, **615**(1) (2004), L29. `astro-ph/0409559`.

Papadopoulos, P.P., Zhang, Z.Y., Xilouris, E.M., et al. ApJ, **788**(2) (2014), 153. `1404.6090`.

Pearson, W.J., Suelves, L.E., Ho, S.C.C., et al. arXiv e-prints (2022), arXiv:2202.10780. `2202.10780`.

Peng, C.Y., Ho, L.C., Impey, C.D., et al. AJ, **139**(6) (2010), 2097. `0912.0731`.

Pérez-González, P.G., Rieke, G.H., Villar, V., et al. ApJ, **675**(1) (2008), 234. `0709.1354`.

Pettini, M., Pagel, B.E.J. MNRAS, **348**(3) (2004), L59. `astro-ph/0401128`.

Popesso, P., Morselli, L., Concas, A., et al. MNRAS, **490**(4) (2019), 5285. `1909.07760`.

Puget, J.L., Abergel, A., Bernard, J.P., et al. A&A, **308** (1996), L5.

Puglisi, A., Daddi, E., Liu, D., et al. ApJ, **877**(2) (2019), L23. `1905.02958`.

Renzini, A., Peng, Y.j. ApJ, **801**(2) (2015), L29. `1502.01027`.

Riechers, D.A., Boogaard, L.A., Decarli, R., et al. ApJ, **896**(2) (2020), L21. `2005.09653`.

Riechers, D.A., Capak, P.L., Carilli, C.L., et al. ApJ, **720**(2) (2010), L131. `1008.0389`.

Riechers, D.A., Carilli, L.C., Walter, F., et al. ApJ, **733**(1) (2011a), L11. `1104.4348`.

Riechers, D.A., Hodge, J., Walter, F., et al. ApJ, **739**(1) (2011b), L31. `1105.4177`.

Rizzo, F., Vegetti, S., Fraternali, F., et al. MNRAS, **507**(3) (2021), 3952. `2102.05671`.

Rodríguez-Zaurín, J., Arribas, S., Monreal-Ibero, A., et al. A&A, **527** (2011), A60. 1009.
   0112.

Rosenberg, M.J.F., van der Werf, P.P., Aalto, S., et al. ApJ, **801**(2) (2015), 72. 1501.02985.

Rybak, M., Calistro Rivera, G., Hodge, J.A., et al. ApJ, **876**(2) (2019), 112. 1901.10027.

Saintonge, A., Lutz, D., Genzel, R., et al. ApJ, **778**(1) (2013), 2. 1309.3281.

Salpeter, E.E. ApJ, **121** (1955), 161.

Sánchez, S.F. ARA&A, **58** (2020), 99. 1911.06925.

Sánchez, S.F., Kennicutt, R.C., Gil de Paz, A., et al. A&A, **538** (2012), A8. 1111.0962.

Sánchez, S.F., Rosales-Ortega, F.F., Jungwiert, B., et al. A&A, **554** (2013), A58. 1304.2158.

Sanders, D.B., Mazzarella, J.M., Kim, D.C., et al. AJ, **126**(4) (2003), 1607. astro-ph/
   0306263.

Sanders, D.B., Mirabel, I.F. ARA&A, **34** (1996), 749.

Sanders, D.B., Soifer, B.T., Elias, J.H., et al. ApJ, **325** (1988), 74.

Sanders, R.L., Shapley, A.E., Kriek, M., et al. ApJ, **799**(2) (2015), 138. 1408.2521.

Sandstrom, K.M., Leroy, A.K., Walter, F., et al. ApJ, **777**(1) (2013), 5. 1212.1208.

Santini, P., Maiolino, R., Magnelli, B., et al. A&A, **562** (2014), A30. 1311.3670.

Schaye, J., Crain, R.A., Bower, R.G., et al. MNRAS, **446**(1) (2015), 521. 1407.7040.

Schinnerer, E., Carilli, C.L., Capak, P., et al. ApJ, **689**(1) (2008), L5. 0810.3405.

Schreiber, C., Pannella, M., Elbaz, D., et al. A&A, **575** (2015), A74. 1409.5433.

Scoville, N., Aussel, H., Brusa, M., et al. ApJS, **172**(1) (2007), 1. astro-ph/0612305.

Scoville, N., Lee, N., Vanden Bout, P., et al. ApJ, **837**(2) (2017), 150. 1702.04729.

Scoville, N., Sheth, K., Aussel, H., et al. ApJ, **820**(2) (2016), 83. 1511.05149.

Serra, P., Oosterloo, T., Cappellari, M., et al. MNRAS, **460**(2) (2016), 1382. 1604.07902.

Shapiro, K.L., Genzel, R., Förster Schreiber, N.M., et al. ApJ, **682**(1) (2008), 231. 0802.
   0879.

Shapiro, K.L., Genzel, R., Quataert, E., et al. ApJ, **701**(2) (2009), 955. `0902.4704`.

Shapley, A.E., Reddy, N.A., Kriek, M., et al. ApJ, **801**(2) (2015), 88. `1409.7071`.

Shapley, A.E., Steidel, C.C., Pettini, M., et al. ApJ, **588**(1) (2003), 65. `astro-ph/0301230`.

Sharon, C.E., Baker, A.J., Harris, A.I., et al. ApJ, **765**(1) (2013), 6. `1212.5955`.

Sharples, R., Bender, R., Agudo Berbel, A., et al. The Messenger, **151** (2013), 21.

Shetty, S., Cappellari, M., McDermid, R.M., et al. MNRAS, **494**(4) (2020), 5619. `2004.07449`.

Shim, H., Lee, D., Kim, Y., et al. MNRAS(2022). `2204.11392`.

Simpson, C., Westoby, P., Arumugam, V., et al. MNRAS, **433**(3) (2013), 2647. `1307.0502`.

Simpson, J.M., Smail, I., Dudzeviciute, U., et al. arXiv e-prints (2020), arXiv:2003.05484. `2003.05484`.

Simpson, J.M., Smail, I., Swinbank, A.M., et al. ApJ, **799**(1) (2015), 81. `1411.5025`.

Simpson, J.M., Smail, I., Swinbank, A.M., et al. ApJ, **880**(1) (2019), 43. `1912.02229`.

Simpson, J.M., Swinbank, A.M., Smail, I., et al. ApJ, **788**(2) (2014), 125. `1310.6363`.

Siringo, G., Kreysa, E., Kovács, A., et al. A&A, **497**(3) (2009), 945. `0903.1354`.

Smail, I., Dudzevičiūtė, U., Stach, S.M., et al. arXiv e-prints (2020), arXiv:2010.02250. `2010.02250`.

Smail, I., Ivison, R.J., Blain, A.W. ApJ, **490** (1997), L5. `astro-ph/9708135`.

Smith, R.J., Collier, W.P., Ozaki, S., et al. arXiv e-prints (2019), arXiv:1911.06338. `1911.06338`.

Smolčić, V., Aravena, M., Navarrete, F., et al. A&A, **548** (2012), A4. `1205.6470`.

Smolčić, V., Karim, A., Miettinen, O., et al. A&A, **576** (2015), A127. `1412.3799`.

Smolčić, V., Novak, M., Bondi, M., et al. A&A, **602** (2017), A1. `1703.09713`.

Soifer, B.T., Rowan-Robinson, M., Houck, J.R., et al. ApJ, **278** (1984), L71.

Solomon, P.M., Downes, D., Radford, S.J.E. ApJ, **387** (1992), L55.

Solomon, P.M., Downes, D., Radford, S.J.E., et al. ApJ, **478**(1) (1997), 144. `astro-ph/9610166`.

Solomon, P.M., Rivolo, A.R., Barrett, J., et al. ApJ, **319** (1987), 730.

Solomon, P.M., Vanden Bout, P.A. ARA&A, **43**(1) (2005), 677. `astro-ph/0508481`.

Soto, K.T., Lilly, S.J., Bacon, R., et al. MNRAS, **458**(3) (2016), 3210. `1602.08037`.

Speagle, J.S., Steinhardt, C.L., Capak, P.L., et al. ApJS, **214**(2) (2014), 15. `1405.2041`.

Spilker, J.S., Marrone, D.P., Aguirre, J.E., et al. ApJ, **785**(2) (2014), 149. `1403.1667`.

Stach, S.M., Dudzevičiūtė, U., Smail, I., et al. MNRAS, **487**(4) (2019), 4648. `1903.02602`.

Stach, S.M., Smail, I., Amvrosiadis, A., et al. MNRAS, **504**(1) (2021), 172. `2102.12510`.

Stach, S.M., Smail, I., Swinbank, A.M., et al. ApJ, **860** (2018), 161.

Steidel, C.C., Rudie, G.C., Strom, A.L., et al. ApJ, **795**(2) (2014), 165. `1405.5473`.

Stott, J.P., Swinbank, A.M., Johnson, H.L., et al. MNRAS, **457**(2) (2016), 1888. `1601.03400`.

Swinbank, A.M., Chapman, S.C., Smail, I., et al. MNRAS, **371**(1) (2006), 465.

Swinbank, A.M., Simpson, J.M., Smail, I., et al. MNRAS, **438**(2) (2014), 1267. `1310.6362`.

Swinbank, A.M., Smail, I., Chapman, S.C., et al. ApJ, **617**(1) (2004), 64. `astro-ph/0412050`.

Swinbank, A.M., Smail, I., Longmore, S., et al. Nature, **464**(7289) (2010), 733. `1003.3674`.

Swinbank, A.M., Smail, I., Sobral, D., et al. ApJ, **760**(2) (2012), 130. `1209.1396`.

Tacconi, L.J., Genzel, R., Neri, R., et al. Nature, **463**(7282) (2010), 781. `1002.2149`.

Tacconi, L.J., Genzel, R., Saintonge, A., et al. ApJ, **853**(2) (2018), 179. `1702.01140`.

Tacconi, L.J., Genzel, R., Smail, I., et al. ApJ, **680**(1) (2008), 246. `0801.3650`.

Tacconi, L.J., Genzel, R., Sternberg, A. ARA&A, **58** (2020), 157. `2003.06245`.

Tacconi, L.J., Neri, R., Chapman, S.C., et al. ApJ, **640**(1) (2006), 228. `astro-ph/0511319`.

Thatte, N., Tecza, M., Clarke, F., et al. *HARMONI: a single-field wide-band integral-field spectrograph for the European ELT*. In I.S. McLean, S.K. Ramsay, H. Takami, editors, *Ground-based and Airborne Instrumentation for Astronomy III*, volume 7735 of *Society of Photo-Optical Instrumentation Engineers (SPIE) Conference Series* (2010), page 77352I.

Tiley, A.L., Bureau, M., Cortese, L., et al. MNRAS, **482**(2) (2019), 2166. `1810.07202`.

Tiley, A.L., Gillman, S., Cortese, L., et al. MNRAS, **506**(1) (2021), 323. `2106.05511`.

Toft, S., Smolčić, V., Magnelli, B., et al. ApJ, **782**(2) (2014), 68. `1401.1510`.

Tremonti, C.A., Heckman, T.M., Kauffmann, G., et al. ApJ, **613**(2) (2004), 898. `astro-ph/0405537`.

Tully, R.B., Fisher, J.R. A&A, **54** (1977), 661.

Turner, O.J., Cirasuolo, M., Harrison, C.M., et al. MNRAS, **471**(2) (2017), 1280. `1704.06263`.

Übler, H., Förster Schreiber, N.M., Genzel, R., et al. ApJ, **842**(2) (2017), 121. `1703.04321`.

Valentino, F., Daddi, E., Puglisi, A., et al. arXiv e-prints (2020a), arXiv:2006.12521. `2006.12521`.

Valentino, F., Magdis, G.E., Daddi, E., et al. ApJ, **869**(1) (2018), 27. `1810.11029`.

Valentino, F., Magdis, G.E., Daddi, E., et al. ApJ, **890**(1) (2020b), 24. `2001.01734`.

van der Vlugt, D., Hodge, J.A., Algera, H.S.B., et al. arXiv e-prints (2022), arXiv:2204.04167. `2204.04167`.

van der Werf, P.P., Isaak, K.G., Meijerink, R., et al. A&A, **518** (2010), L42. `1005.2877`.

Veilleux, S., Kim, D.C., Sanders, D.B. ApJS, **143**(2) (2002), 315. `astro-ph/0207401`.

Veilleux, S., Osterbrock, D.E. ApJS, **63** (1987), 295.

Vieira, J.D., Marrone, D.P., Chapman, S.C., et al. Nature, **495**(7441) (2013), 344. `1303.2723`.

Walter, F., Decarli, R., Aravena, M., et al. ApJ, **833**(1) (2016), 67. `1607.06768`.

Walter, F., Decarli, R., Carilli, C., et al. Nature, **486**(7402) (2012), 233. `1206.2641`.

Wang, S.X., Brandt, W.N., Luo, B., et al. ApJ, **778**(2) (2013), 179. `1310.6364`.

Wardlow, J.L., Simpson, J.M., Smail, I., et al. MNRAS, **479** (2018), 3879.

Wechsler, R.H., Tinker, J.L. ARA&A, **56** (2018), 435. `1804.03097`.

Weiner, B.J., Willmer, C.N.A., Faber, S.M., et al. ApJ, **653**(2) (2006), 1027. `astro-ph/0609090`.

Weiß, A., De Breuck, C., Marrone, D.P., et al. ApJ, **767**(1) (2013), 88. `1303.2726`.

Weiß, A., Henkel, C., Downes, D., et al. A&A, **409** (2003), L41. `astro-ph/0309048`.

Weiß, A., Ivison, R.J., Downes, D., et al. ApJ, **705**(1) (2009), L45. `0909.3177`.

Weiß, A., Kovács, A., Güsten, R., et al. A&A, **490**(1) (2008), 77. `0808.3358`.

Whitaker, K.E., van Dokkum, P.G., Brammer, G., et al. ApJ, **754**(2) (2012), L29. `1205.0547`.

Wilman, D.J., Fossati, M., Mendel, J.T., et al. ApJ, **892**(1) (2020), 1. `2002.09499`.

Wilson, G.W., Austermann, J.E., Perera, T.A., et al. MNRAS, **386**(2) (2008), 807. `0801.2783`.

Wisnioski, E., Förster Schreiber, N.M., Fossati, M., et al. ApJ, **886**(2) (2019), 124. `1909.11096`.

Wisnioski, E., Förster Schreiber, N.M., Wuyts, S., et al. ApJ, **799**(2) (2015), 209. `1409.6791`.

Wisnioski, E., Mendel, J.T., Förster Schreiber, N.M., et al. ApJ, **855**(2) (2018), 97. `1711.02111`.

Wootten, A., Thompson, A.R. IEEE Proceedings, **97**(8) (2009), 1463. `0904.3739`.

Wuyts, E., Wisnioski, E., Fossati, M., et al. ApJ, **827**(1) (2016a), 74. `1603.01139`.

Wuyts, S., Förster Schreiber, N.M., Nelson, E.J., et al. ApJ, **779**(2) (2013), 135. `1310.5702`.

Wuyts, S., Förster Schreiber, N.M., Wisnioski, E., et al. ApJ, **831**(2) (2016b), 149. `1603.03432`.

Yang, C., Omont, A., Beelen, A., et al. A&A, **608** (2017), A144. `1709.04740`.

Younger, J.D., Fazio, G.G., Huang, J.S., et al. ApJ, **671**(2) (2007), 1531. `0708.1020`.

Zhao, Y., Lu, N., Díaz-Santos, T., et al. ApJ, **892**(2) (2020), 145. `2002.04816`.

Zieleniewski, S., Thatte, N., Kendrew, S., et al. MNRAS, **453**(4) (2015), 3754. `1508.04441`.